

Lecture Notes in Mechanical Engineering

Chander Prakash  
Sunpret Singh  
Grzegorz Krolczyk  
B. S. Pabla *Editors*

# Advances in Materials Science and Engineering

Select Proceedings of ICFMMP 2019

 Springer

# **Lecture Notes in Mechanical Engineering**

## **Series Editors**

Fakher Chaari, National School of Engineers, University of Sfax, Sfax, Tunisia

Mohamed Haddar, National School of Engineers of Sfax (ENIS), Sfax, Tunisia

Young W. Kwon, Department of Manufacturing Engineering and Aerospace Engineering, Graduate School of Engineering and Applied Science, Monterey, CA, USA

Francesco Gherardini, Dipartimento Di Ingegneria, Edificio 25, Università Di Modena E Reggio Emilia, Modena, Modena, Italy

Vitalii Ivanov, Department of Manufacturing Engineering Machine and tools, Sumy State University, Sumy, Ukraine

**Lecture Notes in Mechanical Engineering (LNME)** publishes the latest developments in Mechanical Engineering—quickly, informally and with high quality. Original research reported in proceedings and post-proceedings represents the core of LNME. Volumes published in LNME embrace all aspects, subfields and new challenges of mechanical engineering. Topics in the series include:

- Engineering Design
- Machinery and Machine Elements
- Mechanical Structures and Stress Analysis
- Automotive Engineering
- Engine Technology
- Aerospace Technology and Astronautics
- Nanotechnology and Microengineering
- Control, Robotics, Mechatronics
- MEMS
- Theoretical and Applied Mechanics
- Dynamical Systems, Control
- Fluid Mechanics
- Engineering Thermodynamics, Heat and Mass Transfer
- Manufacturing
- Precision Engineering, Instrumentation, Measurement
- Materials Engineering
- Tribology and Surface Technology

To submit a proposal or request further information, please contact the Springer Editor of your location:

**China:** Dr. Mengchu Huang at [mengchu.huang@springer.com](mailto:mengchu.huang@springer.com)

**India:** Priya Vyas at [priya.vyas@springer.com](mailto:priya.vyas@springer.com)

**Rest of Asia, Australia, New Zealand:** Swati Meherishi at [swati.meherishi@springer.com](mailto:swati.meherishi@springer.com)

**All other countries:** Dr. Leontina Di Cecco at [Leontina.dicecco@springer.com](mailto:Leontina.dicecco@springer.com)

To submit a proposal for a monograph, please check our Springer Tracts in Mechanical Engineering at <http://www.springer.com/series/11693> or contact [Leontina.dicecco@springer.com](mailto:Leontina.dicecco@springer.com)

**Indexed by SCOPUS. The books of the series are submitted for indexing to Web of Science.**

More information about this series at <http://www.springer.com/series/11236>

Chander Prakash · Sunpret Singh ·  
Grzegorz Krolczyk · B. S. Pabla  
Editors

# Advances in Materials Science and Engineering

Select Proceedings of ICFMMP 2019


 Springer



*Editors*

Chander Prakash  
School of Mechanical Engineering  
Lovely Professional University  
Phagwara, India

Grzegorz Krolczyk  
Opole University of Technology  
Opole, Poland

Sunpret Singh   
Centre for Nanofibers and Nanotechnology  
National University of Singapore  
Singapore, Singapore

B. S. Pabla  
Department of Mechanical Engineering  
National Institute of Technical Teachers  
Training and Research  
Chandigarh, India

ISSN 2195-4356

ISSN 2195-4364 (electronic)

Lecture Notes in Mechanical Engineering

ISBN 978-981-15-4058-5

ISBN 978-981-15-4059-2 (eBook)

<https://doi.org/10.1007/978-981-15-4059-2>

© Springer Nature Singapore Pte Ltd. 2020

This work is subject to copyright. All rights are reserved by the Publisher, whether the whole or part of the material is concerned, specifically the rights of translation, reprinting, reuse of illustrations, recitation, broadcasting, reproduction on microfilms or in any other physical way, and transmission or information storage and retrieval, electronic adaptation, computer software, or by similar or dissimilar methodology now known or hereafter developed.

The use of general descriptive names, registered names, trademarks, service marks, etc. in this publication does not imply, even in the absence of a specific statement, that such names are exempt from the relevant protective laws and regulations and therefore free for general use.

The publisher, the authors and the editors are safe to assume that the advice and information in this book are believed to be true and accurate at the date of publication. Neither the publisher nor the authors or the editors give a warranty, express or implied, with respect to the material contained herein or for any errors or omissions that may have been made. The publisher remains neutral with regard to jurisdictional claims in published maps and institutional affiliations.

This Springer imprint is published by the registered company Springer Nature Singapore Pte Ltd. The registered company address is: 152 Beach Road, #21-01/04 Gateway East, Singapore 189721, Singapore

# Preface

The book entitled *Advances in Materials Science and Engineering*, by Springer, aims to present the comprehensive and broad-spectrum picture of the state-of-the-art research, development, and commercial perspectives of various discoveries conducted in the real-world materials science and their applications. This book also presents the various synthesis and fabrication routes of functional and smart materials for universal applications such as materials science, mechanical engineering, manufacturing, metrology, nanotechnology, physics, biology, chemistry, civil engineering, and food science. Indeed, the content of this book has opened various scientific horizons which are proved to be of utmost beneficial for uplifting the standards of the day-to-day practices in the biomedical domain. Noticeably, myriads of innovations in the materials science and engineering are transforming our day-to-day life in an extraordinary manner. This book has captured all the aforementioned trends of the materials science and engineering. With this, we are highly confident that this contribution will benefit all the readers in different ways.

Phagwara, India  
Singapore  
Opole, Poland  
Chandigarh, India

Chander Prakash  
Sunpreet Singh  
Grzegorz Krolczyk  
B. S. Pabla

# Contents

<b>A Brief Study on the Heterogeneity of the P91 Welded Joint</b> . . . . .	1
Sachin Sirohi, Chandan Pandey, and Amit Goyal	
<b>Recent Innovation on Synthesis Methods of Graphene-Based Composites</b> . . . . .	11
Ravi Kumar, Rajeev Rathi, and Sumit Sharma	
<b>Evaluation of Mechanical Properties of Carbon Fiber-Reinforced Multiwall Carbon Nanotube-Based Nanocomposites</b> . . . . .	31
Sumit Mahajan, Lochan Sharma, Mandeep Singh Rayat, and Ranjit Singh	
<b>Mechanical Characterization of 60Pb40Sn Reinforced Al6061 Self-healing Composite</b> . . . . .	49
Nitin Kumar Gupta, Manoj Kumar, and G. D. Thakre	
<b>A Brief Overview of Crystal Plasticity Approach for Computational Materials Modeling</b> . . . . .	61
Lakhwinder Singh, Sanjay Vohra, and Manu Sharma	
<b>Evaluation of Creep and Compressive Behavior of MWCNTs Reinforced Polyurethane Composites</b> . . . . .	71
Dinesh Kumar and Prashant Jindal	
<b>Influence of Particle Morphologies of Mesoporous Hydroxyapatite Nanopowders on Controlled Delivery of Vancomycin Drug</b> . . . . .	83
Ravinder Pal Singh and Jagdeep Singh	
<b>Critical Review on Corrosive Properties of Metals and Polymers in Oil and Gas Pipelines</b> . . . . .	99
Kanishka Jha, Dilip Dhakad, and Baljeet Singh	
<b>Synthesis and Characterization of Aluminum Composite Reinforced by Multiwall Carbon Nanotubes</b> . . . . .	115
Sunil Kumar Tiwari, Harsh Sharma, Akula Umamaheswararao, and Sumit Sharma	

<b>Effect of TiC Reinforcement in the Copper Tool on Roundness During EDM Process</b> .....	125
Arminder Singh Walia, Vineet Srivastava, Vivek Jain, and Suneev Anil Bansal	
<b>Mechanical and Microstructural Characterization of Magnesium/ Multi-walled Carbon Nanotubes Composites Fabricated via Friction Stir Processing</b> .....	137
Mayank Mishra, Chander Prakash, Rajashekhara Shabadi, and Subhash Singh	
<b>Influence of Surface Treatment and Molding Temperature on Mechanical Properties of Jute/PLA-Based Green Composites</b> .....	149
Jaiinder Preet Singh, Sehijpal Singh, Vikas Dhawan, Gurjot S. Dhaliwal, Piyush Gulati, Rajeev Kumar, and Manpreet Singh	
<b>Effect of Nanoclay in Unidirectional Carbon–Epoxy Laminated Composites</b> .....	159
Vishaldeep Singh, Manjeet Singh, J. S. Saini, Rohit Badhwar, Akash Gupta, and Nitin Chauhan	
<b>Microstructural Evolution and Mechanical Properties of Aluminum Alloy 7075-T651 Processed by Friction Stir Processing</b> .....	171
Ravi Kumar, Md. Manzar Iqbal, Subhash Singh, and Kaushik Pal	
<b>Pre- and Post-treatment Characterization of Petrol Contaminated Soil</b> .....	185
Shweta Kulshreshtha, Suchita Atreya, Sudhanshu Singh, and Nitesh Singh Rajput	
<b>Microstructural and Mechanical Properties of AA6061 Aluminium Alloy Reinforced with Nano-SiC Particles Using FSP</b> .....	195
Amardeep Singh Kang, Chander Prakash, Jasvinder Singh, and Alokesh Pramanik	
<b>Segregation and Recycling of Plastic Solid Waste: A Review</b> .....	205
Kapil Chawla, Rupinder Singh, and Jaspreet Singh	
<b>Vibration Response of Metal-Ceramic Based Functionally Graded Plate Using Navier Solution</b> .....	223
Yogesh Kumar, Dheer Singh, and Ankit Gupta	
<b>Influence of the Microstructural and Mechanical Properties of Reinforced Graphene in Magnesium Matrix Fabricated by Friction Stir Processing</b> .....	235
Nazish Alam, Md. Manzar Iqbal, Chander Prakash, Subhash Singh, and Animesh Basak	

**Strength Properties of M40 Concrete with Rice Husk Ash as Partial Replacement of Cement** . . . . . 249  
Jaspreet Singh, Vishal kumar, Harkamal Singh, and Amar Singh

**Influence of Graphene on Mechanical Behavior of EVA Composite at Low Strain Rate Loading** . . . . . 261  
Kanwer Ajit Singh, Dinesh Kumar, and Prashant Jindal

**Development and Electrical Properties of Titanium Dioxide-Based Polymer Nanocomposite Structures** . . . . . 271  
Sudhanshu Singh, Nitesh Singh Rajput, Deepshikha Rathore, and Umesh Kumar Dwivedi

**Investigation of Structural and Electronic Properties of BaX (X = S, Se, and Te): A DFT Study** . . . . . 281  
Agnibha Das Majumdar, Neha Munjal, Uma Kamboj, and Karan Dogra

## About the Editors

**Dr. Chander Prakash** is Associate Professor in the School of Mechanical Engineering, Lovely Professional University, Jalandhar, India. He has received Ph.D in mechanical engineering from Panjab University, Chandigarh, India. His area of research is biomaterials, rapid prototyping & 3-D printing, advanced manufacturing, modeling, simulation, and optimization. He has more than 11 years of teaching experience and 6 years' of research experience. He has contributed extensively to the world in the titanium and magnesium based implant literature with publications appearing in Surface and Coating Technology, Materials and Manufacturing Processes, Journal of Materials Engineering and Performance, Journal of Mechanical Science and Technology, Nanoscience and Nanotechnology Letters, Proceedings of the Institution of Mechanical Engineers, Part B: Journal of Engineering Manufacture. He has authored 60 research papers and 10 book chapters. He is also editor of 3 books: "Current Trends in Bio-manufacturing", Springer Series in Advanced Manufacturing, Springer International Publishing AG, Gewerbestrasse 11, 6330 Cham, Switzerland., Dec. 2018; "3D Printing in Biomedical Engineering", Book series Materials Horizons: From Nature to Nanomaterials, Springer International Publishing AG, Gewerbestrasse 11, 6330 Cham, Switzerland., August 2019, and "Biomaterials in Orthopaedics and Bone Regeneration - Design and Synthesis", Book series Materials Horizons: From Nature to Nanomaterials, Springer International Publishing AG, Gewerbestrasse 11, 6330 Cham, Switzerland., March 2019. He is also guest editor of 3 journals: special issue of "Functional Materials and Advanced Manufacturing", Facta Universitatis, Series: Mechanical Engineering (Scopus Index), Materials Science Forum (Scopus Index), and special issue on "Metrology in Materials and Advanced Manufacturing", Measurement and Control (SCI indexed).

**Dr. Sunpret Singh** is researcher in NUS Nanoscience & Nanotechnology Initiative (NUSNNI). He has received Ph.D in Mechanical Engineering from Guru Nanak Dev Engineering College, Ludhiana, India. His area of research is additive manufacturing and application of 3D printing for development of new biomaterials for clinical applications. He has contributed extensively in additive manufacturing

literature with publications appearing in Journal of Manufacturing Processes, Composite Part:B, Rapid Prototyping Journal, Journal of Mechanical Science and Technology, Measurement, International Journal of Advance Manufacturing Technology, and Journal of Cleaner Production. He has authored 10 book chapters and monographs. He is working in joint collaboration with Prof. Seeram Ramakrishna, NUS Nanoscience & Nanotechnology Initiative and Prof. Rupinder Singh, manufacturing research lab, GNDEC, Ludhiana. He is also editor of 3 books: “Current Trends in Bio-manufacturing”, Springer Series in Advanced Manufacturing, Springer International Publishing AG, Gewerbestrasse 11, 6330 Cham, Switzerland., Dec. 2018; “3D Printing in Biomedical Engineering”, Book series Materials Horizons: From Nature to Nanomaterials, Springer International Publishing AG, Gewerbestrasse 11, 6330 Cham, Switzerland., August 2019, and “Biomaterials in Orthopaedics and Bone Regeneration - Design and Synthesis”, Book series Materials Horizons: From Nature to Nanomaterials, Springer International Publishing AG, Gewerbestrasse 11, 6330 Cham, Switzerland., March 2019. He is also guest editor of 3 journals: special issue of “Functional Materials and Advanced Manufacturing”, Facta Universitatis, Series: Mechanical Engineering (Scopus Index), Materials Science Forum (Scopus Index), and special issue on “Metrology in Materials and Advanced Manufacturing”, Measurement and Control (SCI indexed).

**Prof. Grzegorz Krolczyk** is Professor in the Opole University of Technology. He is an originator and a Project Manager of OUTEch’s new Surface Integrity Laboratory. In his career he has held positions such as: head of unit design and technology, product engineer, production manager, product development engineer and production director. He is the co-author and project leader of a project Innovative, energy-efficient diaphragm flow device of a new generation. He is connected with the mechanical industry, where he managed teams from a few to over a hundred people. His industrial engineering experience was gained while working in an European holding company involved in machining of construction materials and plastic injection, where he was responsible for contacts with companies on technical issues such as quotation and implementation of new products. In professional career he was responsible from the implementation to production of products such as peristaltic pumps, ecological sprayers to spray organic pesticides and many pressure equipment operating e.g. in chemical plants. As a production manager, he was responsible from implementation to production and launching the assembly line for innovative sprayer ultra-low volume spraying system. He is author and co-author of over 80 scientific publications and nearly 20 studies and implementation of industry. The main directions of scientific activity are surface metrology, optimization of geometrical and physical parameters of surface integrity, optimization of production and cutting tool wear analysis in dry machining process of difficult-to-cut materials. He is also editor of various Journals and Books.

**Prof. B. S. Pabla** is Dean Extension Services & Consultancy and Professor in Mechanical Engineering, National Institute of Technical Teachers Training & Research, Chandigarh, India. His has received Ph.D in mechanical engineering from Panjab University, Chandigarh, India. His area of research is non-traditional machining, CAD/CAM, biomaterials and bio-manufacturing. He has more than 37 years of teaching and research experience. He has contributed extensively to the world in materials and manufacturing processes literature with publications appearing in Surface and Coating Technology, Materials and Manufacturing Processes, Journal of Materials Engineering and Performance, Journal of Mechanical Science and Technology, Nanoscience and Nanotechnology Letters, Proceedings of the Institution of Mechanical Engineers Part B: Journal of Engineering Manufacture. He has granted 2 patents, published 5 books, and completed more than 10 research projects from various funding agencies.



# A Brief Study on the Heterogeneity of the P91 Welded Joint



Sachin Sirohi, Chandan Pandey, and Amit Goyal

**Abstract** The gradient microstructure occurs along with the P91 steel pipe welds joint which has been characterized in detail. The welding thermal cycle results in variation in mechanical behavior along the welded joint that leads the degradation in the mechanical performance of the welded joint at elevated service temperature in power plants. The gas tungsten arc welded (GTAW) joint has been subjected to as-welded and heat treatment conditions to study the role of heterogeneity on microstructure across the welded joint and the mechanical properties. The P91 welded joints have been subjected to tempering at 760 °C for 2 h (HT1) and post-weld normalizing and tempering (HT2). The precipitation hardening, quenching stress in welded joint and martensite softening are mainly associated with heat treatment. A negligible variation in hardness and microstructure has been observed across the welded joint for HT2 treatment.

**Keywords** P91 · GTAW · Heterogeneity · Welded joint · Microhardness

## 1 Introduction

The 9Cr-1Mo-V-Nb (P91) martensitic steel is an attractive material for fossil power plant components having an operating temperature which is more than 650 °C due to high-temperature microstructure stability and attractive mechanical properties [1–3]. P91 steel offers high oxidation and corrosion resistance, resistance toward corrosion cracking along with high thermal conductivity and low-temperature thermal expansion coefficient [4–6]. Metallurgical behavior and mechanical properties of the P91 steel are highly influenced by the heat treatment, and it is subjected to normalizing and tempering before long-term elevated temperature service [7–9]. The material

---

S. Sirohi (✉) · A. Goyal  
Mechanical Department, SRM IST, Modinagar, Uttar Pradesh 201204, India  
e-mail: [sachinsirohi2008@gmail.com](mailto:sachinsirohi2008@gmail.com)

C. Pandey (✉)  
Department of Mechanical Engineering, IIT Jodhpur, Karwar, Rajasthan 342037, India  
e-mail: [jscpandey@iitj.ac.in](mailto:jscpandey@iitj.ac.in)

© Springer Nature Singapore Pte Ltd. 2020  
C. Prakash et al. (eds.), *Advances in Materials Science and Engineering*,  
Lecture Notes in Mechanical Engineering,  
[https://doi.org/10.1007/978-981-15-4059-2\\_1](https://doi.org/10.1007/978-981-15-4059-2_1)

derives their strength from the tempered martensite along with dislocation density and grain boundaries surrounded by  $M_{23}C_6$  carbide and MX carbonitride [10, 11]. A drastic change in the microstructure is reported during the prolonged service duration and deals with lath widening, grain coarsening, precipitate coarsening and evolution of the inter-metallic Laves and Z-phase [12–17].

In P91 welded joint, the microstructure gradient across the welded joint is reported by the researchers as result of high heat input. The region adjacent to the fusion boundary is subjected to higher temperature, and temperature decreases as to move away from the fusion boundary. The microstructure strongly depends on the temperature experienced by the region, and it leads to variation in the mechanical behavior of the welded joint [18, 19]. The welding cycle also introduces the quenching stress in weld fusion zone along with the formation of the untempered brittle martensitic microstructure. All these factors degrade the mechanical performance of the welded joint. The transition heat-affected zone (HAZ) area forms after the fusion boundary and also shows the gradient microstructure due to the variation in temperature experienced by the region and divided into number of sub-zones. The maximum temperature experienced in coarse-grained HAZ (CGHAZ) that resulted in the formation of coarse grain with high strength and poor Charpy toughness. The region of HAZ near the unaffected base zone experienced the low temperature among all HAZs and forms a complex microstructure of undissolved coarse precipitates and newly formed untempered martensite and tempered martensite. The region is considered as the softest zone and termed as inter-critical HAZ (ICHAZ) [20]. The region deals with high Charpy toughness and poor strength among all HAZs. The fine-grained HAZ (FGHAZ) region experienced the temperature more than the experienced by ICHAZ and less than the experienced by CGHAZ and represents the moderate Charpy toughness and strength. The creep properties and rupture life of welded joint are strongly governed by the variation in mechanical properties of the welded joint. The most common type of the failure for P91 welded joint was reported in soft ICHAZ and termed as Type IV cracking [21, 22]. Hence, heterogeneity across the welded joint is mainly responsible for Type IV cracking and also leads to the poor mechanical strength of the welded joint.

The present work focused to overcome the microstructure gradient across P91 welded joint using different heat treatments.

## 2 Experimental Details

P91 steel pipe of outer diameter 60 mm and thickness of 11 mm has been utilized for making the weld joint using gas tungsten arc welding (GTAW) process using the AWSER90S-B9 electrode, and the composition of pipe material and filler is listed in Table 1. As per the manufacturer, the heat treatment condition was described below: (1) Normalizing was carried out for 10 min at 1040 °C/air cooling, (2) tempering for 120 min at 760 °C/air cooling. The schematic of heat treatment is shown in Fig. 1. The process parameters for root pass and filling passes are depicted in Table 2.

**Table 1** Chemical composition of the steel plats used for joint (wt%)

Element	Fe	C	Si	Ni	Mn	Cr	Mo	V	Nb
P91	Rest	0.11	0.27	0.35	0.54	8.48	0.94	0.14	0.06
AWSER90S-B9 (9CrMoV-N) filler wire	Rest	0.12	0.30	0.50	0.50	9.0	0.90	0.20	0.05

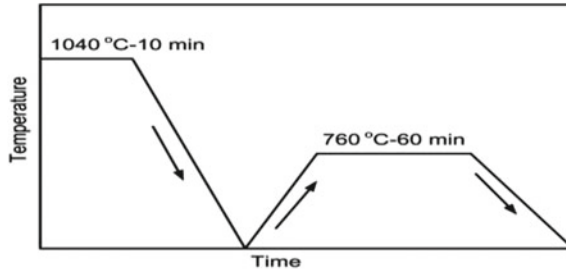


**Fig. 1** Heat treatment applied on received P91 pipe

**Table 2** Welding process parameters and heat treatment for welded joint

No. of passes	Current (amp)	Voltage (V)
Root pass	105–115	12
Filling passes (1–8)	115–125	12–20
<i>Heat treatment</i>		
HT1	–	Tempering at 760 °C/2 h
HT2	Normalizing at 1040°C for 40 min	Tempering at 760 °C for 2 h

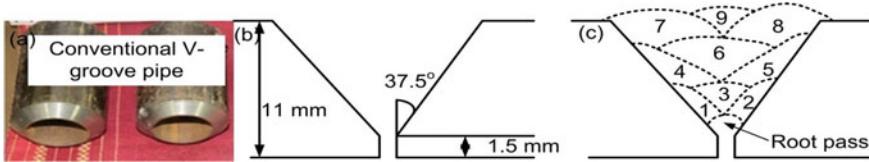


**Fig. 2** a Grooved pipe, b groove design, c schematic of root and filling pass

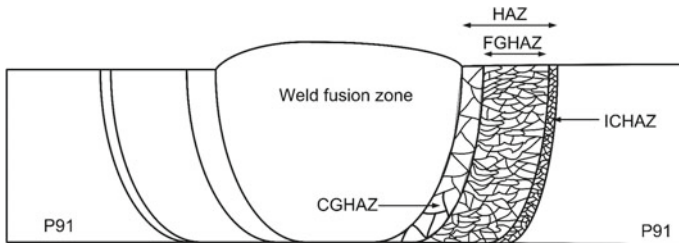


**Fig. 3** Schematic of the weld fusion zone and heat-affected zones in P91 welded pipe

The grooved pipe, groove design and filling pass are shown in Fig. 2. Welding was performed in medium of pure argon gas, and flow rate was 15 l/min. The schematic of the welded joint with different zones is shown in Fig. 3. The welded joint subjected to two different type of the heat treatment process, HT1 and HT2, as shown in Table 2.

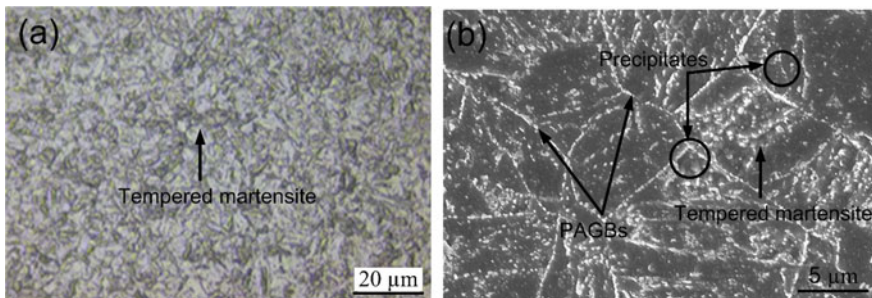
For microstructure characterization, the specimens were removed from the heat-treated samples and subjected to standard polishing and after that etched in Vilella's solution. Optical microscopy and scanning electron microscopy have been utilized for the microstructure characterization, and microhardness tester has been utilized for the hardness measurement at the load of 500 g.

### 3 Results and Discussion

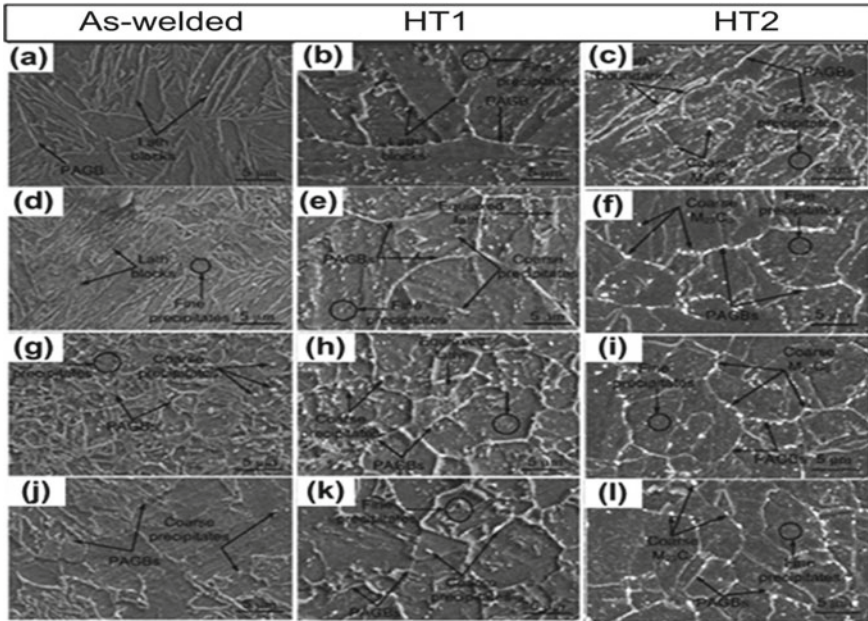
#### 3.1 Characterization of As-received Metal and Weldments

Figure 4a shows the typical optical micrograph of P91 steel consisting of tempered martensite. The micrograph consists of equiaxed prior austenite grains (PAGs) with grain boundaries. The carbide particles are observed to be allocated along the PAGBs, while fine particles are observed inside the boundary region (Fig. 4b). The carbide rich  $M_{23}C_6$  precipitates are confirmed along the lath and PAG boundaries having cylindrical, spherical or globular shape with size in range of 100–200 nm, while the fine particles of V and Nb-enriched carbonitride are inside the boundary region of size in range of 10–40 nm [23, 24].

The typical SEM micrograph of the welded joint is depicted in Fig. 5. For as-welded condition, a micrograph of the weld zone (WZ) consisted of untempered lath martensite with typical columnar laths (Fig. 5a). Precipitates that enhance the strength of the material get dissolved during the welding as a result of high peak temperature and contribute to solid solution strengthening. The CGHAZ is characterized by coarse PAGs with negligible precipitates (Fig. 5d). The dissolution of grain boundaries' particles during the welding cycle results in coarse grain formation in CGHAZ. In FGHAZ, equiaxed grain with partially dissolved precipitates is observed (Fig. 5g). The ICHAZ shows a complex microstructure of coarse and fine



**Fig. 4** a Optical micrograph of P91 steel, b SEM image of P91 steel showing PAGBs and precipitates



**Fig. 5** Typical SEM image of the various zones in P91 welded pipe for weld fusion zone **a** as-welded, **b** HT1, **c** HT2; CGHAZ, **d** as-welded, **e** HT1, **f** HT2; FGAZ, **g** as-welded, **h** HT1, **i** HT2; ICHAZ, **j** as-welded, **k** HT1, **l** HT2

PAGs. The temperature experienced in ICHAZ is not sufficient to dissolve the precipitates and results in the formation of microstructure with undissolved precipitates and new PAGs. Figure 5j shows the typical micrograph of the ICHAZ. Each zone of the P91 welded joint shows a unique characteristic that results in a microstructure gradient across the weld joint. To overcome microstructure gradient and enhance the strength of the welded joint, heat treatment has been performed as discussed below.

The HT1 results in a tempering reaction that imparts the ductility. The tempering reaction leads to the precipitation of dissolved carbide particles that result in softening of the martensitic matrix due to reduction in solid solution hardening. The various zone of the welded joint after the HT1 is shown in Fig. 5. The WZ is characterized by newly precipitated particles with columnar lath morphology, as depicted in Fig. 5b. In CGHAZ, the precipitate gets evolved along the PAGBs and lath boundaries and considered as the Cr, Mo-rich  $M_{23}C_6$ -type carbides. The fine MX and  $M_{23}C_6$  precipitates are also observed inside the lath blocks. However, the microstructure of CGHAZ was observed completely different from the WZ (Fig. 5e). The FGAZ and ICHAZ show similarity in terms of microstructure after the HT1 treatment and consist of tempered martensite with equiaxed laths. However, in both the zone, heterogeneity still exists in terms of particle size as a result of the partial dissolution of the precipitates during the welding cycle. The size of  $M_{23}C_6$  particles was measured in range of 100–250 nm for WZ and CGHAZ; however, it was more

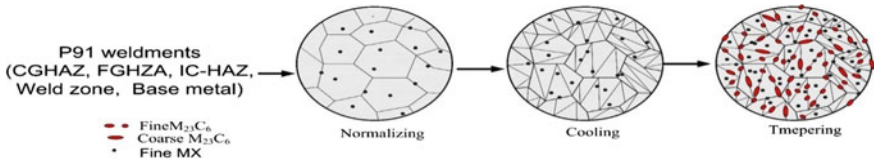


**Fig. 6** Schematic of the sub-zone in P91 welded pipe after the HT2 treatment [18]

than 250 nm in FGHAZ/ICHAZ. The coarse precipitate in soft zone behaves as brittle particles and facilitates the crack nucleation sites. Figure 5h, k shows the micrograph of FGHAZ and ICHAZ, respectively. Hence, it is clear that the HT1 minimizes the microstructure gradient; however, it does not remove it completely.

In HT2 treatment, the micrograph of different zone is shown in Fig. 5. In WZ, the columnar laths and PAGs are observed clearly (Fig. 5c). It looks completely different from the WZ present in HT1 condition. In HT2 condition, normalizing results in the dissolution of the precipitates in weldments and welded joint homogenized in terms of microstructure, but it offers higher strength and hardness due to higher solid solution hardening. The tempering of the normalized welded joint was performed to overcome the brittleness and impart the ductility by reducing the solid solution hardening. A schematic of the precipitates evolution across the welded joint as a result of HT2 treatment is presented by Pandey et al. [18] and shown in Fig. 6. The micrograph of CGHAZ, FGHAZ and ICHZ looks similar in HT2 condition, but it was completely different as compared to the micrograph of HT1 condition. In HT2 condition, coarse PAGs and carbide precipitates are observed as compared to HT1 condition. The gathering of the coarse carbide particles along the PAGs is clearly noticed from the SEM micrograph of HAZs. From the micrograph, it is clear that the heterogeneity present along the weld joint in terms of microstructure gets removed after the HT2 treatment. However, the coarse precipitates in HT2 condition might lead to the failure of the welded joint because of their brittle nature.

The grain size variation along the welded joint was measured in welding and HT conditions. Without HT, the grain size was measured  $250 \pm 35 \mu\text{m}$ ,  $35 \pm 10 \mu\text{m}$  and  $25 \pm 8 \mu\text{m}$  for CGHAZ, FGHAZ and ICHAZ, respectively, that clearly shows the heterogeneity in the microstructure along the welded joint of P91 pipe. In HT1 condition, it was measured  $280 \pm 25 \mu\text{m}$ ,  $55 \pm 10 \mu\text{m}$  and  $52 \pm 12 \mu\text{m}$  for CGHAZ, FGHAZ and ICHAZ, respectively. It is clear that HT1 results in the coarsening of the grains. The grain size measured for the FGHAZ and ICHAZ was almost similar, but it was much lower than the CGHAZ ( $280 \pm 25 \mu\text{m}$ ). In HT2 condition, the grain size was measured  $75 \pm 12 \mu\text{m}$ ,  $72 \pm 13 \mu\text{m}$ ,  $72 \pm 12 \mu\text{m}$  and  $73 \pm 15 \mu\text{m}$  for CGHAZ, FGHAZ, ICHAZ and WZ, respectively. A negligible variation in grain size for HT2 condition confirms the homogeneity across the welded joint.



### 3.2 Microhardness

The variation in the microstructure governs the variation in mechanical properties such as strength, hardness and Charpy toughness. The hardness variation is shown in Fig. 7. In as-welded condition, WZ and CGHAZ show the hardness more than 450 HV that is attributed to untempered lath martensite. The WZ hardness was measured in range of 450–490 HV with average of  $470 \pm 10$  HV, while the peak hardness in CGHAZ was 480 HV due to the formation of untempered martensite. The variation in the hardness in WZ is attributed to the preheating of the filling passes by the subsequent passes. The hardness was noticed as a function of the HAZ width and shows a continuous reduction as to move away from fusion boundary to base metal and maximum variation was measured in FGHAZ. The maximum and minimum hardness were measured 400 HV and 320 HV, respectively. The minimum hardness was measured 232 HV in ICHAZ. For HT1 condition, the variation in hardness of the WZ and FGHAZ gets reduced as compared to that of as-welded condition, and it was measured 235 HV, 230 HV and 243 HV for WZ, FGHAZ and CGHAZ, respectively. The hardness of the soft ICHAZ zone was remained unaffected after the HT1 treatment, and it was 221 HV. From the hardness variation, it is clear that heterogeneity gets reduced as a result of tempering reaction. However, the variation in CGHAZ and ICHAZ hardness is still noticeable.

In HT2 condition, a negligible heterogeneity was measured in the hardness value, and peak hardness was measured  $215 \pm 6$  and  $213 \pm 8$  HV for CGHAZ and ICHAZ, respectively. Hence, it is clear that HT2 is more effective to overcome the gradient across the welded joint.

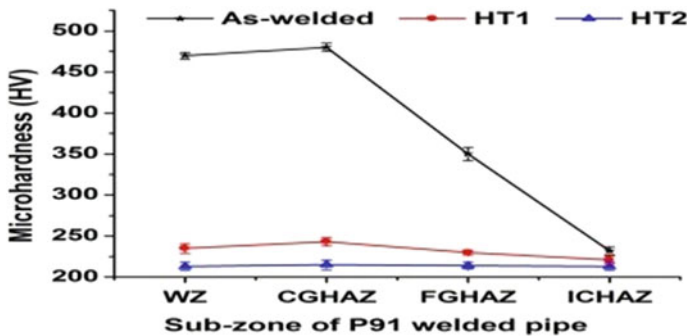


Fig. 7 Variation in hardness for different heat treatment processes



## 4 Conclusions

The paper discussed the effect of the HT on the heterogeneity of the P91 pipe weld joint in terms of microstructure and microhardness. In as-welded condition, the microstructure gradient across the welded joint led to the variation in hardness of the welded joint. The HT1 treatment produced the microstructure with moderate heterogeneity across the welded joint, while in HT2 treatment, a negligible gradient was observed. However, the size of precipitates was measured higher in case of HT2 than that of HT1 condition.

## References

1. Klueh, R.L., Van Der Schaaf, B., Victoria, M.: Ferritic/ martensitic steels—overview of recent results. *J. Nucl. Mater.* **311**, 455–465 (2008)
2. Danon, C.A.: Evolution of minor phases in a P91 steel normalized and tempered at different temperatures. *Procedia Mater. Sci.* **8**, 1089–1098 (2015)
3. Pandey, C., Mohan Mahapatra, M., Kumar, P., Thakre, J.G., Saini, N.: Role of evolving microstructure on the mechanical behaviour of P92 steel welded joint in as-welded and post weld heat treated state. *J. Mater. Process. Technol.* **263**, 241–255 (2018)
4. Wang, Y., Kannan, R., Zhang, L., Li, L.: Microstructural analysis of the as-welded heat-affected zone of a grade 91 steel heavy section weldment. *Weld. J.* **96**, 203–219 (2017)
5. Chen, L., Yamashita, K.: Effects of pwht temperature on mechanical properties of high-cr ferritic heat-resistant. *Weld. World.* **56**, 81–91 (2012)
6. Pandey, C., Giri, A., Mahapatra, M.M., Kumar, P.: Characterization of microstructure of HAZs in as-welded and service condition of P91 pipe weldments. *Met. Mater. Int.* **23** (2017)
7. Elmaoula, A.E.A., Abdelaziz, H.M., Mosa, E.S., Morsi, M.A., Atlam, A.: Effect of post weld heat treatment and filler metals on microstructures and mechanical properties of GTAW and SMAW weldments between P11 and P91 Steels. *Int. J. Sci. Eng. Res.* **6**, 620–631 (2015)
8. Lomozik, M., Hernas, A., Zeman, M.L.: Effect of welding thermal cycles on the structure and properties of simulated heat-affected zone areas in X10CrMoVNb9-1 (T91) steel at a state after 100,000 h of operation. *Mater. Sci. Eng., A* **637**, 82–88 (2015)
9. Pandey, C., Mahapatra, M.M., Kumar, P., Saini, N.: Characterization of cast and forged (C&F) Gr. 91 steel in different heat treatment condition. *Trans. Indian Inst. Met.* (2017)
10. Pandey, C., Mahapatra, M.M., Kumar, P., Saini, N.: Some studies on P91 steel and their weldments. *J. Alloys Compd.* **743**, 332–364 (2018)
11. Pandey, C., Mahapatra, M.M., Kumar, P., Saini, N., Thakre, J.G.: Nano-size particle evolution during heat treatment of P91 steel and their effect on micro hardness. *Trans. Indian Inst. Met.* (2017)
12. Prakash, C., Singh, S., Singh, M., Gupta, M.K., Mia, M., Dhanda, A.: Multi-objective parametric appraisal of pulsed current gas tungsten arc welding process by using hybrid optimization algorithms. *Int. J. Adv. Manuf. Tech.* **101**, 1107–1123 (2019)
13. Pandey, C., Mahapatra, M.M.: Effect of long-term ageing on the microstructure and mechanical properties of creep strength enhanced ferritic P91 steel. *Trans. Indian Inst. Met.* **69**, 1657–1673 (2016)
14. Klueh, R.L.: Elevated temperature ferritic and martensitic steels and their application to future nuclear reactors. *Int. Mater. Rev.* **50**, 287–310 (2005)
15. Sklenička, V., Kuchařová, K., Svoboda, M., Kloc, L., Buršík, J., Kroupa, A.: Long-term creep behavior of 9–12% Cr power plant steels. *Mater. Charact.* **51**, 35–48 (2003)

16. Pandey, C., Mahapatra, M.M., Kumar, P.: Effect of post weld heat treatments on fracture frontier and type IV cracking nature of the crept P91 welded sample. *Mater. Sci. Eng., A* **731**, 249–265 (2018)
17. Pandey, C., Mahapatra, M.M., Kumar, P., Kumar, S.: Effect of post weld heat treatments on microstructure evolution and type IV cracking behavior of the P91 steel welded joint. *J. Mater. Process. Technol.* **266**, 140–154 (2019)
18. Pandey, C., Mahapatra, M.M., Kumar, P., Saini, N.: Homogenization of P91 weldments using varying normalizing and tempering treatment. *Mater. Sci. Eng., A* **710**, 86–101 (2018)
19. Pandey, C., Giri, A., Mahapatra, M.M., Kumar, P.: Characterization of microstructure of HAZs in as-welded and service condition of P91 pipeweldments. *Met. Mater. Int.* **23**, 148–162 (2017)
20. Pandey, C., Mahapatra, M.M., Kumar, P., Saini, N.: Effect of weld consumable conditioning on the diffusible hydrogen and subsequent residual stress and flexural strength of multi-pass welded P91 steels. *Metall. Mater. Trans. B* **49**, 2881–2895 (2018)
21. Watanabe, T., Tabuchi, M., Yamazaki, M., Hongo, H., Tanabe, T.: Creep damage evaluation of 9Cr-1Mo-V-Nb steel welded joints showing type IV fracture. *Int. J. Press. Vessel. Pip.* **83**, 63–71 (2006)
22. Albert, S.K., Matsui, M., Watanabe, T., Hongo, H., Kubo, K., Tabuchi, M.: Variation in the type IV cracking behaviour of a high Cr steel weld with post weld heat treatment. *Int. J. Press. Vessel. Pip.* **80**, 405–413 (2003)
23. Panait, C.G., Zielinska-Lipiec, A., Koziel, T., Czyska-filemonowicz, A., Gourgues-Lorenzon, A.F., Bendick, W.: Evolution of dislocation density, size of subgrains and MX-type precipitates in a P91 steel during creep and during thermal ageing at 600 °C for more than 100,000 h. *Mater. Sci. Eng. A* **527**, 4062–4069 (2010)
24. Pandey, C., Mahapatara, M.M., Kumar, P., Saini, N.: Dissimilar joining of CSEF steels using autogenous tungsten-inert gas welding and gas tungsten arc welding and their effect on  $\delta$  ferrite evolution and mechanical properties. *J. Manuf. Process.* **31**, 247–259 (2018)

# Recent Innovation on Synthesis Methods of Graphene-Based Composites



Ravi Kumar, Rajeev Rathi, and Sumit Sharma

**Abstract** Graphene has been considered as one of the best carbon-based nanofillers for different composites. Recently, the use of graphene as nanofillers has been studied intensively, and several researchers start developing graphene-based composites. Inclusion of graphene in a small quantity in the given matrix can create composites with remarkable functional properties. It is very important to understand various synthesis routes of graphene-based composites because the synthesis route affects the dispersion of the graphene in a matrix material. Despite the exceptional potential of graphene, homogeneous dispersion in a matrix remains the key challenge. In this article, different synthesis methods of graphene-based composites have been explored and made a discussion on different preparation routes of graphene-based composites. Present study provides several insights into preparation methods to researchers and practitioners of graphene-based composites.

**Keywords** Graphene · Synthesis · Composites · Nanofiller · Solution blending · Melt mixing · In situ polymerization

## 1 Introduction

Nowadays, composites with various reinforcement or nanofiller materials are endowed with great mechanical, electrical and optical properties. As per the current scenario, various carbon-based nanofillers are used to boost different properties of the composite. Owing to their distinctive combinations of mechanical, optical and electrical properties, carbon-based nanocomposites have been explored for different industrial applications. The presence of these nanofiller increases the thermal and

---

R. Kumar · R. Rathi (✉)

School of Mechanical Engineering, Lovely Professional University, Phagwara, Punjab 144411, India

e-mail: [rathi.415@gmail.com](mailto:rathi.415@gmail.com)

S. Sharma

Dr. B. R. Ambedkar, National Institute of Technology, Jalandhar, Punjab 144011, India

e-mail: [sharmas@nitj.ac.in](mailto:sharmas@nitj.ac.in)

© Springer Nature Singapore Pte Ltd. 2020

C. Prakash et al. (eds.), *Advances in Materials Science and Engineering*,

Lecture Notes in Mechanical Engineering,

[https://doi.org/10.1007/978-981-15-4059-2\\_2](https://doi.org/10.1007/978-981-15-4059-2_2)

electromagnetic properties of the polymer composites. Carbon-based nano materials such as carbon nanotubes (CNTs), graphene oxide (GO), fullerenes and nanodiamonds are the important materials for various applications in medicine including drug delivery. Mechanical, thermal and electronic properties can readily increase by adding nanofiller contents in various matrix materials. Carbon nanotubes possess outstanding mechanical, thermal, electrical properties and lightweight properties as it shows thermal stability up to 2800 °C, thermal conductivity double as high as diamond and high electric current capacity. It has been studied that increased concentration of CNTs can increase different properties of composites. From the perspective of properties and cost, it is required to find out the alternative of CNTs which can produce potential properties. Several studies reveal that properties of graphene are much better than CNTs upon the same loading in matrix. The entire interest of the researchers has been shifted towards graphene as filler due to its extraordinary properties over all other nanofillers. The reason of their interest is due to significant properties like high electron mobility at room temperature, high thermal conductivity, good electrical conductivity and high modulus of elasticity. The properties of graphene-based composites are affected by their fabrication method adopted during their development. These properties are greatly depending on the dispersion rate of graphene in polymer or metal matrix, and the fabrication route of the composites strongly affects the dispersion rate of graphene. In order to get uniform dispersion of graphene, different preparation routes are used by researchers in literature. Like solution mixing is used to fabricate graphene-based composites by mixing solvent in graphene using ultrasonication. Melt mixing is used by mixing graphene and desired matrix in a molten state by stirring them at the required temperature. Existing methods for synthesis provide only 70–80% dispersion, and 100% uniform dispersion still remains the key challenge. Till now, this is very challenging for a practitioner to pick up a suitable method for the synthesis of graphene-based composites among available methods. So, the present study is to thoroughly review the different synthesis route of graphene-based composites in order to explore the best method for specific application.

Although so many challenges are there in developing graphene-based composites, these specific materials are still able to find their applications in different fields as mentioned in Fig. 1. With high carrier mobility, high electrical conductivity and optical transmittance in visible limits of spectrum, graphene-based composites have been used in solar cells, LCD's and OLED's. Li-ION battery as the energy storage device is considered as the most promising storage system due to its high absolute potential and solution blending and in situ methods are most common methods in the preparation of these storage systems. These composites are also able to find their properties in the field of biomedical where drug delivery, gene delivery, bioimaging, artificial muscles and cancer therapy are the most common application.

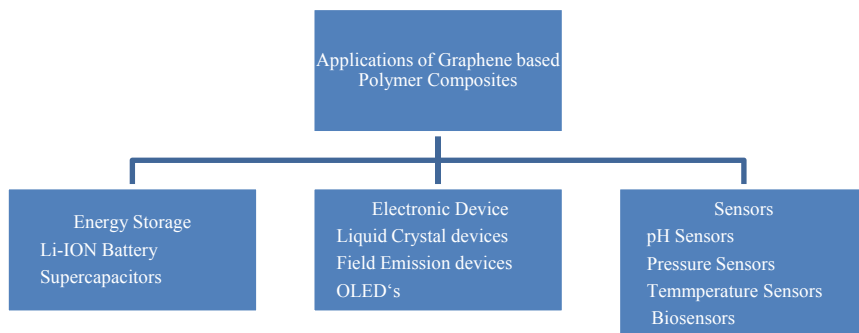


**Fig. 1** Applications of graphene-based composites

## 2 Literature Search Methodology

In this present study, systematic review of the literature, which explores the common factors of dispersion of graphene, has been reviewed. While undertaking literature review, low impact journals were excluded. Thus, only high impact journals like Elsevier, Taylor & Francis, journal of materials chemistry, macromolecules, polymer and advanced materials and interfaces were included in the literature review. While searching for relevant research papers, different keywords have been used such as synthesis of graphene, polymer composites, solution mixing, ultrasonication, melt compounding and in situ polymerization. During this literature review, less than ten-year-old peer-reviewed journal papers were considered. The data which were not relevant to the topic or lacked explanations were removed from the study. While carrying out a review, we filter out nearly 50 relevant papers for deep exploratory analysis of synthesis method of composites. The analysis is processed under various characteristics in response to year of publication, journals, authors, research methods and drawbacks of synthesis methods.

## 3 Graphene as Nanofiller

Graphene is a flat two-dimensional, one atom thick single layer of carbon atoms with distinctive properties. Graphene is composed of pure carbon with atom arranged in a hexagonal pattern as same as graphite. It has attracted the grand attention of academicians and engineers due to its magnificent properties. Graphene can be used as a nanofiller or reinforcement to enhance various properties of polymers, ceramics and metals matrix. It holds astounding high Young's modulus, tensile strength, aspect ratio and surface area. Due to these above-mentioned properties, graphene is used for different applications like OLEDs, LCDs, solar cells, sensors, batteries and super capacitors. Reinforcing efficiency of graphene depends on the homogeneous

**Table 1** Applications and properties of graphene

Author; year	Material	Author's remarks
Wang et al. (2018) [2]	Graphene	Graphene exhibits superior flexibility and reliability over 60,000 cycles of 180° bending and releasing without fracture
Neuberger et al. (2018) [3]	Graphene	Author reviewed the unique applications of graphene in the oil and gas industry which includes drilling and lubrication
Papageorgiou et al. (2017) [4]	Graphene	Author carried out a review study on different preparation and exfoliation routes of graphene. It has been concluded that applications of graphene are practically endless because of its great mechanical properties
Fazli et al. (2015) [5]	Graphene	These materials have been constructed for various applications such as automotive panel body, automotive tires, organic light emitting diodes, liquid crystal devices, solar cells, battery electrodes and super capacitors

dispersion of graphene in the desired polymer matrix. Homogeneous dispersion in poly dimethyl siloxane (PDMS) can be obtained using a shear mixing process [1]. So, uniform dispersion purely depends on synthesis route of preparing graphene and graphene-based nanocomposites. Table 1 shows different applications and properties of graphene.

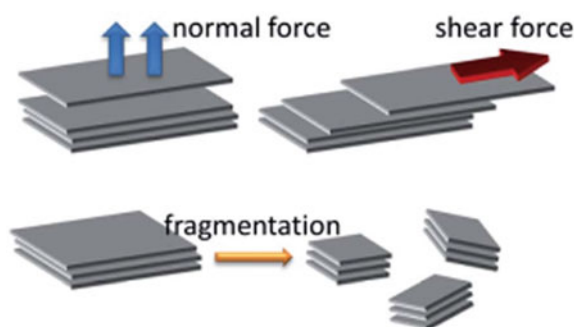
Above discussion describes prominent features of graphene. It can be concluded from the above study that graphene exhibits great mechanical properties, and due to these properties, graphene shows its tremendous application in different engineering fields such as electronics, mechanical and optical.

### 3.1 Preparation Routes of Graphene

Preparation of graphene plays an important role in the properties of the composite. While extracting graphene, lot of impurities came up with the graphene which further causes degradation of properties over the time. So, it is very important to get pure graphene to form healthy composites. Following are certain approaches to extract graphene.

**Mechanical Exfoliation** Mechanical exfoliation is the simplest and cheapest way to extract graphene, and surprisingly this method led to Geim and Novoselov being awarded the noble prize. A repeated scotch tape exfoliation over a piece of graphite is then transferred to the substrate. Number of layers can be peeled off using this

**Fig. 2** Mechanical route of exfoliating graphite into graphene layers



method and can be evaluated using atomic force microscopy, Raman microscopy and optical microscopy (Fig. 2).

**Liquid Phase Exfoliation (LPE)** It is the most promising way in the production of graphene. The speed and simplicity associated with this process make it attractive for mass production of graphene. This method involves three simple steps (i) Dispersion in a solvent (ii) Extraction (iii) Removal of traces of solvent. Ultrasonication time is depending upon concentration of graphene; higher the concentration, higher the ultrasonication time is followed by ultracentrifugation which leads to thinnest flakes with its small lateral size which is useful for composites.

## 4 Graphene-Based Composites: Synthesis Methods

During the preparation of graphene-based polymer composites, the main aim is to ensure the homogeneous dispersion of graphene in a matrix. Dispersion is the key challenge while preparing these types of composites [6]. Uniform dispersion rises the mechanical properties of as prepared composites. The number of synthesis methods has been proposed by various researches, and some majorly used methods have been taken up for deep review in present study.

### 4.1 Solution Mixing

Solution compounding involves the blending of graphene-based polymers that may be in the form of solution or powder. Method comprises these basic steps that involve the dispersion of filler by suspension or ultrasonication, addition of polymer and evaporation of solvent by heating. Thermoplastic polyurethane (TPU)/graphene-based nanocomposites were fabricated where graphene was dissolved in dimethyl formamide (DMF) and stirred for nearly two days. TPU was added to solution and

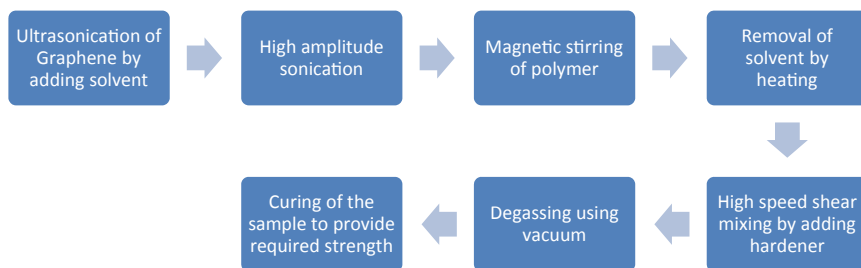


**Fig. 3** Schematic diagram showing solution blending method via sonication

stirred for 5 days, and composites were cast on a glass sheet. During evaporation of solvent, aggregation of solvent was observed. Graphene was added in THF by stirring using a magnetic bar and then ultrasonicated for 30 min to obtain uniform dispersion. THF was evaporated at 120 °C. Graphene-based polyurethane (PU) composites were prepared by solution blending where graphene was dispersed in DMF via ultrasonication. PU was added in a solution. Nano-indentation test reveals excellent improved hardness.

Figure 3 shows the preparation route of composite through solution mixing or blending. Mixing takes place with high amplitude ultrasonication and high-speed mixing. Graphene platelets are first introduced in high amplitude ultrasonicator for the shear mixing with solvent followed by blending with polymer in sonicator and then heated in a furnace to remove the traces of solvent from polymer. This will be followed by curing process to provide better intermolecular bonding between graphene and polymer matrix (Table 2).

From the above discussion, it can be stated that solution mixing provides uniform dispersion of graphene in a polymer matrix. This method also improves mechanical properties of as prepared composites due to higher interfacial bonding between graphene and matrix. There may be chances of agglomeration of graphene in matrix if samples are not dried properly in an oven to remove the traces of solvent. Solution mixing is the most commonly used method in the fabrication of polymer-based composites such as epoxy/graphene, PVA/graphene and PP/graphene.

## 4.2 Melt Blending

Melt blending process involves heating and melting of polymer at high temperature and mixed with graphene. The technique uses high temperature and shear force to disperse nanoparticle in a given matrix. This process involves the use of toxic-free solvent, but generally it is less effective method to disperse graphene in a polymer matrix. Graphene-based polypropylene nanocomposites were prepared via melt mixing route. Addition of 0.1 wt% graphene rises tensile strength, yield strength and



**Table 2** Literature available on fabrication routes using solution mixing

Author; year	Matrix	Method of fabrication	Researcher's view
Arun et al. (2018) [7]	Epoxy	Solution mixing	It was found that composites with 2.5 wt% exhibits high tensile strength, and the sample was much ductile than other wt% fractions
Li et al. (2017) [8]	Epoxy	Solution blending	TEM confirms the uniform dispersion of graphene in epoxy matrix which results high mechanical reinforce efficiency at relatively higher filler contents
Klimek-McDonald et al. (2018) [9]	Epoxy	Solution blending	Tensile modulus and ultimate tensile strength of composite raise to 2.84 Gpa and 81.2 Mpa, respectively, when compared with neat epoxy
Shang et al. (2015) [10]	Polyvinyle chloride (PVA)	Solution mixing	Composite shows large aspect ratio which exhibits good interfacial stress transfer efficiency under loading conditions
Ma et al. (2014) [11]	Epoxy	Solution mixing	Result shows strong adhesion and mechanical interlocking between graphene and matrix
Liao et al. (2014) [12]	Polyimide (PI)	Solution blending	Graphene oxide shows poor compatibility with PI matrix and forms agglomeration of graphene in a matrix

(continued)

**Table 2** (continued)

Author; year	Matrix	Method of fabrication	Researcher's view
Tang et al. (2014) [13]	Epoxy	Solution mixing	Addition of graphene oxide increases tensile strength as well as Young's modulus
Yu et al. (2014) [14]	Polyvinyl chloride (PVA)	Solution mixing	Dispersion of graphene was confirmed by FESEM in PVA indicates crystallinity of graphene oxide/PVA
Wu et al. (2013) [15]	Natural rubber (NR)	Solution mixing	Graphene shows some aggregation at loading up to 2 wt%, still homogeneously dispersed
Wang et al. (2015) [16]	Epoxy	Solution mixing	Tensile modulus of composite has been increased by 49% upon 5 wt% loading of graphene in epoxy matrix
Chong et al. (2016) [17]	Epoxy	Solution mixing	Tensile modulus was enhanced by 24% upon 1 wt% loading of graphene where matrix modulus is found to be 2.9 Gpa
Zakaria et al. (2017) [18]	Epoxy	Solution mixing	Tensile strength and modulus both were increased by 11% and 11.5%, respectively, at 1 wt% loading of graphene
Rafiee et al. (2009) [19]	Epoxy	Solution mixing	Tensile strength and fracture toughness both were found to be increased by 42% and 53%, respectively, upon 0.1 wt% loading of graphene in epoxy matrix

(continued)

**Table 2** (continued)

Author; year	Matrix	Method of fabrication	Researcher's view
Prolongo et al. (2015) [20]	Epoxy	Solution mixing	Tensile modulus has been increased by 28% upon 5% loading of graphene, and tensile strength has been increased by 3% at 1 wt% of graphene in the matrix of graphene where matrix modulus is 2.5 Gpa
Wang et al. (2016) [21]	CTBN/Epoxy	Solution mixing	Fracture toughness has been increased by 109% when polymer reinforced with 3 wt% of graphene
Liu et al. (2012) [22]	Epoxy	Solution mixing	Tensile strength has been enhanced by 97% upon loading of 0.4 wt% of graphene in epoxy matrix
Vadukumpully et al. (2011) [23]	PVC	Solution mixing	Tensile modulus and tensile strength both were increased greatly by 135% and 71%, respectively, when polymer is loaded with 2 wt% of graphene
Wang et al. (2011) [24]	PBS	Solution mixing	Tensile strength has been by increased by 21% upon 2 wt% loading of graphene
Abdolmaleki et al. (2016) [25]	PVA	Solution mixing	Tensile modulus and tensile strength both were increased significantly by 150% and 153% upon 5 wt% loading of graphene

(continued)

**Table 2** (continued)

Author; year	Matrix	Method of fabrication	Researcher's view
Zhao et al. (2010) [26]	PVA	Solution mixing	Tensile strength and tensile modulus both increase by 166% and 990%, respectively, upon 3 vol.% loading of graphene in PVA matrix
Papadopoulou et al. (2016) [27]	Nylon 6,6	Solution mixing	Tensile strength has been increased by 45% upon 10% loading of graphene
Bourque et al. (2016) [28]	PU	Solution mixing	Upon loading of 2 wt% of graphene in PU matrix, there is a increase in tensile strength by 51%
Chen and Lu (2012) [29]	HDPE	Solution mixing	Upon 15 wt% loading of graphene, 13% rise in tensile strength has been observed

Young's modulus up to 33 MPa, 30 MPa and 1.25 GPa, respectively. Polypropylene and graphene were mixed for 10 min after keeping them in an oven for few days at 70 °C. Significant improvement has been observed and indicated high load transfer efficiency. Polyamide (PA 12)/graphene was prepared using melt blending technique. Study reveals that graphene exhibits wrinkled surface which improves its interfacial interactions with matrix material and provides homogeneous dispersion. Author fabricated polyethylene/graphene composites through melt blending route which reveals significant improvement in mechanical properties. Table 3 shows fabrication of composite using melt mixing.

While taking the review of melt blending technique, it has been observed that the technique is not adequate to disperse graphene uniformly in a matrix because the agglomeration of graphene in matrix takes place. Wrinkled surface of graphene increases bonding between graphene and matrix but promotes the failure point while testing. PA12/graphene and PET/graphene composites are generally fabricated using this technique because of increasing chances of strong interfacial bonding. Lot of modification processes have taken place to improve properties and dispersion of the composites. Form of co-extruder which was developed by Baer and co-workers for the making of polymer blends into distinct polymer structure (Fig. 4).

**Table 3** Fabrication of graphene-based composites using melt mixing

Author; year	Matrix	Method of fabrication	Researcher's view
Maio et al. (2015) [30]	Polyamide 12	Melt mixing	Evidence shows that melt intercalation is not adequate to disperse GO in PA 6 matrix
Chatterjee et al. (2013) [31]	Polyamide (PA 12)	Melt mixing	During fabrication process in extruder, the shear force created helps in increasing the chances of re-aggregation in composites
Araby et al. (2013) [32]	Elastomer EPDM	Melt blending	Addition of 26.7 vol.% GnPs in elastomer EPDM enhanced tensile strength and Young's modulus by 404% and 710%, respectively
El Achaby et al. (2012) [33]	(PVDF)	Melt mixing	Properties of PVDF were improved due to good dispersion of graphene in a matrix
Mahmoud (2011) [34]	(PET)	Melt mixing	TEM study reveals uniform distribution/dispersion of graphene sheet in PET polymer matrix and improves electrical conductivity
Kim and Macosko (2009) [35]	Polycarbonate	Melt mixing	Long-term annealing exhibits random orientation of graphene particles in a PC matrix
Valles et al. (2015) [36]	PMMA	Melt mixing	Tensile modulus has been increased by 74% upon 20 wt% loading of graphene
Mayoral et al. (2015) [37]	PA6	Melt mixing	412% increase has been observed in tensile modulus upon 20 wt% loading of graphene

(continued)

**Table 3** (continued)

Author; year	Matrix	Method of fabrication	Researcher's view
Ahamd et al. (2017) [38]	PP	Melt mixing	Tensile modulus has been increased by 54% when PP polymer was reinforced with 1.7 wt% graphene where matrix modulus is 1.3%
Zhong et al. (2016) [39]	PP	Melt mixing	Tensile strength has been increased by 10% upon 10 wt% loading of graphene
Quiles-Diaz et al. (2017) [40]	PP	Melt mixing	Tensile strength enhanced by 8% at 1 wt% loading of graphene
Song et al. [41]	PP	Melt mixing	54% rise in tensile strength has been observed upon 0.42 wt% of graphene
Chieng et al. (2014) [42]	PLA	Melt mixing	Tensile strength has been increased by 24% upon 0.3 wt% loading of graphene
Mittal et al. (2016) [43]	PE	Melt mixing	Tensile strength has been increased by 17% upon 2 wt% of graphene in PE matrix
Guo et al. (2013) [44]	HDPE	Melt mixing	19% increase in tensile strength upon 1 wt% loading of graphene in HDPE matrix
Botta et al. (2012) [45]	Bioflex	Melt mixing	Tensile modulus has found to be increased by 39% of the polymer when loaded with 5 wt% of graphene whose matrix modulus is 0.14 Gpa
Istrate et al. (2014) [46]	PET	Melt mixing	42% rise has been observed in the tensile strength of polymer upon addition of 0.08 wt% of graphene where matrix modulus is 0.8 Gpa

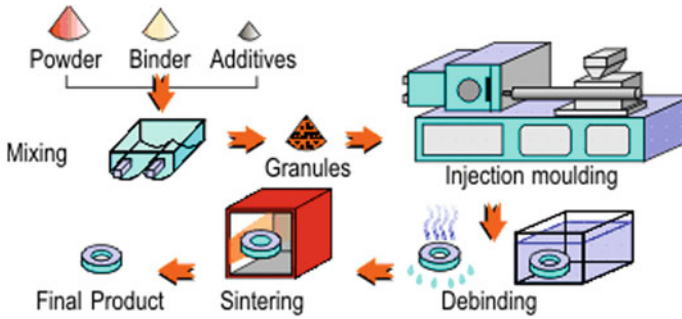


**Fig. 4** Melt blending process using injection moulding

This above-mentioned work is an example of the effect of fillers of graphene along with the modification of the preparation strategies for the improvement of the structure and properties of the composites.

### 4.3 *In Situ Polymerization*

In situ polymerization comprises mixing of graphene with polymer or monomer and polymerization process that is performed afterwards which leads to strong interfacial interaction and better dispersion. Graphene sheets/polypyrrole (PPy) composite was fabricated through in situ polymerization. It has been found that graphene layers homogeneously dispersed in PPy, and no agglomerations have been found in the mixture. Fabrication of nylon-6-graphene composites has been reported by in situ polymerization. Addition of 0.1 wt% of graphene shows increase in tensile strength and Young's modulus by 2.1 folds and 2.4 folds, respectively. Table 4 shows the literature on in situ polymerization route for synthesis.

In situ polymerization provides better load transfer capability due to increased interfacial bonding between graphene and polymer matrix, as prepared composites provide better chemical stability. This method also provides wrinkle-free composites and well dispersion of graphene in a matrix. Method shows less dispersion rate as compared to others fabrication routes.

## 5 Discussion on Findings

Graphene is found to be most prominent carbon-based nanofiller for the fabrication of composite materials. Earlier researchers were using some other nanofillers like SWCNTs, MWCNTs, glass fibres and fullerenes, etc., as a reinforcement in composites, but now graphene takes all the attention of researchers due to its magnificent

**Table 4** Fabrication of graphene-based composites using in situ polymerization

Author; year	Matrix	Method of fabrication	Researcher's view
He et al. (2018) [47]	Silver nanoparticle	In situ	Composite shows the improvement in chemical stability of synthesized nanocomposites when compared with neat polymer
Milani et al. (2013) [48]	Polypropylene (PP)	In situ	PP/graphene composites were investigated. TEM and XRD study reveal uniform dispersion of graphene sheets in PP matrix
Stürzel et al. (2012) [49]	Polyethylene (PE)	In situ	Composites show higher electrical conductivity, stiffness and elongation at break when compared with the electrical conductivity, stiffness and elongation of neat polymer
Wang et al. (2011) [50]	Polyimide (PI)	In situ	Study reveals strong interaction link with PI for high load transfer promoting better dispersion of GO in matrix
Huang et al. (2010) [51]	Polypropylene (PP)	In situ	SEM and TEM study report homogeneous dispersion of graphene oxide in PP matrix
Wang et al. (2009) [52]	Polyaniline	In situ	Fabricated composites shows considerable tensile strength of 12.6 MPa and stable electrochemical capacitance

(continued)



**Table 4** (continued)

Author; year	Matrix	Method of fabrication	Researcher's view
Liu et al. (2013) [53]	PA6	In situ	Prepared composites shows significant rise in the tensile strength by 65% upon 0.1 wt% loading of graphene in PA6 matrix
Yadav and Cho (2013) [54]	PU	In situ	As fabricated composites shows significant rise in the tensile strength by 31% upon 2 wt% loading of graphene in PA6 matrix
Wang et al. (2012) [55]	PMMA	In situ	114% increase has been observed in the tensile strength of composite upon 0.5% loading of graphene when compared with the strength of polymer
Zhao et al. (2013) [56]	PES	In situ	Tensile strength has been increased by 40% when loaded with 0.5 wt% of graphene where matrix modulus is 0.38 Gpa
Yuan et al. (2013) [57]	Nylon 11	In situ	Tensile modulus of the polymer has been increased by 38% when loaded with 0.5 wt% of graphene
Zhao et al. (2014) [58]	PF	In situ	Tensile strength of the composite has been increased by 65% upon 0.5 wt% loading of graphene when compared with neat polymer
Appel et al. (2012) [59]	PU	In situ	242% increase in the tensile strength of the polymer composite has been observed upon loading with 2 wt% of graphene

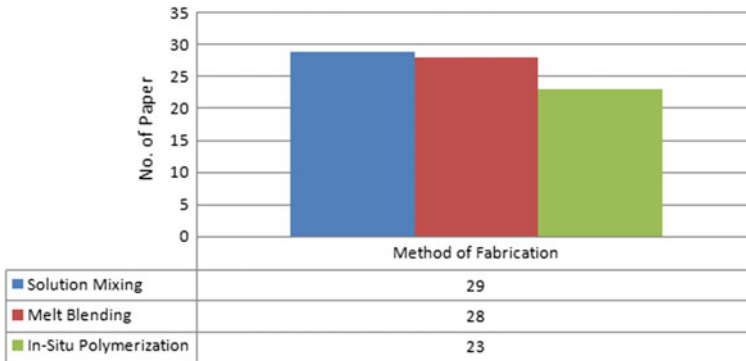


**Fig. 5** Number of papers published on fabrication of graphene-based composites in past 15 years

properties and its extraordinary response when reinforced in any other matrix material. Graphene when used as a reinforcement in a given matrix greatly increases properties of as prepared composites. Present review depicts that different synthesis routes for the fabrication of composites can be used to enhance different properties of composites. Some majorly used methods for synthesis of graphene-based composites have been discussed in the present study. It has been observed that interfacial interaction between graphene and matrix must be strong enough to get better properties, which can be obtained by different synthesis methods like solution mixing, melt blending and in situ polymerization (Fig. 5).

## 6 Conclusion

Graphene when used as reinforcement in a matrix greatly enhances overall properties of the as prepared composites. These properties are affected by the dispersion of graphene in a polymer matrix, but uniform dispersion remains the key challenge. Dispersion of graphene should be uniform to avoid agglomeration of graphene in a matrix which leads to promote weak points while testing. Homogeneous dispersion and efficient load transfer capability will be obtained by different synthesis routes as discussed in literature. Some majorly used methods for synthesis of graphene-based composites have been discussed in the present study. This study shows that solution blending process provides strong interfacial bonding between graphene and polymer matrix with few chances of agglomeration of graphene in a matrix. It can be avoided by proper sintering process that involves drying of composites by maintaining the required temperature. It has been observed from the literature that solution blending also provides homogeneous dispersion of graphene in a matrix. It can be stated from that melt blending technique is not able to provide adequate dispersion of graphene in a matrix because it gives a wrinkled surface of graphene in composites which promotes the failure points while testing. In situ polymerization provides

better chemical stability and avoids the chances of agglomeration of graphene but having less dispersion rate. This process increases the mechanical properties of the composites but less as compared to solution blending. It can be stated from the above discussion that solution blending is a method which provides better dispersion and properties as compared to melt blending and in situ polymerization. It should be stated that still a lot of challenges need to be tackled to produce better composite through dispersion. Issues such as uniform dispersion, orientation and interfacial bonding with polymer matrix still require further research and improvements.

## References

1. Kumar, U., Sharma, S., Rathi, R., Kapur, S., Upadhyay, D.: Molecular dynamics simulation of nylon/CNT composites. *Mater. Today Proc.* **5**(14), 27710–27717 (2018)
2. Wang, N., Samani, M.K., Li, H., Dong, L., Zhang, Z., Su, P., Xu, X.: Tailoring the thermal and mechanical properties of graphene film by structural engineering. *Small*, 1801346 (2018)
3. Neuberger, N., Adidharma, H., Fan, M.: Graphene: A review of applications in the petroleum industry. *J. Pet. Sci. Eng.* **167**, 152–159 (2018)
4. Papageorgiou, D.G., Kinloch, I.A., Young, R.J.: Mechanical properties of graphene and graphene-based nanocomposites. *Prog. Mater. Sci.* **90**, 75–127 (2017)
5. Fazli, A., Moosaei, R., Sharif, M., Ashtiani, S.J.: Developments of graphene-based polymer composites processing based on novel methods for innovative applications in newborn technologies. *Indian J. Sci. Technol.* **8**(S9), 38–44 (2015)
6. Kaswan, M.S., Rathi, R.: Analysis and modeling the enablers of green lean six sigma implementation using interpretive structural modeling. *J. Clean. Prod.* **231**, 1182–1191 (2019)
7. Arun, G.K., Sreenivas, N., Reddy, K.B., Reddy, K.S.K., Kumar, M.S., Pramod, R.: Investigation on mechanical properties of graphene oxide reinforced GFRP. In *IOP Conference Series: Materials Science and Engineering*, vol. 310, no. 1, p. 012158. IOP Publishing (2018)
8. Li, A., Zhang, C., Zhang, Y.F.: Thermal conductivity of graphene-polymer composites: Mechanisms, properties, and applications. *Polymers* **9**(9), 437 (2017)
9. Klimek-McDonald, D.R., King, J.A., Miskioglu, I., Pineda, E.J., Odegard, G.M.: Determination and modeling of mechanical properties for graphene nanoplatelet/epoxy composites. *Polym. Compos.* **39**(6), 1845–1851 (2018)
10. Shang, J., Chen, Y., Zhou, Y., Liu, L., Wang, G., Li, X., Zhi, L.: Effect of folded and crumpled morphologies of graphene oxide platelets on the mechanical performances of polymer nanocomposites. *Polymer* **68**, 131–139 (2015)
11. Ma, J., Meng, Q., Zaman, I., Zhu, S., Michelmore, A., Kawashima, N., Kuan, H.C.: Development of polymer composites using modified, high-structural integrity graphene platelets. *Compos. Sci. Technol.* **91**, 82–90 (2014)
12. Liao, W.H., Yang, S.Y., Hsiao, S.T., Wang, Y.S., Li, S.M., Ma, C.C.M., Zeng, S.J.: Effect of octa (aminophenyl) polyhedral oligomeric silsesquioxane functionalized graphene oxide on the mechanical and dielectric properties of polyimide composites. *ACS Appl. Mater. Interfaces.* **6**(18), 15802–15812 (2014)
13. Tang, G., Jiang, Z.G., Li, X., Zhang, H.B., Hong, S., Yu, Z.Z.: Electrically conductive rubbery epoxy/diamine-functionalized graphene nanocomposites with improved mechanical properties. *Compos. B Eng.* **67**, 564–570 (2014)
14. Yu, D.S., Kuila, T., Kim, N.H., Lee, J.H.: Enhanced properties of aryl diazonium salt-functionalized graphene/poly (vinyl alcohol) composites. *Chem. Eng. J.* **245**, 311–322 (2014)

15. Wu, J., Huang, G., Li, H., Wu, S., Liu, Y., Zheng, J.: Enhanced mechanical and gas barrier properties of rubber nanocomposites with surface functionalized graphene oxide at low content. *Polymer* **54**(7), 1930–1937 (2013)
16. Wang, F., Drzal, L.T., Qin, Y., Huang, Z.: Mechanical properties and thermal conductivity of graphene nanoplatelet/epoxy composites. *J. Mater. Sci.* **50**(3), 1082–1093 (2015)
17. Chong, H.M., Hinder, S.J., Taylor, A.C.: Graphene nanoplatelet-modified epoxy: effect of aspect ratio and surface functionality on mechanical properties and toughening mechanisms. *J. Mater. Sci.* **51**(19), 8764–8790 (2016)
18. Zakaria, M.R., Kudus, M.H.A., Akil, H.M., Thirmizir, M.Z.M.: Comparative study of graphene nanoparticle and multiwall carbon nanotube filled epoxy nanocomposites based on mechanical, thermal and dielectric properties. *Compos. B Eng.* **119**, 57–66 (2017)
19. Rafiee, M.A., Rafiee, J., Wang, Z., Song, H., Yu, Z.Z., Koratkar, N.: Enhanced mechanical properties of nanocomposites at low graphene content. *ACS Nano* **3**(12), 3884–3890 (2009)
20. Prolongo, M.G., Salom, C., Arribas, C., Sánchez-Cabezudo, M., Masegosa, R.M., Prolongo, S.G.: Influence of graphene nanoplatelets on curing and mechanical properties of graphene/epoxy nanocomposites. *J. Therm. Anal. Calorim.* **125**(2), 629–636 (2016)
21. Wang, F., Drzal, L.T., Qin, Y., Huang, Z.: Enhancement of fracture toughness, mechanical and thermal properties of rubber/epoxy composites by incorporation of graphene nanoplatelets. *Compos. A Appl. Sci. Manuf.* **87**, 10–22 (2016)
22. Liu, W., Koh, K.L., Lu, J., Yang, L., Phua, S., Kong, J., Chen, Z., Lu, X.: Simultaneous catalyzing and reinforcing effects of imidazole-functionalized graphene in anhydride-cured epoxies. *J. Mater. Chem.* **22**(35), 18395–18402 (2012)
23. Vadukumpully, S., Paul, J., Mahanta, N., Valiyaveetil, S.: Flexible conductive graphene/poly (vinyl chloride) composite thin films with high mechanical strength and thermal stability. *Carbon* **49**(1), 198–205 (2011)
24. Wang, X., Yang, H., Song, L., Hu, Y., Xing, W., Lu, H.: Morphology, mechanical and thermal properties of graphene-reinforced poly (butylene succinate) nanocomposites. *Compos. Sci. Technol.* **72**(1), 1–6 (2011)
25. Abdolmaleki, A., Mallakpour, S., Borandeh, S.: Improving interfacial interaction of l-phenylalanine-functionalized graphene nanofiller and poly (vinyl alcohol) nanocomposites for obtaining significant membrane properties: morphology, thermal, and mechanical studies. *Polym. Compos.* **37**(6), 1924–1935 (2016)
26. Zhao, X., Zhang, Q., Chen, D., Lu, P.: Enhanced mechanical properties of graphene-based poly (vinyl alcohol) composites. *Macromolecules* **43**(5), 2357–2363 (2010)
27. Papadopoulou, E.L., Pignatelli, F., Marras, S., Marini, L., Davis, A., Athanassiou, A., Bayer, I.S.: Nylon 6, 6/graphene nanoplatelet composite films obtained from a new solvent. *RSC Adv.* **6**(8), 6823–6831 (2016)
28. Bourque, A.J., Locker, C.R., Tsou, A.H., Vadlamudi, M.: Nucleation and mechanical enhancements in polyethylene-graphene nanoplate composites. *Polymer* **99**, 263–272 (2016)
29. Chen, Z., Lu, H.: Constructing sacrificial bonds and hidden lengths for ductile graphene/polyurethane elastomers with improved strength and toughness. *J. Mater. Chem.* **22**(25), 12479–12490 (2012)
30. Maio, A., Fucarino, R., Khatibi, R., Rosselli, S., Bruno, M., Scaffaro, R.: A novel approach to prevent graphene oxide re-aggregation during the melt compounding with polymers. *Compos. Sci. Technol.* **119**, 131–137 (2015)
31. Chatterjee, S., Nüesch, F.A., Chu, B.T.T.: Crystalline and tensile properties of carbon nanotube and graphene reinforced polyamide 12 fibers. *Chem. Phys. Lett.* **557**, 92–96 (2013)
32. Araby, S., Zaman, I., Meng, Q., Kawashima, N., Michelmore, A., Kuan, H.C., Zhang, L.: Melt compounding with graphene to develop functional, high-performance elastomers. *Nanotechnology* **24**(16), 165601 (2013)
33. El Achaby, M., Arrakhiz, F.Z., Vaudreuil, S., Essassi, E.M., Qaiss, A., Bousmina, M.: Preparation and characterization of melt-blended graphene nanosheets–poly (vinylidene fluoride) nanocomposites with enhanced properties. *J. Appl. Polym. Sci.* **127**(6), 4697–4707 (2013)

34. Mahmoud, W.E.: Morphology and physical properties of poly (ethylene oxide) loaded graphene nanocomposites prepared by two different techniques. *Eur. Polym. J.* **47**(8), 1534–1540 (2011)
35. Kim, H., Macosko, C.W.: Processing-property relationships of polycarbonate/graphene composites. *Polymer* **50**(15), 3797–3809 (2009)
36. Valles, C., Abdelkader, A.M., Young, R.J., Kinloch, I.A.: The effect of flake diameter on the reinforcement of few-layer graphene–PMMA composites. *Compos. Sci. Technol.* **111**, 17–22 (2015)
37. Mayoral, B., Harkin-Jones, E., Khanam, P.N., AlMaadeed, M.A., Ouederni, M., Hamilton, A.R., Sun, D.: Melt processing and characterisation of polyamide 6/graphene nanoplatelet composites. *RSC Adv.* **5**(65), 52395–52409 (2015)
38. Ahmad, S.R., Xue, C., Young, R.J.: The mechanisms of reinforcement of polypropylene by graphene nanoplatelets. *Mater. Sci. Eng., B* **216**, 2–9 (2017)
39. Zhong, J., Isayev, A.I., Zhang, X.: Ultrasonic twin screw compounding of polypropylene with carbon nanotubes, graphene nanoplates and carbon black. *Eur. Polym. J.* **80**, 16–39 (2016)
40. Quiles-Díaz, S., Enrique-Jimenez, P., Papageorgiou, D.G., Ania, F., Flores, A., Kinloch, I.A., Gómez-Fatou, M.A., Young, R.J., Salavagione, H.J.: Influence of the chemical functionalization of graphene on the properties of polypropylene-based nanocomposites. *Compos. A Appl. Sci. Manuf.* **100**, 31–39 (2017)
41. Song, P., Cao, Z., Cai, Y., Zhao, L., Fang, Z., Fu, S.: Fabrication of exfoliated graphene-based polypropylene nanocomposites with enhanced mechanical and thermal properties. *Polymer* **52**(18), 4001–4010 (2011)
42. Chieng, B.W., Ibrahim, N.A., Yunus, W.M.Z.W., Hussein, M.Z., Loo, Y.Y.: Effect of graphene nanoplatelets as nanofiller in plasticized poly (lactic acid) nanocomposites. *J. Therm. Anal. Calorim.* **118**(3), 1551–1559 (2014)
43. Mittal, V., Kim, S., Neuhofer, S., Paulik, C.: Polyethylene/graphene nanocomposites: effect of molecular weight on mechanical, rheological and morphological properties. *Colloid Polym. Sci.* **294**(4), 691–704 (2016)
44. Guo, Z., Ran, S., Fang, Z.: Promoting dispersion of graphene nanoplatelets in polyethylene and chlorinated polyethylene by Friedel-Crafts reaction. *Compos. Sci. Technol.* **86**, 157–163 (2013)
45. Botta, L., Scaffaro, R., Mistretta, M.C., La Mantia, F.P.: Biopolymer based nanocomposites reinforced with graphene nanoplatelets. In: *AIP Conference Proceedings*, vol. 1736, no. 1, p. 020156. AIP Publishing (2016)
46. Istrate, O.M., Paton, K.R., Khan, U., O'Neill, A., Bell, A.P., Coleman, J.N.: Reinforcement in melt-processed polymer–graphene composites at extremely low graphene loading level. *Carbon* **78**, 243–249 (2014)
47. He, K., Zeng, Z., Chen, A., Zeng, G., Xiao, R., Xu, P., Huang, Z., Shi, J., Hu, L., Chen, G.: Advancement of Ag–graphene based nanocomposites: an overview of synthesis and its applications. *Small* **14**(32), 1800871 (2018)
48. Milani, M.A., González, D., Quijada, R., Basso, N.R., Cerrada, M.L., Azambuja, D.S., Galland, G.B.: Polypropylene/graphene nanosheet nanocomposites by in situ polymerization: synthesis, characterization and fundamental properties. *Compos. Sci. Technol.* **84**, 1–7 (2013)
49. Stürzel, M., Kempe, F., Thomann, Y., Mark, S., Enders, M., Mühlaupt, R.: Novel graphene UHMWPE nanocomposites prepared by polymerization filling using single-site catalysts supported on functionalized graphene nanosheet dispersions. *Macromolecules* **45**(17), 6878–6887 (2012)
50. Wang, J.Y., Yang, S.Y., Huang, Y.L., Tien, H.W., Chin, W.K., Ma, C.C.M.: Preparation and properties of graphene oxide/polyimide composite films with low dielectric constant and ultrahigh strength via in situ polymerization. *J. Mater. Chem.* **21**(35), 13569–13575 (2011)
51. Huang, Y., Qin, Y., Zhou, Y., Niu, H., Yu, Z.Z., Dong, J.Y.: Polypropylene/graphene oxide nanocomposites prepared by in situ Ziegler–Natta polymerization. *Chem. Mater.* **22**(13), 4096–4102 (2010)
52. Wang, D.W., Li, F., Zhao, J., Ren, W., Chen, Z.G., Tan, J., Wu, Z.S., Gentle, I., Lu, G.Q., Cheng, H.M.: Fabrication of graphene/polyaniline composite paper via in situ anodic

- electropolymerization for high-performance flexible electrode. *ACS Nano* **3**(7), 1745–1752 (2009)
53. Liu, H.H., Peng, W.W., Hou, L.C., Wang, X.C., Zhang, X.X.: The production of a melt-spun functionalized graphene/poly ( $\epsilon$ -caprolactam) nanocomposite fiber. *Compos. Sci. Technol.* **81**, 61–68 (2013)
  54. Yadav, S.K., Cho, J.W.: Functionalized graphene nanoplatelets for enhanced mechanical and thermal properties of polyurethane nanocomposites. *Appl. Surf. Sci.* **266**, 360–367 (2013)
  55. Wang, J., Shi, Z., Ge, Y., Wang, Y., Fan, J., Yin, J.: Solvent exfoliated graphene for reinforcement of PMMA composites prepared by in situ polymerization. *Mater. Chem. Phys.* **136**(1), 43–50 (2012)
  56. Zhao, J., Wang, X., Zhou, W., Zhi, E., Zhang, W., Ji, J.: Graphene-reinforced biodegradable poly (ethylene succinate) nanocomposites prepared by in situ polymerization. *J. Appl. Polym. Sci.* **130**(5), 3212–3220 (2013)
  57. Yuan, D., Wang, B., Wang, L., Wang, Y., Zhou, Z.: Unusual toughening effect of graphene oxide on the graphene oxide/nylon 11 composites prepared by in situ melt polycondensation. *Compos. B Eng.* **55**, 215–220 (2013)
  58. Zhao, X., Li, Y., Wang, J., Ouyang, Z., Li, J., Wei, G., Su, Z.: Interactive oxidation–reduction reaction for the in situ synthesis of graphene–phenol formaldehyde composites with enhanced properties. *ACS Appl. Mater. Interfaces* **6**(6), 4254–4263 (2014)
  59. Appel, A.K., Thomann, R., Mülhaupt, R.: Polyurethane nanocomposites prepared from solvent-free stable dispersions of functionalized graphene nanosheets in polyols. *Polymer* **53**(22), 4931–4939 (2012)

# Evaluation of Mechanical Properties of Carbon Fiber-Reinforced Multiwall Carbon Nanotube-Based Nanocomposites



Sumit Mahajan, Lochan Sharma, Mandeep Singh Rayat, and Ranjit Singh

**Abstract** In the present study, reinforcement of treated multiwall carbon nanotubes (MWCNTs) in the carbon fiber matrix was done. MWCNTs are mixed into epoxy resin in different weight ratio (0.0, 0.2, and 0.5 wt% of weight of resin). By varying the percentage of MWCNTs into the epoxy resin, different sheets are prepared by applying the resin to carbon fiber sheets. Mechanical properties are tested as per the ASTM Standards. From the results, it was found that composite with 0.5 wt% of treated MWCNTs produced better mechanical strength among all the other samples because of the uniform dispersion of treated MWCNTs in the epoxy as compared to non-treated MWCNTs.

**Keywords** Fiber-reinforced plastics · MWCNT · PDAC · Nanocomposites · Chemical vapor deposition

## 1 Introduction

Due to their enhanced thermal conductivity, mechanical and thermal properties, nanocomposites become the major interest for the researchers. Different industries like automobile, aerospace, sports, and marine widely used nanocomposites due to its high strength-to-weight ratio [1, 2]. A small addition of nanoparticles to epoxy resin imparts better mechanical properties and improves the glass transition temperature [3]. To improve the strength, impact toughness, and interlaminar strength, researchers reinforce these fiber-reinforced plastics (FRPs) using nanofillers like montmorillonite nanoclay, MWCNTs, etc. To improve the mechanical and physical properties of the nanocomposites, these nanoparticles are considered to be the most potential fillers. The main advantages of these nanofillers are their huge specific surface areas and their unique properties due to their nanometric size [4–7].

---

S. Mahajan (✉) · L. Sharma  
IIT Jodhpur, Jodhpur, India  
e-mail: [mahajan.1@iitj.ac.in](mailto:mahajan.1@iitj.ac.in)

M. S. Rayat · R. Singh  
Lovely Professional University, Phagwara, India

© Springer Nature Singapore Pte Ltd. 2020  
C. Prakash et al. (eds.), *Advances in Materials Science and Engineering*,  
Lecture Notes in Mechanical Engineering,  
[https://doi.org/10.1007/978-981-15-4059-2\\_3](https://doi.org/10.1007/978-981-15-4059-2_3)

MWCNTs are now being a great interest to the researches due to their extraordinary thermal conductivity, mechanical, and electrical properties. Addition of the very low amount of MWCNTs into FRPs results the improved properties of the FRPs. Many researchers are still using the MWCNTs' addition to the matrix. Using MWCNTs as a reinforcing component in polymer composites requires the ability to tailor the name of the MWCNT walls in order to control the interfacial interaction between the MWCNTs and the polymer chains [2, 8]. Several studies have been reported on the mechanical properties of MWCNT-reinforced polymer nanocomposites, where the MWCNTs were used without surface modifications [2, 8–10]. MWCNT uniform dispersion is one of the challenges faced by the researchers. Homogeneous dispersion of carbon nanotubes into the epoxy resin is one of the major challenges while working with MWCNT-based nanocomposites which affect the performance of recovered composite material. Another main issue in the realization of mechanically reinforced MWCNT/polymer composites is the tuning of interfacial adhesion between the MWCNTs and the polymer. An experimental determination of the interfacial strength is still a difficult procedure; however, some progress has been made in this field, but most of the potential arises from theoretical predictions [7, 10–12]. So, there are a number of methods reported to make the MWCNT-reinforced FRPs, but the basic steps to make the MWCNT nanocomposites are to disperse the MWCNTs to the epoxy resin with the help of mechanical stirrer, then ultrasonicate the mixture for the better dispersion, and apply this mixture using hand lay-up method to produce the nanocomposites. As the exfoliation of the MWCNTs to the mixture is still a challenge, some other methods like homogenization of the MWCNTs to the epoxy and chemical vapor deposition (CVD) show improved results [1, 8, 13].

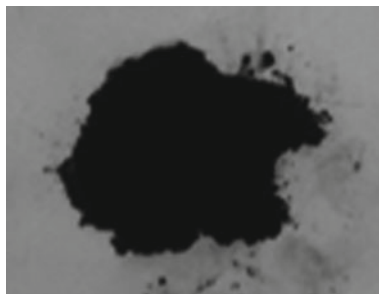
So, this article is an attempt to produce MWCNT-based nanocomposite by chemically treating the MWCNTs to improve the dispersion into the matrix. The effect of MWCNT addition to composite matrix on the mechanical properties of the nanocomposites was also studied.

## 2 Material and Experimental Procedure

The carbon fibers (CFs) used in this study were unidirectional fibers in which a group of CF strands is woven with a fiber thread in a diamond manner supplied by BASF, Delhi, India (Fig. 2). The MWCNTs used here were having an average diameter ranging 10–20 nm and a length of 1.5  $\mu\text{m}$  (item code 280514-33), with the purity of 95% supplied by Autus Nanolab Pvt. Ltd., India (Fig. 1). The matrix resin used in this study is having MasterBrace 4500 Part A epoxy resin and MasterBrace 4500 Part B amine hardener, supplied by BASF Construction Chemicals (India) Pvt. Ltd. The amine hardener and the epoxy resin are mixed in the ratio of 40–100 g by weight. The polyelectrolyte used in this study having cationic polymer without reactive functional group was poly (diallyldimethylammonium) chloride (PDAC) supplied by Flourish Paper & Chemicals Ltd. Some of the polyelectrolytes, including cationic polymer and



**Fig. 1** Carbon nanotubes in powder form



anionic polymer, are listed above in Table 1 with reactive and non-reactive functional groups. The work carried out in this investigation is presented in Fig. 3.

**Fig. 2** Carbon fiber roll



**Table 1** Enumeration of polyelectrolyte having cationic and anionic polymers

Polymer	Name	Abbreviation	Functional group
Cationic polymer	Poly (diallyldimethylammonium) chloride	PDAC	No
		PDACMA	<ul style="list-style-type: none"> <li>• Carboxylic</li> <li>• Hydroxyl</li> </ul>
	DAC-maleic acid copolymer	PEI	<ul style="list-style-type: none"> <li>• Carboxylic</li> <li>• Hydroxyl</li> </ul>
	Polyethyleneimine		
Anionic polymer	Poly (4-styrenesulfonic acid) sodium salt	SPS	No

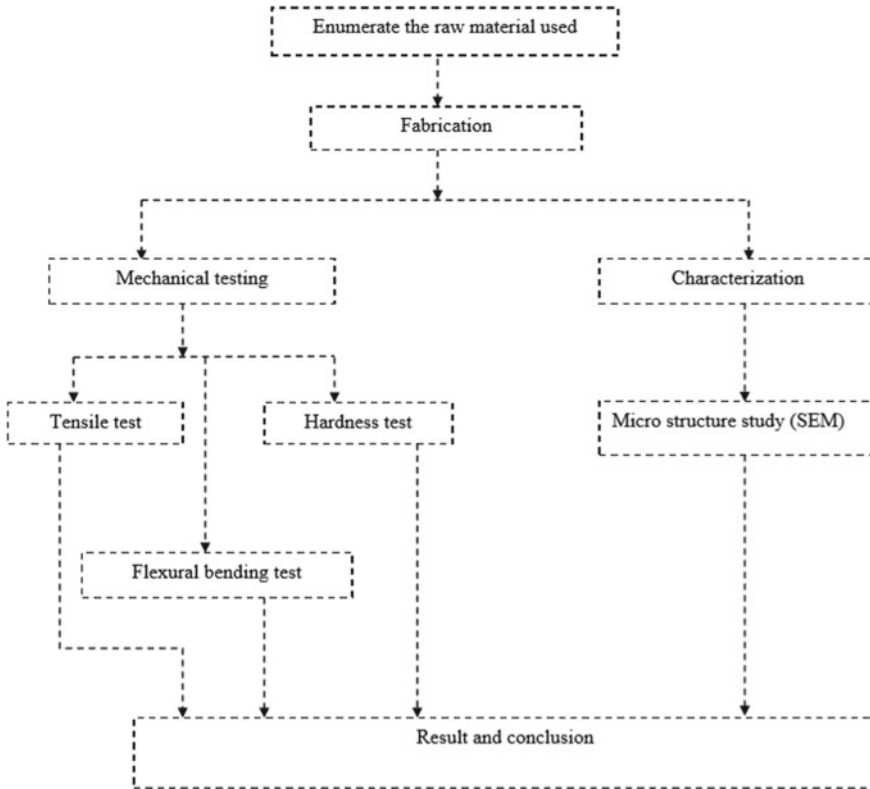


**Fig. 3** Flowchart of the work carried out in this study

## ***2.1 Preparation of Polyelectrolyte-Treated Multiwall Carbon Nanotubes***

Multiwall carbon nanotubes (MWCNTs) were first oxidized by mixing 0.7 g of MWCNTs in 10 ml of nitric acid ( $\text{HNO}_3$ ) and kept for 30 min in ultrasonicator which agitates the mixture. The mixture is then filtered by using 0.2- $\mu\text{m}$ -pore-diameter filter paper (Avarice Laboratories Pvt. Ltd.). The residue obtained on the filter paper was mixed in the solution of polyelectrolyte and sodium chloride (NaCl) in the ratio 0.070 wt% MWCNTs, 0.014 wt% polyelectrolyte, and 0.010 wt% sodium chloride, and the total volume of the aqueous solution was 344 ml. The complete solution was kept into a sonicator for 2 h for proper mixing and agitation of mixture. After 2 h of sonication, the solution was kept for filtration by using 0.2- $\mu\text{m}$ -pore-diameter filter paper. A schematic diagram is shown in Fig. 4.

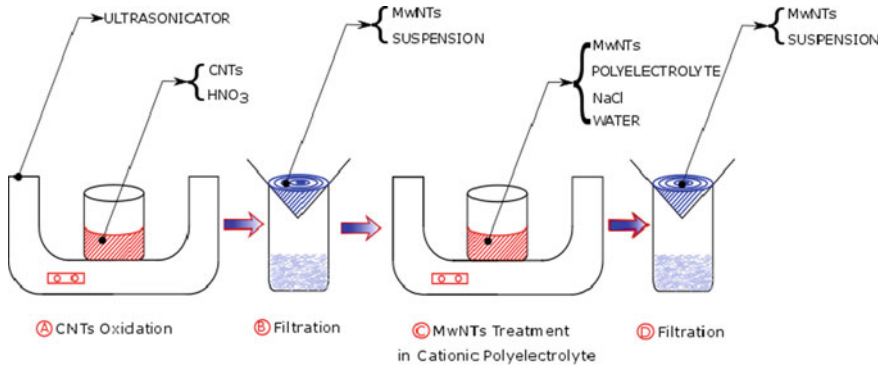


Fig. 4 Schematic explanation of experimental procedure

### 2.2 Preparation of Polyelectrolyte-Treated MWCNT-Coated CF Sheet

The epoxy resin and amine hardener were mixed in a ratio of 40:100. Firstly, 100 g epoxy resin was taken, and 0.7 g of polyelectrolyte-treated MWCNT which is 0.5% wt. of consolidated wt. of 140 g matrix resin was mixed gradually into epoxy resin with the help homogenizer by keeping the shearing speed ranging between 3000 and 4000. Every time, a small amount of MWCNTs was mixed into epoxy resin, by doing so a complete homogenous mixture was obtained. A proper dispersion of MWCNTs into epoxy resin was obtained because of cationic polymer, which charges the MWCNTs with positive charge; due to this, a repulsive force is generated among the positively charged MWCNTs which give the good dispersion of MWCNTs as shown in Fig. 5. Now the 40 g amine hardener was mixed into homogenous mixture by keeping the shearing speed ranging 1000–1500. A CF sheet was cut into a dimension of 30 × 50 cm. Then, the hand lay-up method was used to spread the homogenous mixture onto a CF sheet. A uniform layer 0.1 cm of matrix resin on one side was obtained and kept for one day to cure. The same process on the other side was applied to obtain a double-side-coated CF sheet. Then, coated sheet is kept for 6 days to cure.

### 2.3 Characterization of Treated MWCNT-Coated CF Sheet

The content of matrix resin was evaluated by weighing the CF sheet before and after the coating procedure. The formula for calculating the coating contents is:

$$k = \frac{w_k - w_o}{w_o} \times 100 \tag{1}$$

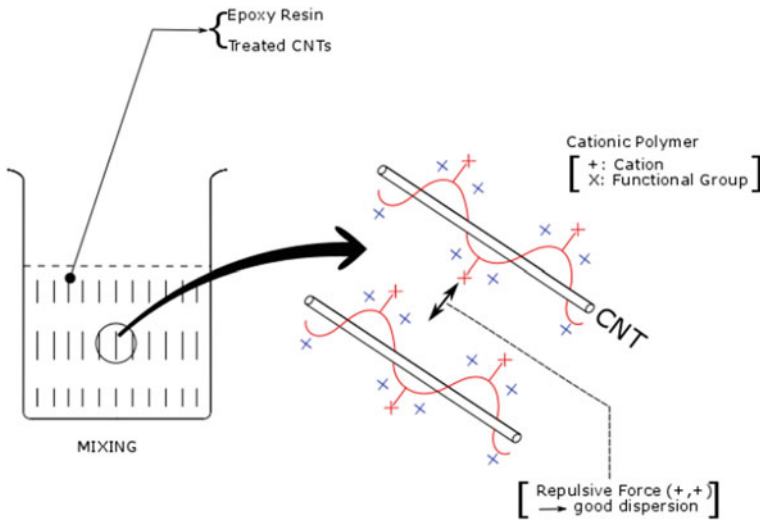


**Fig. 5** Cationic polymer treatment of MWCNT to improve dispersion

where  $k$  is the coating content,  $w_0$  is the weight of CF sheet before coating, and  $w_k$  is the weight of CF sheet after coating.

#### 2.4 Preparation of CF Sheets (Virgin, 0.2–0.5 wt% MWCNT Coated)

The CF sheet was cut into a dimension of  $30 \times 50$  cm. A mix ratio of 40:100 g of amine hardener and epoxy resin, respectively, was taken. The matrix resin was coated on the both the sides of CF sheet by using the hand lay-up method and then kept the coated sheet for 6 days to cure. After these procedures, matrix resin-coated CF sheets were obtained.

A CF sheet was cut into a dimension of  $30 \times 50$  cm. A fresh 0.7 g MWCNT which is 0.5 wt% of 140 g matrix resin is taken; then, this 0.7 g MWCNT was gradually mixed into the epoxy resin by using the same procedure applied above in treated MWCNTs. After mixing, a hand lay-up process is applied to coat the both sides of CF sheet. After these procedures, the MWCNT-coated CF sheet was obtained. Similarly, the MWCNT-coated CF sheets were also prepared using the 0.2 wt.% (0.28 g) of CNT addition to the epoxy resin.

### 3 Results and Discussion

#### 3.1 Dispersion of Carbon Nanotubes

Carbon nanotubes are weighted, and the desired amount of MWCNTs was mixed into epoxy resin after the homogenization of the mixture was done with high-shear homogenizer at a speed of 3000–4000 rpm. The epoxy/MWCNT mixture was then mixed with amine hardener and applied onto the carbon fiber mat using hand lay-up method. For the observation of dispersion behavior of MWCNT in epoxy matrix for treated and non-treated samples, SEM analysis was done.

From the SEM images, agglomeration of MWCNT (Fig. 6) was observed due to the improper mixing with the epoxy matrix. Uniform dispersion of MWCNTs into the matrix is important to achieve better properties of the CFRPs. So, the MWCNTs were then chemically treated, and the same procedure is repeated to produce CFRP sheets. As we can see in Fig. 7, the dispersion of MWCNTs was improved to some extent which was accomplished only due to the treatment of MWCNTs in a cationic polymer. The basic principle behind this improvement is that the MWCNTs get positively charged, and because of same charge among the MWCNTs, it gets the repulsive force among them due to which they get dispersed among the epoxy [2].

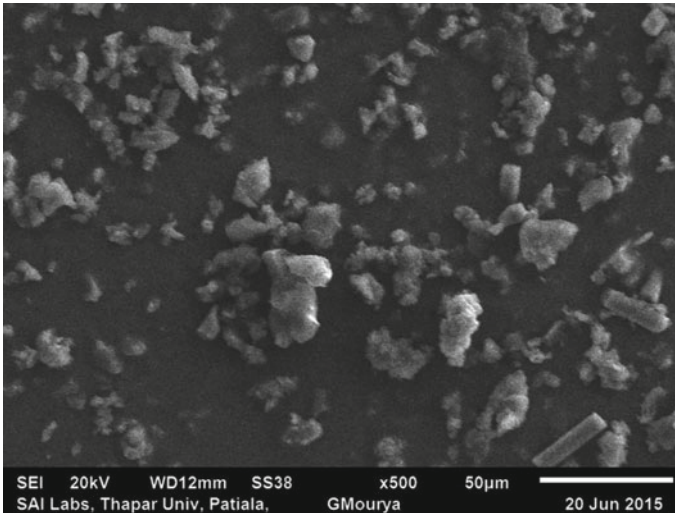


**Fig. 6** SEM micrographs of 0.5 wt% MWCNT-CFRP without treatment

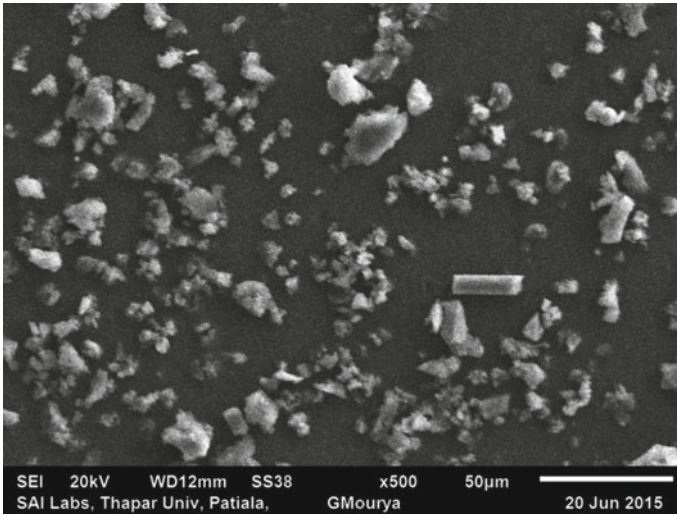


Fig. 7 SEM micrographs of 0.5 wt% MWCNT-CFRP with treatment

### 3.2 Tensile Strength

The specimen was cut from the prepared nanocomposite sheet and prepared as per the ASTM Standards D3037/3039 for tensile testing as shown in Figs. 8, 9, and 10.

Table 2 shows the result produced from the tensile testing of CFRP without MWCNT loading. Different tensile strength was obtained due to the failure of samples from different positions. The samples which are fractured from the center show good results of the tensile strength, while in case of one sample, the failure is from the tab. So, five samples are tested, and the mean value is considered which comes out to be 148.323 MPa. Figures 11 and 12 show the sample conditions before and after tensile testing.

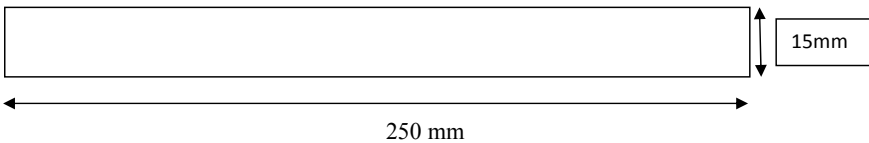


Fig. 8 Tensile test specimen geometry without tabs

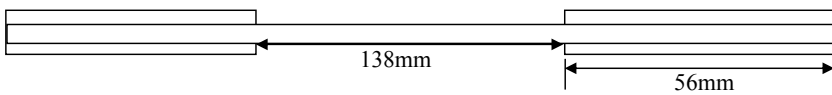


Fig. 9 Tensile test specimen geometry with tabs



**Fig. 10** Specimen for tensile testing

**Table 2** Result showing maximum stress and maximum strain for virgin samples (without MWCNTs)

S. No.	Maximum force (N)	Maximum displacement (mm)	Maximum stress (N/mm <sup>2</sup> )	Maximum strain (%)
1	7120.63	4.18800	207.901	8.37600
2	2553.4	1.45200	92.8185	2.90400
3	3377.81	2.09700	101.497	4.19400
4	4622.34	3.12500	138.559	6.25000
5	5924.69	4.04200	200.837	8.08400
Mean	4719.78	2.98080	148.323	5.96160

**Fig. 11** Samples before test

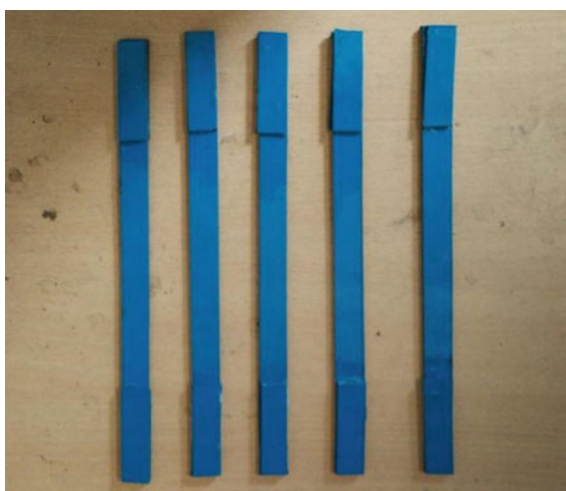


Table 3 and Figs. 13 and 14 show the result outcome of 0.2 wt% MWCNTs. From above results, it can conclude that max stress is varied between 92.9858 and 267.331 N/mm<sup>2</sup> having a mean value of 152.426 N/mm<sup>2</sup>. If we compare the result of 0.2 wt% MWCNTs from virgin sample, we could have found that there is an improvement in tensile strength.

Table 4 and Figs. 15 and 16 show that maximum stress value is varied from 175.593 N/mm<sup>2</sup> to 305.338 N/mm<sup>2</sup> having a mean value of 230.667 N/mm<sup>2</sup> as

**Fig. 12** Samples after test**Table 3** Result outcome of 0.2 wt% MWCNTs

S. No.	Maximum force (N)	Maximum displacement (mm)	Maximum stress (N/mm <sup>2</sup> )	Maximum strain (%)
1	3632.81	1.76400	147.699	3.52800
2	3789.84	1.80300	127.176	3.60600
3	6149.69	3.03400	267.331	6.06800
4	2703.75	1.60100	126.937	3.20200
5	2890.00	1.33600	92.9858	2.67200
Mean	3833.22	1.90760	152.426	3.81520

**Fig. 13** Samples of 0.2 wt% before test



**Fig. 14** Samples of 0.2 wt% after test



**Table 4** Result outcome of 0.5 wt% MWCNTs

S. No.	Maximum force (N)	Maximum displacement (mm)	Maximum stress (N/mm <sup>2</sup> )	Maximum strain (%)
1	6062.19	4.54000	175.593	9.08000
2	8446.88	4.46600	305.338	8.93200
3	8939.38	3.86100	250.108	7.72200
4	9275.63	4.20500	286.444	8.41000
5	7663.13	3.54500	187.491	7.09000
6	7077.50	3.04100	179.087	6.08200
Mean	7910.78	3.94300	230.677	7.88600

**Fig. 15** Samples of 0.5 wt% MWCNTs before test



**Fig. 16** Samples of 0.5 wt% MWCNTs after test



compared to the other outcome of above result; this is quite impressive. Tensile result shows that there is a great improvement from the virgin samples, and even from the 0.2 wt% MWCNTs, the maximum stress value jumps from 148.323 to 230.667 N/mm<sup>2</sup> in virgin samples and in 0.2 wt% MWCNTs, it jumps from 152.426 to 230.667 N/mm<sup>2</sup> which is also quite astonishing.

Table 5 and Figs. 17 and 18 show that the result came from this experiment is quite good and impressive; the maximum stress values are ranging between 216 N/mm<sup>2</sup> and 400 N/mm<sup>2</sup>, having a mean value of 304 N/mm<sup>2</sup> which is greatest among all the samples tested under the same condition. From this, it was concluded that the treated MWCNTs have the highest tensile strength.

From Table 6 and Fig. 19, it was observed that the maximum stress value is increasing as we increase the % of MWCNTs because the stress value is distributed among the dispersed MWCNTs which enhanced the overall tensile strength of the samples, but the treated MWCNTs have quite astonishing result among all which shows that the MWCNTs among the epoxy are uniformly distributed. Maximum force and maximum displacement are fluctuating according to the overall stiffness variation.

**Table 5** Tensile result of 0.5 wt% treated MWCNTs

S. No.	Maximum force (N)	Maximum displacement (mm)	Maximum stress (N/mm <sup>2</sup> )	Maximum strain (%)
1	7488.13	3.89300	311.694	7.78600
2	7356.56	3.53000	292.391	7.06000
3	7525.63	3.76100	299.682	7.52200
4	9667.50	4.81300	400.476	9.62600
5	6125.31	2.98700	216.948	5.97400
Mean	7632.63	3.79680	304.238	7.59360

**Fig. 17** Samples of 0.5 wt% MWCNTs before test



**Fig. 18** Samples of 0.5 wt% MWCNTs after test



**Table 6** Comparison of result of all the different types of samples

S. No.	Maximum force (N)	Maximum displacement (mm)	Maximum stress (N/mm <sup>2</sup> )	Maximum strain (%)
0.0 wt% MWCNTs	4719.78	2.98080	148.323	5.96160
0.2 wt% MWCNTs	3833.22	1.90760	152.426	3.81520
0.5 wt% MWCNTs	7910.78	3.94300	230.677	7.88600
0.5 wt% treated MWCNTs	7632.63	3.79680	304.238	7.59360

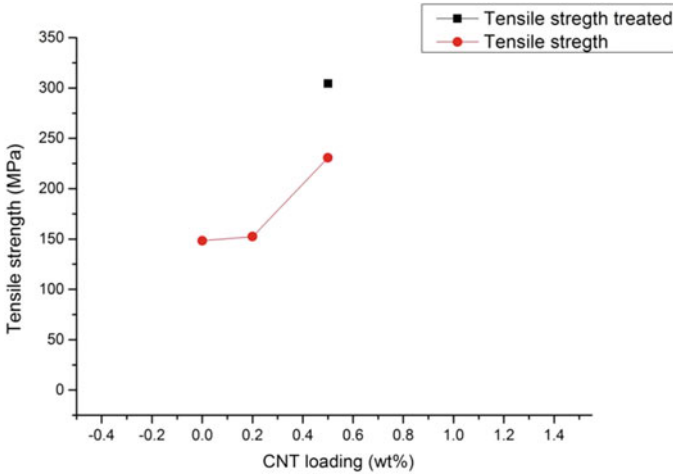


Fig. 19 Tensile strength to MWCNT loading (wt%)

Samples with 0.5 wt% treated MWCNTs show the improved tensile strength which results approx. 51% improvement compared to without MWCNT samples. 0.5 wt% treated MWCNT composites' tensile strength was improved by 24% than 0.5 wt% without treated MWCNT addition.

### 4 Flexural Properties

Flexural properties of the prepared MWCNT polymer nanocomposites were evaluated using three-point bend test. Flexural samples were prepared according ASTM D790 Standard as shown in Figs. 20 and 21.

Six samples were taken from each system, and the three-point bending test was performed using the universal testing machine. The results were shown for all the samples in the following Tables 7, 8, 9, and 10.

Above tables show that maximum stress value is ranging between 51.60 N/mm<sup>2</sup> and 78.85 N/mm<sup>2</sup>, having the mean value of 62.17 N/mm<sup>2</sup>.

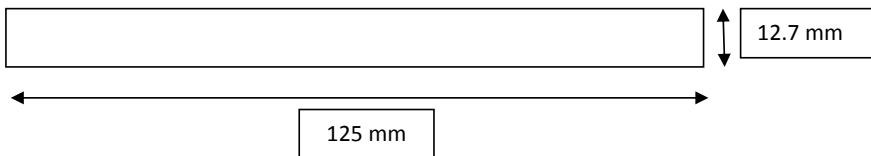
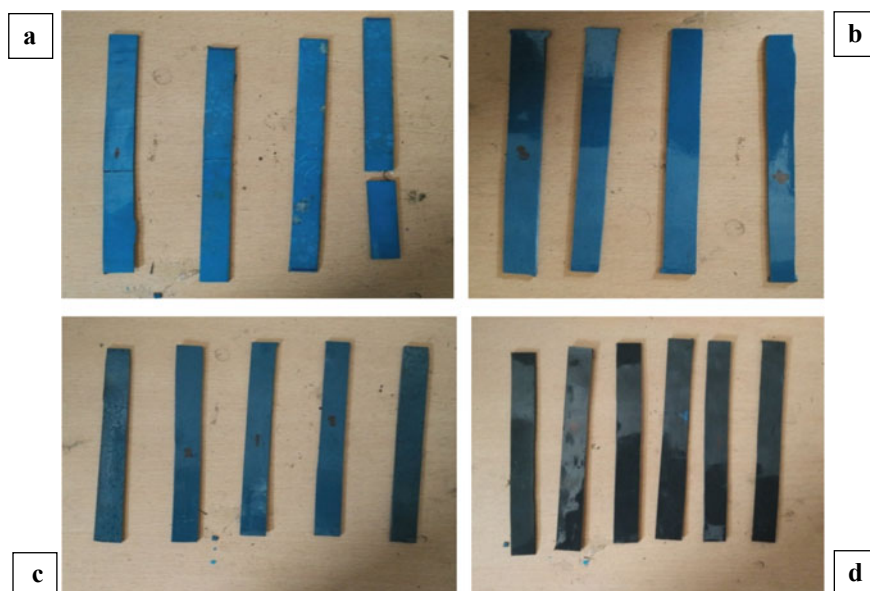


Fig. 20 Specimen dimensions for bending test



**Fig. 21** **a** Samples without MWCNTs after test, **b** samples with 0.2 wt% MWCNTs after test, **c** samples with 0.5 wt% MWCNTs after test, and **d** samples with 0.5 wt% treated MWCNTs after test

**Table 7** Bending result of the virgin samples

S. No.	Maximum force (N)	Maximum displacement (mm)	Maximum stress (N/mm <sup>2</sup> )	Maximum strain (%)
1	38.53	20.06	62.87	3.13
2	33.97	17.73	65.08	2.45
3	26.59	20.36	51.60	2.96
4	41.75	19.71	55.78	3.36
5	39.38	21.13	58.86	3.55
6	49.44	19.33	78.85	3.04
Mean	38.28	19.72	62.17	3.08
Standard deviation	7.65625	1.15114	9.49414	0.37807

Above table shows the different values of bending after which we can conclude that max stress value compared to virgin samples is quite good.

Above table concludes that the maximum stress values are improved as the %wt. of MWCNTs are increased.

From above bending result presented in Fig. 22, the samples without MWCNT show the maximum bending stress 62.17 MPa. It is clearly seen that as the MWCNT

**Table 8** Bending result of 0.2 wt% MWCNTs

S. No.	Maximum force (N)	Maximum displacement (mm)	Maximum stress (N/mm <sup>2</sup> )	Maximum strain (%)
1	18.44	21.42	69.00	2.34
2	22.06	21.92	87.90	2.37
3	22.84	22.55	89.95	2.46
4	20.78	21.32	79.51	2.30
Mean	21.03	21.80	81.59	2.37
Standard deviation	1.92420	0.56323	9.53135	0.06801

**Table 9** Bending result of 0.5 wt% MWCNTs

S. No.	Maximum force (N)	Maximum displacement (mm)	Maximum stress (N/mm <sup>2</sup> )	Maximum strain (%)
1	49.19	20.04	138.27	2.53
2	41.41	20.47	123.96	2.51
3	51.03	5.03	137.23	0.65
4	52.56	10.83	138.52	1.40
5	53.34	12.60	146.41	1.60
Mean	49.51	13.79	136.88	1.74
Standard deviation	4.79568	6.53070	8.10080	0.79691

**Table 10** Bending result of 0.5 wt% treated MWCNTs

S. No.	Maximum force (N)	Maximum displacement (mm)	Maximum stress (N/mm <sup>2</sup> )	Maximum strain (%)
1	51.22	22.00	158.85	2.53
2	60.44	21.45	210.38	2.32
3	58.03	25.28	150.68	3.19
4	51.25	20.38	162.56	2.32
5	51.25	16.41	128.18	2.07
Mean	54.44	21.10	162.13	2.49
Standard deviation	4.46118	3.19841	30.0945	0.42595

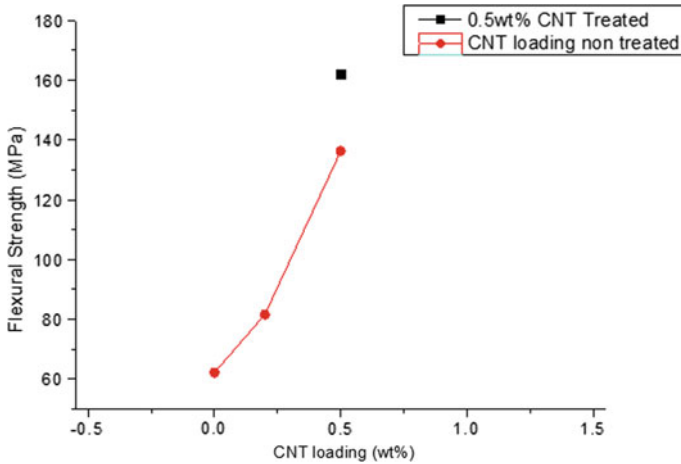


**Fig. 22** Flexural strength to MWCNT loading (wt%)

content is increased, the flexural strength is also increased. There is a significant enhancement in the flexural strength at the 0.5 wt% treated MWCNT loading. After chemical treatment of MWCNTs, it shows a visible increase in the flexural strength of about 101 MPa with the same 0.5 wt% of MWCNT loading. Chemical-treated MWCNT is more efficient as reinforcing agents than non-treated MWCNTs. Chemical-treated MWCNT epoxy matrix also has the better dispersion of MWCNTs than non-treated MWCNT epoxy matrix which enables the effective stress transfer between the epoxy matrixes due to the interfacial bonding.

## 5 Conclusion

Carbon fiber-reinforced composite has been formed by using carbon fiber as reinforcement and epoxy mixed with MWCNTs as a matrix. MWCNTs are mixed into epoxy in different weight percentages.

- The dispersion of MWCNTs is improved when MWCNTs were chemically treated in a cationic polymer.
- Samples with 0.5 wt% treated MWCNTs show the improved tensile strength which results approx. 51% improvement compared to without MWCNT samples. 0.5 wt% treated MWCNT composites' tensile strength is improved by 24% than 0.5 wt% without treated MWCNT addition.
- As the MWCNT content is increased, the flexural strength is also increased. There is a significant enhancement in the flexural strength at the 0.5 wt% treated MWCNT loading. After chemical treatment of MWCNTs, it shows a visible increase in the flexural strength of about 101 MPa with the same 0.5 wt% of MWCNT loading.

## References

1. Siddiqui, N.A., et al.: Tensile strength of glass fibers with carbon nanotube–epoxy nanocomposite coating. *Compos: Part A* **40**, 1606–1614 (2009)
2. Mao, D., Yaniv, Z., Fink, R., Johnson, L.: Carbon nanotube-reinforced epoxy nanocomposites for mechanical property improvement
3. Njuguna, J., Pielichowski, K., Alcock, J.R.: Epoxy based fibre reinforced nanocomposites. *Adv. Eng. Mater.* **9**(10), 835–847 (2007)
4. Prakash, C., Singh, S., Sharma, S., Garg, H., Singh, J., Kumar, H., Singh, G.: Fabrication of aluminium carbon nano tube silicon carbide particles based hybrid nano-composite by spark plasma sintering. *Mater. Today. Proc.* **21**, 637–1642 (2020)
5. Sathyanarayana, S., Hübner, C.: Thermoplastic nanocomposites with carbon nanotubes. In: *Structural nanocomposites* (pp. 19–60). Springer, Berlin, Heidelberg (2013)
6. Gupta, A.K., Harsha, S.P.: Analysis of mechanical properties of carbon nanotube reinforced polymer composites using continuum mechanics approach. *Procedia Mater. Sci.* **6**, 18–25 (2014)
7. Soliman, E., Kandil, U., Taha, M.: Improved strength and toughness of carbon woven fabric composites with functionalized MWCNTs. *Materials* **7**(6), 4640–4657 (2014)
8. Ramana, G.V., Padya, B., Kumar, R.N., Prabhakar, K.V.P., Jain, P.K.: Mechanical properties of multi-walled carbon nanotubes reinforced polymer nanocomposites (2010)
9. Siddiqui, N.A., Khan, S.U., Ma, P.C., Li, C.Y., Kim, J.K.: Manufacturing and characterization of carbon fibre/epoxy composite prepregs containing carbon nanotubes. *Compos. A Appl. Sci. Manuf.* **42**(10), 1412–1420 (2011)
10. Arash, B., Park, H.S., Rabczuk, T.: Mechanical properties of carbon nanotube reinforced polymer nanocomposites: a coarse-grained model. *Compos. B Eng.* **80**, 92–100 (2015)
11. Arash, B., Wang, Q., Varadan, V.K.: Mechanical properties of carbon nanotube/polymer composites. *Sci. Rep.* **4**, 6479 (2014)
12. Akcin, Y., Karakaya, S., Soykasap, O.: Electrical, thermal and mechanical properties of CNT treated prepreg CFRP composites. *Mater Sci Appl* **7**, 465–483 (2016)
13. Siddiqui, N.A., Li, E.L., Sham, M.L., Tang, B.Z., Gao, S.L., Mäder, E., Kim, J.K.: Tensile strength of glass fibres with carbon nanotube–epoxy nanocomposite coating: effects of CNT morphology and dispersion state. *Compos. A Appl. Sci. Manuf.* **41**(4), 539–548 (2010)



# Mechanical Characterization of 60Pb40Sn Reinforced Al6061 Self-healing Composite



Nitin Kumar Gupta, Manoj Kumar, and G. D. Thakre

**Abstract** The present study concentrates on the mechanical characterization of Al6061 self-healing metal matrix reinforced with low-melting points composite. It has been prepared by reinforcing low-melting point alloy in aluminum matrix. The self-healing characteristic has been obtained due to the presence of solder alloy. The developed material has been characterized using SEM and micrograph. The mechanical characteristics of the developed material have been determined experimentally by performing the tensile and Charpy tests. The comparison between self-healing composite with pure matrix material has been developed. And experimental assessment results show a reduction in tensile force as well as stress by 30%. Reduction by 50% in other properties like braking distance and strain in fabricated self-healing matrix. Similarly, in the case of the Charpy test, it reduces by 39% for self-healing samples as compared to pure aluminum sample.

**Keywords** Self-healing · Low-melting point alloy · Tensile strength · Charpy test

## 1 Introduction

After the Stone Age, it was the discovery of metals that has dramatically changed human evolution. Over time, people started using alloys like brass, bronze, gold, etc. in their day-to-day life. Today, materials have become an integral part of industrial development. High strength along with longer useful life has been a primary prerequisite of the materials for industrial applications. This has challenged the material scientists to think beyond the boundaries of conventional materials and develop new generation materials with better characteristics. As a result of which the metal matrix composites (MMCs) have come into existence. The MMCs are prepared by reinforcing different materials in the form of particles or fibers into the parent material

---

N. K. Gupta (✉) · M. Kumar  
DIT University, Dehradun, India  
e-mail: [nitin.gupta@dituniversity.edu.in](mailto:nitin.gupta@dituniversity.edu.in)

G. D. Thakre  
CSIR-IIP Dehradun, Dehradun, India

© Springer Nature Singapore Pte Ltd. 2020  
C. Prakash et al. (eds.), *Advances in Materials Science and Engineering*,  
Lecture Notes in Mechanical Engineering,  
[https://doi.org/10.1007/978-981-15-4059-2\\_4](https://doi.org/10.1007/978-981-15-4059-2_4)

in order to enhance the latter's properties and/or impart unique properties as per the specific design need. They can be developed into materials possessing high; wear resistance, specific stiffness, specific strength, hardness, thermal conductivity, and energy absorption along with being light in weight. The research in MMCs had seen significant interest around the globe paving the way to the development of smart, self-lubricating, synthetic foams, and self-healing composites [1–5].

Self-healing in metals shows a remarkable development in engineering materials. This leads to self-repair itself by some sort of mechanism. Literature shows that there are three important methods have used to develop this kind of self-healing materials. Some of the researchers have followed supersaturated solid solutions methods to fill the developed cracks into the matrix, whereas some of them have used shape memory alloy as reinforcement and the third methods show huge potential by using low-melting point alloy like solder as reinforcement in the metallic matrix [6–8].

The first method initiated by researchers to fabricate the concept of crack closure into materials [8–12]. The method was further improved by notable contributions from [13–16]. Using this technique, Alaneme et al. and Omosule et al. [17–20] setup and experimentations to show the self-healing in Al-Mg-Si alloy. Similarly, Lumley [16] utilized this technique to investigate the self-healing behavior in wrought Al-Cu-Mg-Ag alloy. Laha et al. show a huge potential of these methods by improving self-healing behavior in stainless steel. This method is more suitable to fill the cracks like voids and microcrack; this will restore the mechanical properties [21–23].

The second method of incorporating shape memory alloy into the metal matrix utilizes the capability of material to remember its shape [18]. An exhaustive literature has been reported about the incorporation of SMA into a metal matrix system [19]. As a result, the fabricated self-healing reinforced with shape memory alloy when develop cracks. In such cases, wire will get stretched followed by separation into matrix. And these cracks would be closed by applying temperature to materials. This approach has been reported by [24–27]. Ferguson et al. [20] emphasize the process of development of the self-healing materials through zinc alloy ZA-8 by reinforcing NiTi [28, 29]. However, it is a very expensive development [27].

This method has shown great potential among the material scientists to develop self-healing materials. The solder alloys when exposed to a certain healing temperature, melts and it also flows under gravitational force. The capillary actions play a critical role to fill up the cracked site. After that, they solidify and close the cracks partially. Oladijio et al. [30, 31] reported an experimental work on the impact properties of self-healing composites using an impact test. The authors reported the highest healing efficiency of 61% [30–33].

As per the literature, this reveals that the area of self-healing composites is still in the nascent stage. Various researches are trying to develop techniques that will help them to fabricate efficient self-healing materials. In the present study, the concepts of solder material reinforced in the matrix are taken into consideration to develop the self-healing matrix. And physical characterizations of the fabricated materials are taken to compare the physical properties of the pure matrix. The study will be of significant help for material scientists in developing material for industrial, automotive and aerospace applications.

**Table 1** Al6061 alloy and 60Pb40Sn solder alloys chemical Composition

Al6061		Solder (60Pb40Sn)	
Si	0.65	Sn	40
Cu	0.25	Pb	60
Mn	0.15		
Mg	0.8		
Cr	0.7		
Zn	0.025		
Ti	0.15		
Al	Balance		

**Table 2** Al6061 alloy and 60Pb40Sn solder alloys mechanical properties

Property	Tensile strength (MPa)	Density (g/cm <sup>3</sup> )	Hardness (BHN)	Melting points (°C)	Modulus elasticity (GPa)	% elongation
Al6061	124	2.7	45	>660.3	69	8%
Solder (60Pb40Sn)	37.0	9.27	–	180–238		25%

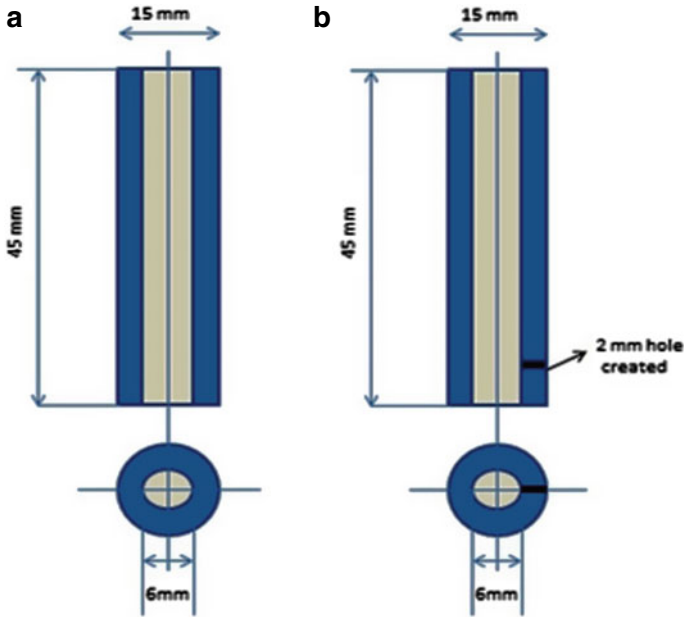
## 2 Materials

Aluminium is the most suitable material to be used in industries due to its various promising properties like lightweight, high strength, less corrosion intensity and ease of availability in the market. In this experimental work Al6061 alloy has been used as a base matrix and solder 60Pb40Sn as the reinforcement. The materials used in the experimental process were purchased from the local Uttarakhand Indian market. The chemical composition and mechanical properties of the matrix and reinforcement are given in Tables 1 and 2.

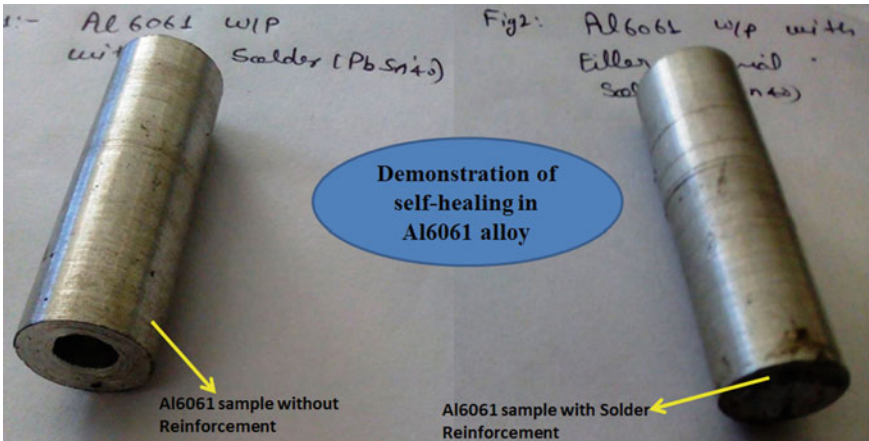
## 3 Concept of Sample Design

Figure 1 shows the drawing of the sample to be fabricated. The samples were prepared through casting followed by drilling and then filling it with solder alloy which exhibits low-melting properties. The detailed methods have been explained in [34–36].

The fabricated samples of Al6061 are shown in Fig. 2. This sample has the reinforcement with and without solder. The samples were exposed to temperature (220–240 °C). After temperature, the sample gets filled by flowing low-melting alloy into the 2 mm drilled hole. The low-melting point alloy at high-temperature melts and under the influence of gravity flow to the crack/gaps thereby healing it. Figure 3 shows the healed Al6061 sample under temperature.

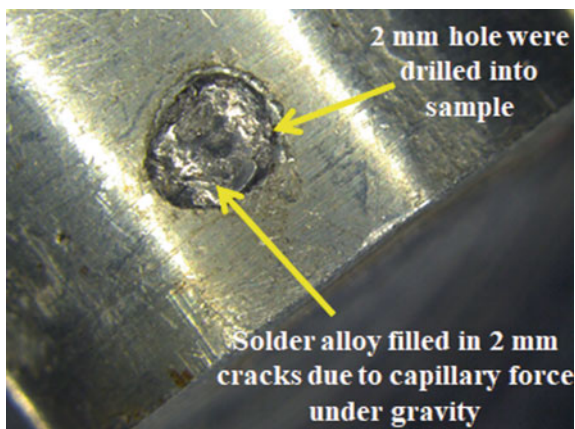


**Fig. 1** Experimental sample of self-healing composite developed **a** sample fabricated without crack and **b** sample fabricated with developing an artificial crack [34]



**Fig. 2** Sample of partially self-healing Al6061 alloy

**Fig. 3** Partially healed sample at 200–240 °C



## 4 Mechanical Characterization

### 4.1 Mechanical Properties

To investigate the mechanical properties of the sample, a standard ASTM method has followed in testing. The following two different test specimens were developed:

- (i) pure Al6061 alloy
- (ii) Al6061 alloy with solder (60Pb40Sn) (this has very low-melting point).

This solder was filled into a sample by a preset procedure. Drilling a through-hole of 3 mm diameter in cast matrix of Al6061 alloy. And then use hydraulics pressure filling setup to forced solder into that hole under preheated condition of the sample. To evaluate the condition of the filling of the cavity, the proper microstructural examination has been performed.

### 4.2 Tensile Test

The test was performed on UTM as per the standard test procedure of ASTM E8M-04. The samples A and sample B were prepared by pure Al6061 alloy. The sample B was then filled with solder 60Pb40Sn based material. Sample C was fabricated through casting methods and it also gets filled with solder material. Figure 4 represents the actual fabricated sample

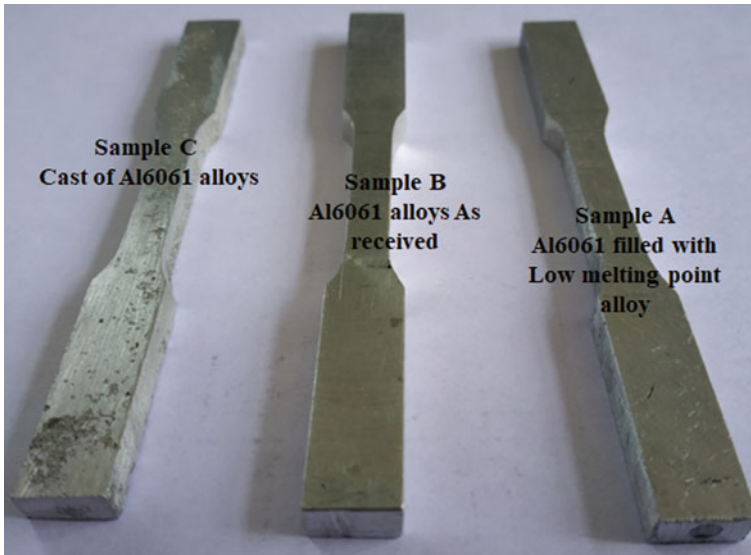


**Fig. 4** Tensile test specimens, fabricated test sample with solder and without solder

### 4.3 Charpy Test

To get the results for impact strength Charpy test has performed. An E-23-07 ASTM standard has followed into this testing. Figure 5 shows the developed samples for the impact test. Two different samples were fabricated; first one was without filling of solder materials and the second sample was filled with the solder materials.

## 5 Results and Discussion

### 5.1 Physical Characteristics

Figure 6 shows the results of the tensile test performed on the developed samples. A Stress–Strain curve has developed for the pure Al6061 and self-healing Al6061 alloy.

From the results, this has observed that the specimen prepared from pure aluminum 6061 alloy has very high strain of about 23%. Whereas self-healing sample has 11% of strain and similarly sample fabricated by casting procedure has 10% strain. Further investigation of the tensile sample shows that the value of ultimate stress of 313 MPa, 219 MPa, 166 MPa, respectively, for the pure Al6061 specimen, self-healing Al alloy, and the cast sample. The results for the tensile tests are given in Table 3. 30% reduction in ultimate force and in ultimate stress has observed in the

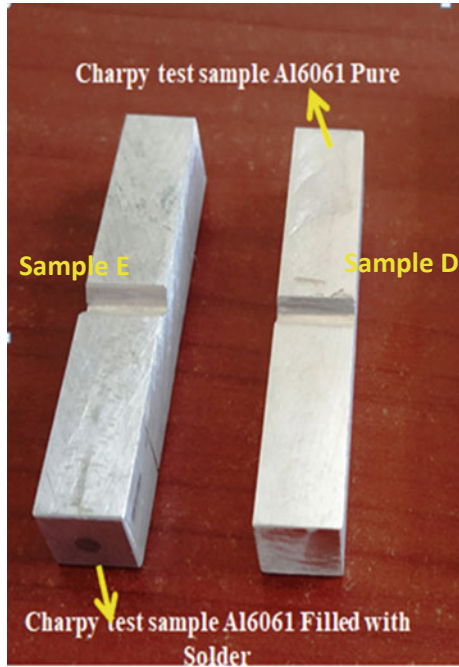


Fig. 5 Impact test specimen

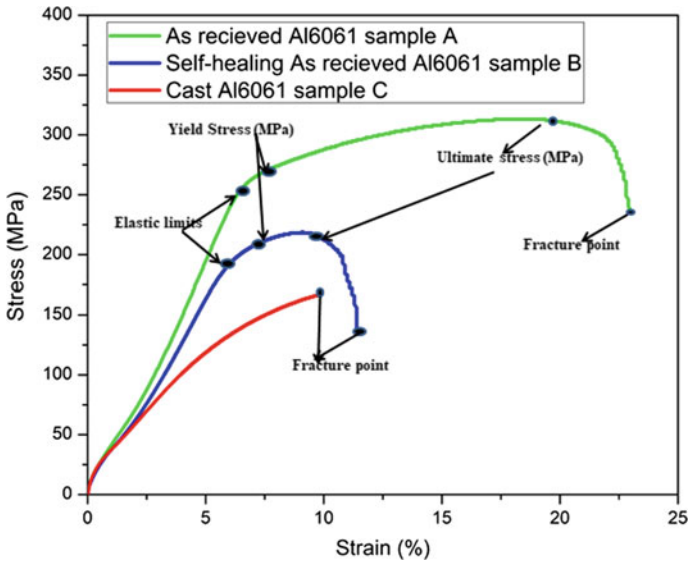


Fig. 6 Stress-strain behavior of pure and self-healing Al alloy

**Table 3** Tensile strength results

Sample—flat sample					Speed of the UTM—4.00 mm/min		
	Width (mm)	Ultimate force (N)	Area (mm <sup>2</sup> )	Thickness (mm)	Breaking distance (mm)	Ultimate stress (MPa)	Strain (%)
Sample A	6.00	10,602	33.8	5.64	5.70	313	22.8
Sample B	6.00	7395	33.8	5.64	2.84	219	11.3
Sample C	6.00	5627	33.8	5.64	2.44	166	9.77

**Table 4** Results of Impact test

Code	Description	Impact energy (J)	Initial energy (hammer) (J)
D	Pure matrix of Al6061	61.447	408
E	Solder material filled	37.427	408

self-healing sample and similarly 50% reduction has noted in Breaking distance and strain [34, 35] as compared to pure Al6061 alloy. Whereas sample made from casting Al6061 shows poor results. Low-melting point alloy does not play a significant role to improve tensile strength of materials. The result shows the load does not transfer from aluminum matrix to solder materials due to weak atomic bonding. Due to this, results for tensile strength are received very poorly in self-healing Al alloy. Similarly, in the case of cast samples, the materials get oxidized and hence brittle resulting in poor tensile properties.

As per the data mention in Table 4 received from testing shows that the impact energy of the self-healing sample is reduced to 37.43 J whereas in the case of sample with Al6061 has 67.14 J of rupture energy, which as more than the self-healing sample. This difference of the results is due to the weak interface between matrix and reinforced solder. Furthermore, the stress concentration may also play a significant role due to 3 mm hole, which created stress concentration in the sample. Material separations were also observed in the process of the testing, the self-healing sample with solder does not allow material to separate into two pieces. But in the case of cast sample and pure aluminum, the sample get to break into two pieces.

## 5.2 Microstructure Examination

The microstructures of the solder reinforced Al6061 alloys sample were investigated using advanced Laboratory Metallurgical Microscope. Figure 7 shows the boundary



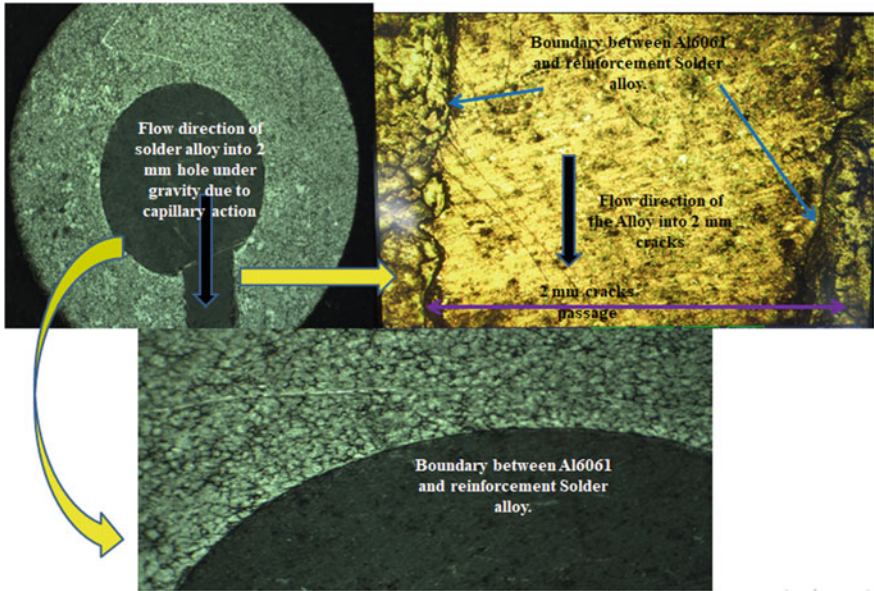


Fig. 7 Microstructure images of self-healing samples

between matrix and reinforced material, which clearly shows the flow pattern of solder materials and self-healing of Al6061 materials.

## 6 Conclusion

This experimental work proves that the solder alloy (low-melting point alloy) can play a major role in self-healing Al6061 alloy. This type of new material will improve the survivability of the materials with the compromise of mechanical properties. The above experimentation results concluded that the developed self-healing material shows a reduction in tensile strength. Similarly, 39% reductions of rupture energy were reported in impact strength of self-healing.

## References

1. Martinez Lucci, J., Rohtagi, P.: Design and Demonstration of Self-Healing Behavior in a Lead Free Solder Alloy. <https://doi.org/10.2514/6.2009-4514>
2. Bruck, H.A., Evans, J.J., Peterson, M.L.: The role of mechanism in biological and biologically inspired materials. *Exp. Mech.* **42**(4), 361–371 (2002)
3. Ferguson, J.B., Rohtagi, P.: Self-healing metals and metal matrix composites. *Miner. Metals Mater. Soc.* <https://doi.org/10.1007/s11837-014-0912-4>

4. Ghosh, S.K.: Self-healing Materials: Fundamentals, Design Strategies, and Applications. ISBN: 978-3-527-31829-2
5. Lumely, R.: Self-healing materials: an alternative approach to 20 centuries of materials science, vol. 100, pp. 219–254. In: Van Der Zwaag, S. (ed.). Springer series in materials science (2007)
6. Alaneme, K.K., Bodurin, M.O.: Self-healing using metallic material systems—a review. <https://doi.org/10.1016/j.apmt.2016.11.002>
7. Rohatgi, P.K., Dorri, A., Schultz, B.F., Ferguson, J.B.: Synthesis and properties of metal matrix Nano composites (MMNCS), syntactic foams, self-lubricating and self-healing metals. In: The Minerals, Metals & Materials Society, pp. 1515–1524 (2013)
8. Van der Zwaag, S., Van Dijk, N.H., Jonkers, H.M., Mookhoeke, S.D., Sloof, W.G.: Self-healing Behavior in Man-Made Engineering Materials: Bio Inspired But Taking into Account Their Intrinsic Character. <https://doi.org/10.1098/rsta.2009.0020>
9. Hautakangas, S., Schut, H., Van der Zwaag, S., del Castillo, P.R.D., Van Dijk, N.H.: The role of the aging temperature on the self healing kinetics in an under aged AA2024 aluminum alloy. In: Proceedings of the First International Conference on Self Healing Materials, 18–20 Apr 2007, Noordwijk aan Zee
10. He, S.M., van Dijk, N.H., Schut, H., Peekstok, E.R., van der Zwaag, S.: Thermally Activated Precipitation at Deformation-Induced Defects in Fe-Cu and Fe-Cu-B-N Alloys Studied by Positron Annihilation Spectroscopy. <https://doi.org/10.1103/physrevb.81.094103>
11. He, S.M., van Dijk, N.H., Paladugu, M., Schut, H., Kohl Brecher, J., Tichelaar, F.D., van der Zwaag, S.: In Situ Determination of Aging Precipitation in Deformed Fe-Cu and Fe-Cu B-N Alloys by Time-Resolved Small-Angle Neutron Scattering. <https://doi.org/10.1103/physrevb.82.174111>
12. He, S.M., Brandhoff, P.N., Schut, H., van der Zwaag, S., van Dijk, N.H.: Positron Annihilation Study on Repeated Deformation/Precipitation Aging in Fe–Cu–B–N Alloys. <https://doi.org/10.1007/s10853-013-7411-9>
13. Zhang, S., Kohlbrecher, J., Tichelaar, F.D., Langelaan, G., Brück, E., van der Zwaag, S., van Dijk, N.H.: Defect-Induced Au Precipitation in Fe–Au and Fe–Au–B–N Alloys Studied by In Situ Small-Angle Neutron Scattering. <https://doi.org/10.1016/j.actamat.2013.08>
14. Laha, K., Kyono, J., Shinya, N.: An Advanced Creep Cavitation Resistance Cu-Containing 18Cr–12Ni–Nb Austenitic Stainless Steel. <https://doi.org/10.1016/j.scriptamat.2006.12.030>
15. Alaneme, K.K., Omosule, O.I.: Experimental Studies of Self Healing Behavior of Under-Aged Al-Mg-Si Alloys and 60Sn–40Pb Alloy Reinforced Aluminum Metal-Metal Composites. <https://doi.org/10.4236/jmmce.2015.31001>
16. Lumley, N., Polmear, I.J.: Advances in self-healing of metals. In: Proceeding of the First International Conference on Self-Healing Materials, Noordwijkaan zee, The Netherlands, 18–20 Apr 2007
17. Shinya, N., Kyono, J., Laha, K.: Self-healing Effect of Boron Nitride Precipitation on Creep Cavitation in Austenitic Stainless Steel. <https://doi.org/10.1177/1045389x060065238>
18. Lumley, R.N., Polmear, I.J., Morton, A.J.: Interrupted aging and secondary precipitation in aluminum alloys. Mater. Sci. Technol. **19**, 1483–1490 (2003)
19. Manuel, M.V., Olson, G.B.: Biomimetic self-healing metals. In: Proceedings of 1st International Conference on Self-Healing Materials, Noordwijk aan Zee, The Netherlands, pp. 18–20 (2007)
20. Ferguson, J.B., Schultz, B.F., Rohatgi, P.K.: Zinc alloy ZA-8/shape memory alloy self-healing metal matrix composite. Mater. Sci. Eng. A **620**, 85–88 (2015)
21. Ferguson, J.B., Schultz, B.F., Rohatgi, P.K.: Self-healing metals and metal matrix composites. JOM **66**(6), 866–871 (2014)
22. Manuel, M.V.: Principles of Self-healing in Metals and Alloys: An Introduction. <https://doi.org/10.1002/9783527625376.ch8>
23. Bhattacharya, K.: Microstructure of martensite: why it forms and how it gives rise to the shape-memory effect. Rev. Contemp. Phys. **45**, 528–529 (2004)
24. Alaneme, K.K., Okotete, E.A.: Reconciling Viability and Cost-Effective Shape Memory Alloy Options—A Review of Copper and Iron Based Shape Memory Metallic Systems. <https://doi.org/10.1016/j.jestch.2016.05.010>

25. Birman, V.: Shape Memory Alloy Springs Used as Reduced Power/Weight Actuators. <https://doi.org/10.1115/imece2004-60401>
26. Krishna Guntur, R., Amano, S., Martinez Lucci, J., Rohtagi, P.K.: Self-Healing Technology for Compressor and Turbine Blades. <https://doi.org/10.1016/j.msea.2014.09.050>
27. Rohatgi, P.K.: Al-Shape Memory Alloy Self-Healing Metal Matrix Composite. <https://doi.org/10.1016/j.msea.2014.09.050>
28. Martinez Lucci, J., Amano, R.S.: Design and Demonstration of Self-Healing Behavior in a Lead Free Solder Alloy. <https://doi.org/10.2514/6.2009-4514>
29. Martinez Lucci, J., Amano, R.S., Rohtagi, P.K.: Self-Healing in an Aluminum Alloy Reinforced With Microtubes. <https://doi.org/10.1115/enic2008-53011>
30. Oladijo, O.P., Bodunrin, M.O., Sobiyi, K., Maledi, N.B., Alaneme, K.: Investigating the self-healing behavior of under-aged and 60Sn-40Pb alloy reinforced aluminum hybrid composites. *Thin Solid Films* **620**, 201–205. <https://doi.org/10.1016/j.tsf.2016.08.071>
31. Zhang, S., Kohlbrecher, J., Tichelaar, F.D., Langelaan, G., Brück, E., van der Zwaag, S., van Dijk, N.H.: Defect-induced Au precipitation in Fe–Au and Fe–Au–B–N alloys studied by in situ small-angle neutron scattering. *Acta Materialia* **61**, 7009–70019 (2013)
32. Lucci, J.M., Amano, R.S., Rohatgi, P., Schultz, B.F.: Experiment and Computational Analysis of Self-Healing in an Aluminum Alloy. [https://doi.org/10.1007/12\\_2015\\_337](https://doi.org/10.1007/12_2015_337)
33. Birman, V.: Review of mechanics of shape memory alloy structures. *Appl. Mech. Rev.* **50**, 629–645 (1997)
34. Gupta, N.K., Thakre, G.D., Kumar, M.: The mechanical and tribological characteristics of Al6061 self-healing materials. *Mater. Res. Express* 6(8), 0865d5 (2019). <https://iopscience.iop.org/article/10.1088/2053-1591/ab23b1>
35. Gupta, N.K., Thakre, G.D., Kumar, M.: Self-Healing Al 6061 Alloy Reinforced with Low Melting Point Alloys. [https://doi.org/10.1007/978-981-13-6412-9\\_53](https://doi.org/10.1007/978-981-13-6412-9_53)
36. Somani, N., Tyagi, Y.K., Kumar, P., Srivastava, V., Bhowmick, H.: Enhanced tribological properties of SiC reinforced copper metal matrix composites. *Mater. Res. Express* **6**, 016549 (2019)

# A Brief Overview of Crystal Plasticity Approach for Computational Materials Modeling



Lakhwinder Singh, Sanjay Vohra, and Manu Sharma

**Abstract** This article presents an overview of crystal plasticity (CP)-based modeling and simulation. A typical CP approach includes the kinematics and constitutive laws to determine the mechanical response of polycrystalline materials. Constitutive laws can be phenomenological or microstructure-based. The latter allows incorporating different deformation mechanisms responsible for deforming the material plastically. For solving the equilibrium and compatibility equations, the types of numerical solvers used are also discussed. For modeling the inhomogeneity in the polycrystalline and multiphase material systems, homogenization techniques are used in CP for the flow of information from single crystal to polycrystalline scale.

**Keywords** Plasticity · Constitutive · Phenomenological · Microstructure · Homogenization · Polycrystalline

## 1 Introduction

Prediction and understanding of the behavior of structural materials can be effectively achieved by incorporating microstructural description of the material into its constitutive model [1]. Continuum models are able to predict materials' behavior by using information about their microstructure, phases (in case of multiphase alloys), crystallographic texture, etc. Results of these continuum models-based simulations can be compared to the experimental results for validation [2–4].

Crystal plasticity (CP) method is used to predict the behavior of polycrystalline materials subjected to external loadings. Crystal plasticity (CP) theory assumes the crystallographic slip to be responsible for plastic deformation of the material [5]. The knowledge of deformation mechanisms from the experiments on single crystals has led to the development of suitable constitutive models. In crystal plasticity modeling, the constitutive models used are mainly of two types: phenomenological and physics/microstructure-based [6]. In phenomenological CP models, the state

---

L. Singh (✉) · S. Vohra · M. Sharma  
Department of Mechanical Engineering, UIET Panjab University, Chandigarh 160014, India  
e-mail: [lakhwinder.fme@gmail.com](mailto:lakhwinder.fme@gmail.com); [lakhwinder@pu.ac.in](mailto:lakhwinder@pu.ac.in)

© Springer Nature Singapore Pte Ltd. 2020  
C. Prakash et al. (eds.), *Advances in Materials Science and Engineering*,  
Lecture Notes in Mechanical Engineering,  
[https://doi.org/10.1007/978-981-15-4059-2\\_5](https://doi.org/10.1007/978-981-15-4059-2_5)

(microstructural) variable used is the slip resistance or critical resolved shear stress (CRSS) while microstructure-based CP models use the internal variables like dislocation densities, second phase fractions, grain shape and size, etc., to describe microstructural state of a material. Nowadays, the microstructure-based constitutive models are gaining more attention as they capture information in terms of microstructural parameters. Further in CP, the generally used numerical solvers for solving governing partial differential equations (PDEs) are the finite element method (FEM) and spectral method. However, in some cases, spectral solvers using fast Fourier transform (FFT) have shown great results over FEM solvers [7, 8]. As in practical applications, polycrystalline materials and multiphase alloys are used, thus homogenization methods are used in CP to address the issue of microstructural inhomogeneity of these materials due to different phases, texture, precipitates, etc. [1]. In this article, a brief overview is presented on above-mentioned aspects of crystal plasticity approach.

Organization of this article is as: Sect. 2 discusses kinematics of CP. Section 3 describes the constitutive models commonly used in CP. In Sect. 4, the types of numerical solvers used in CP are presented. Section 5 describes the various homogenization schemes. Section 6 presents conclusions followed by references.

## 2 Kinematics

For large deformations, multiplicative splitting of the total deformation gradient tensor ' $\mathbf{F} = \frac{\partial \mathbf{x}}{\partial \mathbf{X}}$ ' is done (shown in Fig. 1) into its elastic and plastic components as [6]:

$$\mathbf{F} = \mathbf{F}_e \mathbf{F}_p \quad (1)$$

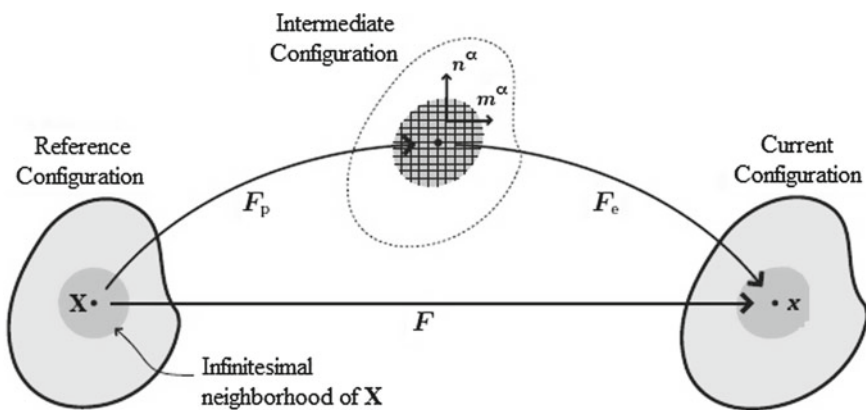


**Fig. 1** Different configurations of a continuum body and splitting of deformation gradient

where ' $\mathbf{x}$ ' and ' $\mathbf{X}$ ' are the position vectors of the material points in current and reference configurations; ' $\mathbf{F}_e$ ' stands for the elastic component of  $\mathbf{F}$  due to the reversible response of the lattice while ' $\mathbf{F}_p$ ' is the plastic component of  $\mathbf{F}$  and is irreversible.

Time evolution of  $\mathbf{F}_p$ , i.e., plastic component of  $\mathbf{F}$  in terms of plastic component of velocity gradient tensor ' $\mathbf{L}_p$ ' is given as:

$$\dot{\mathbf{F}}_p = \mathbf{L}_p \mathbf{F}_p \quad (2)$$

The kinematics remains the same for the different constitutive models used in CP.

### 3 Constitutive Models

Constitutive models are used to predict the material's response when subjected to external loads. In CP, different types of constitutive models are used which have equations for both elasticity and plasticity. The elastic equation is a generalized Hooke's law explained in Sect. 3.1. The plastic constitutive equations involve the slip rates which depends upon the stress ' $\boldsymbol{\sigma}$ ' applied externally and the state (microstructural) variable ' $\mathbf{r}$ ' of the material [6], i.e.,

$$\dot{\gamma} = f(\boldsymbol{\sigma}, \mathbf{r}) \quad (3)$$

Based on the type of constitutive model, state variable ' $\mathbf{r}$ ' and its evolutionary equations are defined for the material.

#### 3.1 Elasticity

The elastic equation is the generalized Hooke's law given as [5]:

$$\mathbf{S} = \mathbb{C} : \mathbf{E} \quad (4)$$

where  $\mathbf{S}$  is the second Piola–Kirchhoff stress tensor,  $\mathbb{C}$  is the fourth-order tensor of elastic stiffness,  $\mathbf{E}$  is the elastic Green–Lagrange strain tensor given as  $\mathbf{E} = (\mathbf{F}_e^T \mathbf{F}_e - \mathbf{I})/2$ ; here  $\mathbf{F}_e$  is the elastic component of  $\mathbf{F}$  and  $\mathbf{I}$  represents the identity tensor of second order.

#### 3.2 Plasticity

The plasticity equations may be phenomenological or physics-based depending on the state variables used for microstructural description. Plastic component of velocity

gradient, i.e.,  $\mathbf{L}_p$  is written as the summation of slip rates on all slip systems [6]:

$$\mathbf{L}_p = \sum_{\alpha=1}^n \dot{\gamma}^{\alpha} \mathbf{m}^{\alpha} \otimes \mathbf{n}^{\alpha} \quad (5)$$

where  $\alpha$  denotes a slip system (combination of one slip plane and one slip direction on that plane),  $\mathbf{n}$  is the number of active slip systems,  $\dot{\gamma}^{\alpha}$  is the slip rate on a particular slip system  $\alpha$ ,  $\mathbf{m}^{\alpha}$  is the unit vector parallel to slip direction, and  $\mathbf{n}^{\alpha}$  is the unit vector normal to slip plane of slip system  $\alpha$ .

The component of shear stress resolved in slip direction on a slip system is responsible for the shearing/slipping on that slip system, and it is given by Schmid's law as [6]:

$$\tau^{\alpha} = \mathbf{S} \cdot (\mathbf{m}^{\alpha} \otimes \mathbf{n}^{\alpha}) = \mathbf{S} \cdot \mathbf{P}_{\text{Schmid}}^{\alpha} \quad (6)$$

where  $\mathbf{S}$  is the second Piola–Kirchhoff stress,  $\mathbf{P}_{\text{Schmid}}^{\alpha} = (\mathbf{m}^{\alpha} \otimes \mathbf{n}^{\alpha})$  is the Schmid tensor. In twinning-based CP models, Eq. (5) contains some additional terms. The plastic velocity gradient  $\mathbf{L}_p$  includes the twin shear  $\gamma_{\text{twin}}$  along with slip rates  $\dot{\gamma}^{\alpha}$ , twin volume fraction  $f^{\beta}$  and its evolution  $\dot{f}^{\beta}$ , unit vectors  $\mathbf{m}_{\text{twin}}^{\beta}$  and  $\mathbf{n}_{\text{twin}}^{\beta}$  of a twin system  $\beta$  [6].

### Phenomenological CP models

Phenomenological models of CP generally use the slip resistance or critical value of resolved shear stress  $\tau_c^{\alpha}$  as microstructural state variable [9–12]. In this class, the most commonly used power law is discussed below.

**Phenomenological Power law** The state variable used to describe the material condition is ‘Slip resistance’  $\tau_c^{\alpha}$  (or critical value of resolved shear stress). The slip rates on a particular slip system  $\alpha$  are given as [6, 10]:

$$\dot{\gamma}^{\alpha} = \dot{\gamma}_0 \left| \frac{\tau^{\alpha}}{\tau_c^{\alpha}} \right|^{\frac{1}{m}} \text{sgn}(\tau^{\alpha}) \quad (7)$$

where  $\dot{\gamma}_0$  is the reference value of slip rate and exponent  $m$  is for rate sensitivity. This power law Eq. (7) has many other variations available in literature like using sinh function [6] or in some places; the exponent in power has different forms [13]. The evolution of critical resolved shear stress is given as [6, 10]:

$$\dot{\tau}_c^{\alpha} = \sum_{\beta=1}^n h_{\alpha\beta} |\dot{\gamma}^{\beta}| \quad (8)$$

Equation (8) describes the effect of some slip system with index  $\beta$  on the hardening action of another slip system with index  $\alpha$  where  $h_{\alpha\beta}$  is the hardening matrix given as [6, 10]:

$$h_{\alpha\beta} = q_{\alpha\beta} \left[ h_o \left( 1 - \frac{\tau_c^\beta}{\tau_s} \right)^a \right] \quad (9)$$

where  $q_{\alpha\beta}$  is the parameter of latent hardening and  $h_o$ ,  $\tau_s$ , and  $a$  are parameters of material for slip hardening. Equation (8) is generally referred as the *hardening law*. Also, there are other variations of hardening law available in literature. In case of twinning-based CP phenomenological models, for a twin system  $\beta$ , the evolution of twin volume fraction  $f^\beta$  is generally described by a power law and the slip hardening law (Eqs. 8 and 9) is also modified [6].

### Microstructure-based CP Models

Physics/microstructure-based CP models incorporate the internal variables like dislocation densities, second phase fractions, grain shape and size, etc., to describe microstructural state of material. Dislocation density is the most important state variable considered in this class of models. In this approach, the dislocation density  $\rho$  and its evolution  $\dot{\rho}$  are incorporated into the constitutive equations and from them flow stress is calculated. Many such models are available in the literature [14–16]. In dislocation density-based models, the equation of kinetics, i.e., Eq. (7), is generally replaced by Orowan equation which relates slip rates  $\dot{\gamma}^\alpha$  to mobile dislocation density  $\rho_m$  as [6, 9]:

$$\dot{\gamma}^\alpha = \rho_m^\alpha b v^\alpha \quad (10)$$

where  $b$  is the Burgers vector (magnitude) and  $v$  represents the velocity (average) of mobile dislocations. Similarly, in this class of CP models, the Eq. (8) in the above phenomenological equations is replaced by the evolutionary equations of dislocation densities. Some dislocation density-based models incorporate statistically stored dislocations (SSDs) and geometrically necessary dislocations (GNDs) into the constitutive equations [17, 18].

## 4 Numerical Solvers

For determining the response of material under loadings, one is required to solve a coupled system of governing partial differential equations (PDEs). Depending upon the configuration chosen, the equilibrium equations can have the forms [19]:

$$\text{Div } \mathbf{P} = \rho_o \ddot{\mathbf{x}} \quad \text{in reference configuration} \quad (11)$$

$$\text{div } \boldsymbol{\sigma} = \rho_t \ddot{\mathbf{x}} \quad \text{in deformed configuration} \quad (12)$$



where  $\mathbf{P}$  is the first Piola–Kirchhoff stress tensor,  $\boldsymbol{\sigma}$  represents the Cauchy stress tensor,  $\rho$  is the mass density of material, and  $\mathbf{x}$  is the position vector of material point in current/deformed configuration. For static case,  $\dot{\mathbf{x}} = \mathbf{0}$  in the above equations.

In crystal plasticity (CP), the above-mentioned PDEs are generally solved by finite element method (FEM) and spectral solvers. FEM discretizes the continuum into finite elements and within the elements, shape functions are defined for interpolating field quantities. The FEM implementations in crystal plasticity are available in the literature in detail [9, 10]. Similarly, the fast Fourier transform (FFT)-based spectral solvers are also used for CP simulations. FFT reduces the coupled system of complex PDEs into ordinary differential equations (ODEs) in the Fourier space. The detailed implementation of FFT-based spectral solvers in CP is available in literature [20–23]. Spectral methods have shown better performance in terms of faster convergence as compared to FEM. FFT solvers need periodic boundary conditions but are more efficient in terms of computational time and memory. Commercial FE packages like ABAQUS allow user-defined constitutive laws with FORTRAN subroutines UMAT and VUMAT. UMAT is used for static or implicit dynamic analysis in ABAQUS while VUMAT is used for explicit dynamic problems. It is easier to write VUMAT as it does not involve the calculation of stiffness matrix which is there in UMAT.

Open-source packages like VPSC [24], DAMASK [19, 26, 25], PRISMS Plasticity [27, 28], and MOOSE [29] are also available for CP simulations. DAMASK includes the spectral solvers based on FFT, and for FEM solution, it provides interface with commercial packages ABAQUS and MSC.MARC. One can incorporate a new constitutive model through FORTRAN in DAMASK like UMAT and VUMAT. PRISMS Plasticity is also an open-source package built on finite element (FE) library deal.II and it is used for crystal plasticity-based FE simulations.

For generating microstructures, Dream.3D [30, 31] and Neper [32] packages are commonly used. DAMASK itself has the inbuilt tool to generate microstructures from EBSD data or randomly. Also, the microstructures generated from Dream.3D can be exported to DAMASK for simulation. PRISMS Plasticity also allows the microstructures generated from Dream.3D and Neper as input for CPFEM simulations.

## 5 Homogenization

In polycrystalline and multiphase materials, the issue of microstructural inhomogeneity due to different phases, texture, precipitates, etc., needs appropriate homogenization methods for switching response of a single crystal to the polycrystalline aggregate. Commonly used homogenization methods in crystal plasticity include isostrain [10, 11], finite element (FE) averaging [10–12], and relaxed grain cluster (RGC) [33]. Isostrain method assumes that all grains/constituents have the same local deformation gradient as that of the macroscopic deformation gradient, and at every material point, the response value of stress is the average of stresses of individual grains/constituents of that material point [5, 10], i.e.,

$$\bar{\mathbf{F}} = \mathbf{F}^{(k)}, \quad (13)$$

$$\text{and } \bar{\sigma} = \frac{1}{N} \sum_{k=1}^N \sigma^{(k)} \quad (14)$$

For a material point,  $\mathbf{F}^{(k)}$  is the local deformation gradient for the  $k$ th grain,  $\bar{\mathbf{F}}$  represents the volume-averaged macroscopic deformation gradient,  $\bar{\sigma}$  is the volume-averaged Cauchy stress,  $\sigma^{(k)}$  stands for the Cauchy stress of  $k$ th grain/constituent, and  $N$  represents the total number of constituents/grains of that material point. Finite element (FE) averaging approach assumes that one grain is represented by an element and an orientation is assigned to it as an initial texture [11, 12].

## 6 Conclusions

This paper provides a brief overview of crystal plasticity (CP)-based approach to study deformation behavior of polycrystalline materials. CP simulations are proving to be great modeling tools for solving problems of materials modeling. Physics-based constitutive models consider the deformation mechanisms like dislocation slip, twinning, martensitic formation, and also their interactions. FFT-based spectral solvers are found to be more efficient than FE simulations, and their implementations in CP are becoming popular nowadays. Homogenization techniques help to study multiphase material systems and allow the user to make transitions from single crystal level to polycrystalline scale. Applications of CP simulations range from micro- to macroscale including microbending, damage initiation, deep drawing, metal forming, nano-indentation, texture formation, texture evolution, etc. For the case of multiphase alloys, even the existing phenomenological models can be enhanced by incorporating the information of different phases present in the material.

**Acknowledgements** This research work is supported by Technical Education Quality Improvement Project III (TEQIP III) of MHRD, Government of India assisted by World Bank under Grant Number P154523 and sanctioned to UIET, Panjab University, Chandigarh (India).

## References

1. Helm, D., Butz, A., Raabe, D., Gumbsch, P.: Microstructure-based description of the deformation of metals: theory and application. *JOM* **63**, 26–33 (2011)
2. Sachtleber, M., Zhao, Z., Raabe, D.: Experimental investigation of plastic grain interaction. *Mater. Sci. Eng.* **336**, 1–87 (2002)
3. Wang, L., Barabash, R.I., Yang, Y., Bieler, T.R., Crimp, M.A., Eisenlohr, P.: Experimental characterization and crystal plasticity modeling of heterogeneous deformation in polycrystalline  $\alpha$ -Ti. *Metall. Mater. Trans. A* **42A**, 626–635 (2010)

4. Pokharel, R., Lind, J., Anand, K., Lebenson, R.A., Li, S.F., Kenesei, P., Suter, R.M., Rollet, A.D.: Polycrystal plasticity: comparison between grain-scale observations of deformation and simulations. *Annu. Rev. Condens. Matter Phys* 317–346 (2014)
5. Xie, H., Zhengyi, J., Zhao, J.: *Microforming technology*. Academic Press (2017)
6. Roters, F., Eisenlohr, P., Hantcherli, L., Tjahjanto, D.D., Bieler, T.R., Raabe, D.: Overview of constitutive laws, kinematics, homogenization and multiscale methods in crystal plasticity finite-element modeling: theory, experiments, applications. *Acta Mater.* **58**, 1152–1211 (2010)
7. Lebensohn, R.A.: N-site modeling of a 3D viscoplastic polycrystal using fast fourier transform. *Acta Mater.* **49**, 2723–2737 (2001)
8. Eisenlohr, P., Diehl, M., Lebenson, R.A., Roters, F.: A spectral method solution to crystal elasto-viscoplasticity at finite strains. *Int. J. Plast* **46**, 37–53 (2013)
9. Roters, F., Eisenlohr, P., Bieler, T.R.: *Crystal plasticity finite element methods in materials science and engineering*. Wiley-VCH (2010)
10. Kalidindi, S.R., Bronkhorst, C.A., Anand, L.: Crystallographic texture evolution in bulk deformation processing of FCC metals. *J. Mech. Phys. Solids* **40**, 537–569 (1992)
11. Kalidindi, S.R., Bachu, V.: On the accuracy of the predictions of texture evolutions by the finite element technique for FCC polycrystals. *Mater. Sci. Eng.* **257**(1), 108–117 (1998)
12. Kalidindi, S.R., Anand, L.: Macroscopic shape change and evolution of crystallographic texture in pre-textured FCC metals. *J. Mech. Phys. Solids.* **42**, 459–490 (1994)
13. Chakraborty, A., Eisenlohr, P.: Chemo-thermo-mechanically coupled crystal plasticity simulation of stress evolution in thermally strained  $\beta$ -Sn films. *J. Electron. Mater.* **27**(9), 1409–1431 (2018)
14. Ma, A., Roters, F., Raabe, D.: A dislocation density based constitutive model for crystal plasticity FEM including geometrically necessary dislocations. *Acta Mater.* **54**, 2169–2179 (2006)
15. Alankar, A., Eisenlohr, P., Raabe, D.: A dislocation density-based crystal plasticity constitutive model for prismatic slip in  $\alpha$ -titanium. *Acta Mater.* **59**, 7003–7009 (2011)
16. Reuber, C., Eisenlohr, P., Roters, F., Raabe, D.: Dislocation density distribution around an indent in single-crystalline nickel: comparing nonlocal crystal plasticity finite-element predictions with experiments. *Acta Mater.* **71**, 333–348 (2014)
17. Ma, A., Roters, F.: A constitutive model for FCC single crystals based on dislocation densities and its application to uniaxial compression for aluminium single crystals. *Acta Mater.* **52**, 3603–3612 (2004)
18. Ma, A., Roters, F., Raabe, D.: On the consideration of interactions between dislocations and grain boundaries in crystal plasticity finite element modeling—theory, experiments, and simulations. *Acta Mater.* **54**, 2181–2194 (2006)
19. Roters, F., Diehl, M., Shantharaj, P., Eisenlohr, P., Reuber, C., Wong, S.L., Maiti, T., Ebrahimi, A., Hochrainer, T., Fabritius, H., Niklov, S., Friak, M., Fujita, N., Grilli, N.: DAMASK—the düsseldorf advanced material simulation Kit for modelling mutliphysics crystal plasticity, thermal, and damage phenomena from the single crystal up to the component scale. *Comut. Mater. Sci.* **158**, 420–478 (2019)
20. Maiti, T., Eisenlohr, P.: Fourier-based spectral method solution to finite strain crystal plasticity with free surfaces. *Scr. Mater.* **145**, 37–40 (2018)
21. Shanthraj, P., Eisenlohr, P., Diehl, M., Roters, F.: Numerically robust spectral methods for crystal plasticity simulations of heterogeneous materials. *Int. J. Plast* **66**, 31–45 (2015)
22. Diehl, M.: A spectral method using fast Fourier transform to solve elastoviscoplastic mechanical boundary value problems (Thesis). Max-Planck-Institut für Eisenforsch, GmbH (2010)
23. Lebenson, R.A., Kanjarla, A.K., Eisenlohr, P.: An elasto-viscoplastic formulation based on fast Fourier transform for the prediction of micromechanical fields in polycrystalline materials. *Int. J. Plast* **32–33**, 59–69 (2012)
24. VPSC Code Homepage. <http://public.lanl.gov/lebenson/>. Last Accessed 29 Aug 2019
25. Roters, F., Eisenlohr, P., Kords, C., Tjahjanto, D.D., Diehl, M., Raabe, D.: DAMASK: the düsseldorf advanced material simulation Kit for studying crystal plasticity using an FE based or a spectral numerical solver. *Procedia IUTAM* **3**, 3–10 (2012)

26. DAMASK Homepage. <http://www.damask.mpie.de>. Last Accessed 29 Aug 2019
27. Aagesen, L.K., Adams, J.F., Allison, J.E., Andrews, W.B., Berman, T., Chen, Z., Daly, S., Das, S., Dewitt, S., Ganesan, S., Garikapati, K., Gavini, V., Githens, A., Hedstrom, M., Huang, Z., Jagadish, H.V., Motamarri, P., Murphy, A.D., Natarajan, A.R., Panwar, S.: PRSIMS: an integrated, open-source framework for accelerating predictive structural materials science. *Miner. Met. Mater. Soc.* **70**, 2298–2314 (2018)
28. PRISMS Homepage. <http://www.prisms-center.org>. Last Accessed 29 Aug 2019
29. MOOSE Homepage. <http://mooseframework.inl.gov>. Last Accessed 29 Aug 2019
30. Groeber, M.A., Jackson, M.A.: DREAM.3D : a digital representation environment for the analysis of microstructure in 3D. *Integr. Mat. Manuf. Innov.* **3**(1), 56–72 (2014)
31. Dream.3D Homepage, <http://dream3d.bluequartz.net>. Last Accessed 29 Aug 2019
32. Neper Homepage. <http://neper.sourceforge.net>. Last Accessed 29 Aug 2019
33. Eisenlohr, P., Roters, F., Tjahjanto, D.: A novel grain cluster-based homogenization scheme. *Model. Simul. Mater. Sci. Eng.* **18**(1), 1–21 (2010)

# Evaluation of Creep and Compressive Behavior of MWCNTs Reinforced Polyurethane Composites



Dinesh Kumar and Prashant Jindal

**Abstract** Polyurethane (PU) has a great potential of use in various low-load-bearing applications. Reinforcing PU with mechanical strong material like MWCNTs can be very useful for improving the mechanical behavior of PU. In this contrast, the present study has been undertaken to evaluate the mechanical behavior of MWCNTs reinforced PU by varying the concentration of MWCNTs. Creep test shows that the presence of MWCNTs into PU matrix results in a reduction in creep strain. A significant reduction of 82% in creep strain of 7 wt% MWCNT composite has been observed in comparison with pure PU. The behavior of MWCNTs reinforced PU composite under compressive load has been evaluated within its elastic limit, and it has been observed that compressive modulus has been increased with the influence of increasing MWCNTs. Significant enhancement of 70% has been observed in the compressive modulus of PU/MWCNT composite with a higher composition of MWCNTs (10 wt%). Uniform dispersion of MWCNTs into PU matrix and their adhesion with PU molecules are the suggested reasons for significant improvement in mechanical properties.

**Keywords** PU · MWCNTs · Creep · Injection molding · Solution mixing · Compressive modulus

## 1 Introduction

Among the thermoplastic category of polymers, polyurethane attracted a lot of attention due to its applicability in various low-load-bearing applications like helmets, shoe sole fabrication, sports equipment, and medical devices. Being composed of soft and hard segments, properties of PU can be easily modified by reinforcing appropriate filler material to its matrix. Nanotechnology considered to be the best

---

D. Kumar · P. Jindal (✉)  
University Institute of Engineering and Technology, Panjab University, Chandigarh, India  
e-mail: [jindalp@pu.ac.in](mailto:jindalp@pu.ac.in)

D. Kumar  
e-mail: [dns Sharma327@gmail.com](mailto:dns Sharma327@gmail.com)

© Springer Nature Singapore Pte Ltd. 2020  
C. Prakash et al. (eds.), *Advances in Materials Science and Engineering*,  
Lecture Notes in Mechanical Engineering,  
[https://doi.org/10.1007/978-981-15-4059-2\\_6](https://doi.org/10.1007/978-981-15-4059-2_6)

approach for developing high strength PU-based composite material for industrial applications [1]. Filler materials like carbon nanotubes are drawn significant attraction by scientists for improving the mechanical performance of soft materials like PU to withstand a moderate amount of load in various applications. The use of CNTs into PU matrix as filler material has the capability to improve the mechanical properties of PU by 100% or well above the performance obtained by traditional filler material like clay [2]. CNTs have excellent mechanical and thermal properties which make them suitable filler candidate for polymer composite fabrication. More importantly, their nanoscale dimensions make them a better choice for reinforcement as they can easily be dispersed into the polymer matrix. CNTs have an excellent value of Young's modulus around 1TPa [3] and tensile strength up to 60 GPa [4]. CNTs have a good value of aspect ratio around 1000 and density around 2.6 g/cc [5]. In addition to excellent mechanical properties, CNTs also have significant thermal properties as they remain stable up to 2400 °C in vacuum [6] and good thermal conductivity around 3000 W/K [4]. Uniform dispersion of CNTs into the polymer matrix is the prime factor [7, 8] to obtain high strength polymer-based composite material. But the dispersion of CNTs into the polymer matrix is still a challenge for scientists due to strong intermolecular forces of CNTs. Several methods have been invented in the past by various groups of scientists to achieve uniform dispersion of CNTs into the polymer matrix. Reports are available in the literature, showing that the mechanical performance of polymer-based CNT composite material can be improved by achieving uniform dispersion. Scientists reported the improved mechanical performance of polymer/CNT composite material by different methods. In situ polymerization, twin-screw extrusion, and solution mixing are some of the techniques used by a different group of scientists in the past for fabrication of polymer-based composite material. Therefore, for fabricating high strength polymer-based composite material, uniform dispersion of filler material is the prime factor to achieve.

Jia et al. [9] worked on creep and creep recovery behavior of TPU with pristine and functionalized MWCNTs. They observed that creep strain has been improved with an increase in temperature; a marked increase of 46% has been observed when temperature raised from 35 to 80 °C for a time span of 30 min. Starkova et al. [10] worked on the evaluation of the creep behavior of epoxy-based MWCNT composite and reported that 1 wt% of MWCNTs has a negligible effect on the creep behavior of Epoxy. Jia et al. [11] studied the creep behavior of polypropylene (PP)/MWCNT composite under the influence of the varying composition of MWCNTs for different temperature conditions. Scientists reported that with 1 and 2.8 vol.% of MWCNTs, the unrecovered creep strain has been reduced by 53% and 73%, respectively, in comparison with pure polymer. Yao et al. [12] used PU/MWCNT composite prepared by in situ polymerization for creep study. Scientist reported that the presence of CNTs results in a significant increase in creep resistance of composite, but the increase is not monotonous with an increase in CNTs as it is highly dependent on the dispersion of filler material.

After the comprehensive study of the previous work, it has been observed that scientists seem not much interested toward the compressive study of the PU-based MWCNTs composite material, and a little attention has been paid toward creep

study of the composite material. As PU has great potential of interest in various low-load-bearing applications, the material has to withstand compressive load for a long period of time. Creep behavior of PU-based composite material is a very important aspect for widening its applicability for the fabrication of quarter (part of the shoe) which undergoes a low loading effect for a long period of time. There are merely few reports which are available on the study of the creep behavior of PU-based CNT composite material. To deeply understand how the presence of CNTs leads to a reduction in creep strain of PU, it is important to further evaluate the time-dependent creep behavior of PU. Therefore, the present study has been undertaken to evaluate the creep behavior of PU-based MWCNT composite material under the influence of the varying composition of MWCNTs. In addition to creep behavior, the mechanical behavior of PU/MWCNT composite under compressive loading within its elastic range has also been evaluated.

## 2 Materials and Methods

### 2.1 Materials

As grown MWCNTs with a diameter around 20–50 nm and length up to few microns have been used as filler material. Beads of pure PU have been used as base material, and the composition of MWCNTs has been varied from 1 to 10 wt%.

### 2.2 Synthesis of PU/MWCNTs Composite

Simple solution mixing [13–22] technique has been used for the fabrication of thin films of PU/MWCNT composite by varying the composition of MWCNTs. Beads of pure PU have been dissolved into dimethyl formamide (DMF) by using magnetic stirring until a clear solution obtained. MWCNTs have also been dispensed into the same solvent, and different suspensions of MWCNTs have been prepared by varying the composition of MWCNTs (0, 1, 3, 5, 7, and 10 wt%) with respect to the weight of PU. Individual suspension then mixed with PU solution and again magnetically stirred for 3–4 h to disperse MWCNTs into PU matrix. After this, the mixed solution allowed for casting in the oven and the solvent gets evaporated. After drying, thin films (0.2–0.3 mm thick) of PU/MWCNT composite with varying composition of MWCNTs have been obtained. These thin films then molded by using injection molding [23–28], and the required shapes of the specimen have been prepared. Before using for molding, these films are used for FESEM to validate the dispersion of MWCNTs (Fig. 1). For creep tests, dog-bone-shaped specimens have

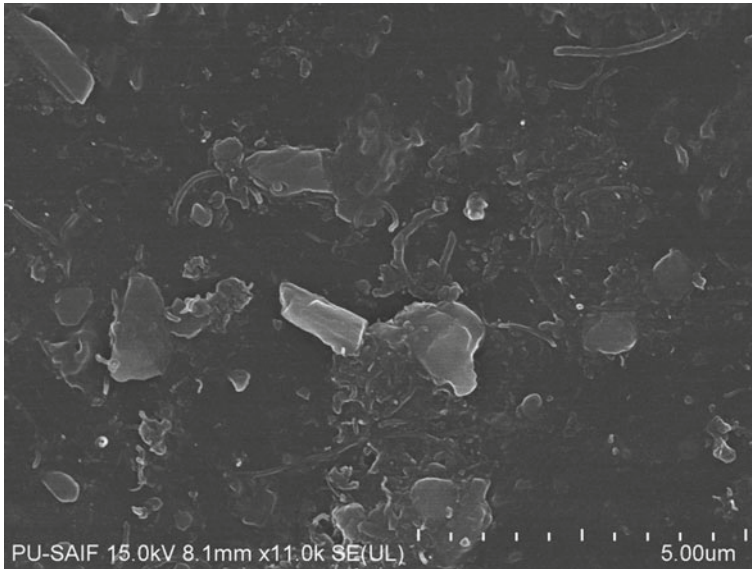


**Fig. 1** FESEM of PU/MWCNT composite film

been prepared according to ASTM D638 Type5, and for compressive tests, small disks with a diameter of 10 mm and thickness of 5 mm have been prepared as shown in Fig. 2.

### **2.3 Mechanical Characterization**

Creep testing has been performed on micro Universal Tensile Machine UTM (model MBA500) having an axial load capacity of 400 N and a stroke length of 50 mm. A load of 20 N has been applied on the moving end of the specimen for a time period of 600 s. These tests have been performed at room temperature and humidity of 47%. The compressive test has been performed on the same UTM by applying a load of 400 N in compression mode. The grip of specimens for creep and compressive tests is shown in Fig. 3.



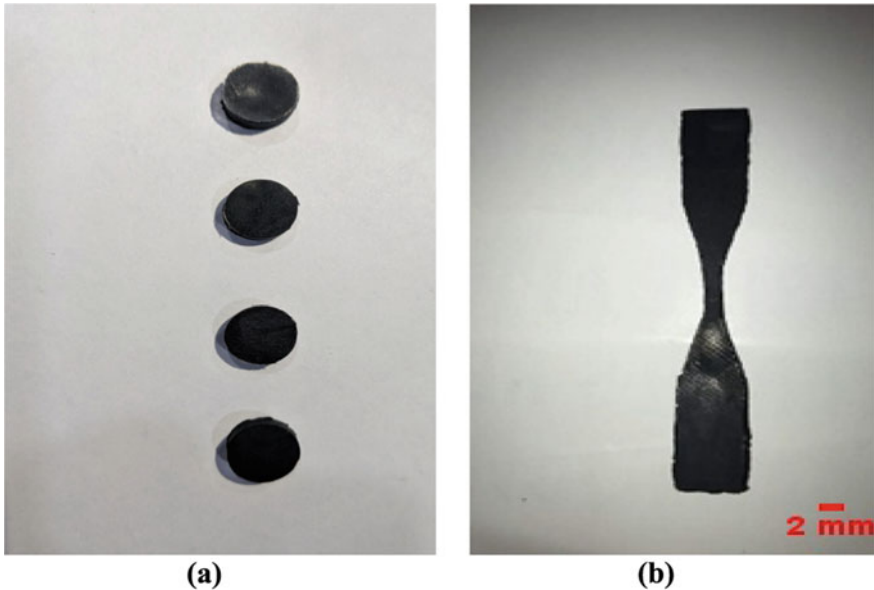


Fig. 2 Images of specimen used for (a) compressive test and (b) creep tests

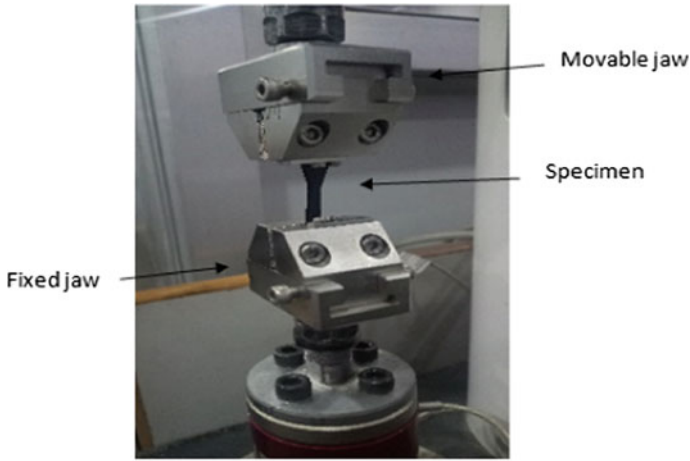
### 3 Results and Discussion

#### 3.1 Creep Behavior

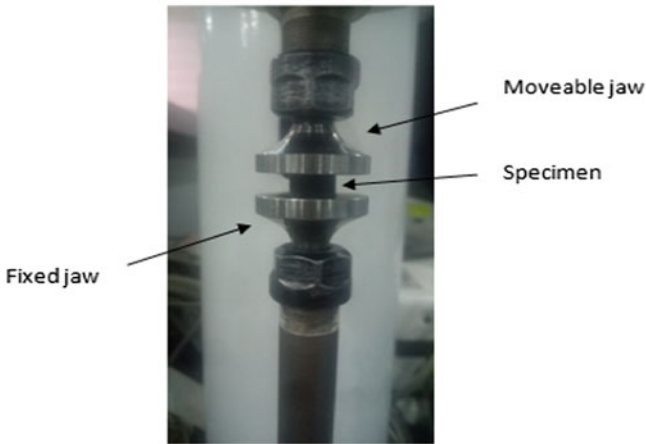
Figure 4 shows the axial load versus time response during creep testing. As shown in Fig. 4, the load has been kept constant to 20 N during the time period taken into consideration. The constant stress of 1 MPa has been induced in the specimen as shown in Fig. 5.

Variation in creep strain with the influence of the varying composition of MWCNTs is shown in Fig. 6. All the specimens have been stretched for 10 min, and corresponding axial strain has been recorded. In Fig. 6, two stages of creep (primary and secondary creep) can be easily observed, but no evidence has been found for tertiary creep, which requires higher stress and a longer time period.

Creep strain of all the PU/MWCNT composite specimens has been reduced in comparison with pure PU for the time period taken into consideration. After characterizing pure PU, our attention turned to analyze the effect of MWCNTs on the creep behavior of PU. A maximum strain of 175% has been observed for pure PU, which reduced to 50% for the higher composition of MWCNTs (10 wt%). Creep strain has been reduced by 23%, 37%, 77%, 82%, and 71% for PU/MWCNTs with 1 wt%, 3 wt%, 5 wt%, 7 wt%, and 10 wt%, respectively, in comparison with pure PU. It is interesting to notice that maximum reduction in strain has been achieved for 7 wt% composition. Therefore, 7 wt% is the optimum value which possesses a



(a)



(b)

**Fig. 3** Grip of the specimen (a) during creep testing and (b) during compressive testing

higher amount of reduction in strain, and beyond this value, no more reduction has been observed, but the creep strain increases (55%) for higher composition (10 wt%) in comparison with 7 wt%. The reduction in creep strain indicates that the creep resistance of the composites has been significantly improved. Jia et al. [11] reported similar behavior for polypropylene and CNT composites. Uniform dispersion and better adhesion [29] of MWCNTs could be the reason for improved creep resistance of the composites. There may be some other reasons, such as alteration of bulk structure [12], and other unknown factors which may also lead to the improved creep resistance are worthy to study in the future.

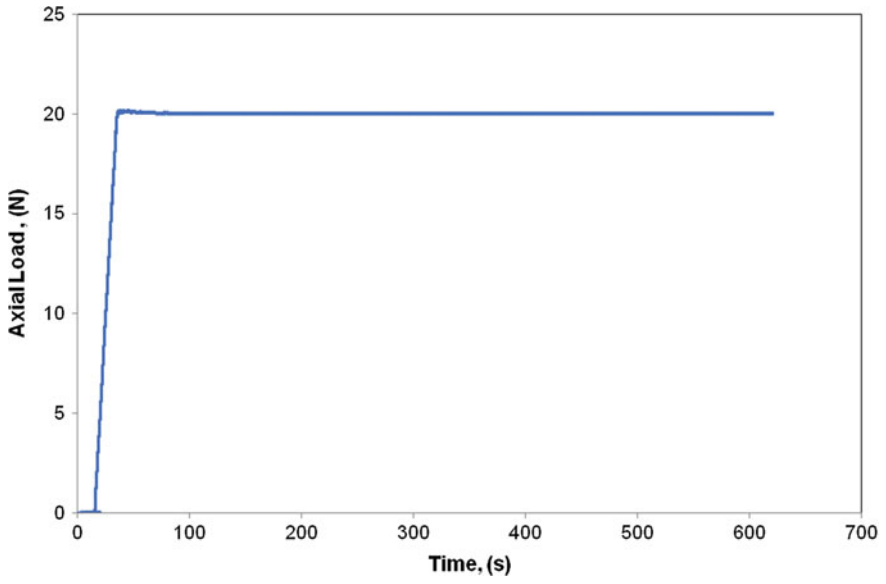


Fig. 4 Axial load versus time response

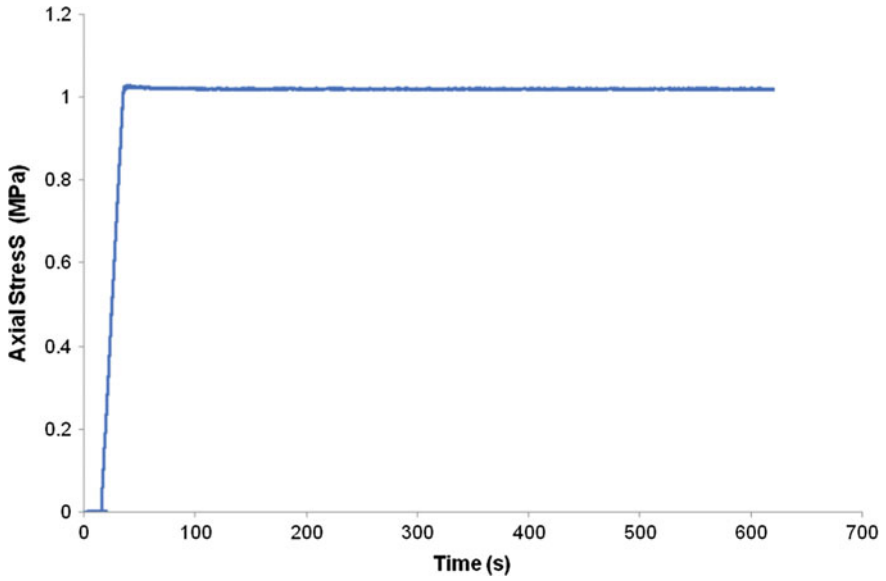


Fig. 5 Axial stress versus time response

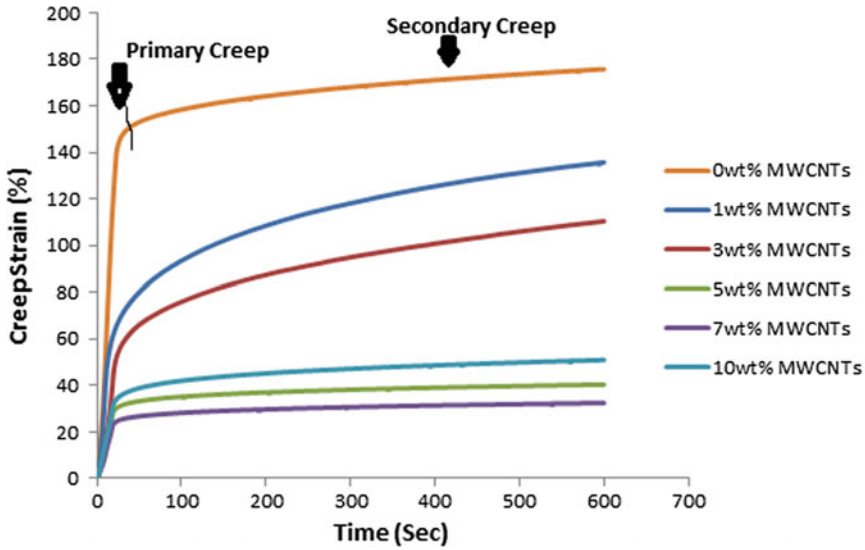


Fig. 6 Creep strain of PU/MWCNT composites at the varying composition of MWCNTs

### 3.2 Compressive Behavior

As discussed above, the compressive behavior of PU/MWCNT composite material has been evaluated within its elastic limits. A load of 400 N has been applied on the surface of the specimen, and corresponding strain has been recorded. As shown in Fig. 7, stress induced in the specimen remains almost the same for all the compositions of MWCNTs.

The corresponding strain of PU/MWCNT composites has been reduced with the increasing composition of MWCNTs. As Fig. 7 depicts, its 7 wt% for which maximum reduction has been observed in comparison with pure PU. In comparison with pure PU, a reduction of almost 50% has been observed for 7 wt% PU/MWCNT composite material.

Figure 8 shows the compressive modulus of PU-based MWCNT composites for varying composition of MWCNTs. It has been observed that the modulus of the specimen under compressive load has been significantly increased with the increase in MWCNT composition. The value of compressive modulus for pure PU has been observed as 13.33 MPa which peaks to 23 MPa for the higher composition of MWCNTs (10 wt%), showing significant enhancement of 72%. A minor composition of 3 wt% is sufficient to improve the compressive modulus by 30% in equivalence to pure PU. For 5 wt%, the value of compressive modulus falls to 15 MPa, but the value is still higher than that of pure PU by 12%. Table 1 shows that the compressive modulus of PU/MWCNT composite material has been enhanced significantly for all the composition of MWCNTs.

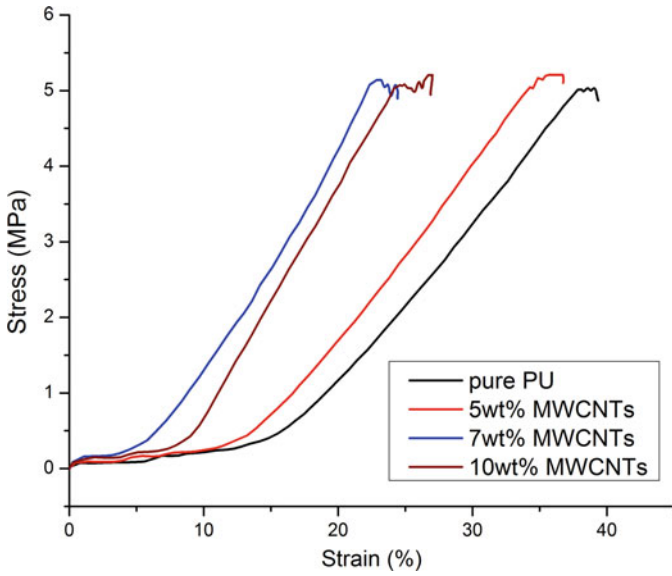


Fig. 7 Stress-strain plots for PU/MWCNT composites under compressive loading

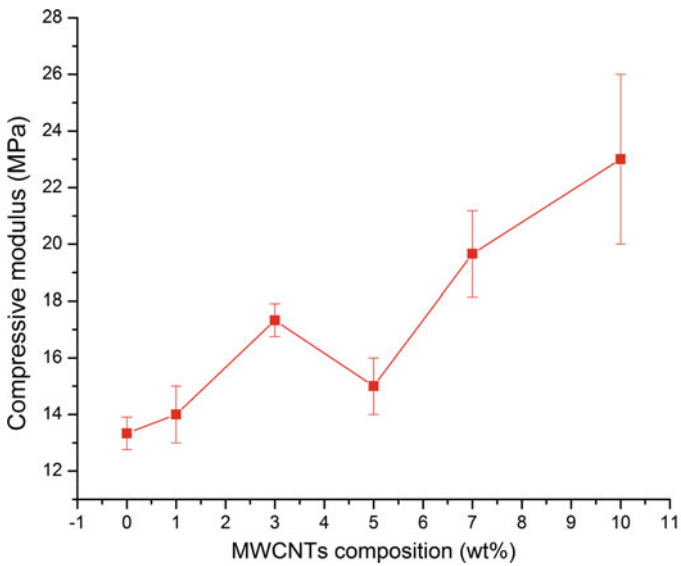


Fig. 8 Compressive modulus under the influence of the varying composition of MWCNTs

**Table 1** Results of compressive tests with their standard deviation

Composition of MWCNTs in PU, wt%	0	1	3	5	7	10
Compressive modulus, MPa	13.33	14	17.33	15	19.66	23
Standard deviation	0.577	1	0.57	1	1.52	3

PU comprised of soft segments, and these segments get displaced easily under compressive loading. Random orientations of MWCNTs into the PU matrix provide strength to PU molecules which result in increased binding of the molecules. The void space between PU molecules is occupied by MWCNTs which restrict the displacement of PU molecules, therefore reducing the strain of PU/MWCNT composite material. Reinforcement with MWCNTs having nanoscale dimension is beneficial for achieving uniform dispersion of MWCNTs throughout the PU matrix. Therefore, uniform dispersion of MWCNTs provides extra resistance to PU molecules against the deformation which results in reduced creep strain of composite material.

The compressive modulus of PU/MWCNTs has also been increased under the influence of increasing composition of MWCNTs. As MWCNTs itself have an excellent value of Young's modulus, reinforcing PU with mechanically strong MWCNTs results in the improved mechanical properties of PU/MWCNT composite. Some reports are available which reported that MWCNTs are reasonably strong in the radial direction in comparison with the axial direction. As MWCNTs are randomly oriented in PU, therefore they undergo a combined effect of axial and radial loading, which results in enhanced mechanical strength of the material. Moreover, in the case of pure PU, slipping of molecules may happen when the load is applied at the surface of the specimen. Reinforcement of MWCNTs into PU matrix can provide resistance to PU molecules against slipping, and therefore, the binding of molecules increased. It is worthy to notice that its 7 wt% composition of MWCNTs which provides maximum reduction in strain creep as well as compressive tests. Therefore, it is safe to conclude that the reinforcement of MWCNTs beyond 7 wt% leads to the agglomeration of MWCNTs. Uniform dispersion of MWCNTs and their adhesion with PU molecules are the other suggested reasons for improved mechanical properties of PU/MWCNT composite material.

## 4 Conclusion

From the present study, the following conclusions can be drawn:

1. Composites of MWCNTs reinforced PU have been successfully prepared by using the solution mixing approach.
2. Creep strain of PU/MWCNT composites has been reduced under the influence of the increasing composition of MWCNTs. Maximum reduction of 82% has been observed for 7 wt% PU/MWCNT composite material in comparison with pure PU.

3. This reduction in creep strain indicates that MWCNTs provide extra resistance to PU molecules to get deformed under constant loading.
4. The compressive modulus of PU-based MWCNTs composite has also been increased with the increasing composition of MWCNTs. A significant improvement of 72% has been observed in compressive modulus of PU/MWCNTs with 7 wt% of MWCNTs.
5. After evaluating the present results, it is safe to conclude that the concentration of MWCNTs around 7–10 wt% is sufficient to enhance the overall mechanical behavior of PU-based composite material which could be beneficial for the fabrication of midsole and quarter of shoes which undergoes creep and compressive loading during its service.
6. Further work can be done on the functionalization of MWCNTs before reinforcement which could enhance the binding of molecules with MWCNTs, therefore increasing the strength of the material.

**Acknowledgements** This research work is financially supported by the Ministry of Human Resource Development (MHRD) under the project (17-11/2015-PN-1) and Council of Scientific Industrial Research (CSIR), New Delhi.

**Conflict of interests** Authors declare no conflict of interest during the present research work.

## References

1. Cai, D., Jin, J., Yusoh, K., Rafiq, R., Song, M.: High performance polyurethane/functionalized graphene nanocomposites with improved mechanical and thermal properties. *Compos. Sci. Technol.* **72**(6), 702–707 (2012)
2. Chen, W., Tao, X., Liu, Y.: Carbon nanotube-reinforced polyurethane composite fibers. *Compos. Sci. Technol.* **66**, 3029–3034 (2006)
3. Prakash, C., Singh, S., Sharma, S., Garg, H., Singh, J., Kumar, H., Singh, G.: Fabrication of aluminium carbon nano tube silicon carbide particles based hybrid nano-composite by spark plasma sintering. *Mater. Today Proc.* **21**, 1637–1642 (2020)
4. Ibrahim, K.S.: Carbon nanotubes-properties and applications : a review. *Carbon Lett.* **14**(3), 131–144 (2013)
5. Merlini, C., et al.: Electromagnetic interference shielding effectiveness of composites based on polyurethane derived from castor oil and nanostructured carbon fillers. *Polym. Compos.* **40**, E78–E87 (2019)
6. McNally, T., et al.: Polyethylene multiwalled carbon nanotube composites. *Polymer* **46**, 8222–8232 (2005)
7. Tserpes, K.I., Chanteli, A., Pantelakis, S., Koumoulos, E.P., Charitidis, C.A.: Mechanical and nanomechanical properties of MWCNT/PP nanocomposite. *Frat. ed Integrita Strutt.* **46**, 73–83 (2018)
8. Ruan, S.L., Gao, P., Yang, X.G., Yu, T.X.: Toughening high performance ultrahigh molecular weight polyethylene using multiwalled carbon nanotubes. *Polymer* **44**, 5643–5654 (2003)
9. Jia, Y., Jiang, Z.M., Gong, X.L., Zhang, Z.: Creep of thermoplastic polyurethane reinforced with ozone functionalized carbon nanotubes. *Express Polym. Lett.* **6**(9), 750–758 (2012)
10. Starkova, O., Buschhorn, S.T., Mannov, E., Schulte, K., Aniskevich, A.: Creep and recovery of epoxy/MWCNT nanocomposites. *Compos. PART A* **43**(8), 1212–1218 (2012)

11. Jia, Y., Peng, K., Gong, X.L., Zhang, Z.: Creep and recovery of polypropylene/carbon nanotube composites. *Int. J. Plast* **27**(8), 1239–1251 (2011)
12. Yao, Z., Wu, D., Chen, C., Zhang, M.: Creep behavior of polyurethane nanocomposites with carbon nanotubes. *Compos. Part A Appl. Sci. Manuf.* **50**, 65–72 (2013)
13. Jindal, P., Yadav, R.N., Kumar, N.: Dynamic mechanical characterization of PC/MWCNT composites under variable temperature conditions. *Iran. Polym. J.* **26**, 445–452 (2017)
14. Bansal, S.A., Singh, A.P., Kumar, A., Kumar, S., Kumar, N., Goswamy, J.K.: Improved mechanical performance of bisphenol-A graphene-oxide nano-composites. *J. Compos. Mater.* **52**(16), 2179–2188 (2018)
15. Buffa, F., Abraham, G.A., Grady, B.P., Resasco, D.: Effect of nanotube functionalization on the properties of single-walled carbon nanotube/polyurethane composites. *J. Polym. Sci. Part B Polym. Phys.* **45**, 490–501 (2007)
16. Chen, G., Kim, H., Hyun, B., Yoon, J.: Multi-walled carbon nanotubes reinforced nylon 6 composites. *Polymer* **47**, 4760–4767 (2006)
17. Yoo, H.J., Jung, Y.C., Sahoo, N.G., Cho, J.W.: Polyurethane-Carbon nanotube nanocomposites prepared by in-situ polymerization with electroactive shape memory. *J. Macromol. Sci. part B.* **45**(4), 441–451 (2006)
18. Chen, Y., Zhang, B., Gao, Z., Chen, C., Zhao, S.: Functionalization of multiwalled carbon nanotubes with uniform polyurea coatings by molecular layer deposition. *Carbon* **82**, 470–478 (2014)
19. Kumar, D., Kumar, N., Jindal, P.: Effect of MWCNTs on damping behaviour of Polyurethane based nano-composites. *Mater. Today Proc.* **5**(2), 5636–5640 (2018)
20. Bansal, S.A., Singh, A.P., Kumar, S.: Reinforcing graphene oxide nano particles to enhance. *J. Nanosci. Nanotechnol.* **18**, 1–7 (2018)
21. Bansal, S.A., Singh, A.P., Kumar, S.: High strain rate behavior of epoxy graphene oxide nanocomposites. *Int. J. Appl. Mech.* **10**(7) (2018)
22. Bansal, S.A., Singh, A.P., Kumar, S.: Synergistic effect of graphene and carbon nanotubes on mechanical and thermal performance of polystyrene. *Mater. Res. Express* **5**(7), 1–7 (2018)
23. KC, B., Tjong, J., Jaffer, S.A., Sain, M.: Thermal and dimensional stability of injection-molded sisal-glass fiber hybrid PP biocomposites. *J. Polym. Environ.* **26**, 1279–1289 (2018)
24. Azenha, J., Gomes, M., Silva, P., Pontes, A.J.: High strength injection molded thermoplastic composites. *Polym. Eng. Sci.* 560–567 (2018)
25. Andrzejewski, J., Przystarczykowski, P., Szostak, M.: Development and characterization of poly (ethylene terephthalate) based injection molded self-reinforced composites. Direct reinforcement by overmolding the composite inserts. *Mater. Des.* **153**, 273–286 (2018)
26. Jindal, P., Sain, M., Kumar, N.: Mechanical characterization of PMMA/MWCNT composites under static and dynamic loading conditions. *Mater. Today Proc.* **2**, 1364–1372 (2015)
27. Kumar, D., Kumar, N., Jindal, P.: Elastic modulus behavior of multi-walled carbon nanotubes/polyurethane composites using nano-indentation techniques. *Indian J. Sci. Technol.* **10**(17), 1–4 (2017)
28. Kumar, D., Jindal, P.: Effect of multi-walled carbon nanotubes on thermal stability of polyurethane nanocomposites. *Mater. Res. Express* **6**, 1–10 (2019)
29. Kim, K.H., Jo, W.H.: Improvement of tensile properties of poly (methyl methacrylate) by dispersing multi-walled carbon nanotubes functionalized with poly (3-hexylthiophene)-graft-poly (methyl methacrylate). *Compos. Sci. Technol.* **68**, 2120–2124 (2008)



# Influence of Particle Morphologies of Mesoporous Hydroxyapatite Nanopowders on Controlled Delivery of Vancomycin Drug



Ravinder Pal Singh and Jagdeep Singh

**Abstract** Mesoporous hydroxyapatite (HAP) nanopowders (NPs) with distinct particle morphologies of nanorods (HAP-NR) and hierarchically nanostructured microspheres (HAP-MS) were synthesized. HAP was a major phase in both products. Crystals were nanodimensional and exposed to tensile strain. HAP-NR was more crystalline than HAP-MS NP. Particles of HAP-NR and HAP-MS NPs were nanorod-like (aspect ratio of five to six) and hierarchically nanostructured microspheres in shape, respectively. Average particle size was  $88 \pm 30$  nm (along c-axis) for HAP-NR and  $1.5\text{--}2$   $\mu\text{m}$  for HAP-MS NP. EDX results were in agreement with XRD phase analysis. Specific surface areas of HAP-NR and HAP-MS NPs were  $15\text{ m}^2\text{ g}^{-1}$  and  $22\text{ m}^2\text{ g}^{-1}$ , respectively. HAP-MS NP was more porous than HAP-NR and, therefore, exhibited 45% higher vancomycin loading efficiency than HAP-NR NP. In addition, drug-releasing rate of HAP-MS NP was more than HAP-NR in simulated conditions.

**Keywords** Nanorods · Microspheres · Hydroxyapatite · Vancomycin · Mesoporous · Drug delivery

## 1 Introduction

In recent years, enormous work has been made in the field of effective drug carriers for loading and controlled release of contraceptives, hormones, antibiotics, etc. In contrast to customary medicinal treatment procedures including systematic administration of drugs, advancement of precisely controlled drug-releasing techniques results in a number of benefits like steady and sustained release of drugs, improvement in therapeutic index, with least harmful impact on neighbouring tissue(s) [1].

---

R. P. Singh (✉)

School of Mechanical Engineering, Lovely Professional University, Phagwara, Punjab 144411, India

e-mail: [er.ravinderpalsingh@gmail.com](mailto:er.ravinderpalsingh@gmail.com)

J. Singh

Department of Mechanical Engineering, Sri Guru Granth Sahib World University, Fatehgarh Sahib, Punjab 140406, India

© Springer Nature Singapore Pte Ltd. 2020

C. Prakash et al. (eds.), *Advances in Materials Science and Engineering*,

Lecture Notes in Mechanical Engineering,

[https://doi.org/10.1007/978-981-15-4059-2\\_7](https://doi.org/10.1007/978-981-15-4059-2_7)

Drug carriers play critical role in controlled delivery of drug(s), as these store and discharge drug molecules progressively with respect to time. Mesoporous hydroxyapatite (HAP) bioceramic has been considered as a potential drug carrier as compared to other materials such as graphene, polymers and silica.

HAP is an inorganic principal constituent of natural bone and teeth, and therefore, synthetic HAP has been extensively employed as an artificial bone substitute [2] and drug delivery systems [3, 4] attributed to its magnificent biocompatibility and bioactivity [1]. Moreover, additional features like surface porosity and structural OH<sup>-</sup> ions enable HAP as an appropriate candidate for loading and discharge of an array of pharmaceutical molecules [3]. Stoichiometric HAP crystals are the most stable family member of calcium phosphate-based materials [5], which do not dissolve quickly in body fluids and thus can be delivered at infected site(s) in human body through surgical placement and inoculation procedures.

A number of drug molecules such as ibuprofen, vancomycin, ciprofloxacin, amoxicillin and many more have been employed as model drugs for drug delivery applications. These are synthetic antibiotic drugs with a broad spectrum of bactericidal capacity against both gram-positive and gram-negative bacterial strains. Vancomycin drug is highly resistant against numerous gram-positive bacteria. It is exceptionally potential against resistant forms of *Staphylococcus aureus* bacteria, which is highly prevailing in hospitals. Therefore, developing efficient delivery methods to avert the development and spread of such resistant strains is profoundly desirable.

For effective loading and releasing efficacy of drug in body fluids, one contemporary technique is to develop mesoporous structures of drug carriers. The drug loading capacity is potentially enhanced in mesoporous materials due to their inherent pore volume and large specific surface area. The drug loading and releasing abilities of carriers are improved by mesoporous nanostructured particles [1]. Apart from mesoporous structure, particle morphology of drug carriers additionally influences the drug administration capacity and biological functions [6]. For instance, microspheres [1], nanorods [6, 7], superparamagnetic nanoworms [8], etc., have been studied for a variety of multifunctional applications including drug delivery systems, molecular imaging and anti-cancer therapies. However, tailoring particle morphology of HAP is generally a complicated process due to complex crystal structure of HAP [1]. Thus, synthesis of distinct particle morphologies of HAP crystals with improved drug loading and releasing abilities has been a challenge to scientific community.

To these aims, mesoporous HAP nanopowders (NPs) having distinct particle morphologies of nanorods (HAP-NR) and microspheres (HAP-MS) were synthesized and tested for drug loading and releasing efficiencies. Structural and physico-chemical properties were comprehensively examined. In addition, the crystallographic structure of products was investigated by the Rietveld refinement technique.

## 2 Materials and Method

Calcium and phosphorus ions were extracted from calcium nitrate tetrahydrate (CNT, Merck) and diammonium hydrogen orthophosphate (DAHP, Merck) reagents, respectively. Trisodium citrate (TSC, Merck) and EDTA (Merck) were employed as templating agents. The pH of solutions was maintained using ammonium hydroxide ( $\text{NH}_4\text{OH}$ ) and nitric acid ( $\text{HNO}_3$ ). Synthesis protocols have been shown in Fig. 1.

Briefly, for the synthesis of HAP-NR NP, a mixture of 0.1 M hydrous CNT and 0.1 M EDTA was drop-wise added to 0.0598 M hydrous DAHP precursor and formed HAP solid solution. Thereafter,  $\text{NH}_4\text{OH}$  was gradually added to maintain pH of HAP solid solution to nine. The solution was then stirred and placed in household microwave at 800 W for 30 min. After cooling to room temperature, resultant solution was centrifuged and washed. This centrifugation–washing cycle was repeated for five times. The resultant precipitates were dried in air oven at  $110 \pm 2$  °C for 24 h. The obtained product was crushed into fine powder.

The synthesis protocol of HAP-MS NP was adopted from a published literature [9]. Briefly, pH of 0.1 M hydrous DAHP solution was adjusted to six using  $\text{HNO}_3$ . Then, hydrous solution of 0.167 M CNT was rapidly added to hydrous DAHP precursor to form HAP solid solution. Its pH was adjusted using  $\text{HNO}_3$ . The TSC solution (0.4175 M) was drop-wise added and stirred for some time. The suspension was hydrothermally heated at 180 °C for 24 h in muffle furnace and subjected to

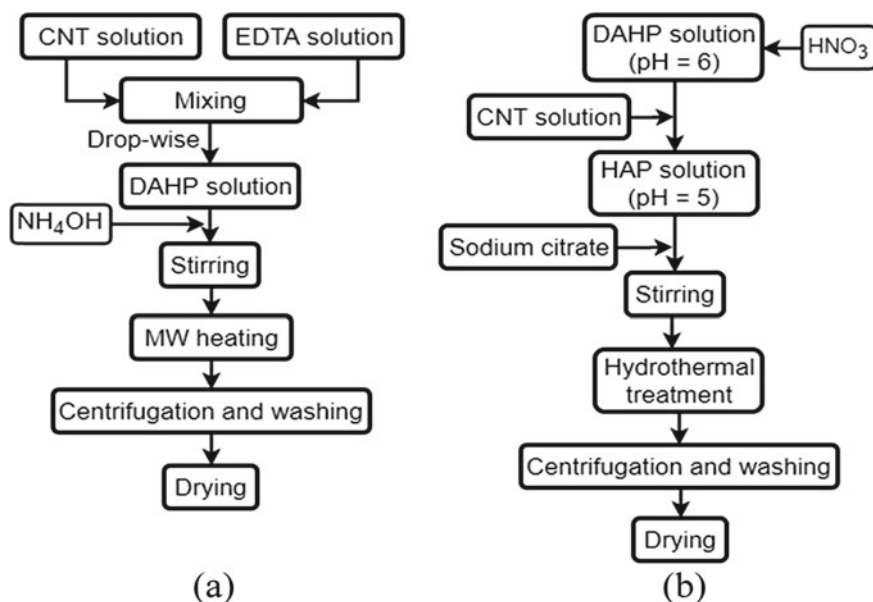


Fig. 1 Synthesis methodology of **a** HAP-NR and **b** HAP-MS NPs

annealing. The resultant precipitates were centrifuged and washed. This centrifugation–washing cycle was repeated for five times. The obtained products were dried in air oven at  $110 \pm 2$  °C for 24 h and later crushed into fine powder.

## 2.1 Characterization

XRD (Bruker D8) with  $\text{CuK}\alpha$  radiations was employed to study the crystal structure. XRD patterns were obtained with scan range from  $20^\circ$  to  $60^\circ$  and step size of  $0.02^\circ$ . The Rietveld refinement of XRD patterns was studied using MAUD software. A fifth-order polynomial function and pseudo-Voigt algorithm were employed for refinement purposes. The PDF data for monetite (01-071-1759), HAP (09-0432),  $\beta$ -TCP (09-0169),  $\text{CaCO}_3$  (5-586), CaO (01-074-1226), sodium nitrate ( $\text{NaNO}_3$ , 01-085-1467), and sodium chlorate dihydrate ( $\text{NaClH}_2\text{O}_5$ , 001-0603) were used.

Crystal size ( $X_s$  in nanometer) of HAP was calculated using Eq. (1).

$$X_s = \frac{0.9\lambda}{\beta \cos\theta} \quad (1)$$

where  $\lambda$  is wavelength of X-rays,  $\beta$  (in radians) is FWHM and  $\theta$  (in degree) is Bragg's angle. The peaks, i.e. (002), (211), (112), (300), (202) and (310) of HAP crystals were selected to calculate crystal size. Degree of crystallinity ( $X_c$ ) was determined using Eq. (2) [9]. WH-ISM (Eq. 3) and WH-ASM (Eq. 4) models were used to calculate lattice strain ( $\varepsilon$ ) and crystal size of HAP crystals.

$$X_c = 1 - (V_{112/300}/I_{300}) \quad (2)$$

$$\beta_{hkl} \cos(\theta_{hkl}) = \frac{0.9\lambda}{X_s} + 4\varepsilon \sin(\theta_{hkl}) \quad (3)$$

$$\beta_{hkl} \cos(\theta_{hkl}) = \frac{0.9\lambda}{X_s} + \frac{4\sigma \sin(\theta_{hkl})}{E} \quad (4)$$

where  $V_{112/300}$  is the intensity of hollow between (112) and (300) diffraction peaks,  $I_{300}$ , is the intensity of (300) diffraction peak of HAP crystals and  $E$  is Young's modulus. FESEM (Hitachi, S-4800) outfitted with EDX (Bruker, XFlash 4010) was employed to examine the particle morphology and elemental composition. HRTEM (FEI Tecnai G2 S-Twin) was employed to examine the particle shape and atomic structure. ImageJ software was employed to quantify the size and aspect ratio of particles [10]. The textural properties of particles were measured using BET method.

## 2.2 *In Vitro Drug Loading*

The 100 mg of NP was uniformly dispersed into measured volume of vancomycin–ethanol solution with initial drug concentration ( $a$ ) of 20 mg ml<sup>-1</sup>. This suspension was incubated at 37 °C for 24 h in dynamic mode. The precipitates and supernatant were alienated following centrifugation process. The final drug concentration ( $b$ ) in supernatant was tested using UV-VIS at 230 nm. Drug loading efficiency (DLE,  $\eta$ ) was determined using Eq. (5).

$$\eta = \left[ \frac{a - b}{a} \right] * 100 \quad (5)$$

## 2.3 *In Vitro Drug Release Test*

The mixture of 1:1 by volume of drug-loaded particles and simulated body fluid (SBF) was incubated in different polyethylene tubes. The 5 ml solution was extracted after selected time intervals and centrifuged at 5000 rpm. Refreshment of SBF was also ensured. Drug concentration in supernatant was measured spectrophotometrically at 230 nm wavelength.

# 3 Results and Discussion

## 3.1 *Particle Development Mechanisms*

During the synthesis of HAP-NR NP, EDTA reacted with Ca<sup>2+</sup> ions and formed strong complex of Ca and EDTA ions [12]. EDTA ions wrapped around metal ions and acted as a hexadentate unit [3]. Initially, 3D clusters formed which acted as nuclei for the formation of HAP crystals. These HAP nuclei further developed into nanodimensional rod-like crystals under MW irradiation [12]. Schematic representation of nucleation and growth of HAP-NR NP has been shown in Fig. 2a [13].

During the synthesis of HAP-MS NP, elevated temperature and pressure in hydrothermal cell improved nucleation and growth of HAP crystals [13]. Following HAP nucleation, citrate ions were absorbed by HAP crystals and resulted in a change in surface energy of crystal facets. It further improved the growth rate of HAP crystals in the direction of absorbed citrate ions [13, 14, 19]. The Ca<sup>2+</sup> ions bonded with COO<sup>-</sup> groups of citrate ions coordinated along c-axis of HAP crystals. The citrate ions caused HAP crystals to grow along c-axis [15]. Thus, citrate ions aggregated the nanoparticles and formed spherical particles [13]. The schematic

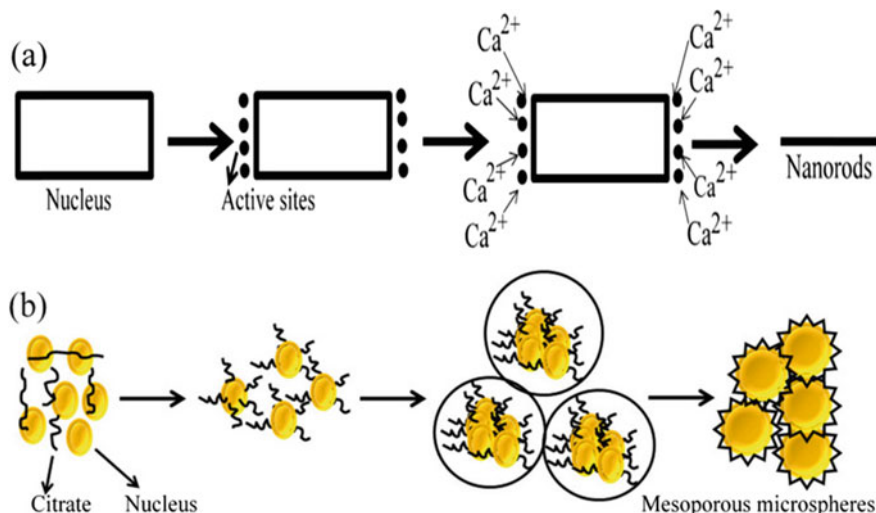
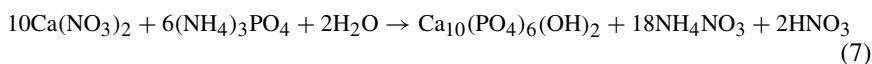
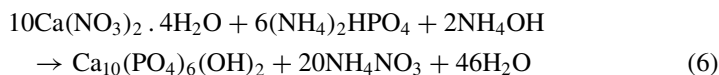


**Fig. 2** Particle formation mechanism of **a** HAP-NR and **b** HAP-MS NPs

representation of particle formation mechanism of HAP-MS NP has been shown in Fig. 2b [14].

### 3.2 Phase Structure

XRD patterns of HAP-NR and HAP-MS NPs have been shown in Fig. 3. Qualitative analysis indicated that HAP-NR was monolithic consisted of HAP phase only, whereas, in addition to HAP, sodium chlorate dihydrate and sodium nitrate phases were present in HAP-MS NP. Characteristic peaks (002), (211), (300), (202) and (310) of HAP crystals were observed in both NPs. Impurities like  $\text{CaCO}_3$  and  $\text{CaO}$  were not observed in both NPs. The chemical reactions pertinent to synthesis of HAP-NR and HAP-MS NPs have been proposed in Eqs. (6) and (7), respectively.



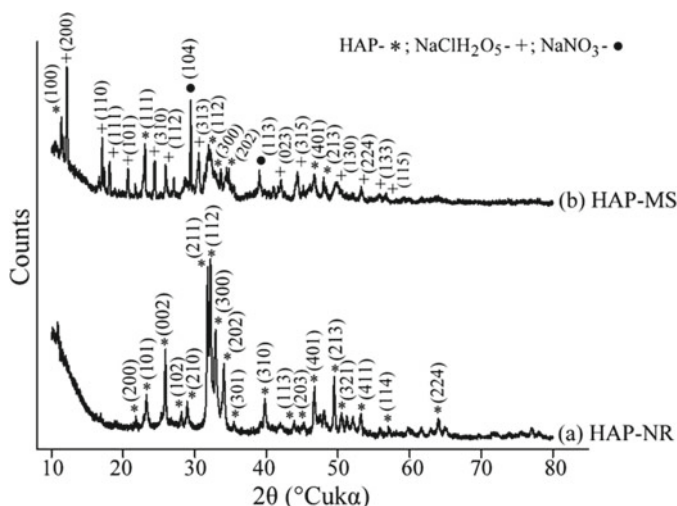


Fig. 3 XRD patterns of **a** HAP-NR and **b** HAP-MS NPs

### 3.3 Crystallographic Structure

The fitted XRD profiles of HAP-NR and HAP-MS NPs have been shown in Fig. 4. The goodness-of-fit parameters ( $\sigma$ ,  $R_{wp}$ ,  $R_{exp}$ ) have been given in Table 1. The value of  $\sigma$  was less than four and was acceptable [16].

Lattice parameters of HAP crystals along both a-axis and c-axis were 9.420 Å and 6.883 Å for HAP-NR and 9.358 Å and 6.893 Å for HAP-MS NP as given in Table 1. Although lattice parameters of HAP-NR were closer to the standard dimensions of stoichiometric HAP ( $a = 9.418$  Å and  $c = 6.884$  Å), some disparity was observed in case of HAP-MS NP. It has been attributed to the presence of citrate ions, which could inhibit growth of HAP crystals in HAP-MS NP [17, 20]. All models affirmed

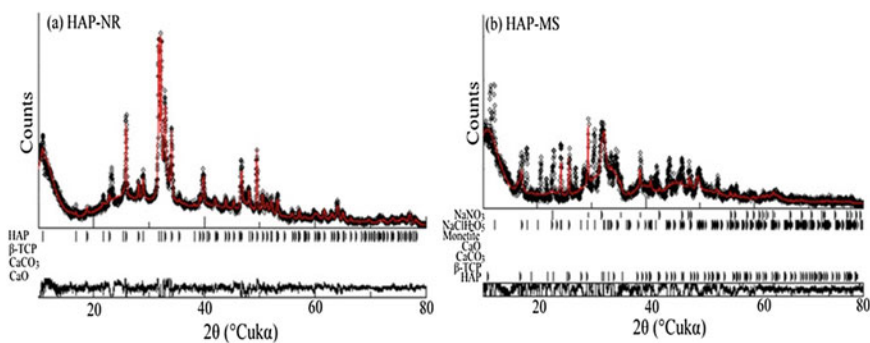


Fig. 4 Fitted XRD profiles of **a** HAP-NR and **b** HAP-MS NPs

**Table 1** Rietveld parameters, lattice parameters, crystal size, microstrain and crystallinity of HAP crystals in HAP-NR and HAP-MS NPs

NP	Goodness-of-fit parameters		Lattice parameter (Å)		Crystal size (nm)			Microstrain			Crystallinity (%)
	$\sigma$	$R_{wp}$	$R_b$	$C$	Rietveld	Scherrer	WH-ISM	WH-ASM	Rietveld	WH-ISM	
HAP-NR	1.69	0.121	0.072	6.883	71	$67 \pm 22$	43	49	0.0041	0.0027	44
HAP-MS	2.87	0.229	0.079	6.893	64	$58 \pm 27$	55	62	0.0036	0.0029	39



the nanodimensional regime of HAP crystals in both HAP-NR and HAP-MS NPs as mentioned in Table 1. Both HAP-NR and HAP-MS NPs were subjected to tensile strain (Table 1). Critical analysis indicated the proportional relationship between microstrain and crystal size. Besides, degree of crystallinity was 44% for HAP-NR and 39% for HAP-MS NP. On the basis of fact that less crystalline HAP NPs dissolve rapidly in body fluids, and hence accordingly, both HAP-NR and HAP-MS NPs have been proposed to be beneficial for controlled drug delivery applications.

### 3.4 Morphology and Elemental Structure

Particle morphology of HAP-NR and HAP-MS NPs has been shown in Fig. 5. HAP-NR NP was agglomerated and constituted of micron-dimensional grains as shown in Fig. 5a. These irregularly shaped grains consisted of rod-like elongated nanoparticles as illustrated in Fig. 5b. However, particles of HAP-MS NP were primarily spherical in shape as shown in Fig. 5c–d. Few long needle-like particles were also observed as shown in Fig. 5c. It was believed that primordial needle-like particles

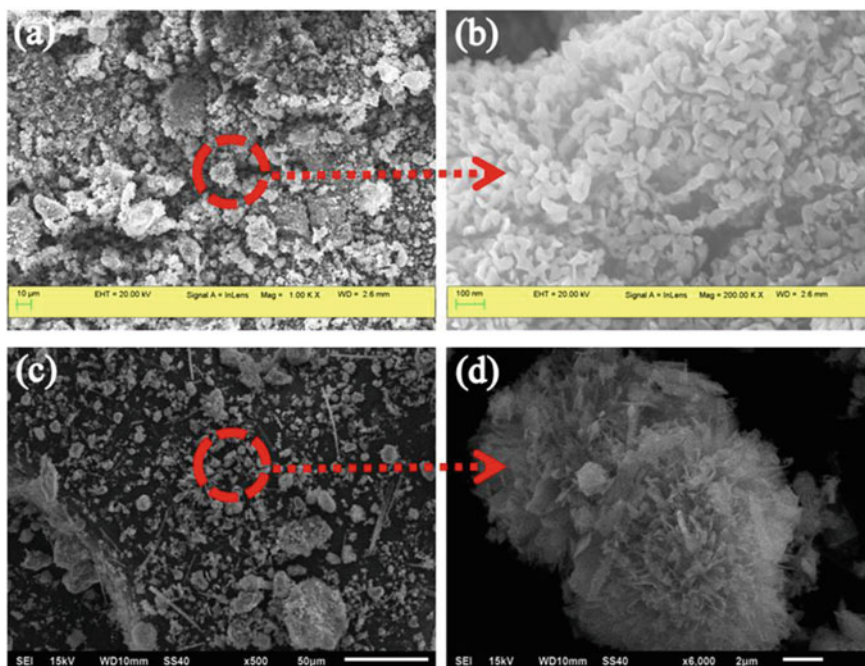


**Fig. 5** Particle morphology of **a, b** HAP-NR and **c, d** HAP-MS NPs

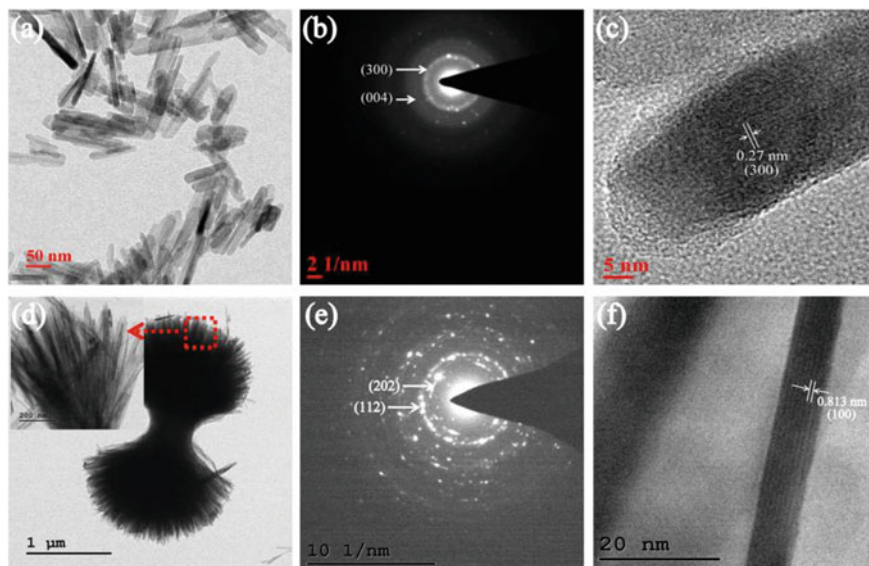


**Fig. 6** TEM, SAED and lattice fringes of **a–c** HAP-NR and **d–f** HAP-MS NPs

transformed into spherical particles during synthesis reaction. Furthermore, numerous nanodimensional elongated plate-like particles united and formed burr-like spherical particles as shown in Fig. 5d. The aggregation of these nanodimensional particles formed mesoporous structure. The interparticle spacing believed to act as channels for soaking and delivery of drug.

TEM micrographs confirmed nanorod-like particles of HAP-NR as shown in Fig. 6a. Average length and width of nanorods for HAP-NR were  $88 \pm 30$  nm and  $15 \pm 5$  nm, respectively. The aspect ratio of nanorods was between 5 and 6. SAED pattern as illustrated in Fig. 6b showed ring-like patterns made up of spots that represented the formation of polycrystalline material. Bright spots were indexed to (300) and (004) planes of HAP phase. The interatomic spacing of 0.27 nm was ascribed to characteristic (300) crystal plane of HAP phase in HAP-NR NP as shown in Fig. 6c. Similarly, Fig. 6d showed dumbbell-shaped spherical ended particles consisted of hierarchically assembled long needle-shaped particles as shown in the inset. Average diameter of spheres was 1.5–2  $\mu\text{m}$ . Diffraction pattern (Fig. 6e) affirmed polycrystalline structure of HAP-MS NP. The interatomic spacing of 0.813 nm was ascribed to (100) crystal plane of HAP phase in HAP-MS NP as shown in Fig. 6f.

The elemental compositions of HAP-NR and HAP-MS NPs have been shown in Fig. 7. Elements required for the formation of HAP crystals were present in both HAP-NR and HAP-MS NPs. The weight ratio and molar ratio of Ca: P were 2.05 and 1.62 for HAP-NR NP and 2.07 and 1.59 for HAP-MS NP, respectively. These values were close to theoretical values of 2.15 and 1.67 for stoichiometric HAP, respectively. Presence of C-element demonstrated the carbonated structure of HAP

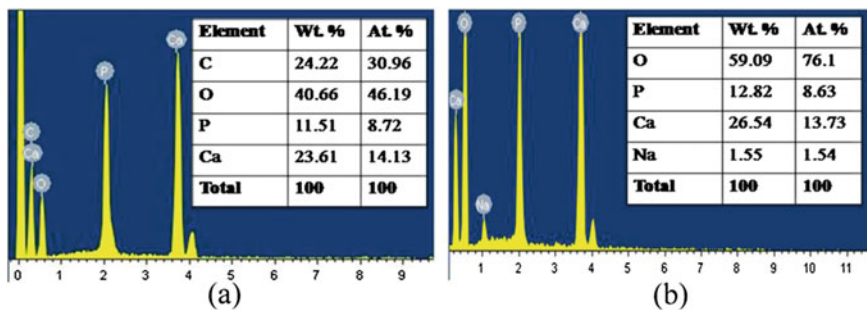


Fig. 7 Elemental composition of a HAP-NR and b HAP-MS NPs

crystals in HAP-NR NP. Natural bone apatite is also carbonated in composition. On the other hand, the use of sodium citrate reagent was the reason for Na element detected in HAP-MS NP.

### 3.5 Mesoporous Structure

The textural properties of HAP-NR and HAP-MS NPs have been shown in Figs. 8 and 9, respectively. Both NPs exhibited similar isotherms of type II with H3 hysteresis

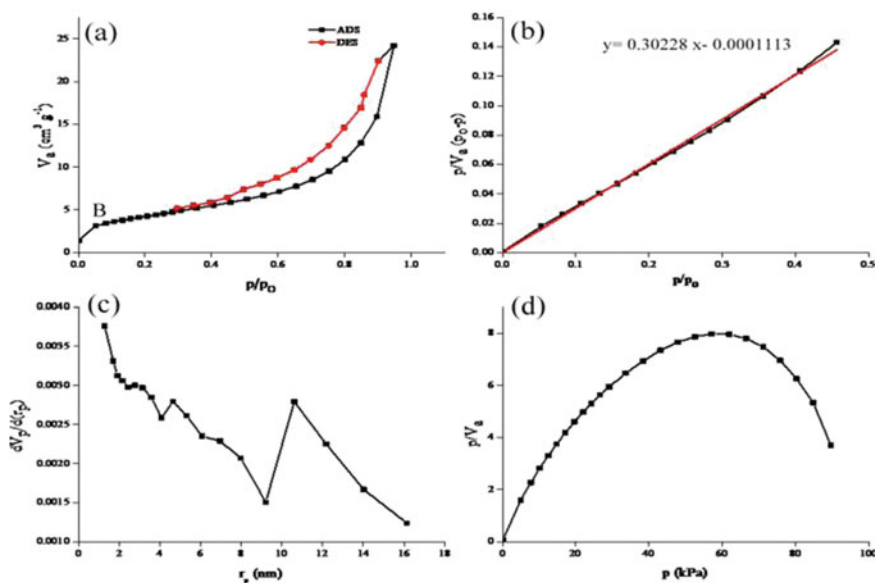
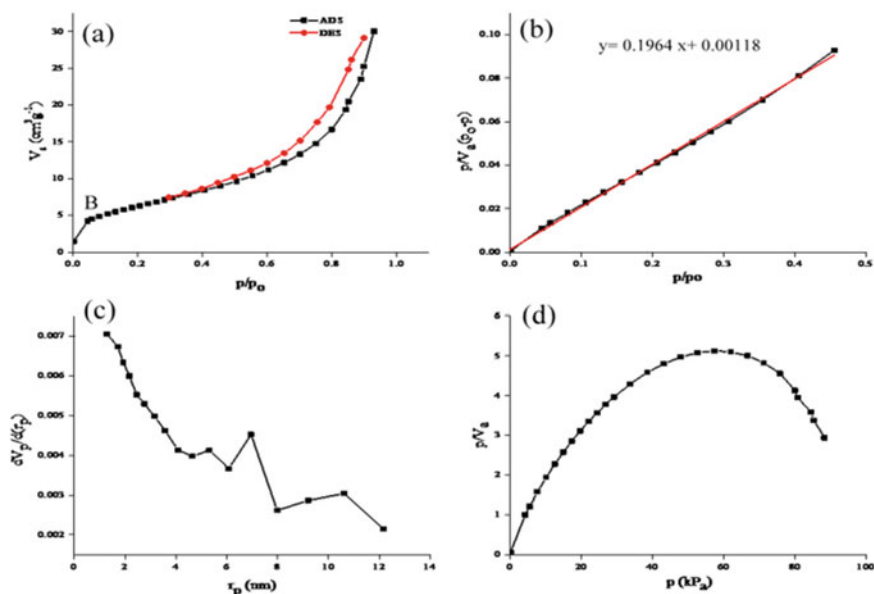


Fig. 8 a Isotherms, b BET, c BJH and d Langmuir plots of HAP-NR NP



**Fig. 9** a Isotherms, b BET, c BJH and d Langmuir plots of HAP-MS NP

loop, illustrating the formation of mesoporous structures, primarily consisted of elongated particles [18]. Moreover, high adsorption of gas suggested the presence of macropores in synthesized products. These outcomes were in agreement with morphological results (Fig. 5). The textural properties have been given in Table 2. Specific surface area of HAP-NR and HAP-MS NPs were  $15 \text{ m}^2 \text{ g}^{-1}$  and  $22 \text{ m}^2 \text{ g}^{-1}$ , respectively. In- addition, HAP-MS NP was  $\sim 24\%$  more porous than HAP-NR NP. Likewise, mean pore diameter in HAP-MS NP was  $\sim 13\%$  more than HAP-NR NP. Presence of ultrafine pores (10–11 nm) affirmed the mesoporous structure of both NPs.

### 3.6 *In Vitro* Drug Loading and Release Properties

The drug loading and release profiles pertinent to HAP-NR and HAP-MS have been shown in Fig. 10. HAP-MS loaded  $\sim 28\%$  more drug than HAP-NR NP as illustrated in Fig. 10a. Higher DLE of HAP-MS NP was attributed to its hierarchical nanostructure made up of large volume of mesopores. Mesoporous particle structure further enhances the surface area of particles [21]. It was an indispensable factor for higher DLE of HAP-MS NP. The mesopores in particles not only improved the diffusion of drug molecules but also provided the space for the attraction of vancomycin drug molecules [21]. The interaction of drug molecules and nanoparticles further increased owing to bonding of hydrogen ions with HAP NPs [1]. In addition, less crystallinity

**Table 2** Textural properties of HAP-NR and HAP-MS NPs

NP	BET		BJH			Langmuir			
	Specific surface area ( $\text{m}^2 \text{g}^{-1}$ )	Pore volume ( $\text{cm}^3 \text{g}^{-1}$ )	Pore diameter (nm)	Constant	Pore volume ( $\text{cm}^3 \text{g}^{-1}$ )	Specific surface area ( $\text{m}^2 \text{g}^{-1}$ )	Pore radius (nm)	Specific surface area ( $\text{m}^2 \text{g}^{-1}$ )	Constant
HAP-NR	15	0.037	10	152.9	0.036	16	1.29	19	0.649
HAP-MS	22	0.046	11	89.3	0.046	25	1.29	28	0.488

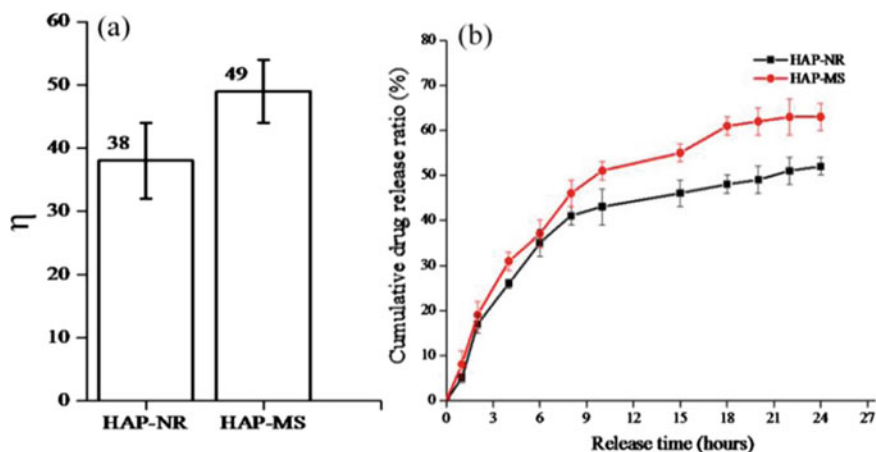


**Fig. 10** a Drug loading efficiency ( $\eta$ ) and b cumulative drug release profiles for HAP-NR and HAP-MS NPs

of HAP-MS NP (Table 1) also enhanced the DLE of HAP-MS NP [1]. Crystal defects caused due to lesser crystallinity offered additional dynamic sites for storing drug molecules [1]. Accordingly, HAP-NR NP exhibited low drug loading efficiency of  $38 \pm 6\%$  as shown in Fig. 10a. Other factors like lesser porosity, smaller specific surface area and pore diameters and higher crystallinity, etc., were also accountable for lower DLE of HAP-NR NP. On the other hand, DLE exhibited by both HAP-NR and HAP-MS NPs was more than the results reported by Guo et al. [21].

The drug release profiles of HAP-NR and HAP-MS NPs have been shown in Fig. 10b. Both NPs exhibited similar trend of drug release without burst release. Absence of burst drug release indicated that drug molecules were strongly bonded to carrier particles instead of weakly adsorbed on them. Besides, the rate of drug release was relatively more in HAP-MS NP. The drug release gradually increased up to 22 h. Afterwards, stability in drug release rate was observed for both NPs. This type of trend has been beneficial for providing rapid healing of infected sites by releasing faster delivery of drug initially. Afterwards, to retain the healing action for longer period, drug release rate decreased [11]. The sites of  $\text{OH}^-$  ions acted as reaction sites, when vancomycin adsorbed on the surface. In the process of drug release, SBF medium passed through the drug carrier matrix through pores. Afterwards, adsorbed drug molecules were gradually mixed into SBF and progressively diffused from carrier system [3]. Therefore, both HAP-NR and HAP-MS NPs exhibited controlled and gradual release of vancomycin drug. Hence, both drug carriers can be appropriately employed for controlled drug delivery applications.

## 4 Conclusion

HAP NPs having nanodimensional rod-like particles and micron-dimensional hierarchical nanostructured sphere-like particles were synthesized using facile synthesis protocols. Particles were comprehensively characterized and tested for drug loading and release efficacies. HAP-NR was monophasic, whereas HAP-MS NP was triphasic composed of HAP, sodium nitrate and sodium chlorate dihydrate phases in decreasing order. HAP was a major phase in both NPs. HAP crystals with suitable lattice parameters were nanodimensional in size and subjected to tensile strain. The HAP-NR NP was more crystalline than HAP-MS NP. Particles of HAP-NR were agglomerated and nanorod-like with aspect ratio varied from 5 to 6. On the other hand, particles of HAP-MS NP were segregated and hierarchically nanostructured microdimensional spheres with average size between 1.5 and 2  $\mu\text{m}$ . Atomic arrangements corroborated polycrystalline structure of apatite in HAP-NR NP. Elemental composition supported formation of HAP crystals. Isotherms suggested mesoporous structure in both HAP-NR and HAP-MS NPs. Specific surface area for HAP-NR and HAP-MS NPs were  $15 \text{ m}^2 \text{ g}^{-1}$  and  $22 \text{ m}^2 \text{ g}^{-1}$ , respectively. HAP-MS was more porous than HAP-NR. Also, capillary pores in HAP-MS NP were  $\sim 13\%$  more than HAP-NR NP. Owing to mesoporous hierarchical nanostructured particle morphology of HAP-MS NP, its DLE was 45% more than HAP-NR NP. Both drug delivery systems exhibited desirable drug-releasing properties without burst-release effect. The controlled and gradual release of vancomycin drug exhibited that both HAP-NR and HAP-MS NPs could be effectively employed for controlled drug delivery applications.

## References

1. Prakash, C., Singh, S., Ramakrishna, S., Królczyk, G., Le, C.H.: Microwave sintering of porous Ti–Nb–HA composite with high strength and enhanced bioactivity for implant applications. *J. Alloys Comp.* **824**, 153774 (2020)
2. Prakash, C., Singh, S., Singh, M., Verma, K., Chaudhary, B., Singh, S.: Multi-objective particle swarm optimization of EDM parameters to deposit HA-coating on biodegradable Mg-alloy. *Vacuum*. **158**, 180–190 (2018)
3. Zhang, C., Li, C., Huang, S.: Self-activated luminescent and mesoporous strontium hydroxyapatite nanorods for drug delivery. *Biomaterials* **31**, 3374–3383 (2010)
4. Yang, P., Quan, Z., Hou, Z.: A magnetic, luminescent and mesoporous core-shell structured composite material as drug carrier. *Biomaterials* **30**, 4786–4795 (2009)
5. Klein, C.P., de Blicke-Hogemrst, J.M.A., Wolket, J.G.C.: Studies of the solubility of different calcium phosphate ceramic particles in vitro. *Biomaterials* **11**, 509–512 (1990)
6. Liu, Y., Tan, J., Thomas, A.: The shape of things to come: Importance of design in nanotechnology for drug delivery. *Ther. Deliv.* **3**, 81–194 (2012)
7. Huang, X., El-Sayed, I.H., Qian, W.: Cancer cell imaging and photothermal therapy in the near-infrared region by using gold nanorods. *J. Am. Chem. Soc.* **128**, 2115–2120 (2006)
8. Park, J.H., von Maltzahn, G., Zhang, L.: Systematic surface engineering of magnetic nanoworms for in vivo tumor targeting. *Small* **5**, 694–700 (2009)

9. Pang, Y.X., Bao, X.: Influence of temperature, ripening time and calcination on the morphology and crystallinity of hydroxyapatite nanoparticles. *J. Eur. Ceram. Soc.* **23**, 1697–1704 (2003)
10. Kothapalli, C.R., Wei, M., Legeros, R.Z.: Influence of temperature and aging time on HA synthesized by the hydrothermal method. *J Mater. Sci. Mater. Med.* **16**, 441–446 (2005)
11. Venkatasubbu, G.D., Ramasamy, S., Ramakrishnan, V.: Nanocrystalline hydroxyapatite and zinc-doped hydroxyapatite as carrier material for controlled delivery of ciprofloxacin. *3 Biotech* **1**, 173–186 (2011)
12. Liu, J., Li, K., Wang, H.: Rapid formation of hydroxyapatite nanostructures by microwave irradiation. *Chem. Phys. Lett.* **396**, 429–432 (2004)
13. Yang, H., Hao, L., Du, C.: A systematic examination of the morphology of hydroxyapatite in the presence of citrate. *RSC Adv.* **3**, 23184–23189 (2013)
14. Martins, M.A., Santos, C., Almeida, M.M.: Hydroxyapatite micro- and nanoparticles: nucleation and growth mechanisms in the presence of citrate species. *J. Colloid Interface Sci.* **318**, 210–216 (2008)
15. Hu, Y.Y., Rawal, A., Schmidt-Rohr, K.: Strongly bound citrate stabilizes the apatite nanocrystals in bone. *Proc. Natl. Acad. Sci.* **107**, 22425–22429 (2010)
16. Wu, E., Kisi, E.H., Gray, E.M.A.: Modelling dislocation-induced anisotropic line broadening in Rietveld refinements using a Voigt function. II. Application to neutron powder diffraction data. *J. Appl. Crystallogr.* **31**, 363–368 (1998)
17. Johnsson, M., Richardson, C.F., Sallis, J.D.: Adsorption and mineralization effects of citrate and phosphocitrate on hydroxyapatite. *Calcif. Tissue Int.* **49**, 134–137 (1991)
18. Mohammadi, M.R., Fray, D.J.: Synthesis of highly pure nanocrystalline and mesoporous  $\text{CaTiO}_3$  by a particulate sol-gel route at the low temperature. *J. Sol-Gel. Sci. Technol.* **68**, 324–333 (2013)
19. Zhang, C., Yang, J., Quan, Z.: Hydroxyapatite nano- and microcrystals with multiform morphologies: controllable synthesis and luminescence properties. *Cryst. Growth Des.* **9**, 2725–2733 (2009)
20. Lopez-Macipe, A., Gomez-Morales, J., Rodriguez-Clemente, R.: Nanosized hydroxyapatite precipitation from homogeneous calcium/citrate/phosphate solutions using microwave and conventional heating. *Adv. Mater.* **10**, 49–53 (1998)
21. Guo, Y.P., Guo, L.H., Yao, Y.B.: Magnetic mesoporous carbonated hydroxyapatite microspheres with hierarchical nanostructure for drug delivery systems. *Chem. Commun.* **47**, 12215–12217 (2011)



# Critical Review on Corrosive Properties of Metals and Polymers in Oil and Gas Pipelines



Kanishka Jha, Dilip Dhakad, and Baljeet Singh

**Abstract** In most of the industries, it is observed that the pipes used in boilers or in transportation of oils, gases, steam, water, etc., are generally made up of different alloys of steel. Although pipes made up of steel alloys offer numerous advantages, it also comprises of severe limitations. One of the major limitations is that they generally get corroded with time and are heavier and costly. Moreover, the metal pipes generally undergo phase transformation with the variation in temperature, which affects the life span of pipes. Therefore, there is a need to overcome these limitations by using suitable material which can be cost-effective, provide superior properties than metals, and ensure higher life. Pipes made up of fiber-reinforced composites provide superior specific strength and stiffness and offer high resistance to corrosion and erosion. This article presents an intensive review on the various polymers used in the manufacturing of oil and gas carrying pipes. This article also addresses the benefits and the challenges encountered during the manufacturing of polymer-based pipes. But there exist a wide range of polymer and composite-based materials that are yet to be tested and can be a boon to the piping industries in the coming decades thus overcoming the limitations encountered by alloy-based steels and increasing the life span of pipes.

**Keywords** Oil and gas pipelines · Corrosion · Metals · Polymers · Composites

## 1 Introduction

Within the industry, piping is a means of transporting fluids (liquids and gases) from one location to another. Some of the materials used in the manufacturing of pipes are carbon steels, titanium, chromium–molybdenum alloy steel, and various other steel alloys. Earlier, metal and various alloys were used as oil and gas pipeline

---

K. Jha · B. Singh

School of Mechanical Engineering, Lovely Professional University, Phagwara, India

D. Dhakad (✉)

School of Mechanical Engineering, Lovely Professional University, Phagwara, India

e-mail: [dilipdhakad2015@gmail.com](mailto:dilipdhakad2015@gmail.com)

© Springer Nature Singapore Pte Ltd. 2020

C. Prakash et al. (eds.), *Advances in Materials Science and Engineering*,

Lecture Notes in Mechanical Engineering,

[https://doi.org/10.1007/978-981-15-4059-2\\_8](https://doi.org/10.1007/978-981-15-4059-2_8)

material, and nowadays, they are made up of polymers like polyethylene and glass fiber-reinforced polymers (GFRP) [1]. Now, the question arises why the polymers have replaced metals? Pipes made up of metals often require internal and external coatings in order to protect them from the atmospheric conditions as well as from the fluid flowing through them. This can result in an increase in the overall cost of the piping [2]. Moreover, metallic pipes cannot be installed in rivers, seas, and oceans since minerals and salt present in the water react with the metal surface and results in extensive corrosion. In many cases, it has been noticed that carbon steel pipes carrying natural gas are subject to corrosion due to the presence of  $\text{CO}_2$  and  $\text{H}_2\text{S}$  [3].

Corrosion is also affected by temperature and increases with increase in temperature. The rate of corrosion exceeds 1 mm/year at a temperature of 200 °C [3]. In a study, carbon steel was not recommended for such environment. As long as  $\text{H}_2\text{S}$  does not come in contact with  $\text{H}_2\text{O}$ , the rate of corrosion observed is not as significant as compared to the case when it comes in contact with water. Rate of corrosion observed in the absence of  $\text{H}_2\text{O}$  with  $\text{H}_2\text{S}$  is 0.1–1 mm/year. But as soon as  $\text{H}_2\text{S}$  comes in contact with  $\text{H}_2\text{O}$  the rate of corrosion increases to 1–3 mm/year. The rate of corrosion in case of carbon steels increases rapidly in the presence of moist  $\text{H}_2\text{S}$ , and therefore, its use is not recommended in such environments [3]. Another factor that affects the rate of corrosion is the presence of liquid  $\text{H}_2\text{O}$  particles. Therefore, in order to prevent corrosion, the pipes carrying gases must be dry [3]. From the corrosion resistance tables of metals, it is being observed that at temperatures below 40 °C carbon is extremely resistant to the environment of  $\text{NH}_3$  (rate of corrosion is below 0.1 mm/ year), taking into consideration a dry gas.  $\text{H}_2\text{S}$  is an exception, against which carbon steels are resistant (rate of corrosion is below 1 mm/ year) as per the corrosion resistance tables of metals [3].

$\text{CO}_2$  corrosion of carbon and low-carbon alloy steels is also very significant. If  $\text{CO}_2$  pressure is less than 7 psi (0.5 bar) then corrosion is unlikely to take place and if it lies as 7 psi (0.5 bar) <  $\text{CO}_2$  pressure < 30 psi (2 bar) then corrosion is more likely to take place where as in case if  $\text{CO}_2$  pressure being more than 30 psi (2 bar) then corrosion is definitely going to take place [4]. Therefore, in such a case, it is preferable to use piping made up of polymer or polymer-based composites. Moreover, metals are generally costly, heavier, and have poor corrosion resistance. Due to these reasons, polymers have taken the place of metals since they show good corrosion resistance, are lighter, and are cost-effective too. Piping made of composites is subjected to harsh environment which may also result in the deterioration of material property. They may get imposed on sudden load which ultimately results in delamination, breaking of fibers, etc. The damage caused can result in a significant reduction in the stiffness of pipes made up of composites [5]. Pipes used in industrial applications are made up of composite materials not only because of their corrosion resistance property but also due to other properties such as low maintenance costs in comparison to steel pipes. Moreover, they have high strength-to-weight ratio and are lighter. But there are a number of barriers that need to be overcome while manufacturing large diameter composite pipes in order to sustain high pressure of natural gas during its transportation [6]. Metallic pipes cannot be used at higher depths in seas, oceans, and rivers due to their high density. Therefore, in order to overcome this drawback, there

is a need to replace metallic pipes with composite pipes which can be a hybrid of metal and polymer [7]. Plastic piping is not without limitations. As already noted, the temperature ratings on all plastic pipe choices are at or below 200 °F, precluding its use for steam applications. It has been observed that the performance of pipes made up of polyethylene generally gets reduced with time [8]. Factors that affect the quality of water during its transportation are piping material, temperature, disinfectant, and amount of oxygen dissolved in water. Many studies have shown that the quality of water changes in pipes depending on the material of pipe due to the formation of biofilms [9].

GFRP pipes are light in weight and provide good specific strength and low modulus of elasticity. Moreover, the cost of installation, transportation, connection, and repairing are tremendously low. Improved mechanical strength and increased life of GFRP pipes in comparison to fatigue have promoted their use in various sectors such as service sector, agricultural sector, manufacturing industries, cooling towers, and mining industries. [10]. Steel has been widely used in the manufacturing of pipes because of its superior mechanical properties and ability to work well under high pressure. But in harsh environment, steel piping undergoes degradation because of corrosion which may result in significant reduction in the life of pipe and may also result in the total failure. For this reason, researchers started searching for some other materials that can prove to be corrosion-resistant and at the same time provide properties similar to that of metals. Pipes made up of GFRP prove to be a fascinating choice in comparison to steel pipes due to the resistance offered by them against corrosion which ultimately reduces the maintenance cost incurred by steel pipes thereby increasing the overall life of pipes [11]. Composites are a mixture of matrix (PAEK, PEEK, PTFE, PP, and PVC) and reinforcements (aramid fiber, boron fiber, glass fiber, and carbon fiber). They exhibit low density, superior strength, and stiffness and offer resistance to corrosion [1]. Plastic piping systems provide long service life and leak-free protection in addition to superior resistance to corrosion and abrasion. Pipes made up of metal or concrete involve high cost of fabrication, transportation, and its installation, but in the case of polymers and composites, it is not the same case. Pipes made up of composites or polymers are strong, durable, lightweight, and flexible, and the cost of fabrication, transportation, and installation is also comparatively less than metals.

Major drawback of using polymer pipes is that they cannot be used to transport materials of high temperature and also cannot sustain high pressure too. The bursting pressure of the polymer has a significant role to play in the polymer pipe selection for particular application. Therefore, before employing polymer pipes to any field especially in the pressure vessels, there must be awareness about its burst pressure [12]. It has been observed that pipes offer resistance to the flow of liquids or gases. The resistance offered to its flow depends upon the material used in the manufacturing of pipes. But the resistance offered can be overcome using suitable material [13]. In order to overcome the limitations encountered by polymer pipes, there is a need to develop and test materials that can prove to be more effective. After going through many research papers it has been found that most of the research work was focused on developing pipes using polymers which can resist temperatures up to 150–200 °C

only. Moreover, the capability to handle large pressure is also poor. So, there is a need to develop a material that can resist high pressure and high temperature and that can replace pipes that are used in boilers. There exists a wide range of polymer and composite-based materials that are yet to be tested which can prove to be a boon to the piping industry in the coming decades thus overcoming the limitations encountered by alloy-based steels and thereby increasing the life span of pipes.

## 2 Corrosion in Oil and Gas Pipelines

Corrosion is the deterioration and the destruction of metal as soon as it comes in contact with air and moisture [14]. Failures related to corrosion constitute 25% as experienced by the petroleum industry [2]. Most of the failures encountered are due to the presence of  $H_2S$ ,  $CO_2$ , and other salts. Carbon dioxide ( $CO_2$ ), hydrogen sulfide ( $H_2S$ ), and free water ( $H_2O$ ) are highly corrosive media. If the rate of corrosion is not controlled in a proper way, then it may result in significant loss of money to the industry. It is reported that the cost of corrosion accounts for nearly 2–3% of the total gross domestic product (GDP) of a country in a span of one year [4]. It is being reported that the pipes made up of steels for the storage of  $H_2SO_4$  undergo corrosion [15]. Therefore, there is a need to find an alternate material to steel in the construction of tanks and pipes for the purpose of transportation and storage. Whenever steel comes in contact with the aqueous environment it gets corroded and is regarded as the most common type of corrosion. Most common types of corrosion that takes place in petroleum industries are general and localized corrosion. Internal corrosion due to stress corrosion cracking is also one of the types of corrosion.

Figure 1 states that the failures in the case of petroleum-related industries are mainly due to corrosion. Other causes of failure can be fatigue, overload, brittle fracture, fabrication defects, welding defects, etc. But the main contributing factor leading to the failure of petroleum pipes is corrosion contributing 33%.

### 2.1 *Common Types of Corrosion that Prevail in Oil and Gas Pipelines*

#### **Sweet corrosion ( $CO_2$ corrosion)**

Carbon dioxide is present in many fluids being produced in industries. These fluids produced are mostly transported using pipelines that can either made up of metal or non-metal depending upon the requirement and the application. Carbon dioxide alone is not responsible for the terrible mode of cracking failure which is usually associated with  $H_2S$ , but it can prove to be very dangerous in the presence of an aqueous phase resulting in high rate of corrosion where the attack mode is often confined such as mesa attack.  $CO_2$  corrosion is well known as sweet corrosion and

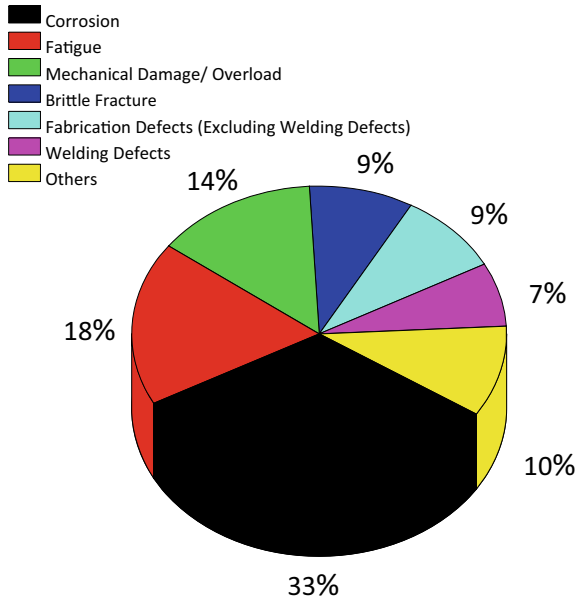


Fig. 1 Failures in petroleum-related industries [4]

is one of the most frequently occurring type of corrosion especially in the pipelines carrying oil and gases [4], as presented in Fig. 2. For many years, the corrosion resulting due to the presence of CO<sub>2</sub> is being regarded as one of the vital problems being faced during the transportation and production of oil [4]. It has proved to be one of the biggest corroding agents in industries involving the transportation or production of oils and gases [16]. Factors that play a crucial role in CO<sub>2</sub> corrosion are temperature, presence of non-aqueous phase, aqueous stream composition, increase or decrease in pH value, and the properties of the material [16, 17]. As soon as the

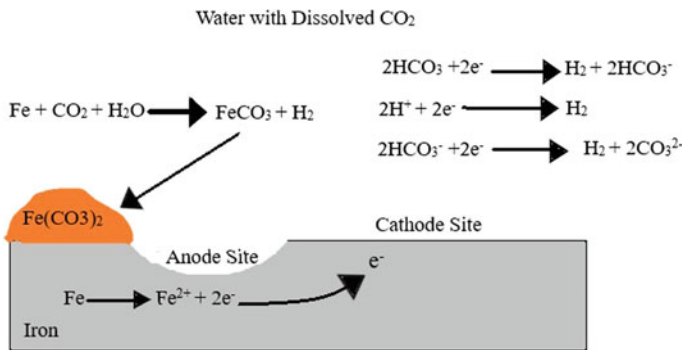


Fig. 2 Schematic representation of sweet corrosion

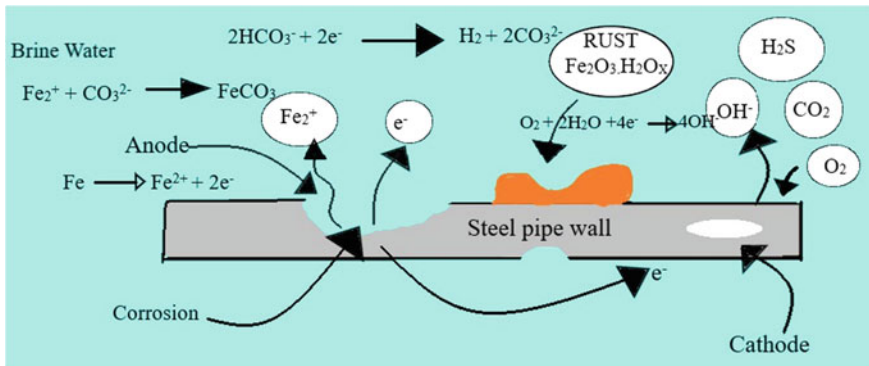


Fig. 3 Schematic representation of pitting corrosion

temperature rises beyond a particular limit, a scale of iron carbide starts to develop as a protective film on the pipes carrying oil and gas, and under these conditions, the corrosion of metal starts to take place. Corrosion due to the presence of  $\text{CO}_2$  mostly occurs in two forms, i.e., pitting and mesa attack as depicted by Fig. 3. Pitting is a type of attack which is confined and results in the removal of metal at a specific area. Mesa attack is a kind of attack which takes place under medium flow conditions [14].

### Sour corrosion ( $\text{H}_2\text{S}$ Corrosion)

The corrosion caused due to the presence of  $\text{H}_2\text{S}$  is most commonly known as sour corrosion and is schematically discussed in Fig. 4. As soon as the metal comes in contact with  $\text{H}_2\text{S}$  and moisture, the deterioration of the metal surface starts to take place and this particular type of corrosion is known as sour corrosion which proves to be quite harmful to pipes. If we talk about  $\text{H}_2\text{S}$  then what we find is that  $\text{H}_2\text{S}$  is not itself corroding, but as soon as it comes in contact with water it becomes extremely corrosive in nature [18], thus resulting in the embrittlement of the pipeline [16]. No doubt that  $\text{H}_2\text{S}$  is a weak acid but when it is dissolved in water it becomes highly corrosive in nature and is also the source of  $\text{H}_2$  ions. The corrosion products thus obtained are iron sulfide and  $\text{H}_2$  gas. Iron sulfide being one of the most corrosive product results in the formation of scale at a relatively lower temperature which acts as a barrier to slow corrosion.

At a temperature of  $20^\circ\text{C}$ , presence of  $\text{H}_2\text{S}$  results in corrosion of carbon steel in the range varying in between 0.1 and 1 mm/year [3]. In case of moist  $\text{H}_2\text{S}$ , the corrosion stays in the range of 1–3 mm/year at a temperature of  $20^\circ\text{C}$ . There is a significant increase in corrosion with increase in temperature. At  $110^\circ\text{C}$ , the rate of corrosion observed can be 10 mm/year [3]. Rate of corrosion in case of alloyed steels was found below 0.1 mm/year at temperature in between 20 and  $100^\circ\text{C}$  [3].  $\text{H}_2\text{S}$  Factors that play a crucial role in  $\text{CO}$  corrosion are temperature, presence of non-aqueous phase, aqueous stream composition, increase or decrease in pH value, and the properties of the material [19]. If the dew point of water is  $-8^\circ\text{C}$  at 70 bar,

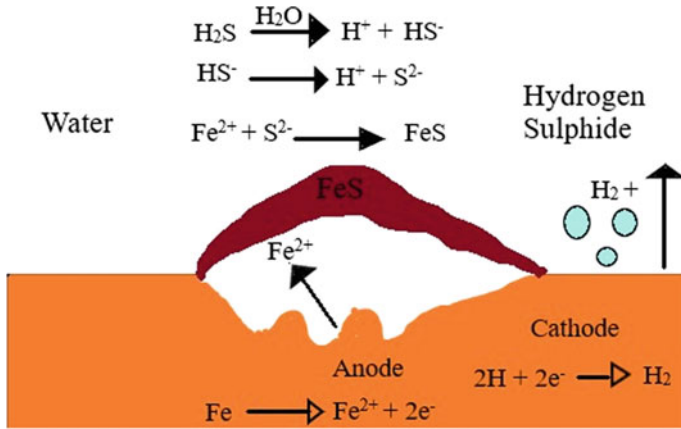


Fig. 4 Schematic representation of sour corrosion

then, in that case, the concentration of H<sub>2</sub>S and CO<sub>2</sub> will be approximately 5 mg/nm<sup>3</sup> and oxygen concentration up to 0.5%, thereby restricting additional corrosion [3].

**Galvanic corrosion**

A corrosion type which mainly occurs when two materials (metals) having different electrochemical potentials are brought in contact and are exposed to an environment having an electrolyte. In that case, a metal having the least or highest negative potential acts as an anode and starts to corrode [16]. Now, the anode starts losing ions in order to maintain the flow of electrons. Since metals are composed of crystals, cells set up thereby resulting in intergranular type of corrosion. The problems arising can become worst if the ratio of the cathode to anode area becomes too large [20]. Setup is shown in Fig. 5.

**Crevice corrosion**

Localized corrosion which generally occurs in places where the fluid generally gets

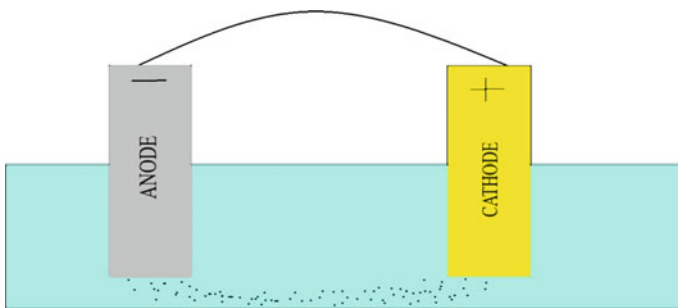
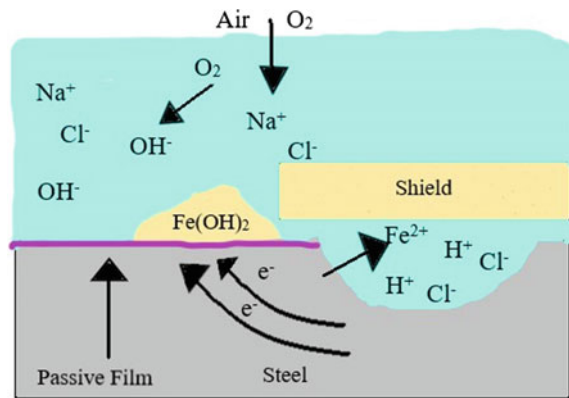


Fig. 5 Setup representation of galvanic corrosion process

**Fig. 6** Schematic representation of crevice corrosion



stuck or stagnant, for example, in the narrow clearances or in the crevices of metal is known as crevice corrosion. It is generally caused due to the difference in the concentration of corrodents on the surface of the metal. Any difference in electrochemical potential can give rise to selective crevice or pitting corrosion attack. Presence of oxygen in fluid enhances the pitting attack of the metal in the region which is being shielded and is the major cause of destruction and washouts in the presence of rubber pipe protectors [14], as explained in Fig. 6.

### Oxygen corrosion

Oxygen is one of the oxidizing agents that react vigorously with metals. And since it reacts vigorously, it results in the corrosion of pipes specially those through which flows the fluid having significant concentration of oxygen. It is recommended that the concentration of oxygen in pipes carrying natural gas should not exceed above 10 parts per million volume (ppmv) [21]. Oxygen enters in fluids through casing, leaking pump seals, open hatches, and process vents. In case of cathodic reactions, oxygen acts as a depolarizer and acceptor of electrons and thereby accelerating the anodic destruction of metal [22]. The flow velocity of the fluid plays a crucial role in the supply of oxygen. If the flow velocity of the fluid over the surface of the pipe is quite high, then it will ensure the supply of oxygen to the metal pipe and is harmful if its concentration lies in between 0 and 5 parts per billion (ppb) [23]. The existence of oxygen boosts the corrosive effect of H<sub>2</sub>S and CO<sub>2</sub>. The hindrance of corrosion lead by the presence of oxygen is hard to achieve and is impractical in any system. The presence of oxygen gives rise to two basic forms of corrosion namely uniform and pitting-type corrosion as explained in Fig. 7. It is being observed that corrosion is stronger especially when the temperature is below the dew point of water. Oxygen has a significant impact on the intensity of corrosion [3].

### Erosion corrosion

It is the loss of material encountered by the pipes due to the flow of liquid at a very high velocity over its surface. The fluid velocity initially attacks the protective film



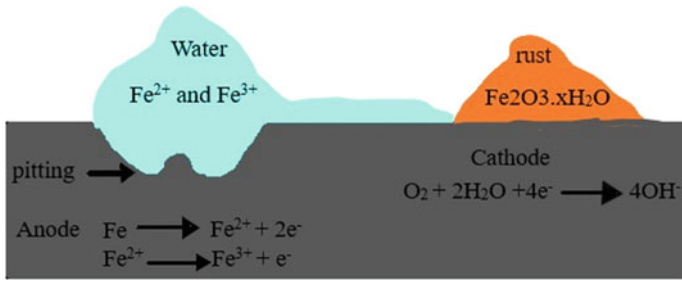


Fig. 7 Schematic representation of oxygen corrosion

thereby exposing the bare metal in direct contact with the fast-flowing water. And when the bare metal is continuously exposed to fast-flowing liquid it gets corroded with time. The protective film acts as a barrier to corrosion since it prevents the direct contact of fast-flowing liquid with the bare metal surface as explained in Fig. 8. Due to high shear stress and turbulence flow regime in the pipe, the protective film may get damaged, thereby, resulting in higher corrosion rate [24, 25] and the rate of corrosion depends upon the density with which the fluid flows and the structure of solid particles present in the fluid [16]. Presence of abrasive particles can also lead to erosion corrosion. Erosion corrosion is often regarded as wear corrosion [7].

**Microbiologically induced corrosion**

Presence of any bacteria or any kind of bacterial activities leads to microbiologically induced type of corrosion. Waste products such as H<sub>2</sub>S, CO<sub>2</sub>, and any other organic acids are being produced by the bacteria, and these waste products are responsible for the corrosion of pipes due to the increased toxicity in the fluid flowing through pipes [26]. Bacteria or microbes always try to find the place which suits best for their growth and after finding a suitable environment, they try to form colonies, thereby,

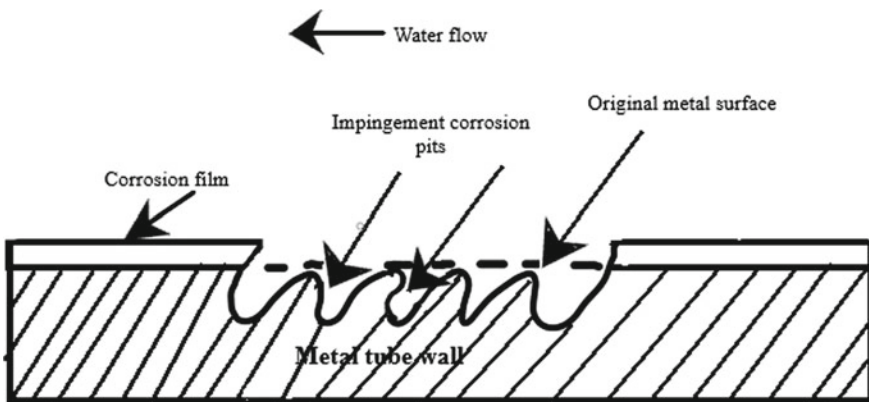


Fig. 8 Schematic representation of erosion corrosion

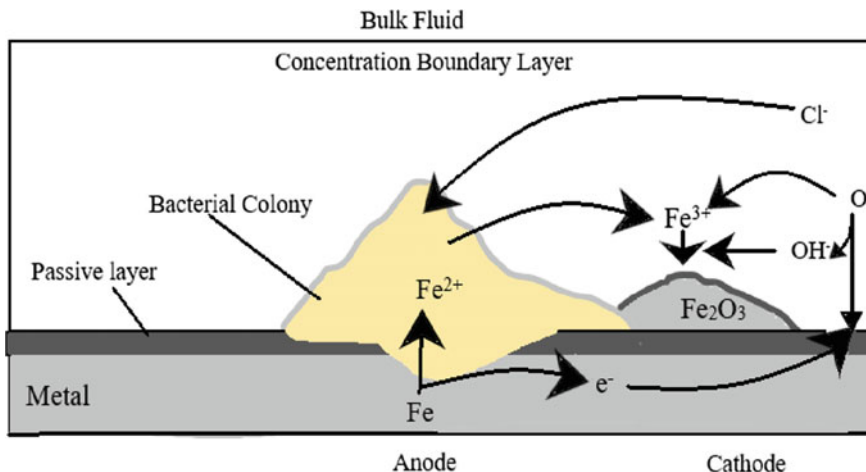


Fig. 9 Schematic representation of microbiologically induced corrosion

resulting in the corrosion of that region as explained in Fig. 9. Stagnant neutral water promotes the formation of these colonies of microbes [16].

### Stress corrosion cracking

One of the forms of corrosion results in the development of cracks due to the coincident action of the corrosive atmosphere and the tensile stress. In other words, we can say that stress corrosion cracking is the result of conjoint action of three components mainly the material, the tensile stress, and the surrounding environment and is shown in Fig. 10. The effect of stress corrosion cracking generally lies between dry cracking and the fatigue threshold of that particular material [27]. If the pH of the surrounding atmosphere is quite high and there is the presence of cracks on the nearby pipe, then we can say that the pipe may have undergone stress corrosion cracking [14]. The hydrogen atoms diffuse to the crack tip and result in the embrittlement of metal. Therefore, we can say that hydrogen embrittlement results in the development of stress corrosion cracking especially in steels and some other alloys like titanium. In the absence of moisture, ammonia does not result in corrosion. The rate of corrosion observed in case of carbon steel is  $<0.001$  mm/year at a temperature range of 16–20 °C. At 300 °C, the corrosion due to the presence of ammonia rises to 0.1 mm/year, and in between 500 and 600 °C, the corrosion found is in between 0.12 and 0.28 mm/year.

Ammonia in the presence of moisture can result in stress corrosion cracking in the case of carbon steels [3]. From Fig. 11 we depict that  $\text{CO}_2$  and  $\text{H}_2\text{S}$  are major forms of corrosion that affects the life span of metallic pipes in petroleum industries.

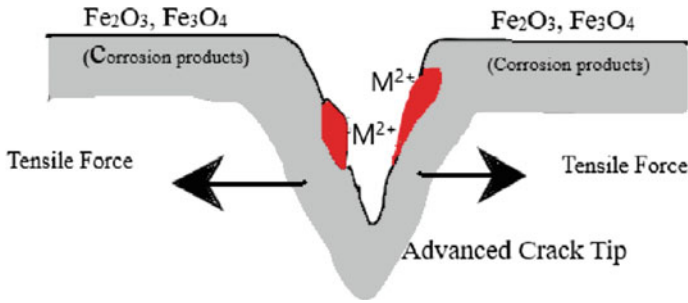


Fig. 10 Schematic representation of stress corrosion cracking

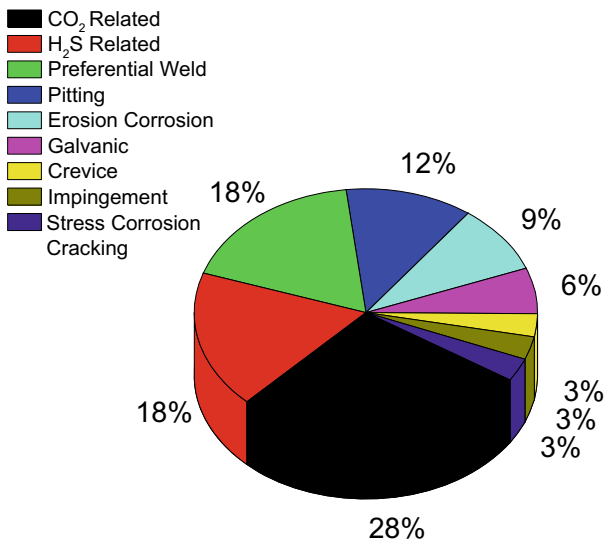


Fig. 11 Major forms of corrosion that prevail in the oil and gas industry

### 3 Wear in Oil and Gas Pipes Made up of Metals

Wear is considered to be the main cause for the loss of mechanical performance and loss of material wastage as well. And this wear is a result of friction. So, we can say that wear directly or indirectly depends on friction. More the friction more will be the wear and vice versa. But we can control the rate of wear and friction depending upon the requirement whether we want high friction and less wear, or less friction and high wear, or high friction and high wear depending on our requirement. Friction plays a significant role in controlling the rate of wear and energy lost. If the friction and wear are controlled in a proper way, then it may result in enormous savings in terms of money, material, labor, energy, time, etc. One of the methods to eradicate

friction is to use the principle of lubrication or a lubricating material in between the two contacting surfaces [28]. The common types of wear that takes place in pipes are erosive wear, cavitation wear, oxidation wear, and corrosion wear. Erosive wear takes place due to the high velocity of the impacting particles, whereas cavitation wear takes place when low pressure bubbles of water burst in the region of very high pressure at a very high velocity. Corrosion wear occurs due to the contact of metal with the atmospheric oxygen and moisture, whereas the oxidative wear occurs due to the metals' affinity toward oxygen [28].

## 4 Corrosion of Polymers

Corrosion is the transformation of the refined metallic material into its stable form (oxide, sulfide, and hydroxide) by chemical or electrochemical reaction. It takes place especially in metals whenever they are exposed to atmosphere. Now, the question arises whether corrosion takes place only in metals? The answer is not at all. Corrosion also takes place in other materials such as ceramics and polymers. Corrosion is not that much prominent in case of polymers as in metals. In the case of polymers, corrosion does not involve the deterioration of material instead it involves the degradation of the properties of the polymer. For example, it results in the softening of the polymer, a decrease in its strength and stiffness, and it also affects the polymer's appearance, i.e., it results in the discoloration of the polymer. Most of the polymers do not undergo corrosion up to certain limits of temperature but beyond that they do experience. Polymers usually undergo solvation, which ultimately leads to the swelling of the polymer followed by softening and ultimately the failure of the polymer.

Polymers are made up of one or more monomers which are linked to one another by a bond which can be strong or weak depending upon the branching. The branching can be linear or cross-linked depending upon the type of polymer. Breaking down of bonds results in the failure of the polymer. Reasons behind the breaking down of these bonds and linkages are temperature, oxidation, hydrolysis, thermal degradation, radiation, absorption of water, etc. Moreover, the nature of the laminate, the symmetry of the structure, the nature of bonding, and the degree of branching are some of the other factors that directly or indirectly affect the life of polymer. Oil, gas, and mining companies are looking for materials other than metals which can prove to be cheaper, lighter, and corrosion-resistant, offer high strength, and can sustain high temperature. Therefore, they may be considering high-density polyethylene (HDPE) pipe as a money-saving alternative to steel pipe. Advantages such as lightweight and resistance to corrosion are offered by reinforced thermoplastic pipes, and because of these advantages, they have been widely used in applications involving moderate temperature and pressure.

- Pipes of polyethylene are resistant to rusting, breaking, and corrosion.
- They are not affected by chemical and their reagents.

- They show resistance to abrasion and can be employed in applications such as mining.
- Are rigid enough to bear extreme loads.
- High service life.
- Leakproof.
- Lightweight PE pipes are easily installed without heavy lifting equipment which will save time, money, energy, resources, etc.

Pipes made up of polyethylene and high-density polyethylene have been widely used in the exploration of oil and gas. Composite pipes comprising of HDPE as a matrix and glass or carbon fiber substrates as reinforcements are being used for pressures ranging from 300 psi up to 3000 psi and in some of the most difficult terrains across the country. The reason why the plastic pipe is being used is because of its flexibility and ability to sustain even earthquakes. And there exists a wide range of polymer and composite-based materials that are yet to be tested which can prove to be a boon to the piping industries in the coming decades thus overcoming the limitations of alloy-based steels, thereby, increasing the life span of pipes.

## 5 Conclusion

We are living in a world surrounded by metals and their alloys and most of them are prone to corrosion. There is no industry that does not employ pipes for the transportation of water, oil, gas, chemicals, steam, etc. Almost all the pipes used for transportation are made of metals that are subjected to corrosion. It should be noted that corrosion not only exists in case of pipes carrying oil and gas or water but also in areas other than transportation such as construction, manufacturing, building, and production. Therefore, it is a thing of global concern that needs a global solution. Until the twenty-first century most of the researchers focused on the study of metals and their alloys, their properties, and ways to eliminate corrosion. Some of the researchers emphasized the use of inhibitors to control corrosion. Very few researchers studied materials other than metals which may have proved to be more effective and superior to metals. These materials include polymers, ceramics, and composites. Composite is one of the new fields of materials which are excellent in terms of specific strength, specific stiffness, toughness, and excellent resistance to corrosion. There is a need to study these materials in detail as they can prove to be a boon to the piping industry thus saving a tremendous amount of cost encountered due to corrosion and thereby enhancing the life of components. There exists no material that can overcome all the limitations of metals.

## References

1. Khelif, R., Chateaufneuf, A.: Reliability-based replacement of polyethylene gas pipeline networks. *Arab. J. Sci.* **39**, 8175–8185 (2014)
2. Samimi, A., Zarinabadi, S.: Application polyurethane as coating in oil and gas pipelines. *Int. J. Sci. Eng. Invest.* **1**(8), 43–45 (2012)
3. Latosov, E., Loorits, M., Maaten, B., Volkova, A., Soosaar, S.: Corrosive effects of H<sub>2</sub>S and NH<sub>3</sub> on natural gas piping systems manufactured of carbon steel. *Energy Procedia* **128**, 316–323 (2017)
4. Kermani, M.B., Harrop, D., Intl, B.P.: The impact of corrosion on the oil and gas industry. In: *SPE Production & Facilities*, pp. 186–190, 2 Jan 1996
5. Deniz, M.E., Karakuzu, R.: Composites: Part B seawater effect on impact behavior of glass—epoxy composite pipes. *Compos. Part B* **43**(3), 1130–1138 (2012)
6. Colombo, C., Vergani, L.: Optimization of filament winding parameters for the design of a composite pipe. *Composites* **148**, 207–216 (2018)
7. *Advanced Fiber-Reinforced Polymer (FRP) Composites for the Manufacture and Rehabilitation of Pipes and Tanks in the Oil and Gas Industry* (2013)
8. Wang, Y., Lan, H., Meng, T.: Lifetime prediction of natural gas polyethylene pipes with internal pressures. *Eng. Fail. Anal.* **95**, 154–163 (2019)
9. Xu, H., et al.: Effects of pipe material on nitrogen transformation, microbial communities and functional genes in raw water transportation. *Water Res.* **143**, 188–197 (2018)
10. Rafiee, R.: On the mechanical performance of glass-fibre-reinforced thermosetting-resin pipes: a review. *Compos. Struct.* **143**, 151–164 (2016)
11. Sebaey, T.A.: Design of Oil and gas composite pipes for energy of and gas composite pipes for energy production assessing the feasibility of using the heat demand-outdoor temperature function for a long-term district heat demand forecast. *Energy Procedia* **162**, 146–155 (2019)
12. Ra, R., Torabi, M.A.: Stochastic prediction of burst pressure in composite pressure vessels. *Compos. Struct.* **185**, 573–583 (2018)
13. Flacconnèche, B., Martin, J., Klopffer, M.H.: Transport properties of gases in polymers: experimental methods. *Oil Gas Sci. Technol.* **56**(3), 245–259 (2001)
14. Popoola, L.T., Grema, A.S., Latinwo, G.K., Gutti, B.: Corrosion problems during oil and gas production and its mitigation. *Int. J. Ind. Chem.* **1**(4), 1–15 (2013)
15. Panossian, Z., Lira, N., Almeida, D., Maria, R., De Sousa, F.: Corrosion of carbon steel pipes and tanks by concentrated sulfuric acid: a review. *Corros. Sci.* **58**, 1–11 (2012)
16. Nalli, K.: *Corrosion and its Mitigation in the Oil and Gas Industries*, 1st edn. Wiley, pp. 673–679 (2012)
17. Kermani, M.B., Smith, L.M.: *CO<sub>2</sub> Corrosion Control in Oil and Gas Production: Design Considerations*. The Institute of Materials, European Federation of Corrosion Publications, London (1997)
18. Ray, J.D., Randall, B.V., Parker, J.C.: Use of reactive iron oxide to remove H<sub>2</sub>S from drilling fluid. In: *53rd Annual Fall Tech, Conference of AIME*, Houston (1979)
19. F. O. F. Science: *Corrosion in Petroleum industry 2016 (Part I)*, vol. 2016, no. Part I (2016)
20. Perez, T.E.: *Corrosion in the Oil And Gas Industry : An Increasing Challenge for Materials*, pp. 565–566 (2014)
21. Groyzman, A.: Corrosion problems and solutions in oil, gas, refining and petrochemical industry. *Korozní problémy při zpracování plynu a ropy*, pp. 100–117 (2017)
22. Aime, M.: *Desorption of Oxygen From Water Using Natural Gas for Countercurrent Stripping*
23. Waters, N.: *Chemical Removal of Oxygen from Natural Waters*, pp. 443–446 (1971)
24. Roberts, K.P., Shirazi, S.A., Shadley, J.R., Rybicki, E.F., Joia, C.: Flow loop study of NaCl concentration effect on erosion, corrosion, and erosion-corrosion of carbon steel in CO<sub>2</sub>-saturated systems. *J. Sci. Eng.* **68**(2), 1–9 (2012)
25. Ajeel, S.A., Ahmed, M.A.: Study synergy effect on erosion-corrosion in oil pipes. *Eng. Tech. J.* **26**(9), 1068–1080 (2008)

26. Ossai, C.I.: *Advances in Asset Management Techniques : An Overview of Corrosion Mechanisms and Mitigation Strategies for Oil and Gas Pipelines*, vol. 2012 (2012)
27. Craig, B.D., Smith, L.: *Corrosion Resistant Alloys (CRAs) in the Oil and Gas Industry— Selection Guidelines Update*
28. Stachowiak, G., Batchelor, A.W.: *E Engineering tribology*, 4th edn (2013)

# Synthesis and Characterization of Aluminum Composite Reinforced by Multiwall Carbon Nanotubes



Sunil Kumar Tiwari, Harsh Sharma, Akula Umamaheswararao, and Sumit Sharma

**Abstract** This research focuses on the characterization of Al-CNTs composites synthesized by mechanical stir casting process. In the sight of Al-CNT composites, researchers have surveyed and opted many approaches for synthesis of Al-CNT composites. Some investigators have effectively fabricated Al-CNT composites, but they have met a common problem of agglomeration of CNTs in the Al matrix. In this study, we are mixing (>99% purity) MWCNTs in the aluminum matrix (Al-7075t651) in different ratio with weight percent. Stirrer with four blades has been used to promote the homogeneity of CNTs in Al matrix. Dimensions of MWCNTs were diameter 10–12 nm and length 4–8  $\mu\text{m}$ . With the addition of 0.1 wt% CNTs and 0.15 wt% CNTs in Al matrix, the tensile strength at peak was approximately increased by 11 and 27%, whereas with the addition of 0.2 wt% CNT, tensile strength at peak was decreased by 7% as compared to 0 wt% CNT in Al matrix. Addition of CNTs up to 0.15 wt% in Al matrix has shown increase in the hardness while further addition of CNTs beyond 0.15 wt% resulted in decrease in hardness.

**Keywords** Aluminum composite · Scanning electron microscopy · Metal matrix · Microstructure

## 1 Introduction

In recent years, light metal matrix composites are broadly used in aerospace industries [1] for making planes, flights, missiles, rockets, etc. In most of the space crafts,

---

S. K. Tiwari (✉)

Doctoral Research Fellow, Research and Development, University of Petroleum and Energy Studies, Dehradun, Uttarakhand 248007, India  
e-mail: [sktiwari@ddn.upes.ac.in](mailto:sktiwari@ddn.upes.ac.in)

H. Sharma · A. Umamaheswararao

Assistant Professor, Dev Bhoomi Institute of Technology, Dehradun, Uttarakhand 248007, India

S. Sharma

Department of Mechanical Engineering, Dr. B.R. Ambedkar National Institute of Technology, Jalandhar, Punjab 144011, India

© Springer Nature Singapore Pte Ltd. 2020

C. Prakash et al. (eds.), *Advances in Materials Science and Engineering*,

Lecture Notes in Mechanical Engineering,

[https://doi.org/10.1007/978-981-15-4059-2\\_9](https://doi.org/10.1007/978-981-15-4059-2_9)



aluminum is used because of its excellent properties, most commonly because of its lightweight [2]. Researchers have reinforced aluminum with different reinforcements, but in the recent scenario, they have used CNTs because of their astonishing characteristics like their elastic modulus (1 ~TPa), strength (~100 GPa), high aspect ratio around (50–500) [3], stability, high stiffness, and low density (1.2–1.8 g/cm<sup>3</sup>). Because of the lightweight and non-corrosive feature of aluminum [4], researchers consider Al composites to be the material for next generation to be used in industries. Seeing the outstanding and exceptional features of Al-CNT composite [5], investigators have used several methods for its fabrication [6–9]. However, they have faced the common problem of the non-uniform dispersion and structural damages. Studies have shown that the strength of Al-CNT composite is extremely dependent on homogeneous distribution of CNTs in the aluminum matrix. Since solid-state synthesis processes are generally used for making large samples, so they are less appropriate for mass production. Liquid-state synthesis processes are anticipated for mass production, and they also provide freedom to produce different shapes. Abbasipour et al. (2010) opted compo-casting method for the synthesis of Al-CNT composite [10]. They coated Al-356 powders with CNTs by Ni-P electroless method. As a result, they found a considerable increase in hardness of the composite. Narayanan et al. (2015) fabricated 6061Al-MWCNTs composite via stir casting method. To increase the homogeneity of CNTs in matrix, they mixed CNTs in molten aluminum at 700 °C and stirred at 300 rpm for 20 min. With the addition of CNTs, researchers reported an upsurge in tensile strength [6]. Sankara Narayanan et al. (2015) synthesized and characterized the mechanical properties of Al-CNT composites. They mixed 1 wt% of CNTs in Al matrix to compare it with Al-0 wt% CNT. They found an enhancement in hardness by 25% and that of ultimate tensile strength by 35% [11]. K. Senthamarai and P. Marimuthu have fabricated Al-CNT composite for microstructural and mechanical characterization. According to the investigations, Brinell (BHN) 17, hardness was increased by 44%, 63%, and 83% in case of 0.5 wt%, 0.75 wt%, and 1 wt% reinforcement, respectively. Ultimate tensile strength was found to be increased by 10.5%, 16.31%, and 23.68% in case of 0.5 wt%, 0.75 wt%, and 1 wt% reinforcement, respectively [6]. Kim et al. (2011) synthesizes Al-CNTs composite via semisolid powder method. They found cavities and blow holes in the case of stir casting process. Authors also reported ductile nature of fracture. This work specifies that distribution of CNTs in Al through stir casting has resulted in the growth of mechanical properties with less agglomeration of CNTs. Results of synthesis of Al-CNT composites have been characterized by tensile and hardness tests.

## 2 Experimental Details

### 2.1 *Synthesis of Al-MWCNT Composites*

Aluminum billets were melted in the crucible of graphite kept in an electric furnace at a temperature of about 630 °C. When the melting of the aluminum was confirmed, it was initially stirred with stirrer of graphite (four-blade stirrer) without adding any reinforcement in the molten material for 3 min at RPM of 300–350 so as to make vortex inside the molten material. While stirring action was going on, 0.1 wt% CNTs were added in the molten aluminum and were stirred for 3 min more at the same RPM. Later on, the RPM of the stirrer was increased up to 500–550, and it was stirred for 5–8 min more. In parallel to the stirring action performed in the furnace, the mold was being heated in a muffle furnace. It was preheated up to the temperature of 320 °C. When stirring was completed, molten material (Al + MWCNTs) was poured in the mold in open environment conditions. While pouring, the temperature of molten material was 700 °C. Poured material was allowed to solidify in the air and was further removed out of the mold. All the samples Al-0 wt% CNTs, Al-0.1 wt% CNTs, Al-0.15 wt% CNTs, and Al-0.2 wt% CNTs were prepared following the same procedure of fabrication.

### 2.2 *Characterization of Composites*

Microstructure and morphology of the composites fabricated were characterized by field emission electron microscopy (Hitachi- PU 5.0 kV) and optical microscopy. Samples for both microscopic investigations were prepared by polishing with emery papers of grades 180, 320, 400, 600, 800, 1000, 1500, 2000, and 2500 followed by diamond polishing to get mirror finished surface. Further, the polished samples were etched with Keller's reagent [12] for 10–15 s and were washed with distilled water and dried [13]. Surface structure cracks, grains, and grain boundaries were analyzed by optical microscopy while the strengthening mechanism between aluminum and CNT was studied through electron microscopy. Tensile tests have been conducted on the computerized UTM machine (DAK system Inc. UTM series 7200) following the standard ASTM D638. Dimensions of the specimen for tensile tests have been shown in Fig. 1. Specimens have been prepared according to ASTM-E8 standards (sub-size specimen). For testing, they were clamped in the jaws of the UTM machine, and the load was applied at strain rate of 50 mm/min up to its fracture. Micro-hardness test was performed on the Vickers hardness testing machine using diamond tool. The load of 200 gf was applied for dwelling time of 12 s.

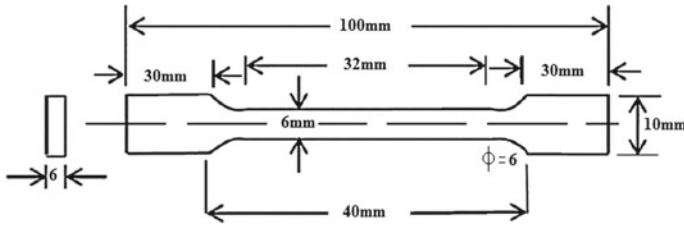


Fig. 1 Dimensions of tensile specimen

### 3 Results

The entire fabrication process was performed in open environment. Crucible and stirrer were made up of graphite so as to provide good lubrication and to reduce the contamination of material in the molten state. Hypothesis was made that four-blade tapered stirrer would help in making good vortex in molten metal while stirring would result in homogeneous distribution of CNTs in the matrix that came to be true. It was found that in open environment, molten aluminum was oxidized while pouring in the mold. Figure 2, optical images (500x), shows that with increase in ratio of

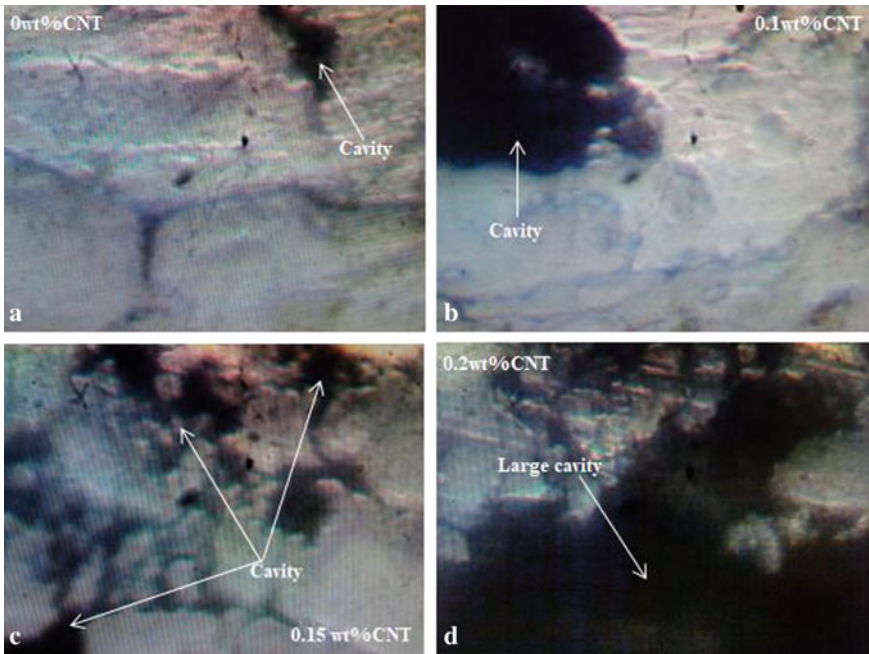
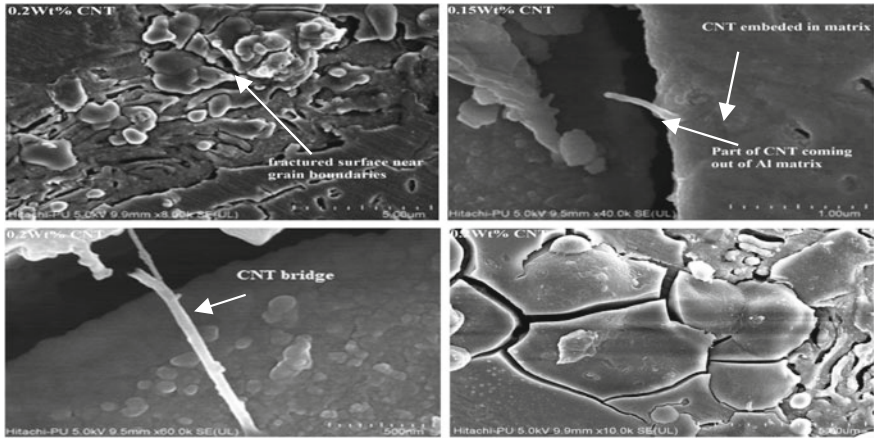


Fig. 2 Optical images of Al-CNT composites



**Fig. 3** SEM images of composites

CNTs in Al matrix, there is continuous increase in surface damage and cracks in the composite.

Figure 3 shows SEM images of the specimen. It was found that cracks and fracture surfaces were more near grain boundaries. Interfacial bond between CNT and Al matrix was seen in the form of CNT bridge. Less amount of CNTs were seen on the surface of the cast composite. This is because the agglomerated CNTs from the surface of the casting were machined while preparing samples for SEM analysis. Figure 4 displays the SEM results of the fractured surface of samples. From figure, it was confirmed that CNTs were dispersed in the Al matrix. Broken CNTs can be seen on the fractured surface. With the addition of 0.1 wt% CNT and 0.15 wt% CNT in Al matrix, the tensile strength of the composite increased with 11.35% and 27.23%, respectively, whereas it decreased with 7.36% with the addition of 0.2 wt% CNT as compared to 0.0 wt% CNT. Increase in tensile strength with increase in percentage of CNTs has been reported by Narayanan [11].

Initially, after mixing 0.1 wt% CNT in Al matrix, composite became ductile but on mixing 0.15 and 0.2 wt% CNT, the composite became brittle as shown in Fig. 5. Young's modulus of composites increased in case of 0.1 and 0.15 wt% reinforcement. While it has decreased in case of 0.2 wt% reinforcement but it has not decreased below the Young's modulus of Al-0 wt% CNT composite. Overall results of the tensile test performed on UTM have been shown in Table 1.

Micro-hardness test was performed on the Vickers hardness testing machine. Flat samples were prepared in the dimensions of (2 × 1 × 0.5) cm and were prepared by polishing it with flat file followed by polishing with emery papers. They were polished in such a way that there were no scratches on the surface on which hardness test was to be done. The grades of emery papers used for polishing were 180, 320, 500, 1000, and 1500. The way of polishing was same as in the case of preparation of samples for SEM analysis. Twelve readings were taken on the polished face of the sample. Samples of hardness test were not prepared according to any standard. They

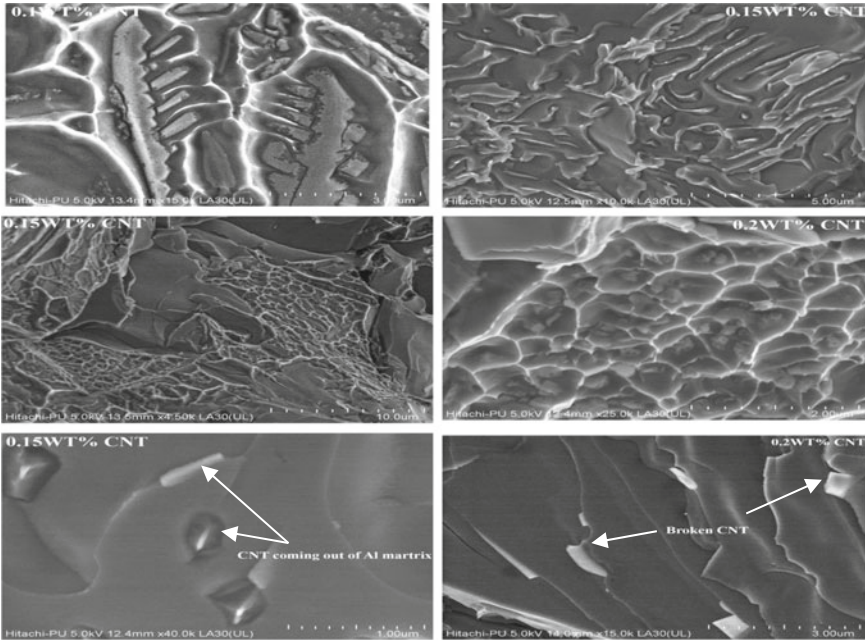


**Fig. 4** Fracture surface of the composite

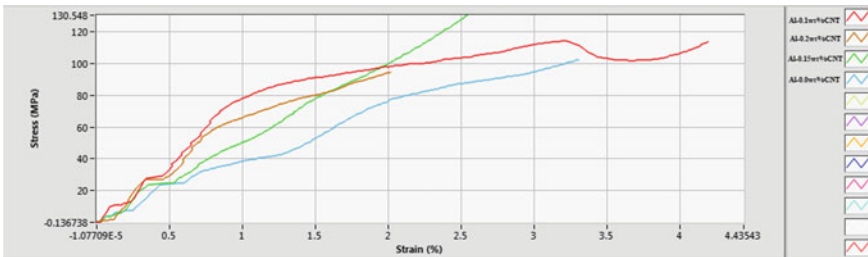


**Fig. 5** Stress–strain graph of all four samples generated in UTM

**Table 1** Readings of tensile tests obtained from UTM

Samples	Tensile strength (at peak) in MPa	Young’s Modulus (MPa)	Elongation (%)
Al-0 wt% CNT	102.607	4040.82	3.321
Al-0.1 wt% CNT	114.258	7353.07	4.211
Al-0.15 wt% CNT	130.548	8164.30	2.56
Al-0.2 wt% CNT	95.051	6453.35	2.037

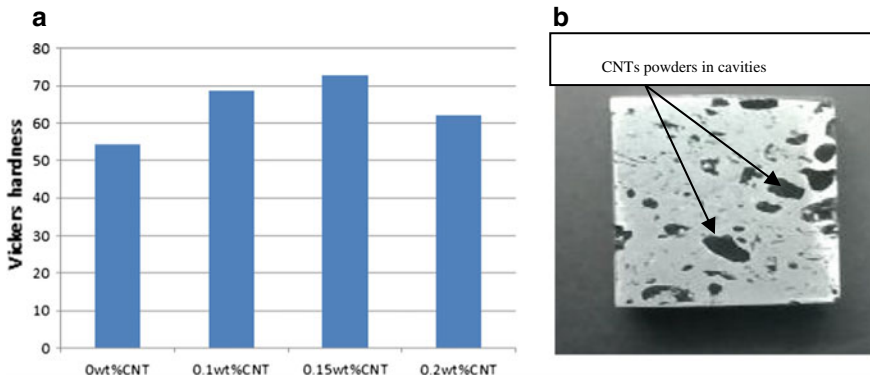


**Fig. 6** **a** Micro-hardness values of composites. **b** CNTs in forms of powders in cavities

were prepared according to the hardness testing machine requirements. For testing, samples were kept at the staying plate of the hardness testing machine one by one. They were initially observed using microscope internally installed in the hardness testing machine so as to confirm the scratch-free spot of the surface of the material to be tested. When the surface or say spot was decided, the load of 200 gf was applied for the dwelling time of 12 s. And thus, the micro-hardness of the material was obtained at 12 different spots, and the final micro-hardness of the composite was calculated as the average of all the hardness value at 12 different spots. It was found that with the addition of 0.1 wt% CNT, 0.15 wt% CNT, and 0.2 wt% CNT, the hardness of the composite was increased by 25.95%, 33.6%, and 13.67%, respectively, with respect to Al-0 wt% CNT as shown in Fig. 6a.

## 4 Discussion

### 4.1 Tensile Strength

Tensile strength of base material (Al-0.0 wt% CNT) has been reported low as compared to the Al-7075-t6-51 alloy. The reason behind this fall in tensile strength is the working and processing conditions which are quite different from the ideal working conditions for the fabrication of Al-7075 t6 51 alloys. Moreover, there is absence of heat treatment and strengthening processes in fabrication of composites. And casting defects also lead to the fall in strength of material. All the three Al-CNT composites have been fabricated in the same operating conditions, so the comparison of the Al-CNT composites with base material (Al-0 wt% CNT) is possible so that strengthening mechanism of CNT in Al matrix can be studied [14]. The strengthening mechanism in Al-CNT composites hinge on the length of the CNTs in loading direction as CNTs have good strengths, Young's modulus, yield strength, and plasticity. In case of the



addition of 0.1 wt% CNTs and 0.15 wt% CNTs in Al matrix, the maximum load in elasticity was beared by CNTs providing good strength to the material because of the high Young's modulus of CNTs (350–970 GPa) as compared to metal matrix. The overall Young's modulus of the composite has been increased for 0.1 and 0.15 wt% reinforcement. Moreover, due to the random distribution of CNTs, there is dislocation pileup [15] which puts restriction in plastic flow and increases the strength of the material in elasticity and thus results in improved tensile strength of the composite. In case of 0.2 wt% CNTs in Al matrix, decrease in Young's modulus of the composite has been seen because of agglomeration of CNTs which can be even seen clearly by naked eyes in the form of powder Fig. 6b. CNTs can be seen as black powder on the surface of the Al-0.2 wt% CNT composite leading to the formation of high amount of cavities (Fig. 2) which also leads to the decrease in the strength of the material. In the case of addition of 0.15 wt% CNT in Al matrix, the CNTs present in the Al matrix were distributed homogeneously in the molten metal giving good strength to the composite as compared to Al-0.1 wt% CNT. Because of the comparatively large amount of CNTs in the matrix, some amount of the CNTs was agglomerated. CNTs were seen on the surface and in interior of the composite after fracture (Figs. 3 and 4). Decrease in tensile strength of Al-0.2 wt% CNT is due to the weak interfacial bond between CNTs and Al matrix as CNTs agglomerates. Agglomeration of CNT causes decrease in the density (distribution) of CNT in matrix resulting in weak bond and thus in low tensile strength. The presence of CNTs in the matrix can increase the slip distance of dislocation during deformation which could be the reason behind the reduced elongation that results in showing the brittle behavior of the Al-CNT composites.

## 4.2 Hardness

Hardness of the composite was increased continuously up to the mixing of CNTs by 0.15% and beyond this at 0.2 wt%; it decreased because of the agglomeration of the CNTs. Due to agglomeration, it was not spread homogeneously in the matrix and thus resulted in the low density of MWCNTs in the molten aluminum that results in the decrease in the hardness of the composite. However, at some spots increase in hardness was observed because of the presence of the CNTs which were found to be homogeneously mixed. Due to excess amount of CNTs used as reinforcement and due to their agglomeration, overall hardness has been decreased. Same results have been shown by Senthil Kumar et al. [16].

## 4.3 Microstructure and Morphology

Through optical and FESEM, it can be said that CNTs agglomerated in the matrix. While preparing samples for tensile and SEM testing, a large amount of cavities

were seen which were further decreased when machined more. CNTs were found in those cavities as particulate material. Through SEM results (Fractography), it is clear that CNTs were embedded in the matrix, and they have helped in strengthening mechanism in the composite. These results have also shown casting defects in the matrix like the formation of cavities and damaging of surface. Large amount of cavities were seen in Al-0.2 wt% CNT composite which lead to the fall in tensile strength and hardness of the composite. Fractography has shown the formation of fine dimples on the fractured surface with embedded CNTs as shown in Fig. 4 [17].

## 5 Conclusion

In this study, the mechanical and morphological characterization has been done. An attempt has been taken to increase the strength and hardness of the material. Moreover, optical and SEM results have shown agglomeration of the material in the form of particulate and fiber both. Results withdrawn from this study have been mentioned below:

1. With increase in CNTs %, the Young's modulus of composite has increased. Highest Young's modulus has been reported in Al-0.15 wt% CNT composite.
2. With the addition of 0.1 wt% CNT and 0.15 wt% CNT in Al matrix, tensile strength of the composite improved by 11.35% and 27.23%, respectively, and decreased with 7.36% with addition of 0.2 wt% CNT as compared to 0.0 wt% CNT as reported by UTM machine.
3. With the addition of 0.1 wt% CNT, 0.15 wt% CNT, and 0.2 wt% CNT, the hardness of the composite was increased by 25.95%, 33.6%, and 13.67%, respectively, with respect to Al-0 wt% CNT.
4. With the addition of 0.1 wt% CNT, the composite has become ductile. Further addition of CNTs has resulted in brittleness of the material [8].

**Acknowledgements** This work has been supported by Lovely Professional University, Phagwra, Punjab, India. Moreover, we would like to thank IIT Ropar and CIPET Amritsar for their help and coordination throughout the research. Special thanks to Vaibhav Rajendra Nanaware for his tremendous help and support.

## References

1. Basak, A.K., Pramanik, A., Prakash, C.: Deformation and strengthening of SiC reinforced Al-MMCs during in-situ micro-pillar compression. *Mater. Sci. Eng. A.* **763**, 138141 (2019)
2. Uddin, M., Basak, A., Pramanik, A., Singh, S., Krolczyk, G.M., Prakash, C.: Evaluating hole quality in drilling of Al 6061 alloys. *Mater.* **11**, 2443 (2018)



3. Prakash, C., Singh, S., Sharma, S., Garg, H., Singh, J., Kumar, H., Singh, G.: Fabrication of aluminium carbon nano tube silicon carbide particles based hybrid nano-composite by spark plasma sintering. *Mater. Today Proc.* **21**, 1637–1642 (2020)
4. Manjunatha, L.H., Dinesh, P.: Fabrication, microstructure, hardness and wear properties of Extruded MWCNT reinforced with 6061 Al metal matrix composites. *ARPN J. Eng. Appl. Sci. Int. J. Sci. Eng. Res.* **4**(4), 974–990 (2013)
5. Laha, T., Chen, Y., Lahiri, D., Agarwal, A.: Tensile properties of carbon nanotube reinforced aluminum nanocomposite fabricated by plasma spray forming. *Compos. Part A Appl. Sci. Manuf.* **40**(5), 589–594 (2009)
6. Tiwari, S.K., Midathada, A., Sharma, S., Ravella, U.K.: Study of fabrication processes and properties of Al-CNT composites reinforced by carbon nano tubes—a review. *Mater. Today Proc.* **5**(14), 28262–28270 (2018)
7. Tiwari, S.K., Sharma, H., Deepmala, K.M., Chamola, R.: Characterization of mechanical properties of Al-B4C composite fabricated by stir casting
8. Tiwari, S.K., Sharma, S.: Synthesis and characterization of mechanical properties of carbon nanotubes reinforced aluminium composite. Doctoral dissertation, Lovely Professional University (2017)
9. Sharma, H., Tiwari, S.K., Deepmala, K., Gupta, A.: Investigation of mechanical and tribological properties of the Al7075-B4C composite fabricated by friction stir processing
10. Abbasipour, B., Niroumand, B., Vaghefi, S.M.: Compcasting of A356-CNT composite. *Trans. Nonferrous Met. Soc. China* **20**(9), 1561–1566 (2010)
11. Narayanan, S.S., Manickavasaham, G., Moorthy, S.: Experimental investigation of aluminium alloy with MWCNT composite to increase the technical properties by stir casting method. *IOSR J. Mech. Civ. Eng. (IOSRYJMCE)* **12**(4) (2015). eYISSN: 2278Y1684, pY ISSN: 2320Y334X
12. Esawi, A.M., Morsi, K., Sayed, A., Gawad, A.A., Borah, P.: Fabrication and properties of dispersed carbon nanotube–aluminum composites. *Mater. Sci. Eng. A* **508**(1–2), 167–173 (2009)
13. Tiwari, S.K., Sharma, H., Deepmala, K.M., Umamaheswararao, A.: Investigation of mechanical and tribological properties of aluminum composite reinforced by boron carbide, silicon carbide and carbon nanotubes (2019)
14. Mansoor, M., Shahid, M.: JART-78 1–10 (2016)
15. Sentharamaia, K., Marimuthub, P.: Experimental investigation on microstructure and mechanical behaviour of stir cast metal matrix composite AA6061 with MWCNT. *Int. J. Adv. Eng. Tech.* **VII**(II), 1115, 1117 (2016)
16. Senthil Kumar, P.B., Hushein, R., Logesh, K., Inbarasan, K.: *IJMET* **8**(8), 1383–1400 (2017)
17. Mansoor, M., Shahid, M.: Carbon nanotube-reinforced aluminum composite produced by induction melting. *J. Appl. Res. Technol.* **14**(4), 215–224 (2016)

# Effect of TiC Reinforcement in the Copper Tool on Roundness During EDM Process



Arminder Singh Walia, Vineet Srivastava, Vivek Jain,  
and Suneev Anil Bansal 

**Abstract** In the present work, a copper (Cu) tool, reinforced with titanium carbide (TiC) particles, synthesized using powder metallurgy, is used to machine EN31 die steel using EDM machining. Various parameters were selected as process parameters to study tool shape as response. RSM was used to design the experiments and 52 experiments performed. The shape of tool was studied in terms of roundness of tool. Change in roundness of tool was analysed by analysis of variance and regression. Results revealed current and pulse on/off most significant parameters. Roundness value rose with increase in discharge current. On the other hand, it fell with rise in time of pulse on/off. Profile of tool and shape of tool were investigated by scanning electron microscopy (SEM). Comparison of Cu-TiC with Cu tooltip was performed to understand the effect cermet tooltip. The comparison of results showed that Cu-TiC tool was reduced out of roundness by 25%.

**Keywords** EDM · Discharge current · Out of roundness · Pulse on/off time

## 1 Introduction

There is a perception in machining to use right tool for the job. A right tool for machining operation is the first step in success of any machining operation. The selection of cutting tool material depends on the work material and the operation to be performed. Often, there are possible choices of tool materials that will produce the parts successfully but not cost-effectively. Copper (Cu) is preferred tool material for EDM owing its superior electrical and thermal properties, but low melting point of copper enhances wear rate of electrode that leads to change in shape of tool. Titanium

---

A. S. Walia · V. Srivastava · V. Jain  
Department of Mechanical Engineering, Thapar Institute of Engineering & Technology, Patiala  
147004, India

S. A. Bansal (✉)  
Department of Mechanical Engineering, MAIT, Maharaja Agrasen University,  
Baddi, H.P. 174103, India  
e-mail: [suneev@gmail.com](mailto:suneev@gmail.com)

© Springer Nature Singapore Pte Ltd. 2020  
C. Prakash et al. (eds.), *Advances in Materials Science and Engineering*,  
Lecture Notes in Mechanical Engineering,  
[https://doi.org/10.1007/978-981-15-4059-2\\_10](https://doi.org/10.1007/978-981-15-4059-2_10)

and titanium carbide (TiC) have been successfully used as reinforcement material for copper [1–3].

For the fabrication of tool, many methods have been used. Geometry consideration and level of precision commonly determine the manufacturing cost and fabrication technique for fabrication of the electrodes. The conventional methods take more processing time, and the wastage of material is also more, especially during the fabrication of complex shape tool profiles. For complicated shapes, machining, electro-forming, casting, rapid prototyping or powder metallurgy (PM) can be used to synthesize electrode [4–6]. Rather in PM, there was better control of the properties of the final product [7].

Khanra et al. [8] obtained wear resistance by varying the percentage of Cu with  $ZrB_2$ . The tool removal rate was lesser for the composite tool compared to Cu tool; however, higher diametral overcut was recorded for the composite tool. Samuel and Philip [9] concluded that it was easier to synthesize and control properties using PM technique to fabricate tool. The compaction at lower pressure and sintering at lower temperature resulted in higher electrode wear. Li et al. [10] fabricated the tool by adding TiC to copper powder. The densification of the pellets obtained after sintering and nickel powder was used to improve it. The composites with 15% TiC obtained minimum electrical resistivity, highest relative density and maximum MRR. Singh et al. [11] investigated performance of tool electrodes during the machining of EN31 steel. The diametral overcut was maximum with Cu-Ti electrode due to larger spark dispersion. Higher material removal rates were obtained with high discharge current with aluminium and copper electrodes followed by copper–tungsten electrode. Very less tool wear was exhibited by copper, and copper–tungsten tools succeeded by aluminium tool. Brass tool showed the highest tool wear.

Copper–tungsten, copper–graphite and graphite tools were used by Janmanee and Muttamara [12] during the machining of WC–cobalt using EDM. Higher energy available at higher current resulted in increased tool wear rate compared to lower current values. The electrodes produced by powder metallurgy resulted in lower tool wear rate and higher MRR. Srivastava and Pandey [13] investigated results of Cu–TiC tool and Cu tool during EDM under cryogenic conditions. Cu–TiC tool showed little changes in tool geometry. Balasubramanian and Senthilvelan [14] employed cast and sintered PM tool for EDM. The cast tool improved MRR and decreased tool wear ratio.

Pal and Choudhry [15] drilled holes using Cu and brass tool fabricated by abrasive water jet machining. Dimensional inaccuracies were observed between the tool size and profile obtained on the workpiece. The reasons cited for the inaccuracies were the instinctive property of abrasive water jet machining jet which produced kerf on the fin length and machining of the sidewalls of the blind cavities due to the absence of masking on the tool sides. Alloys ( $Ti_{50}Ni_{50}$ ,  $Ti_{50}Ni_{49.5}Mo_{0.5}$  and  $Ti_{30}Nb_{1}Fe_{1}Hf$ ) used for biomedical implant applications were machined by Hseih et al. [16] using pure titanium electrode in the EDM process. EDM of Al–Si–C was done by Satpathy

et al. [17]. Walia et al. [18] used graphite, SiC and TiC materials for the fabrication of tooltip for the EDM process. The tooltip with 75Cu–25TiC showed the highest hardness and relative density with acceptable electrical and thermal conductivity.

Composites tools have been used in EDM process [19, 20], but there is little work related to the development of model predicting tool shape for the tooltip in EDM process. There is only one study [13] available where the shape profile of the tool has been evaluated. The study of shape of the tool has been done. In the present work, a Cu–TiC was synthesized using powder metallurgy. EDM tool synthesized was used to machine EN31 to understand effect on geometry of tool.

## 2 Experimental Studies

### 2.1 *Cermet Tooltip Electrode*

EN31 die steel was cut into pieces of  $15 \times 15 \times 6 \text{ mm}^3$ . Workpieces' heat treatment increased from hardness 20 HRC to 56 HRC. The purpose treatment process was to increase hardness that is difficult to machine by conventional machining.

The cermet tooltip was prepared by the mixture of copper powder (99.9 wt% particle size  $44 \mu\text{m}$ ) and TiC powder (99 wt% particle size  $44 \mu\text{m}$ ). Tool material was copper due to its higher thermal and electrical conductivity. TiC was added as reinforcement due to its admirable hardness and wear characteristics. Copper powder was mixed with TiC in a V-shape blender to prepare the composite powder. The pellets were prepared by the cold compaction of composite powder uniaxially in a hydraulic press at a load of 12 t (1238.73 MPa) in a tungsten carbide die. The sintering of pellets was done in a tubular furnace in inert (argon) gas atmosphere at  $1000 \text{ }^\circ\text{C}$  for 1 h.

The hardness of the sintered tool was 127 HV, whereas copper tool was 65 HV. The prepared pellets were polished and brazed to the copper rod to fabricate the cermet tooltip tool (Fig. 1).

### 2.2 *Process Parameter: Implications and Selection*

The performance of EDM process on steels is deeply influenced by various parameters [21, 22]. The range of these process parameters and their level had been chosen based on the machine capability, exploratory pilot experiments (Table 1).

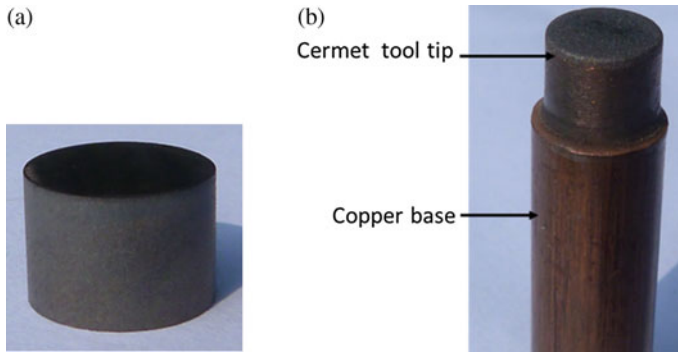


**Fig. 1** Digital photograph of cermet tool **a** tip of tool and **b** full electrode with cermet tip

**Table 1** Process levels design and variation levels

Levels	Discharge current, $I_p$ (A)	Gap voltage, $V_g$ (V)	Pulse on time, $T_{on}$ ( $\mu s$ )	Pulse off time, $T_{off}$ ( $\mu s$ )	Dielectric pressure, $P$ ( $kgf/cm^2$ )
-2	3	40	100	10	12
-1	5	50	200	20	14
0	7	60	300	30	16
1	9	70	400	40	18
2	11	80	500	50	20

### 2.3 Planning of Experiments

Based on RSM, the experiments were conducted [23]. For the five sets of process variables, 52 experimental were conducted. Out of roundness was selected as response variable to represent the shape of the tool. Die sinking EDM (RELIABLE, 55300) was used to carry out the experiments. EDM oil (flash point 90 °C) was used as dielectric. Machining was performed for 30 min for all the experiments. Change in the shape of the tool was determined by measuring the out of roundness of the tool before and after machining. The experiments were performed according to design of experiment, and the results for the out of roundness were measured. CMM (Accurate, model Spectra 564) was used for the measurement of the out of roundness. Data was analysed using Accusoft.

### 3 Analysis of Experimental Data and Modelling of Response Variable

In this work, a statistical model for out of roundness was obtained by analyzing the experimental results. Effect of process parameters on the selected response variable was assessed. After initial elimination, the equation for the model has been established as Eq. (1).

$$\begin{aligned}
 \text{OOR} = & -0.0078 + (0.00303 \times I_p) - (0.000048 \times V_g) + (0.000122 \times T_{on}) \\
 & - (0.0004 \times T_{off}) - (0.00057 \times P) + (0.00019 \times I_p^2) + (0.000003 \times T_{off}^2) \\
 & - (0.000025 \times I_p \times V_g) - (0.000004 \times I_p \times T_{on}) - (0.000021 \times I_p \times T_{off}) \\
 & - (0.000001 \times V_g \times T_{on}) + (0.000032 \times V_g \times P) + (0.000001 \times T_{on} \times T_{off}) \\
 & - (0.000005 \times T_{on} \times P)
 \end{aligned} \tag{1}$$

ANOVA was used to understand the effect of parameters [24]. The predicted *F*-ratio (135.86) was compared with the standard *F*-ratio (3.45) at intervals. Further, the *F*-value of lack of fit for the specified degree of freedom (1.42) was analysed with the standard *F*-value for the degree of freedom (3.19). It was concluded that the quadratic model was adequate. *R*<sup>2</sup> (98.1%) represents relation of response with selected independent parameters. From Fig. 2a, it can be clearly observed that *I* and

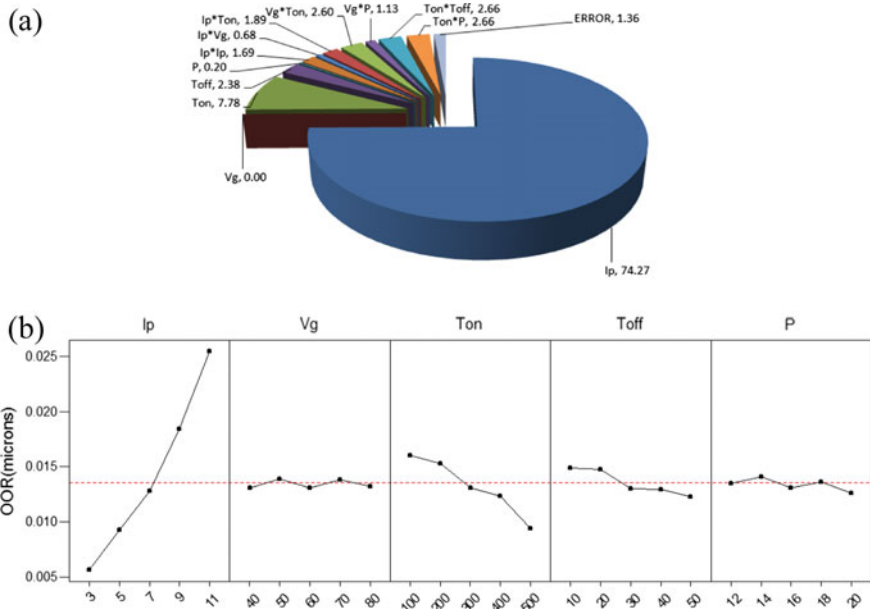
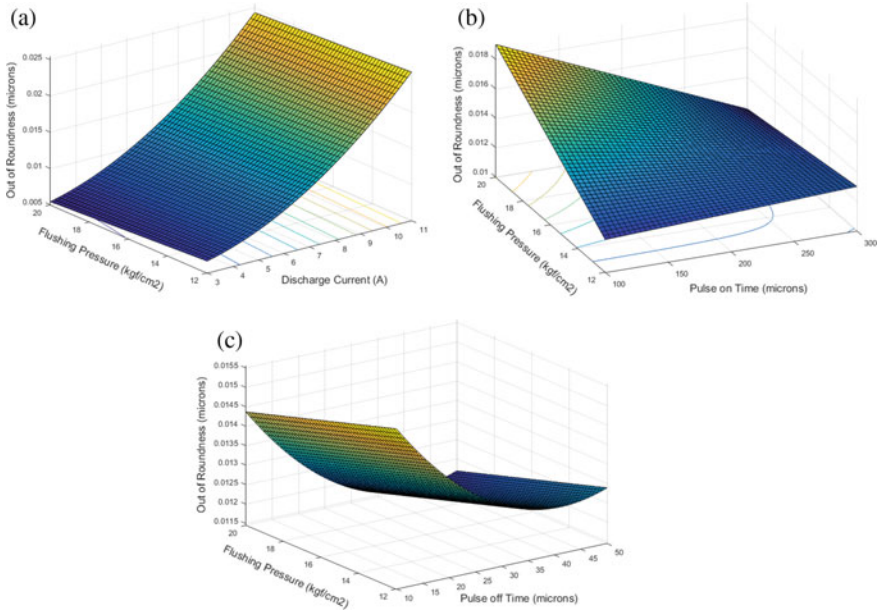


Fig. 2 a Out of roundness: effect of various parameters. b Main effects plots for out of roundness



**Fig. 3** Roundness variation by varying **a** current, **b** pulse on and **c** off time

$T_{on/off}$  time were significantly affecting the out of roundness. Figure 2b shows that out of roundness increased with  $I$  and decreased with increase in  $T_{on/off}$  time. It can be concluded from Fig. 2a and b,  $V_g$  and  $P$  do not contribute in out of roundness. Figure 3 shows the influence of  $I$  and  $T_{on/off}$  time on out of roundness.

### 4 Optimization of Process and Precision

The confidence interval is given  $Z \pm \Delta Z$ , where  $\Delta Z$  is given by

$$\Delta Z = t_{\alpha/2, DOF} \sqrt{V_{err}} \tag{2}$$

where ‘Z’ response, out of roundness; ‘t’  $t$ -distribution to DOF; ‘ $\alpha$ ’ confidence level and ‘ $V_{err}$ ’ predicted response variance of error.  $\alpha$  is considered as 0.001 and  $\Delta OOR$  calculated as 0.0024 mm (Table 2). An attempt was made to optimize the machining parameters to minimize the out of roundness within the specified range. The values of the parameters were found by applying trust-region approach. The optimization was carried out by optimization *fmincon*. Table 3 shows optimum set of parameters.

**Table 2** Confirmation experiments

Exp. No.	Machining parameters					OOR (mm)	
	$I_p$	$V_g$	$T_{on}$	$T_{off}$	$P$	Exp.	Predicted
1	4	45	150	15	13	0.0065	$0.0071 \pm 0.0024$
2	6	45	350	35	13	0.0118	$0.0129 \pm 0.0024$
3	8	55	250	25	15	0.0155	$0.0167 \pm 0.0024$
4	10	65	350	45	17	0.0177	$0.0184 \pm 0.0024$
5	10	75	450	45	19	0.0138	$0.0132 \pm 0.0024$

**Table 3** Optimum process parameters

Response	$I_p$	$V_g$	$T_{on}$	$T_{off}$	$P$	Calculated (mm)	Exp. (mm)
Minimum OOR	4	40	170	50	14	0.0025	$0.0013 \pm 0.0024$

## 5 Comparison

Tool's out of roundness was investigated for both Cu and cermet tooltip. At least 12 points were identified on the circumference of each sample, as shown in Fig. 4. Difference in roundness of the tool before and after EDM was termed as response. It is evident from Fig. 4 that the change in roundness was more in the case of Cu (0.032 mm) as compared to the cermet tool (0.026 mm).

Change in cermet tooltip roundness values was lesser compared to Cu tool (Fig. 5). The TiC present in cermet improved wear resistance that prompted stable tool geometry. Stability of enhancement in tool shape varied from 9% (experiment 10) to 25% (experiment 1). Therefore, it can be concluded that the shape retention is better in cermet tools that are also evident from the SEM images shown in Fig. 6.

## 6 Conclusions

- Cu–TiC cermet tooltip was successfully produced by powder metallurgy process followed by sintering. EDM tool was fabricated from cermet tooltips brazed to the copper rods.
- Comparison of performance was made for copper–TiC tooltips at different process parameters with conventional tool.
- Out of roundness was chosen as a criteria to measure tool shape changes, and statistical model was developed to estimate roundness in EDM process using cermet tooltip by correlating the selected input parameters.
- The adequacy of the model was checked with ANOVA. Developed statistical analysed effect of each parameter on out of roundness.



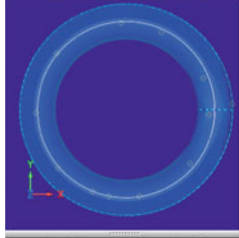
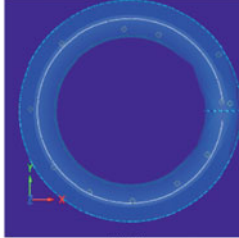
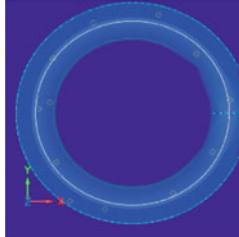
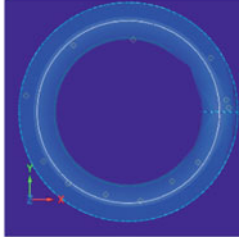
	OUT OF ROUNDNESS BEFORE MACHINING	OUT OF ROUNDNESS AFTER MACHINING	CHANGE																																																								
Copper TOOL TIP	 <table border="1"> <thead> <tr> <th></th> <th>Mea</th> <th>Nom</th> <th>Dev</th> </tr> </thead> <tbody> <tr> <td>X</td> <td>196.9330</td> <td>196.9330</td> <td>0.0000</td> </tr> <tr> <td>Y</td> <td>176.0468</td> <td>176.0468</td> <td>0.0000</td> </tr> <tr> <td>Z</td> <td>110.7446</td> <td>110.7446</td> <td>0.0000</td> </tr> <tr> <td>DIAM</td> <td>9.9978</td> <td>9.9978</td> <td>0.0000</td> </tr> <tr> <td>CIRLTY</td> <td>0.0599</td> <td>0.0000</td> <td>0.0599</td> </tr> <tr> <td>SIGMA</td> <td>0.0192</td> <td>0.0000</td> <td>0.0192</td> </tr> </tbody> </table>		Mea	Nom	Dev	X	196.9330	196.9330	0.0000	Y	176.0468	176.0468	0.0000	Z	110.7446	110.7446	0.0000	DIAM	9.9978	9.9978	0.0000	CIRLTY	0.0599	0.0000	0.0599	SIGMA	0.0192	0.0000	0.0192	 <table border="1"> <thead> <tr> <th></th> <th>Mea</th> <th>Nom</th> <th>Dev</th> </tr> </thead> <tbody> <tr> <td>X</td> <td>196.9330</td> <td>196.9330</td> <td>0.0000</td> </tr> <tr> <td>Y</td> <td>176.0468</td> <td>176.0468</td> <td>0.0000</td> </tr> <tr> <td>Z</td> <td>110.7446</td> <td>110.7446</td> <td>0.0000</td> </tr> <tr> <td>DIAM</td> <td>9.9978</td> <td>9.9978</td> <td>0.0000</td> </tr> <tr> <td>CIRLTY</td> <td>0.0599</td> <td>0.0000</td> <td>0.0599</td> </tr> <tr> <td>SIGMA</td> <td>0.0192</td> <td>0.0000</td> <td>0.0512</td> </tr> </tbody> </table>		Mea	Nom	Dev	X	196.9330	196.9330	0.0000	Y	176.0468	176.0468	0.0000	Z	110.7446	110.7446	0.0000	DIAM	9.9978	9.9978	0.0000	CIRLTY	0.0599	0.0000	0.0599	SIGMA	0.0192	0.0000	0.0512	0.032 mm
	Mea	Nom	Dev																																																								
X	196.9330	196.9330	0.0000																																																								
Y	176.0468	176.0468	0.0000																																																								
Z	110.7446	110.7446	0.0000																																																								
DIAM	9.9978	9.9978	0.0000																																																								
CIRLTY	0.0599	0.0000	0.0599																																																								
SIGMA	0.0192	0.0000	0.0192																																																								
	Mea	Nom	Dev																																																								
X	196.9330	196.9330	0.0000																																																								
Y	176.0468	176.0468	0.0000																																																								
Z	110.7446	110.7446	0.0000																																																								
DIAM	9.9978	9.9978	0.0000																																																								
CIRLTY	0.0599	0.0000	0.0599																																																								
SIGMA	0.0192	0.0000	0.0512																																																								
	Out of Roundness = 0.0192 mm	Out of Roundness = 0.0512 mm																																																									
CERMET TOOL TIP	 <table border="1"> <thead> <tr> <th></th> <th>Mea</th> <th>Nom</th> <th>Dev</th> </tr> </thead> <tbody> <tr> <td>X</td> <td>194.7618</td> <td>194.7618</td> <td>0.0000</td> </tr> <tr> <td>Y</td> <td>178.1486</td> <td>178.1486</td> <td>0.0000</td> </tr> <tr> <td>Z</td> <td>110.7119</td> <td>110.7119</td> <td>0.0000</td> </tr> <tr> <td>DIAM</td> <td>10.0060</td> <td>10.0060</td> <td>0.0000</td> </tr> <tr> <td>CIRLTY</td> <td>0.0585</td> <td>0.0000</td> <td>0.0585</td> </tr> <tr> <td>SIGMA</td> <td>0.0206</td> <td>0.0000</td> <td>0.0206</td> </tr> </tbody> </table>		Mea	Nom	Dev	X	194.7618	194.7618	0.0000	Y	178.1486	178.1486	0.0000	Z	110.7119	110.7119	0.0000	DIAM	10.0060	10.0060	0.0000	CIRLTY	0.0585	0.0000	0.0585	SIGMA	0.0206	0.0000	0.0206	 <table border="1"> <thead> <tr> <th></th> <th>Mea</th> <th>Nom</th> <th>Dev</th> </tr> </thead> <tbody> <tr> <td>X</td> <td>194.7618</td> <td>194.7618</td> <td>0.0000</td> </tr> <tr> <td>Y</td> <td>178.1486</td> <td>178.1486</td> <td>0.0000</td> </tr> <tr> <td>Z</td> <td>110.7119</td> <td>110.7119</td> <td>0.0000</td> </tr> <tr> <td>DIAM</td> <td>10.0060</td> <td>10.0060</td> <td>0.0000</td> </tr> <tr> <td>CIRLTY</td> <td>0.0585</td> <td>0.0000</td> <td>0.0585</td> </tr> <tr> <td>SIGMA</td> <td>0.0466</td> <td>0.0000</td> <td>0.0466</td> </tr> </tbody> </table>		Mea	Nom	Dev	X	194.7618	194.7618	0.0000	Y	178.1486	178.1486	0.0000	Z	110.7119	110.7119	0.0000	DIAM	10.0060	10.0060	0.0000	CIRLTY	0.0585	0.0000	0.0585	SIGMA	0.0466	0.0000	0.0466	0.026 mm
	Mea	Nom	Dev																																																								
X	194.7618	194.7618	0.0000																																																								
Y	178.1486	178.1486	0.0000																																																								
Z	110.7119	110.7119	0.0000																																																								
DIAM	10.0060	10.0060	0.0000																																																								
CIRLTY	0.0585	0.0000	0.0585																																																								
SIGMA	0.0206	0.0000	0.0206																																																								
	Mea	Nom	Dev																																																								
X	194.7618	194.7618	0.0000																																																								
Y	178.1486	178.1486	0.0000																																																								
Z	110.7119	110.7119	0.0000																																																								
DIAM	10.0060	10.0060	0.0000																																																								
CIRLTY	0.0585	0.0000	0.0585																																																								
SIGMA	0.0466	0.0000	0.0466																																																								
	Out of Roundness = 0.0206 mm	Out of Roundness = 0.0466 mm																																																									

Fig. 4 Out of roundness at:  $I_p = 11$  A,  $V_g = 60$  V,  $T_{on} = 300 \mu s$ ,  $T_{off} = 30 \mu s$ ,  $P = 20$  kgf/cm<sup>2</sup>

- The experimental results pointed that discharge current, pulse on/off time vital parameters that influences out of roundness.
- To prove the sufficiency of developed model for 99.9% confidence interval, confirmation experiments were done at different process parameter conditions using copper–TiC cermet tooltip.
- The comparison of results showed up to 25% reduction in out of roundness for while using Cu–TiC.

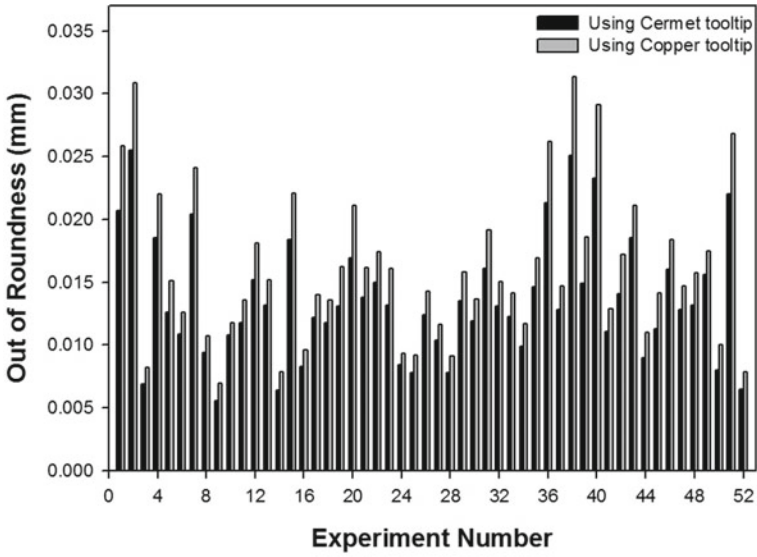


Fig. 5 Comparison of out of roundness when using copper tooltip and cermet tooltip

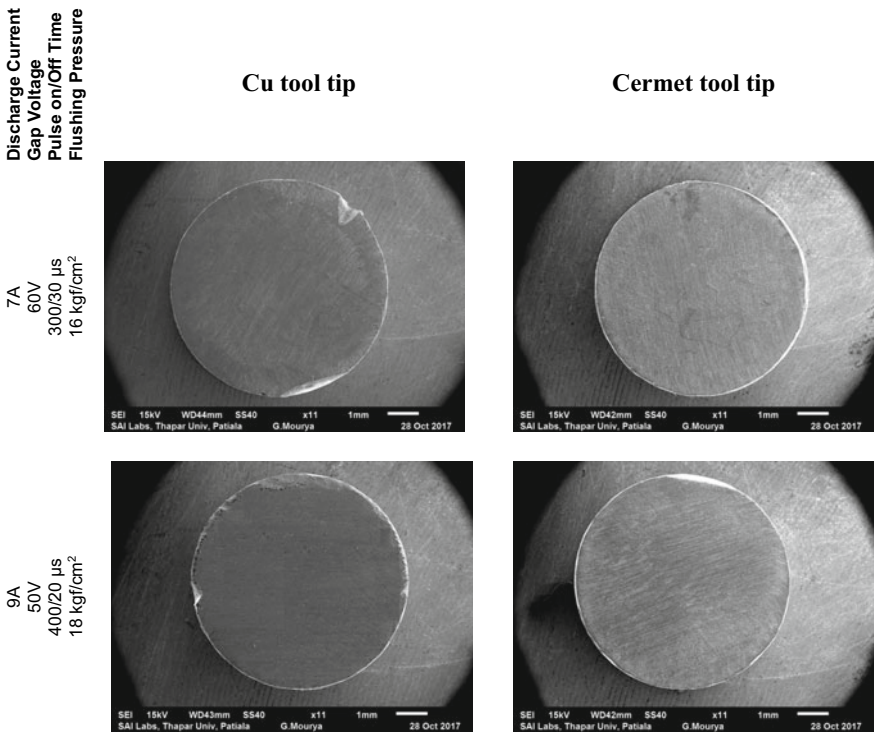


Fig. 6 Morphology of cermet and Cu tooltips at various process parameters of machining

## References

1. Li, L., Wong, Y.S., Fuh, J.Y.H., Lu, L.: EDM performance of TiC/copper-based sintered electrodes. *Mater. Des.* **22**, 669–678 (2001)
2. Kumar, P.M., Sivakumar, K., Jayakumar, N.: Multiobjective optimization and analysis of copper–titanium diboride electrode in EDM of monel 400<sup>TM</sup> alloy. *Mater. Manuf. Process.* **33**, 1429–1437 (2018). <https://doi.org/10.1080/10426914.2017.1415439>
3. Walia, A.S., Srivastava, V., Jain, V.: Impact of copper-titanium carbide tooltip on machined surface integrity during Electrical Discharge Machining of EN31 steel. *Mater. Res. Express.* (2019). <https://doi.org/10.1088/2053-1591/ab3ac4>
4. Zaw, H.M., Fuh, J.Y.H., Nee, A.Y.C., Lu, L.: Formation of a new EDM electrode material using sintering techniques. *J. Mater. Process. Technol.* **89**, 182–186 (1999)
5. Dimla, D.E., Hopkinson, N., Rothe, H.: Investigation of complex rapid EDM electrodes for rapid tooling applications. *Int. J. Adv. Manuf. Technol.* **23**, 249–255 (2004)
6. Singh, M., Singh, S.: Electrochemical discharge machining: a review on preceding and perspective research. *Proc. Inst. Mech. Eng. Part B J. Eng. Manuf.* **233**, 1425–1449 (2019). <https://doi.org/10.1177/0954405418798865>
7. Valarmathi, T.N., Sekar, S., Anthony, G., Suresh, R., Balan, K.N.: Experimental studies on surface roughness of H12 tool steel in EDM using different tool materials. In: *Innovative Design, Analysis and Development Practices in Aerospace and Automotive Engineering (I-DAD 2018)*, pp. 241–247. Springer, Berlin (2019)
8. Khanra, A.K., Sarkar, B.R., Bhattacharya, B., Pathak, L.C., Godkhindi, M.M.: Performance of ZrB<sub>2</sub>–Cu composite as an EDM electrode. *J. Mater. Process. Technol.* **183**, 122–126 (2007)
9. Samuel, M.P., Philip, P.K.: Power metallurgy tool electrodes for electrical discharge machining. *Int. J. Mach. Tools Manuf.* **37**, 1625–1633 (1997)
10. Li, L., Wong, Y.S., Fuh, J.Y.H., Lu, L.: Effect of TiC in copper–tungsten electrodes on EDM performance. *J. Mater. Process. Technol.* **113**, 563–567 (2001)
11. Singh, S., Maheshwari, S., Pandey, P.C.: Some investigations into the electric discharge machining of hardened tool steel using different electrode materials. *J. Mater. Process. Technol.* **149**, 272–277 (2004)
12. Janmanee, P., Muttamara, A.: Performance of difference electrode materials in electrical discharge machining of tungsten carbide. *Energy Res. J.* **1**, 87–90 (2010). <https://doi.org/10.3844/erjssp.2010.87.90>
13. Srivastava, V., Pandey, P.M.: Study of ultrasonic assisted cryogenically cooled EDM process using sintered (Cu–TiC) tooltip. *J. Manuf. Process.* **15**, 158–166 (2013)
14. Balasubramanian, P., Senthilvelan, T.: Optimization of machining parameters in EDM process using cast and sintered copper electrodes. *Procedia Mater. Sci.* **6**, 1292–1302 (2014)
15. Pal, V.K., Choudhury, S.K.: Fabrication of texturing tool to produce array of square holes for EDM by abrasive water jet machining. *Int. J. Adv. Manuf. Technol.* **85**, 2061–2071 (2016). <https://doi.org/10.1007/s00170-015-7875-7>
16. Hsieh, S.-F., Lin, M.-H., Chen, S.-L., Ou, S.-F., Huang, T.-S., Zhou, X.-Q.: Surface modification and machining of TiNi/TiNb-based alloys by electrical discharge machining. *Int. J. Adv. Manuf. Technol.* **86**, 1475–1485 (2016). <https://doi.org/10.1007/s00170-015-8257-x>
17. Satpathy, A., Tripathy, S., Senapati, N.P., Brahma, M.K.: Optimization of EDM process parameters for AlSiC-20% SiC reinforced metal matrix composite with multi response using TOPSIS. *Mater. Today Proc.* **4**, 3043–3052 (2017)
18. Walia, A.S., Jain, V., Srivastava, V.: Development and performance evaluation of sintered tool tip while EDMing of hardened steel. *Mater. Res. Express.* **6**, 086520 (2019). <https://doi.org/10.1088/2053-1591/ab1c7a>
19. Prakash, C., Singh, S., Pruncu, C.I., Mishra, V., Królczyk, G., Pimenov, D.Y., Pramanik, A.: Surface modification of Ti-6Al-4V alloy by electrical discharge coating process using partially sintered Ti-Nb electrode. *Mater.* **12**, 1006 (2019)

20. Czelusniak, T., Higa, C.F., Torres, R.D., Laurindo, C.A.H., de Paiva Júnior, J.M.F., Lohrengel, A., Amorim, F.L.: Materials used for sinking EDM electrodes: a review. *J. Braz. Soc. Mech. Sci. Eng.* **41**, 14 (2019). <https://doi.org/10.1007/s40430-018-1520-y>
21. Wu, K.L., Yan, B.H., Huang, F.Y., Chen, S.C.: Improvement of surface finish on SKD steel using electro-discharge machining with aluminum and surfactant added dielectric. *Int. J. Mach. Tools Manuf.* **45**, 1195–1201 (2005)
22. Lin, Y.-C., Cheng, C.-H., Su, B.-L., Hwang, L.-R.: Machining characteristics and optimization of machining parameters of SKH 57 high-speed steel using electrical-discharge machining based on Taguchi method. *Mater. Manuf. Process.* **21**, 922–929 (2006)
23. Prakash, C., Kansal, H.K., Pabla, B.S., Puri, S.: Multi-objective optimization of powder mixed electric discharge machining parameters for fabrication of biocompatible layer on  $\beta$ -Ti alloy using NSGA-II coupled with Taguchi based response surface methodology. *J. Mech. Sci. Tech.* **30**, 4195–4204 (2016)
24. Prakash, C., Singh, S., Singh, M., Verma, K., Chaudhary, B., Singh, S.: Multi-objective particle swarm optimization of EDM parameters to deposit HA-coating on biodegradable Mg-alloy. *Vacuum* **158**, 180–190 (2018)

# Mechanical and Microstructural Characterization of Magnesium/Multi-walled Carbon Nanotubes Composites Fabricated via Friction Stir Processing



Mayank Mishra, Chander Prakash, Rajashekhara Shabadi,  
and Subhash Singh

**Abstract** The need for new generation high-performance lightweight materials for automotive and aerospace applications has gripped manufacturers and engineers around the world to enhance the strength-to-weight ratio and fuel efficiency of the vehicles, thus improving the economics of mass production and novel product development processes. Metal matrix reinforced with nanoparticles has tremendously risen in the strength of the composite material by effectively carrying out load transfer between reinforcement and parent matrix metal. In this research work, magnesium and various volume percentage of multi-walled carbon nanotubes were fabricated via friction stir processing (FSP) and the significant influence of addition of multi-walled carbon nanotubes into pure magnesium was examined. The microstructural features, mechanical behaviours such as tensile strength, were investigated. The X-ray diffraction (XRD) analysis has confirmed the presence of parent phases of materials without any reactive phases. The optimum increase in the tensile strength of the composite material was obtained to be 203% more than that of cast pure magnesium at 20 vol.% MWCNT reinforcement.

**Keywords** Pure magnesium · Multi-walled carbon nanotubes · X-ray diffraction · Scanning electron microscope · Friction stir processing

---

M. Mishra · S. Singh (✉)

Department of Production & Industrial Engineering, National Institute of Technology  
Jamshedpur, Jamshedpur, Jharkhand 831014, India  
e-mail: [Subh802004@gmail.com](mailto:Subh802004@gmail.com)

C. Prakash

School of Mechanical Engineering, Lovely Professional University, Phagwara 144411, India

R. Shabadi

Faculty of Science and Technology, University of Lille, Lille, France

© Springer Nature Singapore Pte Ltd. 2020

C. Prakash et al. (eds.), *Advances in Materials Science and Engineering*,

Lecture Notes in Mechanical Engineering,

[https://doi.org/10.1007/978-981-15-4059-2\\_11](https://doi.org/10.1007/978-981-15-4059-2_11)

## 1 Introduction

Composite materials have found a strong footing in almost every sphere of life from household, electronics, electrical, medical, chemical and sports to structure, construction, transportation, marine, military, aviation and heavy-duty industrial applications because of their lightweight, high strength, toughness, durability, energy efficiency and performance [1]. Composites are multiphase materials made up by combining the two or more dissimilar materials having distinct composition, form and properties to produce superior materials without losing their original identities and chemical compositions. Thus, they are not a product of any chemical reaction [2]. They consist of one or more dispersed phases or reinforcements distributed in a continuous medium called matrix where both reinforcements and matrix are separated by interfacial layer. This layer is responsible for effective stress transfer from reinforcements to matrix in composite materials. Composites with specific properties can be prepared by carefully selecting the reinforcement, matrix material, their composition, processing technique and the process conditions. The dispersion, orientation, concentration, properties, size and type of reinforcement are used to determine the properties of the composite [1].

Composites can be broadly classified into natural composites and synthetic composites, as shown in Fig. 1. Examples of natural composites are bone, wood, bamboo and seashell nacre. Synthetic composites are man-made composites that make use of a combination of matrix a reinforcement to derive exact properties. Based on the type of reinforcements, they can be classified as fibre-based and particulate-based composites. Composites are than further grouped into metal, polymer and ceramic composites [3]. Metal matrix composites (MMCs) have helped open newer doors to material utilization and deployment for applications where the primary objective is to obtain a specific property like better creep resistance at elevated temperatures, higher young's modulus, higher tensile and yield strength, enhanced corrosion resistance, increased fatigue strength, biocompatibility. The enhanced properties have pushed to use of light metals like aluminium (Al)and magnesium (Mg) in MMCs [4]. Ever since the invention of an other kind of carbon structure called as carbon nanotube (CNT) by Sumio Iijima in 1991 [5] while studying cathodic soot formed in the arc evaporation apparatus, it has been a subject of immense interest and research

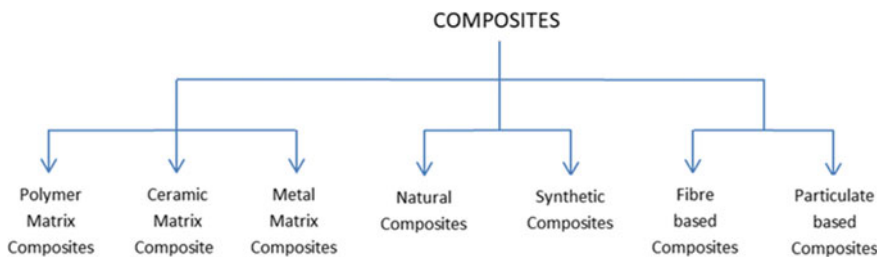


**Fig. 1** Classification of composite materials

in its industrial applications due to the revolutionary mechanical, electrical, thermal, optical and magnetic properties [6, 7]. It was initially discovered in the form of multi-walled carbon nanotube (MWCNT). It is made up of helical coaxial cylinders which consist of 2–50 graphite sheets having diameters spanning between 2 and 100 nm and distance between sheets of about 0.34 nm [8]. Experimental evidences have repeatedly underlined that the carbon nanotube has unique and extraordinary physical properties such as stiffest and strongest fibres. SWCNTs have been proved to have very high Young's modulus in the range of 1 TPa, which is approximately five times that of steel, and very high tensile strength of about 150 GPa [5, 9–11]. Even more impressive is their low density and high aspect ratio. MWCNTs have very high thermal conductivity, greater than  $3000 \text{ W m}^{-1} \text{ K}^{-1}$  at room temperature with low thermal expansion coefficient [12]. CNTs have also demonstrated unique electrical properties [13, 14]. They are excellent electrical conductors possessing electrical conductivity of about  $2 \times 10^7 \text{ S m}^{-1}$  and current densities up to  $10^{11} \text{ Am}^{-2}$ . Depending on the graphitic sheet rolling direction to form the characteristic tubular structure, they can either be metals or semiconductors [15].

Friction stir processing (FSP) is a new kind of solid-state composite processing technique that originated from friction stir welding process. It carries out localized microstructural refinement by plastically deforming the material and not melting them, thus leading to dynamic recrystallization. The resulting material has improved, refined and homogeneous microstructure in the stir zone. This is achieved by employing a rotating tool consisting of a shoulder with pin structure of desired dimensions. The rotating tool is impinged into the surface of material such that only the pin gets dipped into the material and the shoulder only touches the surface providing downward locking force. The friction between the rotating pin and the contact surface of material led to generate high temperature which results in plastic deformation of the material. This is followed by slow and steady translation of the tool along specified direction. If the material is reinforced with fine nano-powders of additives, it will help evenly and homogeneously distribute the additives in the material, thus forming a composite structure. The controllable process parameters which are used in FSP are tool geometry, tool rotation speed, translation speed of the tool, tool tilt angle, axial downward force and number of passes [16–18].

Huang et al. [19] were studied that the addition of carbon nanotubes (CNTs) in Mg-6Zn composites enhanced the grain refinement as well as mechanical properties such as yield strength, ultimate tensile strength; elongation was drastically improved as compared with base alloy. Lim et al. [20] had fabricated aluminium alloy/multi-walled carbon nanotubes through friction stir processing. Scanning electron microscope (SEM) and transmission electron microscope (TEM) micrographs were indicated that the nanotubes are uniformly dispersed into aluminium alloy matrix at the stir zone. The mechanical properties also depend upon the microstructure of the composites. Jamshidijam et al. [21] investigated the microstructural characterization as well as mechanical behaviours such as microhardness and wear properties of the multi-walled carbon nanotubes reinforced into magnesium alloy (AZ31) composite fabricated via friction stir processing. The composites materials exhibited higher microhardness as well as superior resistance to wear compared to as-received alloy.

This is because of uniform dispersion of reinforced material as well as fine grain of matrix. Morisada et al. [22] prepared surface composite by reinforcing CNTs into AZ31 Mg alloy and found it to generate grain refinement and almost twofold increase in the hardness. Singh and Pal [23] were successfully fabricated Al metal matrix composite by incorporating the tailored SiC particles via friction stir processing. Morphology of SiC was changed via addition of MgO as well as nanocrystalline  $\text{MgAl}_2\text{O}_4$  spinel through sol-gel process. It was concluded that ultrafine equiaxed grains were found after FSP. Mechanical properties of the composite materials were significantly improved after FSP. Izadi et al. [24] had investigated uniformly distributed multi-walled carbon nanotube at high-volume fraction (>50%) into aluminium matrix fabricated through multi-pass friction stir processing. SEM and TEM micrographs had confirmed the uniform dispersion of reinforcement. The microhardness of composites showed two times higher than the as-received aluminium alloy. Zhou et al. [25] were studied the thermal expansion response of aluminium/multi-walled carbon nanotube (MWCNT). It was found that it enhanced the load transfer at the interface of the matrix and reinforcement. Aluminium carbide ( $\text{Al}_4\text{C}_3$ ) nanostructure was formed by the heat treatment process, which led to the increasing the yield strength of composites. Liu et al. [17] fabricated CNT/2009Al composite and found that uniform distribution of carbon nanotubes (CNTs) into aluminium matrix through multi-pass friction stir processing (FSP). It was also concluded that maximum strength was obtained after three-pass FSP. The reason is because of the overall influence of cluster reduction, uniform distribution of reinforcement, grain refinement as well as CNT shortening.

It was observed that comparatively lesser amount of research work has been done on magnesium matrix composite and nanocomposite. Thus, pure magnesium was selected as parent metal matrix material with MWCNT reinforcements. The main aim of this research work is to study the effect of large and varying reinforcement of MWCNT in pure magnesium plates on its mechanical properties and phase characteristics. Novel friction stir processing technique is used in place of traditional processes like stir casting and powder metallurgy.

## 2 Materials and Methodology

Magnesium is the lightest structural element. Its density ( $1.738 \text{ g/cm}^3$ ) is two-third of that of aluminium ( $2.7 \text{ g/cm}^3$ ). Pure magnesium billet (Fig. 2a) (purity > 99.8%) of weight 7.5 kg was purchased from Parshwamani Metals, Mumbai, Maharashtra. Multi-walled carbon nanotubes (MWCNTs) of purity > 99%, average diameter of 10–15 nm and average length of about  $5 \mu\text{m}$  were purchased from Ad-Nano Technologies Private Limited, Shivamogga, Karnataka. The tool material was chosen as D3 tool steel (AISI D3) and was purchased from local supplier in Jamshedpur, Jharkhand. The shoulder length of 15 mm and diameter of 18 mm with pin length and diameter of 5.5 and 6 mm were prepared with the aid of centre lathe and drilling machines as shown in Fig. 3. These values were selected after careful literature studies. Pure Mg



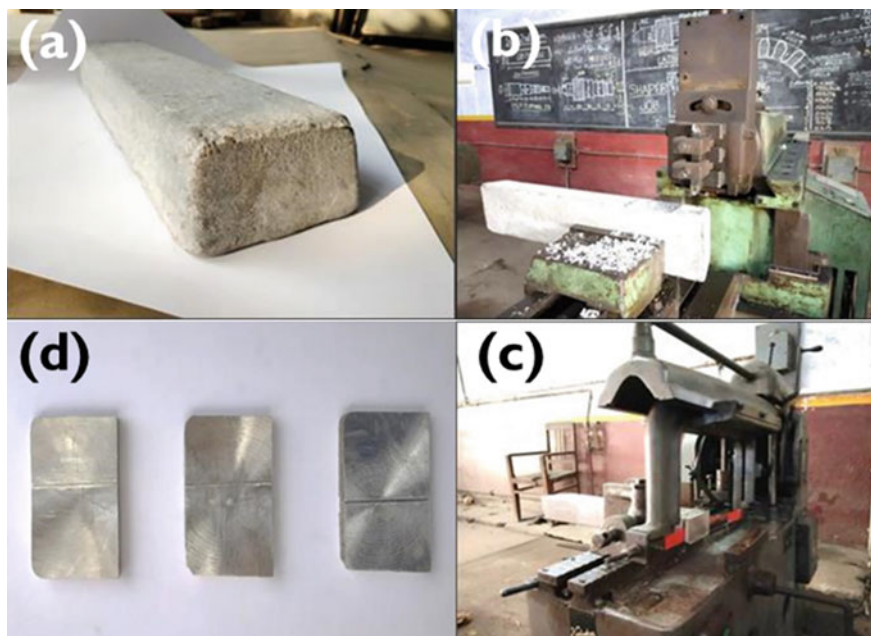


Fig. 2 Steps in making plates from billet of pure magnesium

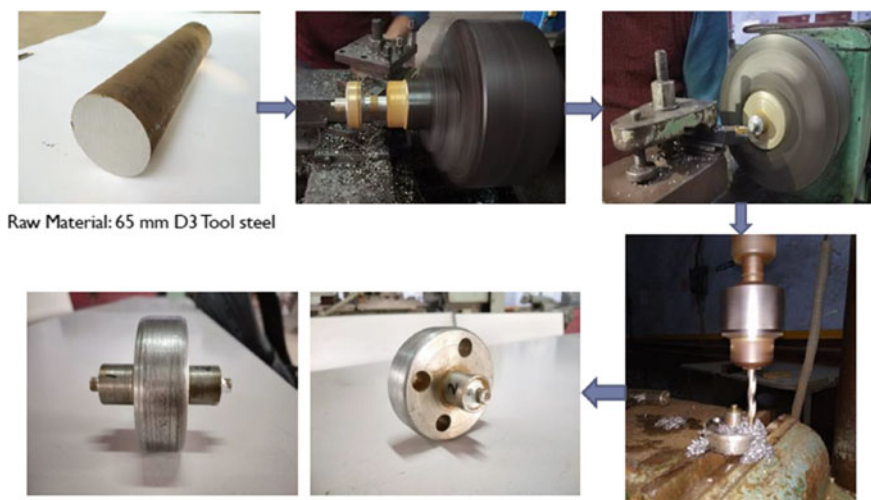
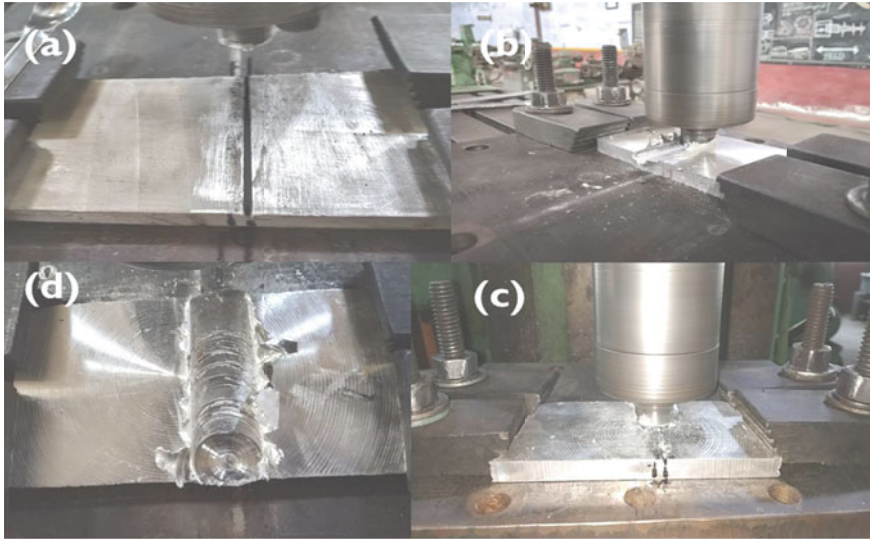


Fig. 3 Tool making procedure



**Fig. 4** Steps in friction stir processing method

plates have thickness 8 mm were cut from the as-received Mg cast billet by using the power hacksaw cutter (Fig. 2b). Also, the edges of the plates were made plane with the help of shaper machine (Fig. 2c). Hence, the size of the plates obtained was 100 mm \* 50 mm \* 8 mm. Then, longitudinal continuous grooves of depths 1 mm, 2 mm and 3 mm were made by shaper machine on three different plates, respectively, each having width of 1 mm, as shown in Fig. 2d. These grooves were parallel to the 50 mm side and were created at approximately the midway of the plate. The FSP tool was first fitted in the collar of the vertical milling machine (VMM), and tighteners were fitted and optimally screwed. The prepared specimen of pure Mg was placed on the bed of the VMM and properly clamped (Fig. 4a). The groove was filled with multi-walled carbon nanotube powder with the help of spatula as shown in Fig. 4b. Then, the friction stir processing (FSP) was carried out with tool rotation velocity of 1000 rpm/min, tool traverse velocity of 10 mm/min and tool tilt angle of 1.5°, as shown in Fig. 4c. The FSP processed finished sample is depicted in Fig. 4d.

### 3 Characterizations

For tensile testing, the FSPed samples were first milled and cut as per ASTM standard into the following shape by the wire-cut electrical discharge machining (EDM) machine, and the dimensions are shown in Fig. 5.

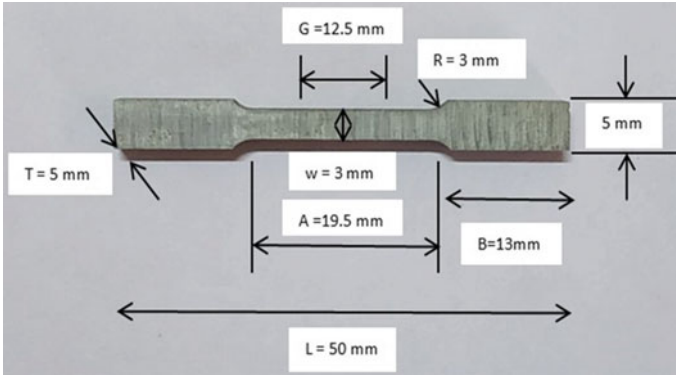


**Fig. 5** Tensile test sample dimensions

Four test samples were prepared.

1. Pure magnesium sample (pure Mg).
2. Friction stir processed pure magnesium sample with 10 vol.% MWCNT (10 MWCNT/Mg).
3. Friction stir processed pure magnesium sample with 20 vol.% MWCNT (20 MWCNT/Mg).
4. Friction stir processed pure magnesium sample with 30 vol.% MWCNT (30 MWCNT/Mg).

The tensile samples were then tested for tensile strength in the universal testing machine (Tinius Olsen, 20 KN). X-ray diffraction (PANalytical Empyrean) analysis was carried out by using an incident Cu  $K\alpha$  radiation ( $\lambda = 1.5418 \text{ \AA}$ ). The voltage of the tube was 30 kV with a step size of 0.013 and a counting time of 37.995 s/step with two theta values between  $15^\circ$  and  $90^\circ$ .

## 4 Results and Discussion

Figure 6 shows stress–strain plots for pure Mg and MWCNT reinforced Mg with 10, 20, 30 vol.% composites, respectively. It can be clearly inferred that after single pass friction stir processing, the tensile strength of the composites increases as the amount of reinforcement is increased but only until an optimum value after which it starts to fall. The tensile strengths for pure magnesium were found out to be 68 MPa; for 10 MWCNT/Mg composite, it was 98 MPa and peaking at 138 MPa for 20 MWCNT/Mg composite. Then there is a drastic reduction in the tensile strength value for 30 MWCNT/Mg composite which measured 109 MPa.

The main reason attributed to this common trend in the literature [19–24] is the increase in brittleness of the composite after certain point of reinforcement. Also, processing defects like abnormal heat generation and tunnelling effect cause

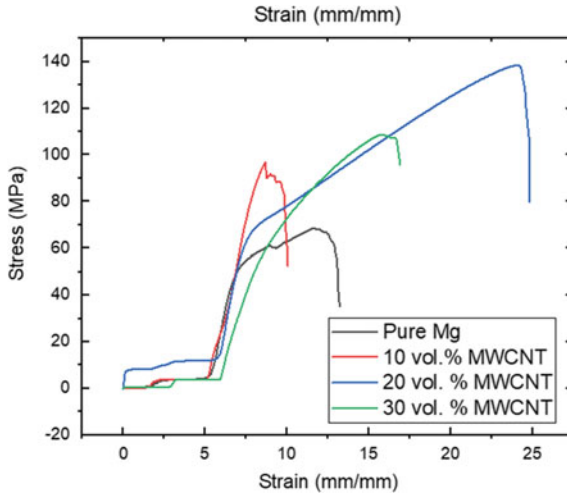


**Fig. 6** Stress–strain plots for pure Mg and 10 MWCNT/Mg, 20 MWCNT/Mg, 30 MWCNT/Mg composites

reduction in strength of the composite. To avoid tunnelling defect, the tool rotation speed should be maximum and the tool traverse speed should be minimum. Also, tool tilt angle should also be given appropriately. But this also leads to higher contact time between tool and material, thus causing increased heat generation which in turn may cause localized melting of the metal which must be avoided at all cost.

In the test above, it is clear that at 20 vol.% MWCNT reinforcement, the tensile strength of the composite reaches maxima at 138 MPa as compared to 68 MPa of pure magnesium which represents about 203% enhancement. Thus, it was found that 20 vol.% MWCNT is the optimal value for the reinforcement content in the context of this paper. Figure 7 represents the SEM micrographs of fractured surfaces for pure Mg and MWCNT reinforced Mg composite. Irregular grain shapes and sizes

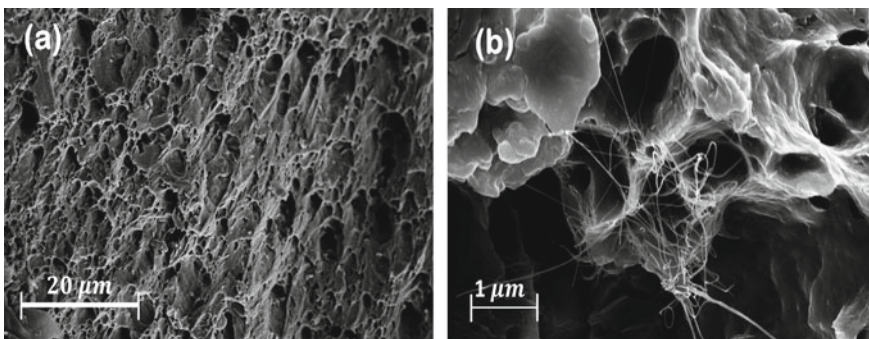
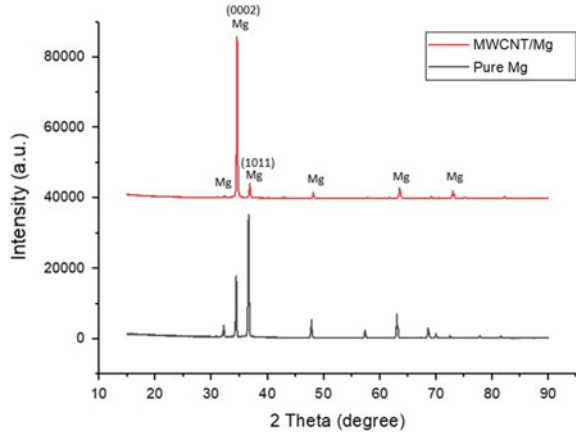


**Fig. 7** SEM micrographs of fractured surfaces for pure Mg and MWCNT reinforced Mg composite

**Fig. 8** X-ray diffraction plots for pure Mg and MWCNT/Mg composite



are shown in SEM micrograph. The micrograph of Mg was elongated with some cluster pattern as shown in image. MWCNT seems to be flaky-like structure.

In the X-ray diffraction (XRD) tests, very clear and distinct peaks of Mg are observed in both the plots for pure magnesium and reinforced composite. For pure magnesium, the highest reflection for non-oriented grains is observed in (1011) plane. After FSP, the oriented grains show maximum reflection in (0002) plane instead of (1011) plane. The new orientation is resulted in the complex shear as well as compression stresses generated by reason of friction between tool and the material [19]. However, the peak for MWCNT is not very distinctive due to their small dimensions and limited content in the composite (Fig. 8).

## 5 Conclusions

It was found that the friction stir processing (FSP) is an effective process fabricating the metal matrix composite in terms of improvement of mechanical properties of the composite. Nano-reinforcements are quite effective when used in optimum quantity to improve the physical properties of the metal matrix composite given that suitable care is being taken to ensure proper material dispersion with no agglomeration or in situ reactions. In this paper, the optimum increase in the tensile strength of the composite was found to be 203% more than that of cast pure magnesium at 20 vol.% MWCNT reinforcement. After this value, any increase in MWCNT content led to deterioration in the mechanical properties of the composite because of the composite becoming brittle in nature. The XRD analysis showed the presence of parent phases of materials without any reaction phases. The orientation of grains was occurred in the direction of tool travel in the surface of the composite in the stir zone (SZ).

## References

1. Prakash, C., Singh, S., Sharma, S., Garg, H., Singh, J., Kumar, H., Singh, G.: Fabrication of aluminium carbon nano tube silicon carbide particles based hybrid nano-composite by spark plasma sintering. *Mater. Today Proc.* **21**, 1637–1642 (2020)
2. Kang, J., Li, J., Shi, C., Nash, P., Chen, D., Zhao, N.: In situ synthesis of carbon onion/nanotube reinforcements in copper powders. *J. Alloys Compd.* **476**(1–2), 869–873 (2009)
3. Chu, K., et al.: Thermal properties of carbon nanotube-copper composites for thermal management applications. *Nanoscale Res. Lett.* **5**(5), 868–874 (2010)
4. Li, H., Misra, A., Zhu, Y., Horita, Z., Koch, C.C., Holesinger, T.G.: Processing and characterization of nanostructured Cu-carbon nanotube composites. *Mater. Sci. Eng. A* **523**(1–2), 60–64 (2009)
5. Iijima, S.: Helical microtubules of graphitic carbon. *Nature* **354**(6348), 56–58 (1991)
6. Subramoney, S.: Novel nanocarbons—structure, properties and potential applications. *Adv. Mater.* **10**(15), 1157–1171 (1998)
7. Baughman, R.H., et al.: Carbon nanotubes—the route toward applications. *Science* **297**(5582), 787–792 (2002)
8. Paradise, M., Goswami, T.: Carbon nanotubes—production and industrial applications. *Mater. Des.* **28**(5), 1477–1489 (2007)
9. Bethune, D.S., et al.: Cobalt-catalysed growth of carbon nanotubes with single-atomic-layer walls. *Nature* **363**(6430), 605–607 (1993)
10. Terrones, M.: Science and technology of the twenty-first century: synthesis, properties, and applications of carbon nanotubes. *Annu. Rev. Mater. Res.* **33**(1), 419–501 (2003)
11. He, C., et al.: An approach to obtaining homogeneously dispersed carbon nanotubes in Al powders for preparing reinforced Al-matrix composites. *Adv. Mater.* **19**(8), 1128–1132 (2007)
12. Zhou, W., Sasaki, S., Kawasaki, A.: Effective control of nanodefects in multiwalled carbon nanotubes by acid treatment. *Carbon* **8**, 121–129 (2014)
13. Kwon, H., Estili, M., Takagi, K., Miyazaki, T., Kawasaki, A.: Combination of hot extrusion and spark plasma sintering for producing carbon nanotube reinforced aluminum matrix composites. *Carbon* **47**(3), 570–577 (2009)
14. Cho, S., Kikuchi, K., Kawasaki, A., Kwon, H., Kim, Y.: Effective load transfer by a chromium carbide nanostructure in a multi-walled carbon nanotube/copper matrix composite. *Nanotechnology* **23**(31), 315705 (2012)
15. Ci, L., Ryu, Z., Jin-Phillipp, N.Y., Rühle, M.: Investigation of the interfacial reaction between multi-walled carbon nanotubes and aluminum. *Acta Mater.* **54**(20), 5367–5375 (2006)
16. Deng, C.F., Wang, D.Z., Zhang, X.X., Li, A.B.: Processing and properties of carbon nanotubes reinforced aluminum composites. *Mater. Sci. Eng.* **444**(1–2), 138–145 (2007)
17. Liu, Z.Y., Xiao, B.L., Wang, W.G., Ma, Z.Y.: Analysis of carbon nanotube shortening and composite strengthening in carbon nanotube/aluminium composites fabricated by multi-pass friction stir processing. *Carbon* **69**, 264–274 (2014)
18. Jafari, J., et al.: Mechanical and microstructural characterization of Cu/CNT nanocomposite layers fabricated via friction stir processing. *Int. J. Adv. Manuf. Technol.* **78**(1–4), 99–209 (2015)
19. Huang, Y., Li, J., Wan, L., Meng, X., Xie, Y.: Strengthening and toughening mechanisms of CNTs/Mg-6Zn composites via friction stir processing. *Mater. Sci. Eng. A* **732**, 205–211 (2018)
20. Lim, D.K., et al.: Synthesis of multi-walled CNT reinforced aluminium alloy composite via friction stir processing. *Mater. Sci. Eng. A* **507**(1–2), 194–199 (2009)
21. Jamshidijam, M., et al.: Wear behavior of multiwalled carbon nanotube/AZ31 composite obtained by friction stir processing. *Tribol. Trans.* **56**(5), 827–832 (2013)
22. Morisada, Y., et al.: MWCNTs/AZ31 surface composites fabricated by friction stir processing. *Mater. Sci. Eng. A* **419**(1–2), 344–348 (2006)
23. Singh, S., Pal, K.: Influence of surface morphology and UFG on damping and mechanical properties of composite reinforced with spinel  $MgAl_2O_4$ -SiC core-shell microcomposites. *Mater. Charact.* **123**, 244–255 (2017)

24. Izadi, H., et al.: Distribution and stability of carbon nanotubes during multi-pass friction stir processing of carbon nanotube/aluminum composites. *Carbon* **50**(12), 4744–4749 (2012)
25. Zhou, W., et al.: Effectively enhanced load transfer by interfacial reactions in multi-walled carbon nanotube reinforced Al matrix composites. *Acta Mater.* **125**, 369–376 (2017)

# Influence of Surface Treatment and Molding Temperature on Mechanical Properties of Jute/PLA-Based Green Composites



Jaiinder Preet Singh, Sehijpal Singh, Vikas Dhawan, Gurjot S. Dhaliwal, Piyush Gulati, Rajeev Kumar, and Manpreet Singh

**Abstract** In the present study, the main focus is to increase the interfacial bonding between jute fiber with polylactic acid (PLA) with the help of surface modifications of jute fiber using alkali, potassium permanganate, and potassium dichromate treatments. FTIR spectroscopy result confirms the removal of hemicellulose layer which results in an increase in adhesion of jute fiber with polylactic acid. Jute/PLA composites are prepared using hot compression molding process using treated jute fibers and PLA matrix. This study also exposes the effect on the mechanical properties of developed composites of molding temperatures ranging from 160 to 180 °C. Alkali treatments resulted in an increase of 56.1% and 51%, respectively, in the tensile and flexural strength of jute/PLA composites. It is so observed that for alkali-treated jute/PLA composite with 170 °C molding temperature, maximum tensile and flexural strength were recorded.

**Keywords** Jute fibers · Compression molding · Molding temperature · Surface treatment · Green composites

---

J. P. Singh (✉)

IKG-PTU Kapurthala, Guru Nanak Dev Engineering College, Ludhiana 141006, India  
e-mail: [jaiinderpreetsingh@gmail.com](mailto:jaiinderpreetsingh@gmail.com)

J. P. Singh · P. Gulati · R. Kumar · M. Singh  
Lovely Professional University, Phagwara 144401, India

S. Singh  
Guru Nanak Dev Engineering College, Ludhiana 141010, India

V. Dhawan  
Shree Guru Gobind Singh Tricentenary University, Gurugram 122006, India

G. S. Dhaliwal  
Intertribal Research and Resource Center, United Tribes Technical College, Bismarck, ND, USA



## 1 Introduction

Composite material also can be found in our households. For example: concrete is made up of cement, sand, and gravel. It can also be reinforced with steel which improves around 10,000 BC; the houses were made up of straw bricks, and then in around 4000 BC, the writing material was fabricated from the papyrus plant. Egyptians also made fibers by heat treating the glass material to very high temperature. In around 1200 BC, Mongols develop the first modern composite bow. Phenolic resin was used for the first time in the fighter planes by the British Royal Air Force in its mosquito bomber aircraft. Plywood is also a form of good composite used for making furniture. Our bone is also a composite material containing collagen fiber and hydroxyl appetite matrix.

Composite material is nothing but two or more basic materials combining different physical or chemical properties to create a new material, but the individual properties of the material process. The new material may be chosen for many reasons: common examples contain materials which are stronger, lighter, or less expensive when compared to traditional materials. With rise in global temperature, depletion of fossil fuels and a need of sustainable development forced the researchers to develop the green composites [1]. Green composites are materials derived from the natural resource. It consists generally of strengthening as natural fibers and material matrix. Green composites are additional categories in two categories, i.e. partially biodegradable green composites and composites that are fully biodegradable [2, 3]. Partially green composites consist of at least one constituent which should be derived from natural resource such as jute/epoxy composites, carbon fiber/PLA composites. In the case of fully biodegradable green composites, both constituents should be derived from natural resources such as composites of jute/PLA, composites of Jute/PHB.

Lots of research is currently underway to develop green composites. Sareena et al. [4] the biodegradation behavior and its effect on the mechanical properties of natural rubber developed reinforced with natural fillers such as coconut shell and peanut shell powder were studied. The chemical treatment, filler content, and filler size help in improving the durability. The composite containing treated fillers were resistant to soil erosion. The results progressed that after the soil burial testing, the hardness and tensile strength were decreased. Zhong et al. [5] studied to strengthen interfacial adhesion of phenolic resin/cellulose fiber in compound sites consisting of aramid and sisal fiber by surface microfibrillation of cellulose fiber. Sisal fiber's surface microfibrillation to 24 SR surges the internal bonding strength, wear resistance and tensile strength values by 124%, 31%, 93%, respectively [6]. The thermal, morphological and mechanical properties of a bio-composite derived from banana plants were studied, and the results showed that the device decreased at high temperatures. Thermal stability has been enhanced with the increase of glass transition temperature. The mechanical test revealed increase of tensile strength, tensile modules, and flexural modulus by 15%, 12%, and 25%, respectively. Mohanty et al. [7] explored the physicommechanical and inter-phasic properties of "all green composites" acquired from poly-bioresin and kenaf natural fiber. The optimal properties of composites

were accomplished by 20 wt% which results in major increment in flexural strength (48%), tensile strength (310%), and storage modulus (123%). Up to 89% for flexural, 82% for impact, and 83% for tensile strength were absorbed after exposing the composite to boiling water. Bourban et al. [8] Comparison of unidirectional and 2/2 flax fiber damping and mechanical properties including thermoplastic (PP), PLA and thermoset (epoxy) with epoxy composites of glass (GF) and carbon fiber (CF). The best compromise amid damping and stiffness were found with flax fiber-reinforced PLA. The composite with flax fiber showed better damping with respect to carbon fiber and glass fiber-reinforced composite.

Trujillo et al. [9] studied involves a long bamboo fiber and its high end uses as a reinforcement for composite materials. At different gauge lengths, Weibull distribution, which requires only three parameters, explained accurately the fiber strength of fibers. With increasing gauge lengths, the fiber strength decreases. While comparing with natural fibers, Weibull shape parameter had shown low strength variability, indicating high quality.

Singh et al. [10] developed epoxy-based composites reinforced jute fiber and studied the influence of temperature healing on its mechanical properties. Test results showed that at 100 °C, the peak tensile strength was registered at 32.3 MPa. Georgiopoulou et al. [11] developed the unidirectional flax fiber composites, which are exposed to a different dynamic mechanical analysis. It was fabricated by film stacking method. There were different treatment processes used, named as plasticization, silanization, and treatment with maleic anhydride. A strong adhesion between matrix and fibers was observed as a result of these surface treatments. There was also an increase in crystallinity, Young's modulus, processing module, and flexural modulus. Singh et al. [12] studied the effect of surface treatment on jute/epoxy composite mechanical properties. Surface treatment of natural fibers results in the enhancement of tensile and flexural strength; however, impact strength has been tremendously decreased. The literature study clearly reflects that a great deal of work has been done in the field of manufacturing and testing PMC using synthetic fibers and synthetic resins, and the increasing concern for the environment clearly requires the need for environmentally friendly and cost-effective substitute polymer composites. The present initiative is to develop green composites and to study and improve their mechanical properties.

Jute fiber is used as reinforcement and polylactic acid (PLA) as the matrix material derived from the maize starch in this paper. At molding temperatures ranging from 160 to 180 °C, and at fiber volume by weight, all the composites developed 30% fiber volume. Different surface treatments such as sodium hydroxide, potassium dichromate, and potassium permanganate, were employed on jute fiber and studied the effect on their mechanical properties. In order to investigate the chemical interactions between fibers and chemical agents, Fourier transform infrared spectrometry was performed on treated jute fibers.

## 2 Materials and Method

The matrix material used to develop the composites is polylactic acid (PLA), which in granular form is a commercial grade of 3052D, acquired from Natur-Tec India Pvt Ltd. The reinforcement is selected as jute fiber which is easily available and very economical in nature. Jute fibers consist of alpha cellulose, hemicellulose, lignin, fats, and waxes, pectin, protein/nitrogenic matter, etc., and ash [13].

The optical view of woven jute mat and PLA in granule form is shown in Fig. 1a, b.

### 2.1 Fiber Surface Treatment

Jute fibers were exposed to three different surface treatments with the motive to the enhancement of mechanical properties.

In alkali treatment, fiber mat was dipped into 5% by weight concentrated NaOH solution for 2 h and then washed away with the acetic acid having 1% concentration by weight to ensure the PH value of the fiber attains 7. Fibers were further washed with water after achieving the 7 PH quality and dried for 2–3 days.

In potassium permanganate and potassium dichromate treatment, fibers were soaked in 0.02% by weight concentrated solution for 2 min at room temperature. Rest same procedure was adopted as used in alkali treatment.

### 2.2 Spectral Analysis

Using FTIR spectroscopy, both untreated and treated jute fibers were analyzed. It shows the change in molecular fiber structure due to physical and chemical treatments.

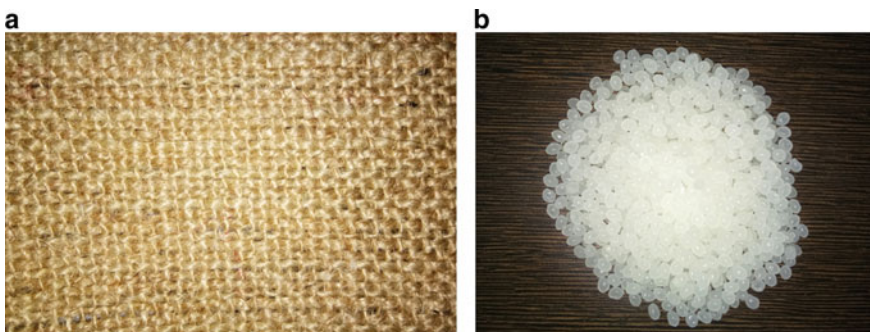


**Fig. 1** a Of a jute mat woven. b Granular PLA

At first, 1 mg of jute fibers were ground into the powder form and then mixed with KBr powder infrared grade. The mixture was then pressed for measurement into a pallet. The spectrum of 500–4000  $\text{cm}^{-1}$  was reported.

### 2.3 Composite Fabrication

Hot pressing and compression molding methods have been introduced for experimental purposes. After chemical fiber treatment, the treated jute mat was cut according to the specific heating die size, and the amount of PLA granules required was measured and placed in the oven at 80 °C for 4 h preheating. Fix the Teflon sheet and strips once the die temperature has reached the required temperature. For the manufacturing process, split the PLA granules into two parts. First, the first half of the granules is spread evenly into the cavity and then the treated jute fabric layers are placed over the PLA granules, and then the remaining PLA granules is distributed into the cavity over the placed jute fabrics. The Teflon sheet is eventually placed on the lower die, and the die is closed later. Eventually, the entire die structure is kept in the molding compression unit. In this fabrication process, the machine molding temperature was kept as operating parameter which ranged from 160 to 180 °C. The selection of the molding temperature parameter was based on the pilot study were temperature range was selected as 160–210 °C and later found that fibers were degraded due to increase in the temperature. That is why, the temperature range was selected as 160–180 °C. The complete composite was kept under the load of 250 KN for 15 min, and then, heaters were stopped and kept at the complete die under the pressure to cool, and finally, the complete die was open at 80 °C, and final composite was kept in desiccator.

### 2.4 Mechanical Test

1. **Tensile testing:** On the universal testing machine, the tensile test was carried out in accordance with ASTM standards D3039 [14]. Specimens were cut to 250 mm  $\times$  25 mm  $\times$  4 mm as required. All tensile tests were conducted at 2 mm/min cross speed. Figure 2a and b shows the specimens fractured during tensile and flexural testing.
2. **Flexural Testing:** The flexural strength of the formed jute/PLA composites was measured using a three-point bend test conducted on the UTM machine in accordance with the D790-02 [15] ASTM standard with dimensions of 120 mm  $\times$  15 mm  $\times$  4 mm.

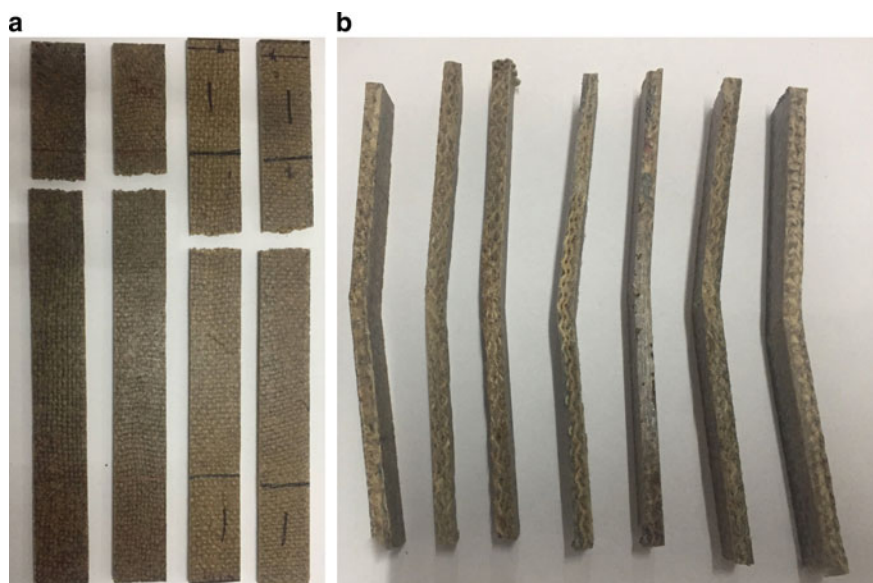


Fig. 2 a Fractured tensile specimens. b Fractured flexural specimens

### 3 Results and Discussion

#### 3.1 FTIR Spectroscopy

FTIR spectra are shown in Fig. 3a, b for untreated and alkali-treated jute fiber. One finds different bands of absorption in the spectra from  $4500$  to  $400\text{ cm}^{-1}$  in this figure. Due to the stretching vibration of hydroxyl (OH), the absorption band around  $3300\text{--}3280\text{ cm}^{-1}$  is indicated. This could be a facility for desorption of water as well as decomposition of hemicellulose and lignin. An indication of C–H spreading vibration in cellulose and hemicellulose for methyl and methylene groups is a high peak observed in both spectra around  $2900\text{ cm}^{-1}$ . Table 1 shows the transmittance peaks for untreated and treated jute fibers.

C=O stretching carboxylic acid vibration and hemicellulose ester components cause the sharp peak observed at  $1750\text{ cm}^{-1}$  in untreated jute fiber (Fig. 3a). In the case of alkali-treated jute fiber, due to structural changes that are incompatible with Goripathi et al. [16], the height of  $1740\text{ cm}^{-1}$  corresponding to C=O spreading hemicellulose vibration vanished. It clearly shows that the hemicellulose layer was removed in alkali treatment as compared to other surface treatments.

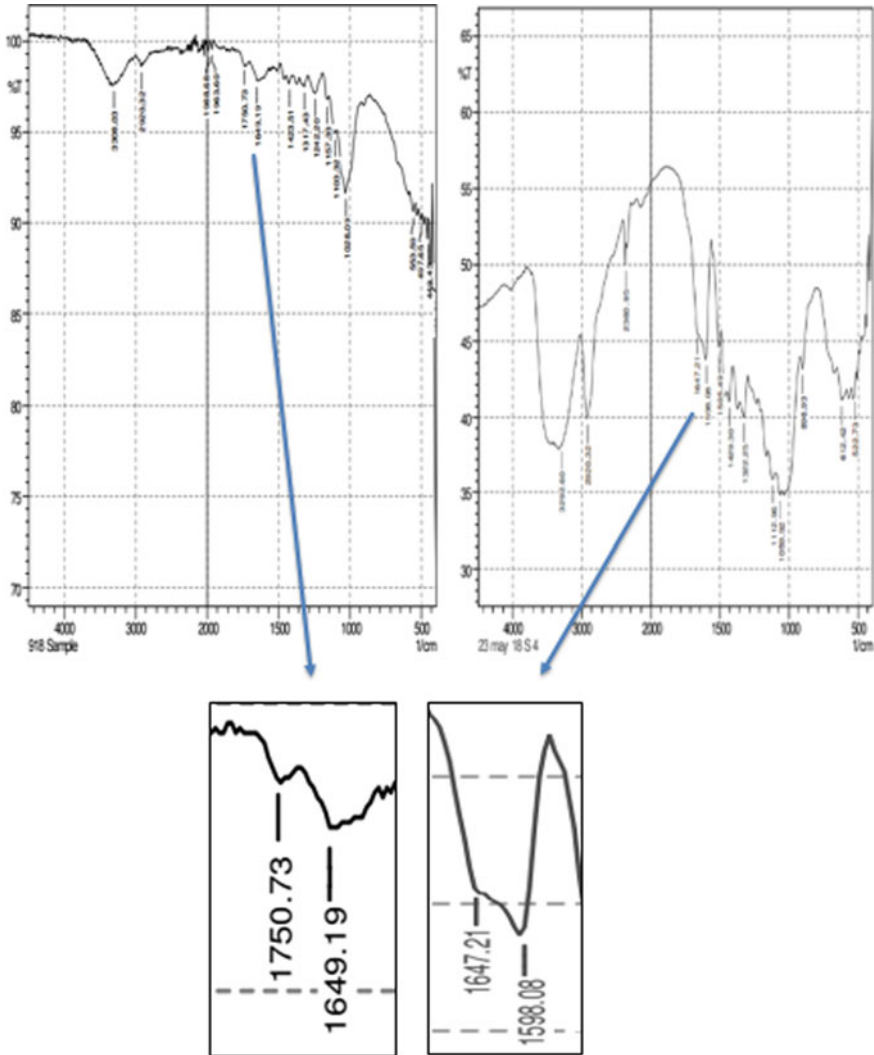


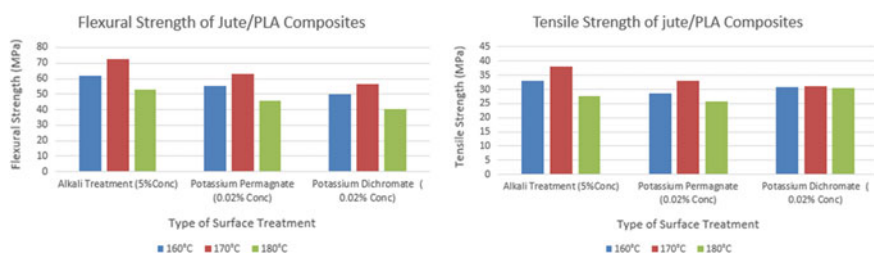
Fig. 3 a, b Untreated or alkali-treated FTIR spectra of jute material

### 3.2 Composites and Its Mechanical Properties

Figure 4 shows the effects of surface treatments on jute/PLA composites' tensile and flexural properties. The untreated jute/PLA's tensile strength and flexural strength were 24.42 MPa and 48 MPa, respectively. After different treatments, the tensile

**Table 1** FTIR spectra for untreated and treated jute fibers

Possible assignments	Untreated	Alkali	Potassium dichromate	Potassium permanganate
–OH stretching vibration (cellulose)	3308	3292	3330	3520
C–H stretching vibration	2920	2920	2920	2920
C=O stretching vibration (hemicellulose)	1750	–	1740	1740
CH <sub>2</sub> symmetric bending	1423	1429	1430	1439
C–O stretching vibration (lignin)	1242	1235	1244	1245

**Fig. 4** Flexural and tensile properties of surface-treated jute/PLA composites

strength varies on the basis of different temperatures and surface treatments. Maximum tensile strength of 38.12 MPa was recorded for alkali-treated jute/PLA composite. Increment of tensile properties follows an order of alkalization > potassium dichromate > potassium permanganate > untreated.

Composites' mechanical properties depend on the interaction of the fiber matrix. It was also observed that the tensile strength decreases at higher temperatures. This may be due to higher temperature burning of the fibers. At higher curing temperature, the interfacial strength between matrix and natural fibers reduces due to thermal degradation of natural fibers at higher temperature [10]. Maximum flexural strength of 72.5 MPa was observed at 170 °C molding temperature with alkali-treated jute/PLA composites.

## 4 Conclusion

In this study, composites based on polylactic acid based on surface-treated jute fiber have been developed. Three different chemicals have been selected for the surface

treatment of jute fibers, such as sodium hydroxide, potassium permanganate, and potassium dichromate. Mechanical properties such as tensile strength and flexural strength have been evaluated.

The following conclusions will be drawn from this study.

1. The surface improvement in each treatment is shown by the FTIR spectra of all treated jute fibers.
2. Alkali-treated reinforced jute fiber shows the highest tensile strength and flexural strength relative to other fiber surface treatment.
3. The peak tensile strength is reported as 38.12 MPa for alkali-treated jute fiber composites.
4. Maximum flexural strength is reported as 72.5 MPa of alkali-treated jute fiber composite.

## References

1. Singh, J.I.P., Singh, S., Dhawan, V.: Mechanical and biodegradation behaviour of jute/polylactic acid green composites. *Asian J. Eng. Appl. Technol.* **7**(2), 52–57 (2018)
2. Singh, H., Singh, J.I.P., Singh, S., Dhawan, V., Kumar Tiwari, S.: A brief review of jute fibre and its composites. *Mater. Today Proc.* **5**(14), 28427–28437 (2018)
3. Singh, S., Dhawan, V., Singh, J.I.P.: Development and characterization of green composites: a review. *ELK Asia Pac. J.* **2**(1), 1–6 (2015)
4. Sareena, C., Sreejith, M., Ramesan, M., Purushothaman, E.: Biodegradation behaviour of natural rubber composites reinforced with natural resource fillers—monitoring by soil burial test. *J. Reinf. Plast. Compos.* **33**(5), 412–429 (2013)
5. Zhong, L.X., Fu, S.Y., Zhou, X.S., Zhan, H.Y.: Effect of surface microfibrillation of sisal fibre on the mechanical properties of sisal/aramid fibre hybrid composites. *Compos. Part A Appl. Sci. Manuf.* **42**(3), 244–252 (2011)
6. Paul, V., Kanny, K., Redhi, G.: Mechanical, thermal and morphological properties of a bio-based composite derived from banana plant source. *Compos. Part A Appl. Sci. Manuf.* **68**, 14–21 (2015)
7. Deka, H., Misra, M., Mohanty, A.: Renewable resource based “all green composites” from kenaf biofiber and poly(furfuryl alcohol) bioresin. *Ind. Crops Prod.* **41**(1), 94–101 (2013)
8. Duc, F., Bourban, P.E., Plummer, C.J.G., Manson, J.A.E.: Damping of thermoset and thermoplastic flax fibre composites. *Compos. Part A Appl. Sci. Manuf.* **64**, 115–123 (2014)
9. Trujillo, E., Moesen, M., Osorio, L., Van Vuure, A.W., Ivens, J., Verpoest, I.: Bamboo fibres for reinforcement in composite materials: strength Weibull analysis. *Compos. Part A Appl. Sci. Manuf.* **61**, 115–125 (2014)
10. Singh, J.I.P., Singh, S., Dhawan, V.: Effect of curing temperature on mechanical properties of natural fiber reinforced polymer composites. *J. Nat. Fibers* **15**(5), 687–696 (2018)
11. Georgiopoulos, P., Christopoulos, A., Koutsoumpis, S., Kontou, E.: The effect of surface treatment on the performance of flax/biodegradable composites. *Compos. Part B Eng.* **106**, 88–98 (2016)
12. Singh, J.I.P., Dhawan, V., Singh, S., Jangid, K.: Study of effect of surface treatment on mechanical properties of natural fiber reinforced composites. *Mater. Today Proc.* **4**(2), 2793–2799 (2017)
13. Bajpai, P.K., Singh, I., Madaan, J.: Development and characterization of PLA-based green composites: a review. *J. Thermoplast. Compos. Mater.* **27**(1), 52–81 (2012)



14. ASTM Committee D-30 on Composite Materials: Standard test method for tensile properties of polymer matrix composite materials, vol. 1, pp. 1–13 (2013)
15. ASTM International. ASTM D790-02: Flexural properties of unreinforced and reinforced plastics and electrical insulating materials, vol. 14, pp. 146–54 (2002)
16. Goriparthi, B.K., Suman, K.N.S., Rao, M.N.: Effect of fiber surface treatments on mechanical and abrasive wear performance of polylactide/jute composites. *Compos. Part A Appl. Sci. Manuf.* **43**(10), 1800–1808 (2012)

# Effect of Nanoclay in Unidirectional Carbon–Epoxy Laminated Composites



Vishaldeep Singh, Manjeet Singh, J. S. Saini, Rohit Badhwar, Akash Gupta, and Nitin Chauhan

**Abstract** Carbon fiber composites are highly demanded in aerospace structure due to their elevated strength but less weight in comparison to the metals and alloys. The main aim is to study the consequence of nanoclay in carbon–epoxy composite by examining the mechanical properties. The compression molding technique was used to prepare the laminates of composite. The specimens were prepared from the epoxy as a matrix and carbon fiber as reinforcing material which were oriented at  $[0^\circ/45^\circ/90^\circ]$ . The tensile strength and bending strength were analyzed for the specimens, both numerically and analytically. The nanoclay was mixed with different wt% with carbon fiber laminates so as to improve the mechanical properties of the composite. The strength of the composite was improved by 25–30% when nanoclay with 3 wt% is added to carbon–epoxy laminates as compared to the strength of composite without nanoclay.

**Keywords** Carbon-reinforced laminates · Nanoclay · Failure analysis · FEM

## 1 Introduction

For the past years, the engineering materials are being replaced by fiber-reinforced composite materials in most of the engineering applications because of their mechanical properties and their strength. The primary and secondary structures of engineering applications are focusing on composite materials because of the lightweight and also the high strength of these composite materials. Among all the natural and synthetic fibers available, the carbon fibers are one of the strongest fibers. The strength of the carbon fibers if compared with that of steel is approximately five times whereas the weight of these fibers is one third. This is why the carbon fibers are being used in

---

V. Singh · M. Singh (✉) · A. Gupta · N. Chauhan  
Mechanical Engineering Department, Lovely Professional University, Phagwara, Punjab, India  
e-mail: [manjeet.21545@lpu.co.in](mailto:manjeet.21545@lpu.co.in)

J. S. Saini · R. Badhwar  
Mechanical Engineering Department, Thapar Institute of Engineering & Technology, Patiala, Punjab, India

engineering applications like spacecrafts, aircrafts, automobiles, civil structures like beams, and other sports equipment like rackets and many more [1].

The fiber-reinforced composites are used by many researchers for the different applications for reducing the weight and cost without compromising the strength of the structure. Many researchers had studied the properties of the fiber-reinforced composites. The main objective is to study how the properties of the composite change when nanoclay is added to the epoxy during the fabrication of composite. The tensile strength and bending stresses are analyzed in this paper. A brief review of work done in carbon–epoxy reinforced composites with and without nanoparticles is discussed.

Djabali et al. [2] inspected the mechanical properties of the carbon–epoxy composite. The vacuum bag technique was used to prepare the composite. The three-point flexural test was performed using ASTM-D790-03 standards. The nondestructive tests and monitoring technique was used to study the composite material. Zakaria et al. [3] studied the graphene nanoparticles and multi-walled carbon nanotubes-based polymer matrix composite. The mechanical, thermal, and dielectric properties of the composite were analyzed. Tensile test and flexure tests were performed on the samples of composite as per ASTM standards D638 and D790, respectively. The failure behavior of the composite was analyzed by scanning electron microscopy (SEM) scanning. Also, the X-Ray Diffraction (XRD) was done to analyze the crystalline structure. The result shows the improvement in properties with the addition of nanoparticles. The nanoparticles enhanced the strength by 11–25%. Wang et al. [4] prepared the carbon fiber composite with silver nanoparticles and graphene oxide. They studied the tensile and shear strength of the composite. The electrodeposition method was used to prepare the composite. The morphological characterizations of the samples were done by SEM, transmission electron microscopy (TEM), and atomic force microscopy (AFM). The silver and graphene nanoparticles improved the mechanical properties by 35%. Shah et al. [5] inspected the mechanical properties of carbon fiber-reinforced epoxy composite in which the iron nanoparticles were added. Also, the electromagnetic properties of the laminated composites were analyzed. Das et al. [6] reviewed the fabrication of the composite and properties of carbon fiber-reinforced composites. They also studied the different processes used for the fabrication of composite and also the applications of carbon fiber-reinforced composites. Azeez et al. [7] reviewed the epoxy clay nanocomposites. They discussed about the influence of different parameters for the preparation of nanocomposites. They have also discussed about the mechanical and thermal properties of nanocomposites prepared. XRD method was used to differentiate the different clay structures prepared for nanocomposite. Qin et al. [8] discussed about the various effects on the properties of carbon fiber-reinforced composite with the addition of silicon dioxide nanoparticles. The mechanical properties were analyzed with varying percentages of nanoparticles. The morphological characterization of the samples was done by X-Ray Photoelectron Spectroscopy (XPS), Thermo Gravimetric Analysis (TGA), and SEM. The shear strength was observed for the composite and was observed that with the addition of nanoparticles the strength was improved by 44%. Landowski et al. [9] discussed about the impact behavior on carbon fiber-reinforced epoxy composite with

silica nanoparticles. The main objective of the composite is for marine applications. The damage of the composite during low impact was analyzed by X-Ray radiography. The nanoparticles have a significant improvement on mechanical properties as compared with the composite without nanoparticles. Spanos and Kontsos [10] studied the mechanical properties of polymer nanocomposite which was reinforced with carbon nanotubes. A multi-scale Monte Carlo FEM was used to analyze the properties. Murugan et al. [11] examined the damaging effect of carbon-reinforced epoxy composite with nanoclay. The nanoclay present in the composite improves the impact properties as compared to the composite without nanoclay. The breaking of fibers and the cracks in the matrix were analyzed by SEM images whereas the delamination of the layers and the porosity of the damaged specimens were analyzed by X-Ray computed tomography scanning. Limam et al. [12] estimated the ultimate failure load experimentally of pin-loaded composite laminate made of graphite/epoxy and compared it with the theoretical results. Tension, shear and bearing failure were analyzed for a given ply. Aluko [13] analyzed the joint strength and failure analysis for graphite-epoxy laminate using Yamada-Sun failure criteria and characteristic model. The characteristic dimensions were generated analytically for the construction of the characteristic model. Oner et al. [14] examined the mechanical properties of hybrid carbon and glass fiber composite with nanoclay. The tensile and flexural tests were executed as per ASTM D3039 and D7264 standards. The addition of nanoclay to the matrix material improved the strength of the composite material by 6%. Alsaadi et al. [15] studied the tensile and flexural properties of carbon-kevlar fiber-reinforced with epoxy. The effect of nano-silica particles was analyzed. The tensile test and flexure test were performed as per ASTM D638 and D790 standards. The proper adhesion of nano-silica particles with fiber and epoxy leads to better tensile and flexure strength. Tsai et al. [16] discussed fracture and fatigue behavior of the composites. They added silica nanoparticles to improve the properties. The silica nanoparticle in the sized form leads to proper adhesion between fibers and matrix which ultimately increases the properties. The double cantilever beam tests were performed on the specimens as per ASTM D5528 standards and the morphological study of the specimens was done using SEM images. Ulus et al. [17] studied the mechanical as well as physical properties of the carbon-epoxy composite with calcium carbonate nanoparticles. The vacuum-assisted resin infusion method was used to prepare the samples and the tensile test and flexural tests were executed as per ASTM D3039 and 7136 standards. The morphological study of the samples was done using SEM images. It was found that the strength was improved by 22%. Kaybal et al. [18] investigated the effect of alumina nanoparticle in carbon fiber-reinforced composite. The composite was prepared using vacuum-assisted resin infusion method. The impact strength of the specimens was checked and the test was performed as per ASTM D7136. The result shows that the addition of nanoparticle up to a certain extent increases the strength and then it decreases.

From the literature review, it is observed that the mechanical properties are varied when nanoparticles are added. The researcher had found that the mechanical properties are improved with the addition of nanoparticles. Moreover, very less work

has been done on the study of mechanical properties of the composites when nanoclay as a filler material is added to the epoxy resin for the fabrication of carbon fiber-reinforced composites laminates. Hence, the work presented in this paper is to study the effect of Cloisite 30B which is used as a filler material for the preparation of nanocomposite. The samples prepared were analyzed also the morphological classification of the material is done by XRD.

## 2 Experimentation

For experimentation, the samples are prepared to study the mechanical properties. The materials used for the preparation of the samples and the method used are discussed in this section.

### 2.1 Raw Material Used to Prepare the Composite

**Resin**—To prepare the composite, the laminates are prepared. For the fabrication of laminates, the epoxy resin was prepared with the addition of hardener and accelerator to it. They were mixed in the ratio of 100:100:0.1–2 for the preparation of the matrix. Lapox was used as epoxy which is in a liquid state with medium viscosity. The viscosity of resin at 77°F is within the range 9000–12,000 mPa s. It is also known as Bisphenol-A Di Glycidyl Ether (BADGE). It is the organic compound that is cross-linked with the help of hardener. The hardener and accelerator which were used for making the resin were liquid anhydride and benzyldimethylamine. The mix viscosity at 104°F is 450 cPs and minimum curing temperature is 248°F for 2 h and 320°F for half-hour. The materials for preparing the resin were provided by Atul Ltd., Gujarat, India ([www.atul.co.in](http://www.atul.co.in)). The tensile strength and flexural strength of the resin is 70–90 N/mm<sup>2</sup> and 100–120 N/mm<sup>2</sup>, respectively, which was provided by the supplier.

**Carbon Fabric**—To prepare the composite carbon fabric was used as a reinforcing agent. The unidirectional 214.5 gsm fabric having fiber thickness as 0.11 mm was supplied by the AURO Carbon & Chemicals, Vadodara, Gujarat, India.

Nanoclay Cloisite 30B used for the experimental work was provided by the Connell Bros. Company (India) Pvt. Ltd., Mumbai, India. The quaternary ammonium salt was used to modify Cloisite 30B which is natural montmorillonite. It is used to improve physical properties.

For the proper mixing of nanoclay with epoxy during the preparation of resin, acetone was added to the mixture. The solvent used to mix the nanoclay and epoxy was provided by the Loba Chemie Pvt. Ltd, Mumbai, India.

**Table 1** Weight % of epoxy, carbon fiber, and clay

S. No.	Sample code	Fiber orientation	Number of layers	Weight fraction %		
				Epoxy	Carbon fiber	Cloisite 30B
1	CB-0	[0°/45°/90°/-45°/90°/0°]	6	67	33	0
2	CB-1	[0°/45°/90°/-45°/90°/0°]	6	59.67	39.71	0.62
3	CB-2	[0°/45°/90°/-45°/90°/0°]	6	59.23	39.53	1.24
4	CB-3	[0°/45°/90°/-45°/90°/0°]	6	58.94	39.20	1.86
5	CB-4	[0°/45°/90°/-45°/90°/0°]	6	58.13	38.82	3.05
6	CB-5	[0°/45°/90°/-45°/90°/0°]	6	58.11	38.80	3.09

## 2.2 Preparation of Sample

The BADGE-based epoxy was used as matrix and carbon fiber as reinforcement for the preparation of laminates. The nanoclay was mixed with epoxy in the ratio as per standards; the mass ratio of resin is given in Table 1. For the preparation of resin, the solution was stirred with homogenizer for 15 min and thereafter sonication was done for 15 min, so that the nanoclay is properly dispersed in the epoxy resin. After the sonication process, hardener and accelerator was added to the mixture and kept for 15 min under homogenization for the proper mixing of the resin.

For the preparation of laminate, the carbon fabric was cut and the resin was applied to it. Then the second layer was placed on it and so on, to form the laminate with six layers of carbon fiber. When the layers were placed on each other, the air particles were trapped inside the layers. These air particles reduce the strength of the composite, so to remove the air particles from the layers the hand roller was used. For the proper bonding between the layers, the laminates were compressed and were treated at room temperature for 24 h. Thereafter, the curing of the laminates is necessary, this was done at constant pressure and temperature of 120 N/mm<sup>2</sup> and 302°F respectively for 2 h. Thereafter, the plate was brought to room temperature at 120 N/mm<sup>2</sup> pressure. The thickness of the plate obtained was 2 mm. The flow chart explaining the preparation of samples is shown in Fig. 1.

## 2.3 Testing

### Tensile and Flexural test

The tensile tests and flexural tests were executed at  $77 \pm 3^\circ\text{F}$  on a Zwick-Roell Universal Testing Machine on samples according to ASTM D3039 and D7264 standard respectively. For the tensile test, the samples prepared for the test were having a gauge length of 150 mm with a start position of 250 mm. For flexural test, the width of specimen was 7 mm and thickness was 2 mm whereas the length to thickness

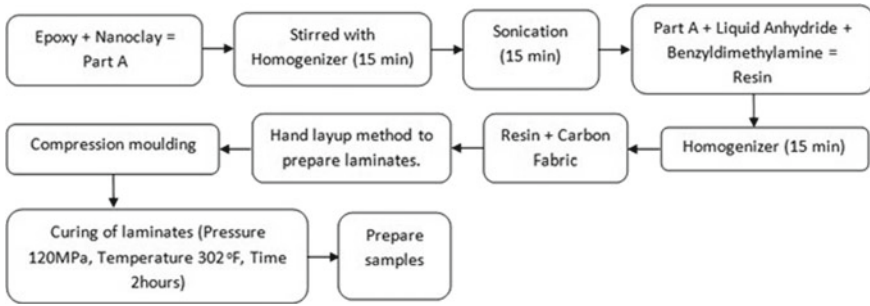


**Fig. 1** Flow chart for preparing samples

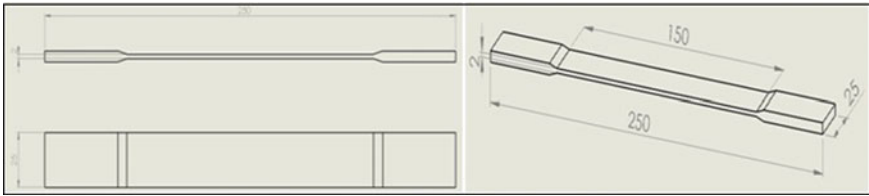


**Fig. 2** Schematic diagram of sample for tensile test (all in mm)

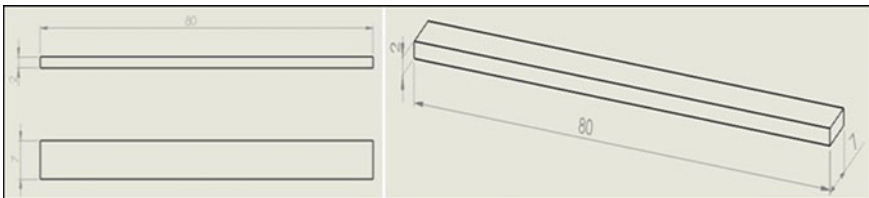


**Fig. 3** Schematic diagram of sample for flexural test (all in mm)

ratio was 40:1. The schematic diagrams for the samples to be tested are shown in Figs. 2 and 3. The crosshead speed for tensile and flexural tests was 2 mm/min and 1 mm/min, respectively. At least three specimens of each sample were tested and the mean values were taken. The samples are tested as per ASTM standards. The loads applied on the specimens are shown in Figs. 4a and 5, whereas Fig. 4b shows the actual sample prepared from the carbon–epoxy composite.

### 3 Results and Discussions

The tensile test was performed on the specimens prepared from carbon fiber-reinforced epoxy with nanoclay. The results were obtained on the samples with

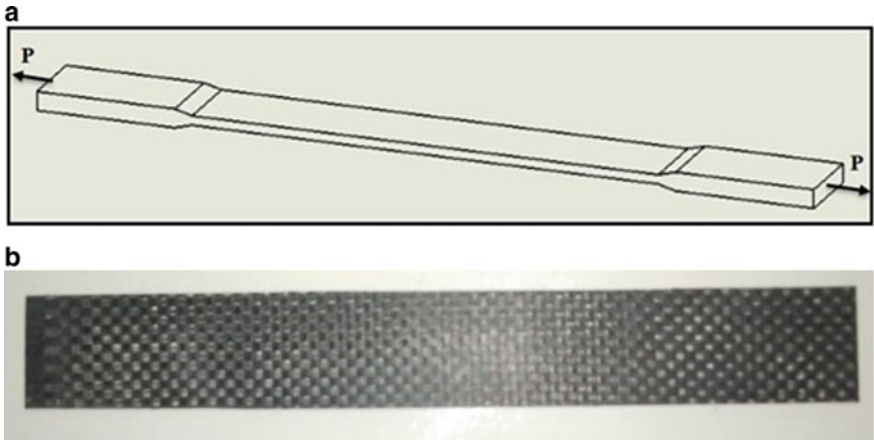


Fig. 4 a Tensile load applied on specimen in tensile test as per ASTM D3039 standards. b Actual specimen for tensile test

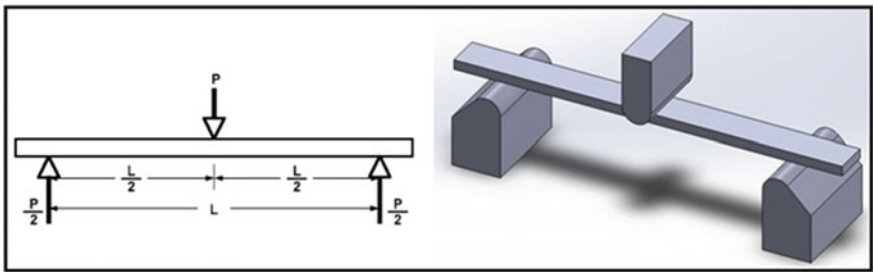
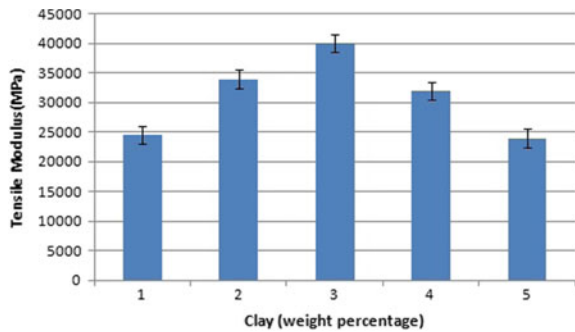


Fig. 5 Load applied on a sample in flexural test as per ASTM D7264 standards

nanoclay wt% of 1, 2, 3, 4, and 5 in the laminates and the changes in the properties are analyzed. To analyze the results, the test was executed on three samples of each type and the mean values were taken. The results obtained are shown in Fig. 6. The

Fig. 6 Tensile modulus versus clay (wt%)





three-point flexural test was performed on samples with different nanoclay wt% and the results are shown in Fig. 7.

The stress–strain curve for the composite without nanoclay and with varying percent of nanoclay is shown in Fig. 8. The strength of the composite with nanoclay particles with 3% of nanoclay was increased by approximately 28–32%, also the modulus is increased by 25–30%. It is clear from the results that the strength of the composite with wt% up to 3 increases and then it decreases.

### X-Ray Diffraction

Nanoclay Cloisite 30B which was used in the experimentation is a layered aluminosilicate. There are three layers of aluminum octahedral and silicon tetrahedral.

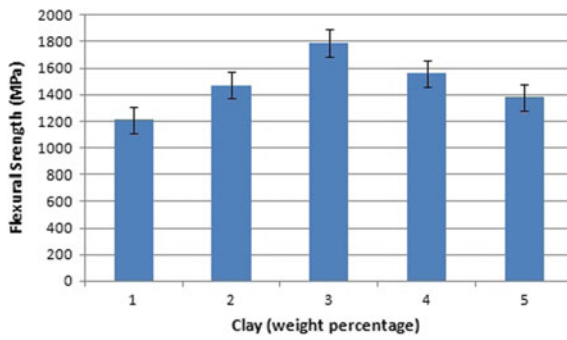


Fig. 7 Flexural strength versus clay (wt%)

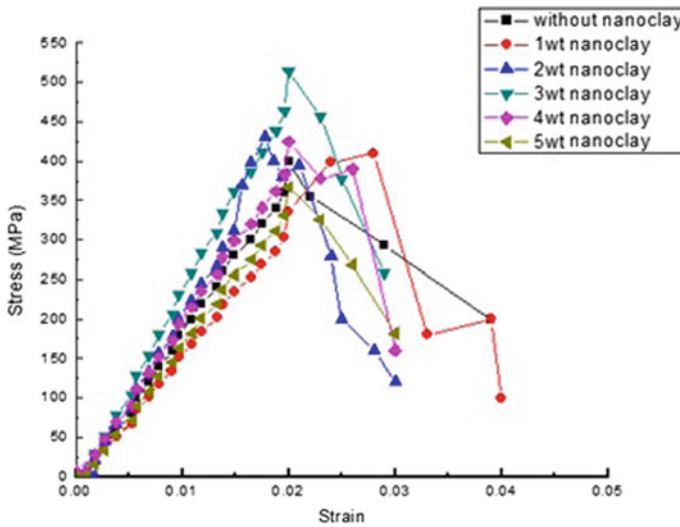
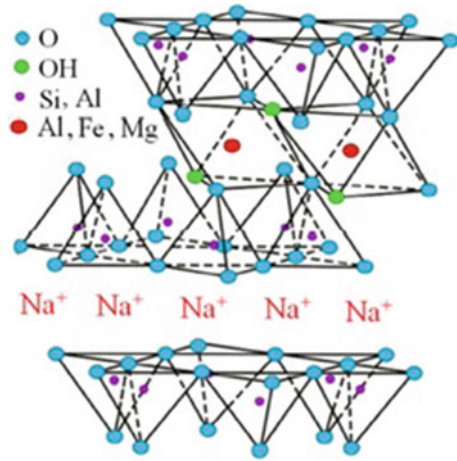


Fig. 8 Stress strain curve for composite without nanoclay and varying wt% of nanoclay

**Fig. 9** Crystallographic structure of Cloisite 30B [19]



The outer layers are of silicon tetrahedral and the inner layer is of aluminum octahedral. The crystallographic structure of Cloisite 30B is as shown in Fig. 9. These layers contain platelet-shaped particles. These particles when mixed with epoxy the sonication process is required.

To understand the structure XRD examination is required. The X-Ray Diffraction will give the results in the form of *d*-spacing and angle 2 theta. The *d*-spacing can be measured using Bragg’s Law. The X-Ray Diffraction was carried on a Panalytical X-Ray diffractometer. The Copper K(alpha) radiation was used in the diffractometer to measure the *d*-spacing and the angle 2 theta. The wavelength which strikes the atom is of intensity 0.154 nm with a scanning speed of 1.2°/min. The XRD scans were conducted on the samples through 2 theta of 0–20° and the results are shown in Figs. 10 and 11. In Fig. 10, the results are for the samples of pure epoxy and it

**Fig. 10** XRD pattern of pure epoxy

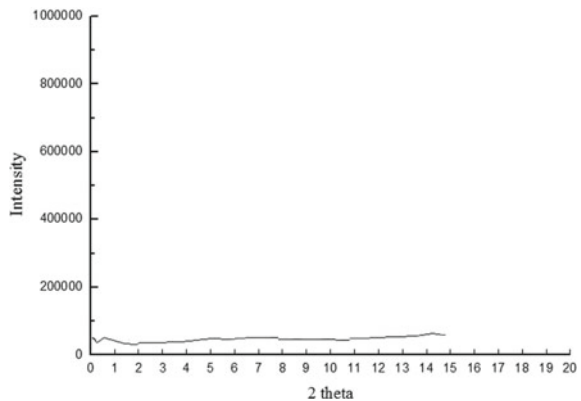
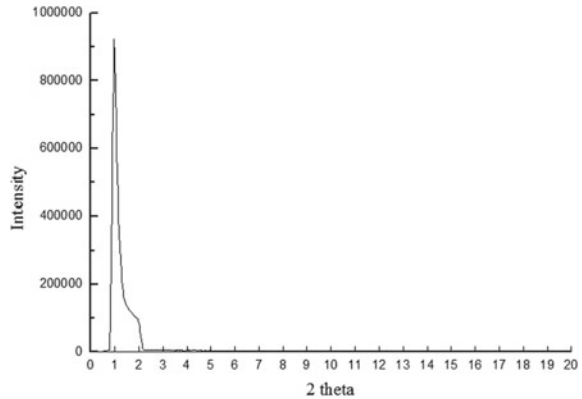


**Fig. 11** XRD pattern of epoxy with 3 wt% of nanoclay



is clear from the figure that there is no peak because of the amorphous structure of epoxy whereas Fig. 11 shows the strong peak which is because of the intercalated structure.

From the XRD, it is observed that there is an increase in strength is because of the mechanical interlocks between carbon fiber and epoxy whereas a decrease in strength with further increase in wt% is because of the clusters formed in the matrix. When the nanoclay is mixed with the epoxy for the formation of composite, up to 3 wt% of nanoclay, will make the intercalated structure which leads to the increase in load-carrying capacity of nanocomposite. This ultimately leads to an increase in strength of the composite. Similarly, the flexural strength was increased because of improved interfacial properties. Figure 12a, b are the SEM images of carbon laminates with 3 wt% and without nanoclay. It can be seen from SEM in Fig. 12b that the amount of matrix material around the fiber is more as compared to Fig. 12a which is indicating the strong interfacial bond between fiber and matrix. Due to this carbon laminate with an addition of 3 wt% of nanoclay gives high strength.

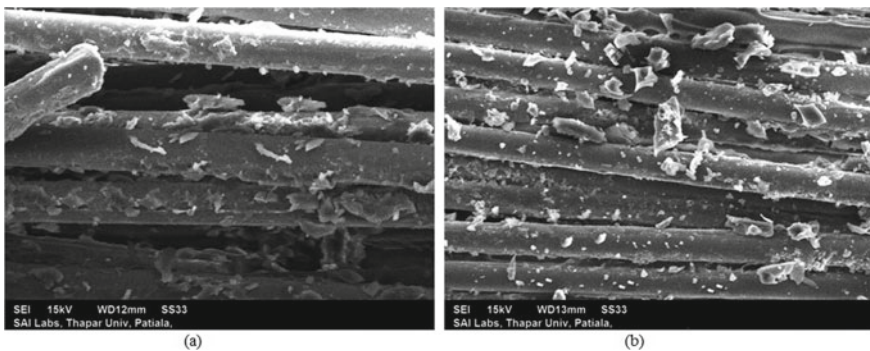


**Fig. 12** SEM images of the sample

## 4 Conclusion

In the present work, the tensile and flexural properties of the carbon fiber-reinforced composite with nanoclay are examined under ASTM D3039 and D7264, respectively. The tensile strength and modulus are improved by 28–32% and 25–30%, respectively, with the addition of nanoclay up to 3 wt%. Zakaria and Wang also investigate that the strength of the laminates was increased by 35% with different nanoparticles, which is considerably the same in our case also [3, 4]. The significant increase in the properties of the composite is observed because of the intercalated structure formed when the nanoclay was mixed with epoxy. The intercalated morphology was examined by XRD scan. The nanoclay beyond 3 wt% will reduce the strength of the composite. This reduced mechanical properties with the increase in wt% of nanoclay in epoxy resin lead to agglomeration between the nanoclay and epoxy.

## References

1. Sekhon, M., Saini, J.S., Singla, G., Bhunia, H.: Influence of nanoparticle fillers content on the bearing strength behavior of glass fiber-reinforced epoxy composites pin joints. *Proc. Inst. Mech. Eng. Part L J. Mater. Des. Appl.* **231**, 641–656 (2017)
2. Djabali, A., Toubal, L., Zitoune, R., Rechak, S.: An experimental investigation of the mechanical behavior and damage of thick laminated carbon/epoxy composite. *Compos. Struct.* **184**, 178–190 (2018)
3. Zakaria, M.R., Abdul Kudus, M.H., Md. Akil, H., Mohd Thirmizir, M.Z.: Comparative study of graphene nanoparticle and multiwall carbon nanotube filled epoxy nanocomposites based on mechanical, thermal and dielectric properties. *Compos. Part B Eng.* **119**, 57–66 (2017)
4. Wang, C., Zhao, M., Li, J., Yu, J., Sun, S., Ge, S., Guo, X., Xie, F., Jiang, B., Wujcik, E.K., Huang, Y., Wang, N., Guo, Z.: Silver nanoparticles/graphene oxide decorated carbon fiber synergistic reinforcement in epoxy-based composites. *Polymer (Guildf)* **131**, 263–271 (2017)
5. Shah, A., Ding, A., Wang, Y., Zhang, L., Wang, D., Muhammad, J., Huang, H., Duan, Y., Dong, X., Zhang, Z.: Enhanced microwave absorption by arrayed carbon fibers and gradient dispersion of Fe nanoparticles in epoxy resin composites. *Carbon N. Y.* **96**, 987–997 (2016)
6. Das, T.K., Ghosh, P., Das, N.C.: Preparation, development, outcomes, and application versatility of carbon fiber-based polymer composites: a review. *Adv. Compos. Hybrid Mater.* **2**, 214–233 (2019)
7. Azeez, A.A., Rhee, K.Y., Park, S.J., Hui, D.: Epoxy clay nanocomposites—processing, properties and applications: a review. *Compos. Part B Eng.* **45**, 308–320 (2013)
8. Qin, W., Vautard, F., Askeland, P., Yu, J., Drzal, L.: Modifying the carbon fiber-epoxy matrix interphase with silicon dioxide nanoparticles. *RSC Adv.* **5**, 2457–2465 (2015)
9. Landowski, M., Strugała, G., Budzik, M., Imielińska, K.: Impact damage in SiO<sub>2</sub> nanoparticle enhanced epoxy-carbon fibre composites. *Compos. Part B Eng.* **113**, 91–99 (2017)
10. Spanos, P.D., Kotsos, A.: A multiscale Monte Carlo finite element method for determining mechanical properties of polymer nanocomposites. *Probab. Eng. Mech.* **23**, 456–470 (2008)
11. Murugan, P., Naresh, K., Shankar, K., Velmurugan, R., Balaganesan, G.: High velocity impact damage investigation of carbon/epoxy/clay nanocomposites using 3D computed tomography. *Mater. Today: Proc.* **5**(9), 16946–16955 (2018)
12. Limam, O., Foret, G., Zenzri, H.: Ultimate strength of pin-loaded composite laminates: a limit analysis approach. *Compos. Struct.* **93**, 1217–1224 (2011)

13. Aluko, O.: An analytical method for failure prediction of composite pinned joints. In: Proceedings of the World Congress on Engineering, vol. III, p. 7 (2011)
14. Oner, G., Unal, H.Y., Pekbey, Y.: Mechanical performance of hybrid carbon/fiberglass composite laminates reinforced with nanoclay. *Acta Phys. Pol. A* **134**, 164–167 (2018)
15. Alsaadi, M., Bulut, M., Erklığ, A., Jabbar, A.: Nano-silica inclusion effects on mechanical and dynamic behavior of fiber reinforced carbon/kevlar with epoxy resin hybrid composites. *Compos. Part B Eng.* **152**, 169–179 (2018)
16. Tsai, S.N., Carolan, D., Sprenger, S., Taylor, A.C.: Fracture and fatigue behaviour of carbon fibre composites with nanoparticle-sized fibres. *Compos. Struct.* **217**, 143–149 (2019)
17. Eskizeybek, V., Ulus, H., Kaybal, H.B., Şahin, Ö.S., Avcı, A.: Static and dynamic mechanical responses of CaCO<sub>3</sub> nanoparticle modified epoxy/carbon fiber nanocomposites. *Compos. Part B Eng.* **140**, 223–231 (2018)
18. Kaybal, H.B., Ulus, H., Demir, O., Ömer, S.S.: Effects of alumina nanoparticles on dynamic impact responses of carbon fiber reinforced epoxy matrix nanocomposites. *Eng. Sci. Technol. Int. J.* **21**, 399–407 (2018)
19. Zabihi, O., Ahmadi, M., Nikafshar, S., Chandrakumar Preyeswary, K., Naebe, M.: A technical review on epoxy-clay nanocomposites: structure, properties, and their applications in fiber reinforced composites. *Compos. Part B Eng.* **135**, 1–24 (2018)

# Microstructural Evolution and Mechanical Properties of Aluminum Alloy 7075-T651 Processed by Friction Stir Processing



Ravi Kumar, Md. Manzar Iqbal, Subhash Singh, and Kaushik Pal

**Abstract** Aluminum-based alloys are broadly utilized in the automobile and aerospace industry due to its lightweight, excellent electrical and thermal conductivity, good machinability, and superior resistance to corrosion. In this experimental study, several tests have been carried out for obtaining the overall mechanical properties before and after friction stir processing (FSP) through suitable processing parameters: tool speed, feed rate, and tool tilt angle with overlapping ratio. Some mechanical properties have been reduced while the ductility of the FS processed alloy has been improved caused by fine grain refinement in the stir zone. It is also clearly shown from the electron backscattered diffraction (EBSD) and transmission electron microscopy (TEM) results that the grain refinement of average grain size  $4.5\ \mu\text{m}$  has been obtained which is responsible for increasing the ductility and also various intermetallic particles were homogeneously distributed into the matrix.

**Keywords** Lightweight materials · Metal matrix composites · Electron backscattered diffraction (EBSD) · Friction stir processing · Ductility

## 1 Introduction

Aluminum alloy (AA) 7075 has good corrosion resistance and strength, suitable to be used in the aircraft and automobile industry, but it has a drawback due to its poor ductility as well as poor formability. This limitation of the alloy is restricting the application of AA7075 in various applications. In this work, AA7075 is processed via

---

R. Kumar

Mechanical Engineering Department, Institute of Engineering and Technology, Dibrugarh University, Dibrugarh, Assam 786004, India

Md. M. Iqbal · S. Singh

Department of Production & Industrial Engineering, National Institute of Technology Jamshedpur, Jamshedpur, Jharkhand 831014, India

K. Pal (✉)

Department of Mechanical and Industrial Engineering, IIT Roorkee, Roorkee, UK 247667, India  
e-mail: [kaushik@me.iitr.ac.in](mailto:kaushik@me.iitr.ac.in)

© Springer Nature Singapore Pte Ltd. 2020

C. Prakash et al. (eds.), *Advances in Materials Science and Engineering*,

Lecture Notes in Mechanical Engineering,

[https://doi.org/10.1007/978-981-15-4059-2\\_14](https://doi.org/10.1007/978-981-15-4059-2_14)

friction stir processing technique by keeping in mind to modify the basic mechanical properties for instance ductility and formability, by superplastic deformation of grains of AA7075.

Friction stir processing (FSP) is a solid-state process that is an advanced version of friction stir welding (FSW). In FSP, modification of microstructure and enhancement of surface takes place, but there are needs for further improvement in analysis of correlation between parameter of friction stir processing and different mechanical properties [1, 2]. This processing method was first discovered in the year 1991 by The Welding Institute (TWI) [3]. Aluminum 1050 exhibits a very fine microstructure at a lower speed (rpm) as well as low transverse speed. In this process, it is highly sensitive to optimize the processing parameters which take part in the formation of microstructure [4]. By the result of multipass overlapping FSP, a relatively uniform ultrafine grain (UFG) microstructure formed. In short, FSP could be used to fabricate any required size of sheet to create ultrafine grain structure, AA7075 T-6 aluminum alloy was a high strength heat treatable alloy. This alloy has been dynamically recrystallized to nanosize grains which are done by frictional heat between tooltip and alloy itself. The tool rotation, rate of feed, and process overlapping have significant effect on the microstructure distribution of the alloy [5]. The mechanical properties of alloy with UFG are strongly connected to microstructure variation and distribution. Hall–Patch relationship shows that the properties like hardness increased due to the UFG structure described that microhardness is inverse to the grain size. The more homogeneous and finer UFG structure through friction stir processing tried to enhance the formability and ductility of material at an increasing temperature [6]. An overlapping pass was a good technique also to develop a UFG (ultrafine grain) structure. Hall–Patch relationship describes that the hardness is inversely related to the grain size, and decreasing the rotational speed enhances the hardness property of the magnesium alloy AZ31 material. It is also noted that hardness is inversely proportional to the rotational speed [6]. The decrease in size to micron level leads to drastically improve superplastic ductility, decreasing the flow stress, and reducing the optimum temperature. The key role which leads to the superplastic deformation mechanism for finer grain materials is grain boundary sliding (GBS). Also, one of the best mechanisms for superplastic deformation in FSP Al7075 alloy is GBS [7]. It was also observed that fine equiaxed as well as homogeneous grain microstructure has been formed because of dynamic re-crystallization under the overlapped FSP having the  $OR = 1/2$  for AA7022 aluminum alloy, multipass overlapping with the threaded tool tip profile has large area of superplastic deformation [8].

The study reported the variation of mechanical properties of AA6063-T6 at different axial load 8, 10, 12 kN and shown that 10 kN at 1400 rpm 6063 gave the best mechanical properties due to proper microstructural conditions, it was impractical to get an accurate stirring to fulfill the whole combination of the various process parameters. Therefore, it becomes very important to decide to make the most suitable combination of the process parameters which lead to valuable hardness [9]. But a study on AA7075 at 700 rpm and 3° tool tilt achieved good mechanical properties and microstructure, specific tooltip geometry and profile of shoulder exhibits critical impact on superplastic flow of material [10]. A lot of studies had been performed

on FSP to enhance the microstructure properties, mechanical properties, and grain structure properties. Accurate relationship between the process parameters results in process optimization. Alloy has been processed by inserting a cylindrical tool with concentric tip also shoulder which run along the line of intersect. Generation of localized heat due to frictional heating between tool and alloy due to continuous contact lead to an increment in the temperature of alloy and here the grains were plastically deformed resulted in significant grain refinement at elevated temperature [11–15]. The friction stir processing becomes valuable for plastic material that can be used in multiple passes which led to the production of more regions of a material having superplastic properties, due to multiple passes of aluminum alloy elongation gained which is superplastic in nature, while the materials processed by single-pass has shown somewhat superior elongation [16]. Mechanical properties for instance hardness and bending strength has been enhanced locally by multipass overlapping [17]. Tool shoulder diameter was also a very important parameter in tool geometry. Variation of tool shoulder diameter causes the variation of the microhardness of the material irrespective of tooltip, so to enhance the mechanical properties standard tool shoulder diameter is required [18]. FSP processing is dynamically recrystallized the grain which has shifted the morphology of grain from elongated grain of base alloy (AA 5083) to the fine with a high-angle of grain boundary and equiaxed grain of FS processed sample which resulted in the enhancement in the ductility of the base alloy after FSP [19].

So, to overcome these problems authors have tried to perform this research. In this research work, the authors tried to modify the ductility of the AA7075 through friction stir processing by the variation in suitable processing parameters like tool speed, feed rate as well as tool tilt angle with overlapping ratio (OR) = 1/2. There were several tests like tensile, three-point bending and microhardness test, microstructure analysis, etc. conducted to justify it.

## 2 Materials and Methodology

Energy-dispersive X-ray spectroscopy (EDX) analysis examined the chemical composition of rolled plate of AA 7075 T-651 aluminum alloy which is indicated in Fig. 1. The experiment was carried out by a workpiece of the dimension of 25 cm × 10 cm × 6 mm. A nonconsumable tool of die steel material (D2 steel) with threaded cylindrical tool geometry. The diameter of the shoulder was 19 mm, 25 mm shoulder-length, 8 mm pin diameter and 4 mm length.

Friction stir processing was performed through the suitable value of process parameters like the rotational speed of tool 508 rpm, tool feed rate was taken 20 mm/min, tool tilt angle 1° and overlapping for the next pass was approximately 50%. Also, the samples were applied with an axial force of 12 kN. The overall schematic diagram of tool and work material arrangement in friction stir processing is illustrated in Fig. 2.



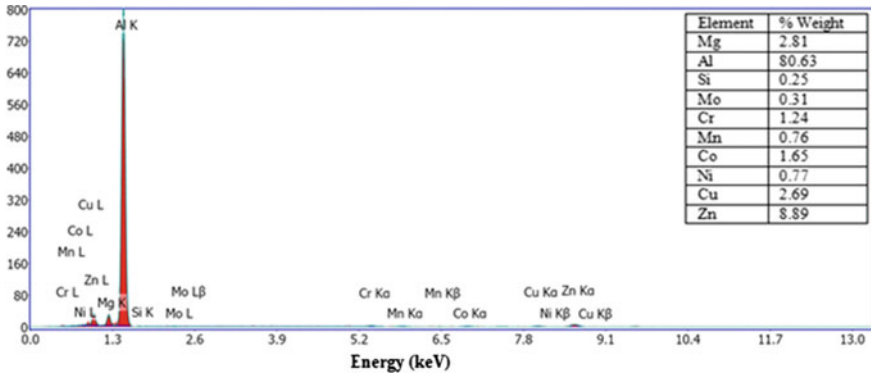


Fig. 1 Energy-dispersive X-ray spectroscopy (EDX) analysis of AA 7075 T-651 aluminum alloy

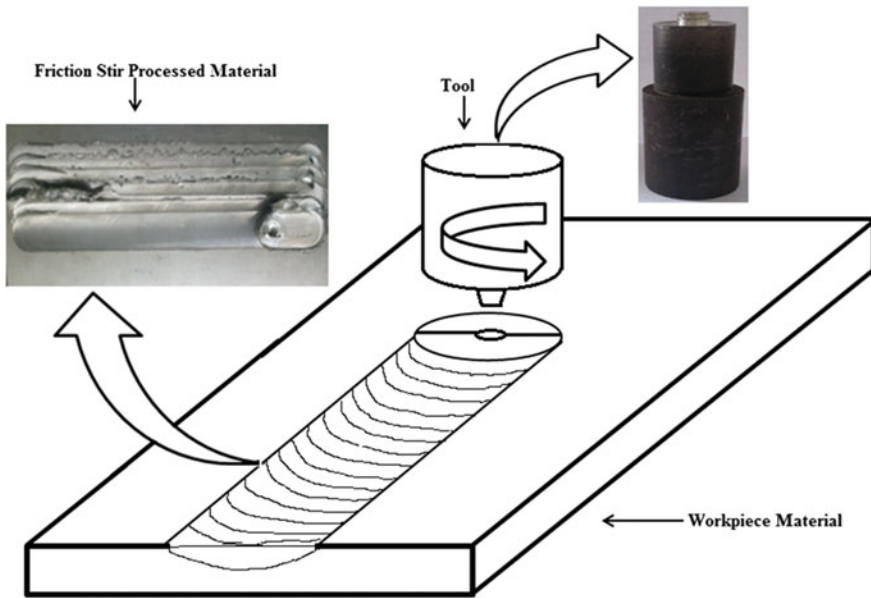
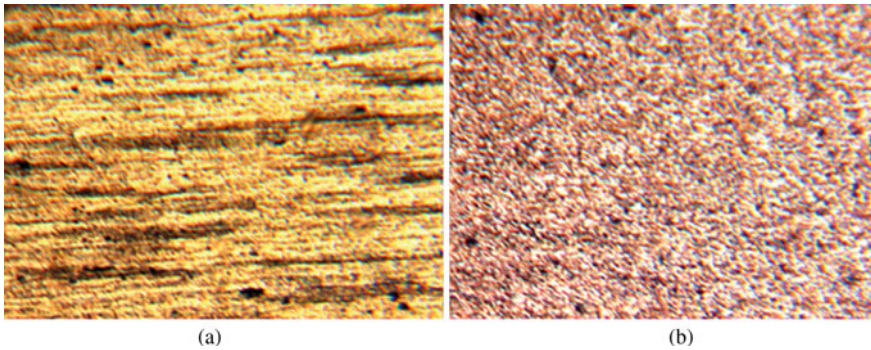


Fig. 2 Schematic diagram of tool and base alloy in friction stir process

### 3 Results and Discussion

#### 3.1 Microstructure Analysis

The microstructure image of as received and fabricated AA7075-T651 was obtained by optical microscope of Weltzar Leitz MM6 by using Leica DFC 295 magnifying



**Fig. 3** Optical micrographs for the **a** base alloy and **b** FSPed alloy

lens at magnifications of 200. Then, the microstructure analysis samples were polished by various sandpaper grades ranging from 320 to 2000 as well as cloth polishing was carried out by using abrasive powder of magnesium oxide (MgO). Further, for a sample was given glassy appearance by etching with Keller's solution. The samples were then completely dried to microstructure analysis. Figure 3 exhibits the microstructure of the prepared samples for unprocessed and processed alloy, which indicates that a very fine and equiaxed grain of AA 7075-T651 as shown in Fig. 3b because of the dynamic recrystallization source by intense plastic deformation. The microstructure of the base alloy seems to be shaped like elongated grain characteristic of a hot rolled structure as shown in Fig. 3a. Finally, the initial structure of base alloy was destroyed; also, it was found that homogeneous distribution of precipitates all over the region.

### 3.2 EBSD Analysis

Electron backscattered diffraction (EBSD) analysis was done to identify the friction stir processing (FSP) effect on the alloys. It has been found that after FSP grain microstructure is refined with an average size of grain was measured as 4.5 micron. The EBSD analysis of original alloy and the friction stir processed (FSPed) alloy were done with Quanta 200FEG from FEI Netherlands. EBSD analysis was done by polishing the samples with various grades of sandpapers as well as by the magnesia powder. Further, electropolishing was done for obtaining a very fine surface with a glassy appearance. The experiment work revealed that the quantity of grain refinement happened in a single step with overlapping. After FSP, the grain refinement and size of the grains was found to be mostly a function of process parameters as well as the tool geometry [20]. The EBSD map that is shown in Fig. 4b exhibits finer and more equiaxed grains at the processing region, by dynamic recrystallization (DRX). The color orientation communicates to the orientation of the grains; [001]

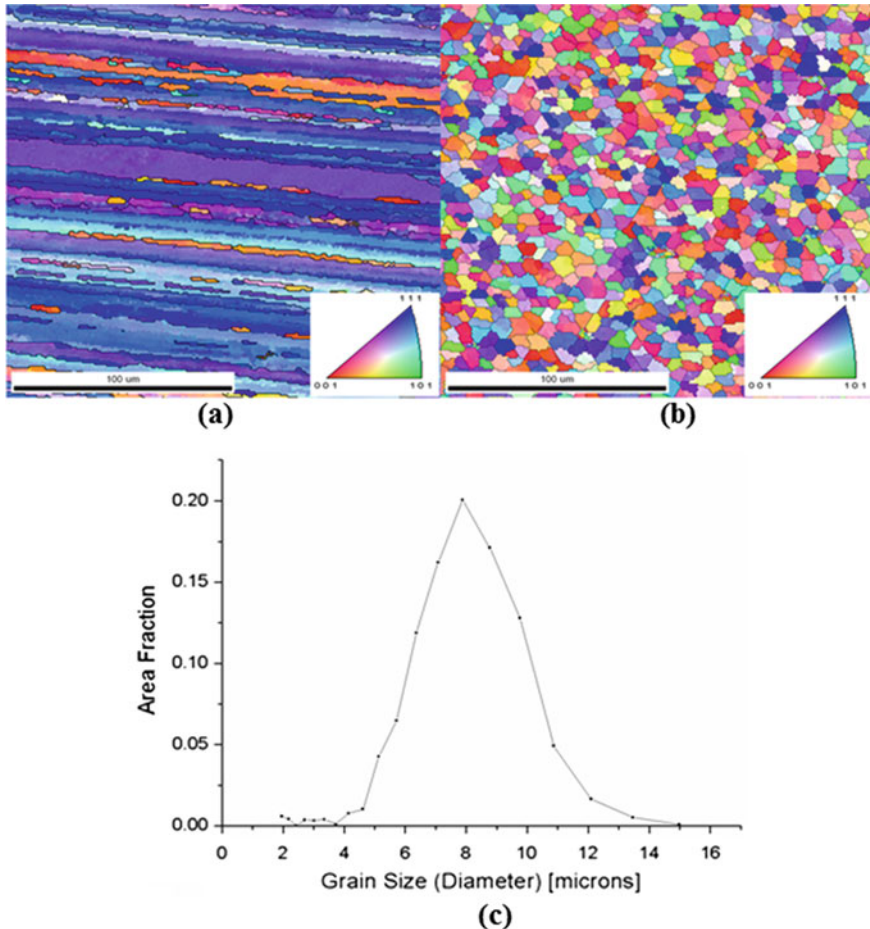


**Fig. 4** EBSD map represents **a** base alloy, **b** FSPed alloy and **c** distribution of grain size

inverse pole figure shows the color orientations developed at the forward, center and backward side of the stir zone (SZ). A strong peak in the direction of [001] color orientation which shows in the center is confirmed through EBSD color representation. EBSD map has a % of high-angle grain boundary (HAGB) in Fig. 4b for FS processed is 56.1% and low-angle grain boundary 24.7% with misorientation angle  $>15^\circ$  and for base alloy HAGBs is less than FS processed alloy. So, from the result, it can be expected that grains have been refined into equiaxed grains with high-angle grain boundary which represents the stability of the grains. Figure 4c shows the distribution of the grain size at the center of the (SZ).

The mechanical properties of materials are directly related to grain refinement. There are numerous techniques by which grain refinement can be achieved. The ultrafine grain structure elements can be gained through severe plastic deformation

(SPD) methods. The reason behind that at high strain rate and quite low temperature, the material was substantially deformed. After FSP, the average grain size is drastically reduced which resulted in the refining of microstructure of the composites in the form of ultrafine grain size. Also, refinement of grain at stir zone in FSP is significantly depended upon the chemistry of the material, tool geometry, vertical downward force, and temperature of the surrounding environment [21].

The transition of base alloy into elongated grains of FS processed in the stir zone (SZ) is disclosed from the EBSD color map as shown in Fig. 4a, b. The areas where microvoids occur belong to that region which faces lower temperatures as well as strain rate as compared to stir zone within the processing area, which can be attributed to the fault of the processing technique and processing parameter. The dynamic recrystallization (DRX) is not occurring in that region where microvoids have existed because of inadequate strain along with a high percentage of dynamic recovery (DRV). Microvoids produced through DRV organizes itself at low-angle subgrain boundaries (LASGBs) during deformation providing up to a large section of low-angle boundaries in that area. Finally, the microstructure has equiaxed with a greater number of fine grains with healthy explained grain boundaries along with high-angle grain boundaries.

### 3.3 TEM Analysis

Transmission electron microscopy (TEM) was done by TECNAI G220 S-TWIN (FEI Netherlands) to examine the microstructure refinement at stir zone made by friction stir processing (FSP) and to differentiate the structure of the original alloy. For TEM analysis, the samples of base alloy and FSPed alloy were processed by mechanical grinding operation with a thickness of 3 mm and further thinning through a twin jet electropolishing unit having a mixture of 20% nitric acid and 80% methanol at a temperature of  $-30^{\circ}\text{C}$ . TEM micrographs of the base as well as FSPed alloy are shown in Fig. 5. The pictures in Fig. 5a, b depicts the elongated gains and Fig. 5c, d shows the fine and more equiaxed grain microstructure in addition to grain boundaries that were well-defined. Grains were refined into separate subgrains and subgrain boundaries from main region of a well-defined grain boundary. Higher magnification TEM micrograph shows that these subgrain boundaries occur because of the collection of different dislocations loaded on a plane. These subgrain boundaries show that dislocations occur at low-angle subgrain boundaries with low misorientation angle ( $<15^{\circ}$ ) with the act of dynamic recovery (DRV) which normally occur in aluminum and microvoids generated at the time of plastic deformation in friction stir processing are changed to sub-grain boundaries to convert them into low-angle ( $<15^{\circ}$ ) grain boundaries. Over a permanent type dynamic recrystallization (DRX) process, it is possible that these low-angle grain boundaries (LAGBs) or the subgrain boundaries turn to high-angle grain boundaries (HAGBs), which is represented as the fine grain structure with well-described high-angle grain boundary [22–24]. Friction stir processing is a good technique to form equiaxed grains from the elongated

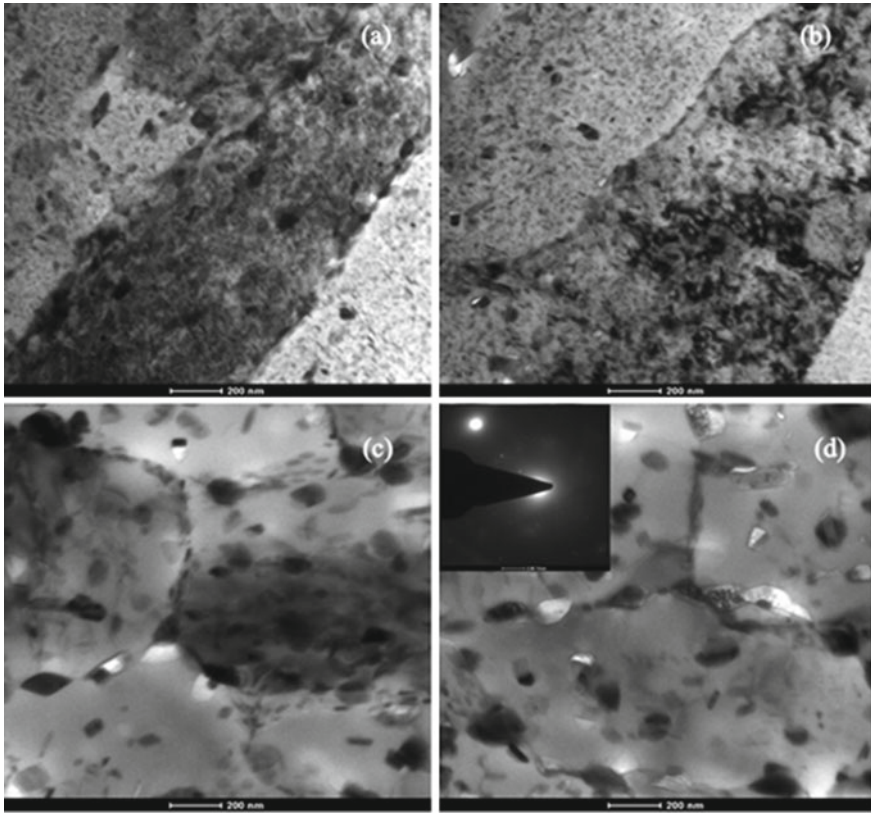


**Fig. 5** TEM micrograph represents **a, b** elongated grains of the base alloy and **c, d** equiaxed fine grains in stir zone after FS processed alloy with corresponding selected area diffraction (SAED) pattern

grains of parent alloy which characterize the mechanical properties of the alloy. From these results, GSP can be distinguished or recognized as better than other special deformation processes.

It has been noted that most of the other deformation processes include several steps for better grain refinement. While refinement of grain occurs, there are no clearly identified grain boundaries and are collected in uneven distribution of microstructure displacement or the subgrains structure. The size of grain scattering is also usually broad. Besides, the crystal lattice is wrapped in high inner stresses inside the grains [25, 26].



### 3.4 Tensile Testing

Specimen has been prepared for both base alloy (7075-T651) and FS processed alloy with the help of a shaper machine by using a round nose cutting tool. Specimens have the geometrical specification corresponding to ASTM standard (B557M-10). The tensile test was done on a universal testing machine of INSTRON (Model 5982), USA, at a load of 100 kN. The plot between the tensile stress and tensile strain for the base and FSPed alloy specimens is shown in Fig. 6 and the tensile properties are shown in Table 1. It is clear from the figure that after performing the friction stir process the ductility of the base alloy is increased and simultaneously the tensile strength is reduced. Here, the reduction in strength is mostly caused by the dissolution of very fine hardening precipitate and the reduction in preexisting dislocation and it is seen that modifying the rolled structure to an equiaxed refined structure resulted to a distinct rise in ductility.

The image of fractured surfaces of both base material as well as FSPed AA 7075 is exhibited in Fig. 7a, c. Also, Fig. 7b, d demonstrates the enlarged view of the base and FSPed alloy. The FE-SEM analysis for the fracture surfaces was carried out with Quanta 200FEG from FEI Netherlands. The fracture surface of the 7075 alloy, after

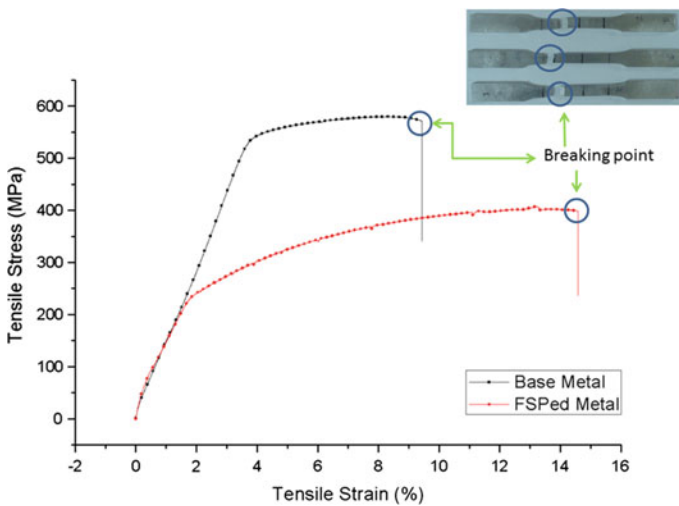
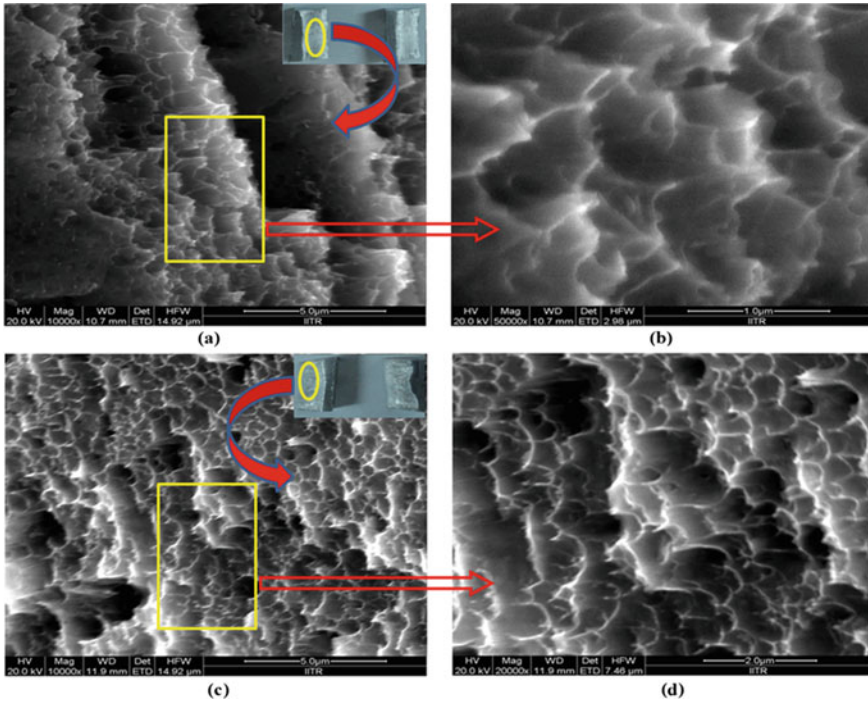


Fig. 6 Graph between tensile stress and tensile strain for the base and FSPed alloy

Table 1 Tensile properties of base and FSPed aluminum alloy

Material	0.2% proof stress (MPa)	UTS (MPa)	% elongation	Time to failure (s)
Base AA 7075	544.440	571.093	9.44	499.60
FSPed AA7075	241.267	398.918	14.58	787.10



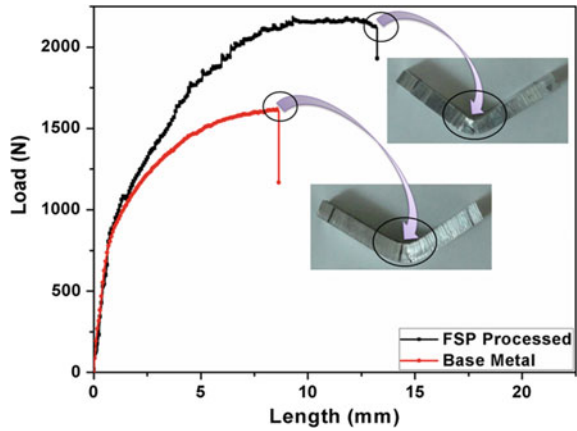
**Fig. 7** FE-SEM image of the fractured surfaces of both base alloy and FSPed Al alloy

the tensile test, has resulted in microscopic cavities of various sizes and shapes, as the observation made by FE-SEM test revealed that there is a ductile fracture mechanism and improvement in the ductility or the delay in necking is due to the presence of fine cavities at the fracture surface of the FSPed sample. The fine-grained material having a high portion of high-angle grain boundary (HAGB) and grain boundary sliding (GBS) plays a significant function in the deformation process.

### 3.5 Three-Point Bending Test

A three-point bending test sample has been prepared with specific dimensions such as gauge length 50 mm, width 10 mm, and thickness 5 mm for both base and processed alloy. The bending tests have been conducted on universal testing machine made by Kalpaks, K test series Pune (INDIA), having specification S.R. No. 130502, model KIC-2-300-C, and a maximum loading capacity 30 kN. Figure 8 reveals the graph between the applied force and displacement for the base and FSPed alloy. It is quite

**Fig. 8** Plot of the applied load versus length for base and FSPed alloy



clear from the graph that the displacement for the base alloy is less as compared to the stir alloy. After FSP, the ductility of the material is increased, and the bending strength of the stirred material also increases.

### 3.6 X-Ray Diffraction Analysis

AA 7075 contains a huge quantity of various intermetallic particles like magnesium, silicon, molybdenum, chromium, manganese, cobalt, nickel, copper, zinc, etc. with various sizes. Most of the particles were identified through the EDX analysis and XRD analysis as indicated in Figs. 1 and 9, respectively. The samples which are used for XRD analysis were cut from the FSPed alloy of different zones. Further, the samples were tested by using apparatus Bruker D8 X-ray diffractometers consist of Cu K $\alpha$  radiation ( $\lambda = 1.5405 \text{ \AA}$ ), the angle range 5–120°, the accelerating voltage was taken up to 40 kV, electron current ranges up to 40 mA and equipped with Laptop and EVA software. From the XRD pattern shown in Fig. 9, it can be noted that there is a new peak formed due to the precipitation of metastable phase of the particles in the overlap friction stir processed alloy sample. Also, as a result of the severe plastic deformation in the overlap region, the intensity of the peaks changed rapidly and obtained the highest peak intensity. The change in the peak intensities is caused by the refinement of grain and homogeneous distribution of various intermetallic particles in the matrix after processing.



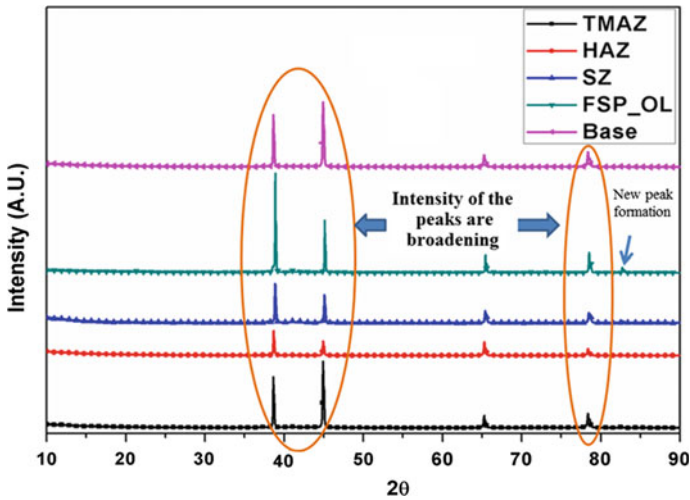


Fig. 9 XRD pattern of the different zones of FSPed alloy

## 4 Conclusions

In summary, we have concluded that severe plastic deformation has been taken place by performing the friction stir process on to the base alloy (AA 7075-T651). It is clear from the optical microscopy, EBSD, and TEM microstructure analysis that the elongated grain structure of the base alloy converted in the form of ultrafine grain structure with an average grain size of  $4.5 \mu\text{m}$  after processing. Homogeneous distribution of various intermetallic particles into the matrix was showed in XRD pattern. Mechanical properties like microhardness and tensile strength have been reduced while the ductility of the FS processed alloy has been increased due to fine grain refinement in stir zone.

## References

1. Ma, Z.Y.: Friction stir processing technology: a review. *Metall. Mater. Trans. A* **39**(3), 642–658 (2008)
2. Mishra, R.S., Ma, Z.Y.: Friction stir welding and processing. *Mater. Sci. Eng. R Rep.* **50**(1–2), 1–78 (2005)
3. Su, J., Nelson, T.W., Sterling, C.J.: Friction stir processing of large area bulk UFG aluminum alloys. *Scr. Mater.* **52**(2), 135–140 (2005)
4. Kurt, A., Uygur, I., Cete, E.: Surface modification of aluminum by friction stir processing. *J. Mater. Process. Technol.* **211**(3), 313–317 (2011)
5. Su, J., Nelson, T.W., Sterling, C.J.: Microstructure evolution during FSW/FSP of high strength aluminum alloys. *Mater. Sci. Eng.: A* **405**(1–2), 277–286 (2005)
6. Darras, B.M., Khraishes, M.K., Abu-Farha, F.K., Omar, M.A.: Friction stir processing of commercial AZ31 magnesium alloy. *J. Mater. Process. Technol.* **191**(1–3), 77–81 (2007)

7. Ma, Z.Y., Mishra, R.S., Mahoney, M.W.: Superplastic deformation behaviour of friction stir processed 7075 Al alloy. *Acta Mater.* **50**(17), 4419–4430 (2002)
8. Nascimento, F., Santos, T., Vilaca, P., Miranda, R.M., Quintino, L.: Microstructure modification and ductility enhancement of surface modified by FSP in aluminum alloys. *Mater. Sci. Eng.: A* **506**(1–2), 16–22 (2009)
9. Karthikeyan, L., Kumar, V.S.S.: Relationship between process parameter and mechanical properties of friction stir processed AA6063-T6 aluminum alloy. *Mater. Des.* **32**(5), 3085–3091 (2011)
10. Cavaliere, P., Squilace, A.: High temperature deformation of friction stir processed 7075 aluminum alloy. *Mater. Charact.* **55**(2), 136–142 (2005)
11. Mishra, R.S., Mahoney, M.W.: Friction stir processing: a new grain refinement technique to achieve high strain rate super plasticity in commercial alloys. *Mater. Sci. Forum* **357–359**, 507–514 (2001)
12. Mishra, R.S., Mahoney, M.W., Mcfadden, S.X., Mara, N.A., Mukherjee, A.K.: High strain rate superplasticity in a friction stir processed 7075 Al alloy. *Scr. Mater.* **42**, 163–168 (2000)
13. Charit, I., Mishra, R.S.: High strain rate superplasticity in a commercial 2024 Al alloy via friction stir processing. *Mater. Sci. Eng. A* **359**(1–2), 290–296 (2003)
14. Saito, N., Shigematsu, I., Komaya, T., Tamaki, T., Yamauchi, G., Nakamura, M.: Grain refinement of 1050 aluminum alloy by friction stir processing. *J. Mater. Sci. Lett.* **20**(20), 1913–1915 (2001)
15. Know, Y.J., Shigematsu, I., Saito, N.: Mechanical properties of fine-grained aluminum alloy produced by friction stir process. *Scr. Mater.* **49**(8), 785–789 (2003)
16. Johannes, L.B., Mishra, R.S.: Multiple passes of friction stir processing for the creation of superplastic 7075 aluminum. *Mater. Sci. Eng. A* **464**(1–2), 255–260 (2007)
17. Gandra, J., Miranda, R.M., Vilaca, P.: Effect of overlapping direction in multipass friction stir processing. *Mater. Sci. Eng.: A* **528**(16–17), 5592–5599 (2011)
18. Elangovan, K., Balasubramanian, V.: Influences of pin profile and rotational speed of the tool on the formation of friction stir processing zone in AA2219 aluminum alloy. *Mater. Sci. Eng. A* **459**(1–2), 7–18 (2007)
19. Ehab, A., Danaf, E., Magdy, M., Rayes, E., Soliman, S.M.: Friction stir processing: an effective technique to refine grain structure and enhance ductility. *Mater. Des.* **31**(3), 1231–1236 (2010)
20. Yadav, D., Bauri, R.: Effect of friction stir processing on microstructure and mechanical properties of aluminium. *Mater. Sci. Eng. A* **539**, 85–92 (2012)
21. Singh, S., Pal, K.: Effects of texture evolution on mechanical and damping properties of SiC/ZnAl<sub>2</sub>O<sub>4</sub>/Al composite through friction stir processing. *J. Mater. Res. Technol.* **8**(1), 222–232 (2019)
22. Jata, K.V., Semiatin, S.L.: Continuous dynamic recrystallization during friction stir welding of high strength aluminium alloys. *Scr. Mater.* **43**, 743–749 (2000)
23. Yadav, D., Bauri, R.: Processing, microstructure and mechanical properties of nickel particles embedded aluminium matrix composite. *Mater. Sci. Eng. A* **528**(3), 1326–1333 (2011)
24. Ko, Y.G., Shin, D.H., Park, K.T., Lee, C.S.: An analysis of the strain hardening behaviour of ultra-fine grain pure titanium. *Scr. Mater.* **54**(10), 1785–1789 (2006)
25. Valiev, R.Z.: Structure and mechanical properties of ultrafine-grained metals. *Mater. Sci. Eng. A* **234–236**, 59–66 (1997)
26. El Danaf, E.A.: Mechanical properties and microstructure evolution of 1050 aluminum severely deformed by ECAP to 16 passes. *Mater. Sci. Eng. A* **487**(1–2), 189–200 (2008)

# Pre- and Post-treatment Characterization of Petrol Contaminated Soil



Shweta Kulshreshtha , Suchita Atreya, Sudhanshu Singh, and Nitesh Singh Rajput 

**Abstract** The demand and use of petroleum products are increasing nowadays and giving rise to the problem of soil pollution. The physical, chemical and biological properties of soil are affected critically in such a way that soil becomes inefficient in supporting the growth and development plant and microbial communities. There is need to treat these polluted soils for its reclamation. In this paper, an approach to bioremediation of petrol contaminated soil has been discussed. The *Candida albicans* mediated degradation of the functional groups of petrol was analyzed by FTIR. FTIR analysis revealed the breakdown of many bond-like carbonyl ( $1670\text{--}1820\text{ cm}^{-1}$ ), alkene C=C ( $1620\text{--}1680\text{ cm}^{-1}$ ),  $\text{--C--H}$  ( $2850\text{--}3000\text{ cm}^{-1}$ ),  $=\text{C--H}$  ( $2820\text{--}2850\text{ cm}^{-1}$ ), and NH ( $3300\text{--}3500\text{ cm}^{-1}$ ). The pH of petrol contaminate soil was found to be in the basic range, i.e. 8.8 and has high conductivity. Further research on the remediating microbes and their remediation potential is required for restoring the soil quality and plant growth.

**Keywords** Petrol · Degradation · FTIR · *Candida albicans* · Soil characterization

## 1 Introduction

The increase in human activities, accidentally discharge processes lead to an increase in the release of petroleum hydrocarbon in the soil from the petrol filling station. These act as pollutants which affect the physical, chemical and biological properties of the soil and become a major problem of concern due to their effect on soil porosity, aeration, microbial population and adverse effect on the plant growth [1]. Besides this, processes at petroleum refinery such as petroleum production, purification, drilling operations and inappropriately fastened abandoned wells are the sources of soil and groundwater contamination [2–4].

---

S. Kulshreshtha · S. Atreya · S. Singh · N. S. Rajput (✉)  
Amity University Rajasthan, SP-1, Kant Kalwar, NH-11C, RIICO Industrial Area, Jaipur,  
Rajasthan 303002, India  
e-mail: [niteshthakur72@yahoo.com](mailto:niteshthakur72@yahoo.com)

© Springer Nature Singapore Pte Ltd. 2020  
C. Prakash et al. (eds.), *Advances in Materials Science and Engineering*,  
Lecture Notes in Mechanical Engineering,  
[https://doi.org/10.1007/978-981-15-4059-2\\_15](https://doi.org/10.1007/978-981-15-4059-2_15)

The physical, chemical and biological methods have been reported for cleaning off the petrol contaminated sites [5]. Bioremediation is a facile, ecofriendly and cost-effective approach for treating soil polluted sites [6–10]. Recently, microbial remediation approaches are gaining importance due to their potential not only to degrade hydrocarbon but also to improve plant health and soil reclamation [11, 12]. The plant growth-promoting rhizobacteria, fungi, bacteria are considered as a potential source to degrade hydrocarbon and therefore, these are becoming important in the field of bioremediation [13–16]. Many aerobic bacteria such as *Pseudomonas sp.*, *Rhodococcus aetherivorans*, *Bacillus licheniformis* ATHE9 and *Bacillus mojavensis* ATHE13 [17–19], white-rot fungi *Phanerochaete chrysosporium* [20], *Cunninghamella echinulata* and *mycorrhizal* fungi [20, 21] have been reported to be the tool to carry out bioremediation. The potential of many microbes is still untapped in the degradation of petrol from petrol contaminated sites.

The application of beneficial free-living bacteria which are associated with plant growth-promoting rhizobacteria (PGPR) for different bioremediation activity is gaining importance. These bacterial strains have the potential to degrade hydrocarbons in oil-contaminated sites as well as improving plant health [13–16]. Many soil microorganisms have great potential for bioremediation. They can degrade organic pollutants and using carbon as a source of energy. Besides this, certain fungi have the ability to degrade organic pollutants, like white-rot fungus (*P. chrysosporium*) is an example of ligninolytic fungi, capable of degrading hydrocarbons and other harmful environmental pollutants [20]. *C. echinulata* and *mycorrhizal* fungi have also been reported for the remediation of hydrocarbon polluted soil [20, 21].

In this study, petrol contaminated soil was analyzed for its physicochemical characteristics. Further, treatment of contaminated soil was done using yeast strains which were isolated from hydrocarbon-contaminated soil. Naturally, yeast is present in the soil in a low amount which has the ability to degrade hydrocarbon. The amount of such yeast can be amplified using culture techniques. Further, the augmented yeast inoculum is applied to the soil to promote bioremediation/biodegradation process of petrol contaminated soil [22]. The biodegradability of petrol is analyzed by Fourier Transform Infrared spectroscopy (FTIR) after every withdrawal. This data will be helpful in deciding the effect of soil augmentation by yeast for petrol degradation and soil reclamation.

Therefore, the soil sample collected from the petrol pump area in Jaipur, Rajasthan for studying the effect of microorganisms in degrading the hydrocarbon. However for studying the effect on hydrocarbon, the soil (unautoclaved) is artificially contaminated with petrol, in order to isolate highly potent yeast strain.

## **2 Material and Method**

### ***2.1 Collection of the Sample from Petrol Contaminated Site and its Characterization***

Soil samples were collected from agricultural fields located near the petrol pump area in the rural part of Jaipur city, India. The distance between the petrol pump and sampling site was 200 m. Soil was dug up to 5 cm depth and then soil samples were collected. Prior to physicochemical and biological analysis, soil samples were passed through a sieve with 2 mm pore-size to separate large particles like plant debris, roots residues and pebbles. Water suspension was prepared by mixing 1:2.5 ratio with water and then, pH was measured using Systronics Water Analyser 371 which is a microcontroller-based instrument. The same instrument was used for measuring dissolved oxygen (D.O.), salinity, conductivity and temperature of the soil sample.

### ***2.2 Pre- and Post-analysis by FTIR***

The appearance and disappearance of major functional groups of petrol (pre-treatment and post-treatment) were assessed using FTIR spectroscopy. The soil was mixed with potassium bromide (KBr) into a mold in 1:100 ratio. The FTIR spectrum was captured in the 4000–400  $\text{cm}^{-1}$  region with a resolution of 4  $\text{cm}^{-1}$  using GX FTIR system (Shimadzu). Similar process was adopted for the soil withdrawn at weekly interval.

### ***2.3 Inoculation on Basal Media for the Isolation of Yeast***

Soil sample was taken in sterile centrifuge tube and centrifuged at 5000 rpm for 20 min by taking the soil in Eppendorf tubes and putting 0.75% saline solution (NaCl), i.e. 200  $\mu\text{l}$ . The solution was spread on the sterile basal media having composition for g/l, i.e. 3 g of  $\text{NaNO}_3$ ; 1 g of  $\text{KH}_2\text{PO}_4$ ; 0.5 g of  $\text{MgSO}_4 \cdot 7\text{H}_2\text{O}$ ; 0.5 g of KCl; 1 g of yeast extract; and 20 g agar-agar. This was followed by the addition of petrol and incubation at 37 °C for 7–15 days. To isolate the high tolerating strain of yeast, the amount of petrol was increased from 1 to 3 ml/plate.

The high petrol tolerating yeast strain was selected and obtained in pure culture using streaking technique and then, preserved at 4 °C.

## 2.4 Strain Characterization

For strain characterization test like gram staining, catalase, oxidase, nitrate reductase, DNase and IMVIC have been done. Further, characterization was done by sequencing methods. Sequencing was done by Xcelaris Ltd. Ahmedabad, Gujarat.

## 2.5 Biodegradation of Petrol

Petrol degradation was carried out in the soil in a laboratory experiment. The strain of yeast was cultured in BMS broth and then, vortexed for 10 min. The yeast cells were uniformly distributed in the broth. 2 ml of this broth was added in the flask containing 30 g of moist soil (unautoclaved soil sample). This was followed by the addition of 3 ml of petrol. These inoculated flasks were incubated at 37 °C for 21 days. 1.5 g of sample was withdrawal every week from the flask and analyzed for petrol degradation by FTIR.

## 2.6 Analysis of Yeast Growth

To check the microbial growth, the withdrawal soil samples were mixed with 0.75% of 200  $\mu$ l NaCl solution. After vortexing, the solution for 5 min, 100  $\mu$ l of the solution was spread on the BMS media in the plates and then 3 ml petrol was added, incubated at 37 °C to observe the growth.

# 3 Result and Discussion

## 3.1 Soil Characterization

The soil was characterized for the physicochemical parameters which are mentioned in Table 1. The temperature of petrol polluted soil was 27.1 °C and pH was towards the basic scale, i.e. 8.8. salinity of soil was 0.11 ppt and conductivity was 18.5 and dissolved oxygen was 31.5 ppm.

**Table 1** Characterization of soil

Parameters	Soil sample
Temperature/pH	27.1 °C/8.80
Temperature/salinity	27.8 °C/0.11 ppt
Conductivity	27.9 °C/18.5 mS/cm
Dissolved oxygen (D.O.)	30.5 °C/31.5 ppm

### 3.2 Characterization of Yeast Strain

The morphological characteristics of yeast strain showed that it was oval-shaped, Gram-negative and found in small groups of cells (Fig. 1). The biochemical characteristics of yeast strain are shown in Table 2. It was catalase, oxidase and DNase positive. However, it was found to be negative for the nitrate reductase, indole, methyl red, Voges Proskauer test and citrate utilization test. Analysis of strain by sequencing technique confirmed it as the strain of *Candida albicans*.

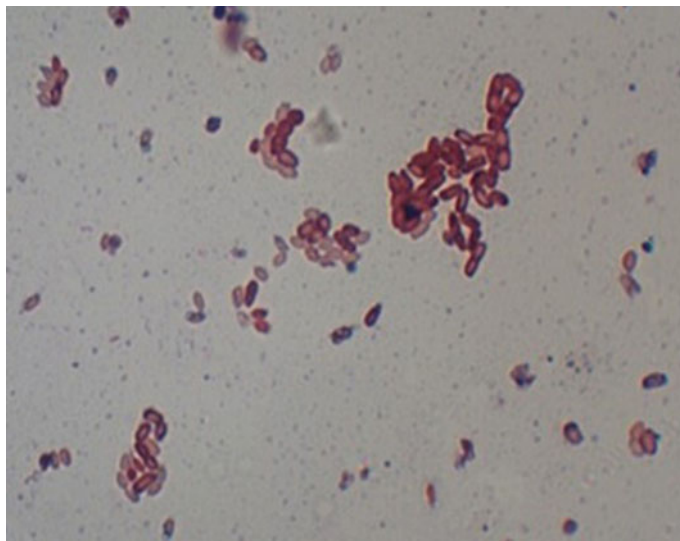


**Fig. 1** Morphological characterization of yeast strain by Gram staining technique

**Table 2** Characteristics of yeast strain

Test	<i>Candida albicans</i>
Gram staining	Gram-negative
Catalase	+
Oxidase	+
Nitrate reductase	–
DNase	+
Indole	–
Methyl red	–
VP	–
Citrate	–

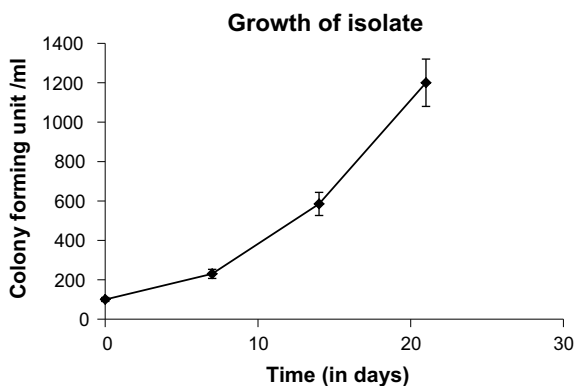


**Fig. 2** Growth of *Candida albicans* in the petrol contaminated soil

### 3.3 Analysis of Yeast Growth in Petrol Contaminated Soil

Soil samples inoculated with petrol and *C. albicans* strain on the initial day. Soil samples were weekly withdrawal and assessed for the growth of *C. albicans* strain. The increase in the number of colonies after every withdrawal represented the growth of *C. albicans* in the petrol contaminated soil (Figs. 2 and 3).

### 3.4 Pre- and Post-treatment Analysis of Petrol Degradation by FTIR

The FTIR results showed the degradation of functional groups, i.e. ether C–O ( $1000\text{--}1300\text{ cm}^{-1}$ ), –C–H ( $1350\text{--}1480\text{ cm}^{-1}$ ), N–H ( $1550\text{--}1640\text{ cm}^{-1}$ ), aldehyde C=O ( $1740\text{--}1720\text{ cm}^{-1}$ ) in the first withdrawal (7th day). This was followed by a carbonyl ( $1670\text{--}1820\text{ cm}^{-1}$ ), alkene C=C ( $1620\text{--}1680\text{ cm}^{-1}$ ). Similar results at  $1647\text{ cm}^{-1}$  were observed for petroleum-contaminated site was obtained for weak –C=C– (stretch) aromatic carbon by Ahmad et al. [23]. In the present study, another peak was observed in  $3100\text{--}3500\text{ cm}^{-1}$  for C=O. Similar peaks of C=O absorption of petroleum oil was also reported to be in the same range, i.e. at about  $1700\text{ cm}^{-1}$ , the C=C absorption at about  $1600\text{ cm}^{-1}$  by Abdulkadir et al. [24]. Furthermore, changes in the alcohol O–H ( $3200\text{--}3700\text{ cm}^{-1}$ ), NH ( $3300\text{--}3500\text{ cm}^{-1}$ ) peaks were observed in the second withdrawal of the sample. The dissociation in the groups was also observed in second withdrawal (14th day) and found to be present in C=C ( $1400\text{--}1600\text{ cm}^{-1}$ ), carbonyl ( $1670\text{--}1820\text{ cm}^{-1}$ ), =C–H ( $2820\text{--}2850\text{ cm}^{-1}$ ), –N–H ( $3300\text{--}3500\text{ cm}^{-1}$ ), and amide ( $3100\text{--}3500\text{ cm}^{-1}$ ). Moreover, new peaks were seen and dissociation increased in third withdrawal (21st day). These withdrawals revealed the degradation of petrol in the contaminated soil with respect to the initial day. Hence, FTIR reported the effectiveness of the microbial degradation of petrol.



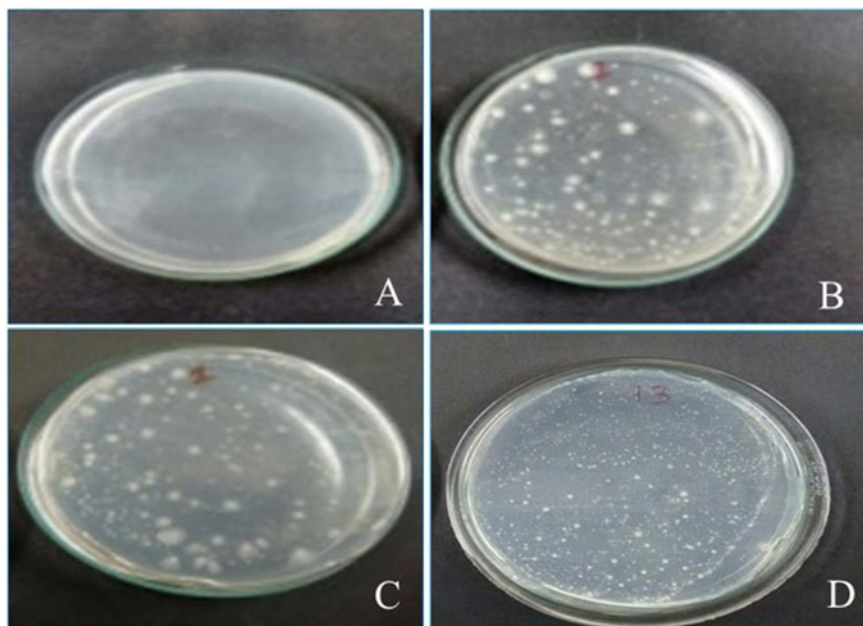


**Fig. 3** Growth of isolated yeast strain. **A** Initial day **B** at 7th day, i.e. 1st withdrawal, **C** at 14th day, i.e. 2nd withdrawal, **D** at 21st day, i.e. 3rd withdrawal

This was found to be in favour of Bhat et al. [25]. The analysis of petroleum hydrocarbon through FTIR is an easy, economically viable, versatile and efficient method (Fig. 4).

## 4 Conclusion

The results of this study reported the efficiency of *C. albicans* in degrading the petrol at the petrol contaminated sites, near the petrol pumps in the rural area. The degradation of the functional groups in soil contaminated with petrol was confirmed by the FTIR analysis. Therefore, *C. albicans* can be used for cleaning-off the polluted sites, as they increased the efficiency of this method of remediation. These findings prove that isolated strain *C. albicans* is a potential tool for biodegradation of petrol which may attract its future application.

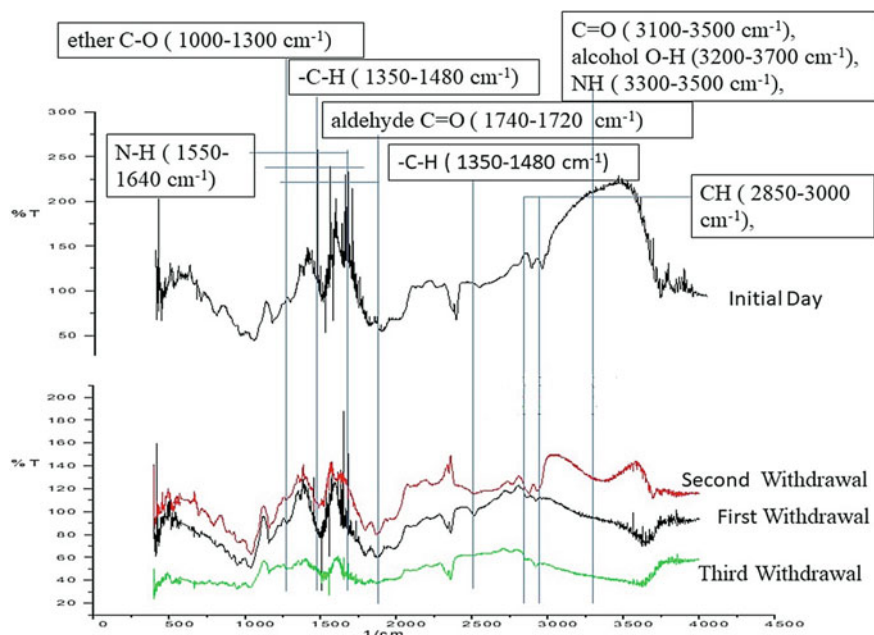


**Fig. 4** FTIR analysis of sample withdrawal every week to find out the effect of *Candida albicans* on petrol degradation

## References

1. Johnsen, A.R., Schmidt, S., Hybholy, T.K., Hendriksen, S., Jacobsen, C.S., Andersen, O.: Strong impact on the polycyclic aromatic hydrocarbon (PAH)-degrading community of a PAH-polluted soil but marginal effect on PAH degradation when priming with bioremediated soil dominated by Mycobacteria. *Appl. Environ. Microbiol.* **73**(5), 1474–1480 (2007)
2. Kharaka, Y.K., Hanor, J.S.: Deep fluids in the continents: I. Sedimentary basins. In: Drever, J.I. (ed.) *Treatise on Geochemistry*, vol. 5, pp. 499–540 (2003)
3. Adebajo, M.O., Frost, R.L., Klopogge, J.T., Carmody, O.: Porous materials for oil spill cleanup: a review of synthesis and absorbing properties. *J. Porous Mater.* **10**(3), 159–170 (2003)
4. US Environmental Protection Agency (USEPA): *Technical Support Document on Risk Assessment of Chemical Mixture*. US Environmental Protection Agency, Cincinnati, OH (1987)
5. Frick, C.M., Farrell, R.E., Germida, J.J.: *Assessment of Phytoremediation as an In-situ Technique for Cleaning Oil Contaminated Sites*. PTAC Petroleum Technology Alliance, Calgary, Canada (1999)
6. Glick, B.R.: Phytoremediation: synergistic use of plants and bacteria to clean up the environment. *Biotechnol. Adv.* **21**(5), 383–393 (2003)
7. Radetic, M., Jovic, D., Jovancic, P., Petrovic, Z., Thomas, H.: Recycled wool-based nonwoven material as an oil sorbent. *Environ. Sci. Technol.* **37**(5), 1008–1012 (2003)
8. Sarma Roy, A., Yenn, R., Singh, A.K., Deka Boruah, H.P., Saikia, N., Deka, M.: Bioremediation of crude oil contaminated tea plantation soil using two *Pseudomonas aeruginosa* strains AS 03 and NA 108. *Afr. J. Biotechnol.* **12**(19), 2600–2610 (2013)
9. Zhuang, X., Chen, J., Shim, H., Bai, Z.: New advances in plant growth promoting rhizobacteria for bioremediation. *Environ. Int.* **33**(3), 406–413 (2007)

10. Dercova, K., Sejakova, Z., Skokanova, M., Barancikova, G., Makovnikova, J.: Bioremediation of soil contaminated with pentachlorophenol (PCP) using humic acids bound on zeolite. *Chemosphere* **66**(5), 783–790 (2007)
11. Texas Research Institute, Inc.: Enhancing the Microbial Degradation of Underground Gasoline by Increasing Available Oxygen. Report to the American Petroleum Institute, Washington, DC (1982)
12. Glick, B.R.: Using soil bacteria to facilitate phytoremediation. *Biotechnol. Adv.* **28**(3), 367–374 (2010)
13. Kuppasamy, S., Thavamani, P., Megharaj, M., Naidu, R.: Biodegradation of polycyclic aromatic hydrocarbons (PAHs) by novel bacterial consortia tolerant to diverse physical settings—assessments in liquid- and slurry-phase systems. *Int. Biodeterior. Biodegrad.* **108**, 149–157 (2016)
14. Lebeau, T.: Bioaugmentation for in situ soil remediation: how to ensure the success of such a process. *Bioaugmentation Biostimulation Biocontrol* **108**, 129–186 (2011)
15. Parthipan, P., Preetham, E., Machuca, L.L., Rahman, P.K.S.M., Rajasekar, A.: Biosurfactant and degradative enzymes mediated crude oil degradation by bacterium *Bacillus subtilis* A1. *Front. Microbiol.* **8**, 1–14 (2017)
16. Cappelletti, M., Pinelli, D., Fedi, S., Zannoni, D., Frascari, D.: Aerobic co-metabolism of 1,1,2,2-tetrachloroethane by *Rhodococcus aetherivorans* TPA grown on propane: kinetic study and bioreactor configuration analysis. *J. Chem. Technol. Biotechnol.* **93**(1), 155–165 (2018)
17. Eskandari, S., Hoodaji, M., Tahmourespour, A., Abdollahi, A., Mohammadian-Baghi, T., Eslamian, S., et al.: Bioremediation of polycyclic aromatic hydrocarbons by *Bacillus licheniformis* ATHE9 and *Bacillus mojavensis* ATHE13 as newly strains isolated from oil-contaminated soil. *J. Geogr. Environ. Earth Sci. Int.* **11**, 1–11 (2017)
18. Gu, C., Wang, J., Liu, S., Liu, G., Lu, H., Jin, R.: Biogenic fenton-like reaction involvement in cometabolic degradation of tetrabromobisphenol A by *Pseudomonas* sp. fz. *Environ. Sci. Technol.* **50**, 9981–9989 (2016)
19. Pal, S., Patra, A.K., Reza, S.K., Wildi, W., Pote, J.: Use of bio-resources for remediation of soil pollution. *Nat. Res.* **1**(2), 110–125 (2010)
20. Alarcón, A., Davies Jr., F.T., Autenrieth, R.L., Zuberer, D.A.: Arbuscular mycorrhiza and petroleum-degrading microorganisms enhance phytoremediation of petroleum-contaminated soil. *Int. J. Phytoremediation* **10**(4), 251–263 (2008)
21. Karan, C.P., Rengasamy, R.S., Das, D.: Oil spill clean-up by structured fibre assembly. *Int. J. Fibre Text. Res.* **36**(2), 190–200 (2011)
22. Lim, T.T., Huang, X.: Evaluation of kapok (*Ceiba pentandra* (L.) Gaertn.) as a natural hollow hydrophobic–oleophilic fibrous sorbent for oil spill cleanup. *Chemosphere* **66**(5), 955–963 (2007)
23. Ahmad, I., Sohail, S.M., Khan, H., Khan, R., Ahmad, W.: Characterization of petroleum crude oils by fourier transform infrared (FT-IR) and gas chromatography-mass spectroscopy. *Pet. Petrochem. Eng. J.* **2**(2), 1–7 (2018)
24. Abdulkadir, I., Uba, S., Salihu, A., Almstapha, M.N.: A rapid method of crude oil analysis using FT-IR spectroscopy. *Niger. J. Basic Appl. Sci.* **24**(1), 47–55 (2016)
25. Bhat, M.M., Kumar, D., Narain, K., Yunus M.: Mycoremediation of hydrocarbon contaminated soil-FTIR based analysis. *World Appl. Sci. J.* **15**(11), 1547–1552 (2011)

# Microstructural and Mechanical Properties of AA6061 Aluminium Alloy Reinforced with Nano-SiC Particles Using FSP



Amardeep Singh Kang, Chander Prakash, Jasvinder Singh,  
and Alokesh Pramanik

**Abstract** Friction stir processing has incredible potential in the field of thermo-mechanical processing of different alloys particularly the aluminium alloys. In the ongoing years, FSP to manufacture aluminium composites has been examined around the world. With developing significance of condition amicable and low-outflow transportation vehicles, the need to utilize the more grounded high strength low weight alloys has expanded altogether. For fulfilling this purpose a small percentage of particulates need to be added in aluminium or its alloys. Addition of these particulates not only improves the microstructure of the aluminium but also modifies its mechanical properties like ultimate strength, tensile strength and yield strength. In present work, the effect of the addition of SiC nanoparticles on mechanical and metallurgical properties of friction stir processed AA6061 aluminium alloy has been studied. It has been learnt from the results that reinforced particles play a vital role in improving the mechanical and metallurgical properties of the base metal. The recrystallized grain structure was seen in the FSPed zone. The microhardness of friction stir prepared plates was dissected utilizing a Vickers hardness analyzer. SiC-reinforced Al compound surface composite came about higher microhardness. Tensile properties of as processed and heat-treated surface composites have also been evaluated. Post-processing heat treatment at 350 °C for 1 h has also been performed to ascertain its effect on microstructural and mechanical properties.

**Keywords** SiC · Friction stir processing · Reinforcement · Mechanical properties

---

A. S. Kang (✉) · C. Prakash · J. Singh  
School of Mechanical Engineering, Lovely Professional University,  
Phagwara 144411, India  
e-mail: [amardeepkang@gmail.com](mailto:amardeepkang@gmail.com)

J. Singh  
Department of Mechanical Engineering, Punjabi University, Patiala 147001, India

A. Pramanik  
School of Civil and Mechanical Engineering, Curtin University,  
GPO Box U1987, Perth, WA 6845, Australia

© Springer Nature Singapore Pte Ltd. 2020  
C. Prakash et al. (eds.), *Advances in Materials Science and Engineering*,  
Lecture Notes in Mechanical Engineering,  
[https://doi.org/10.1007/978-981-15-4059-2\\_16](https://doi.org/10.1007/978-981-15-4059-2_16)

## 1 Introduction

With developing significance of environment-friendly and low-discharge transportation vehicles, the need to utilize the more grounded high strength low weight alloys has expanded fundamentally. To cater the need of high strength to weight proportion, surface composites have been created utilizing friction stir handling (FSP) procedure. Surface composites show improved attributes of composites on the surface while holding properties of the base material. Friction stir processing (FSP) is a promising technique to develop the surface composites and one of the techniques for fabricating surface composites and improving microstructural features [1]. FSP was introduced by Mishra et al. [2] who has introduced FSP technique using the major friction stir welding (Invented at The Welding Institute, UK in 1991). Many researchers [3, 4] have revealed that ultrafine-grained particles are produced through severe plastic deformation (SPD) method.

In the category of high-performance materials, aluminium metal matrix composites (AMMCs) have developed for several engineering applications owing to their improved mechanical properties [5–8]. FSP is a favourable technique to develop AMMCs by preparing surface composite layers by which microstructural and mechanical properties are enhanced to a great extent [2, 9, 10]. From the past literature [11–14], it is revealed that FSP is useful to process surface composites, grain refinement, and microstructural change and to impart super-plasticity in cast alloys. Various studies have been reported on the fabrication of AMMCs [15–23]. The influence of grain refinement on the mechanical properties of AA6061- $\text{Al}_2\text{O}_3$  has been reported by Guo et al. [16]. It has been observed that reinforced AA6061 alloy exhibited more homogenous microstructure and improved mechanical properties in contrast to unreinforced AA6061 alloy. Yuvaraj et al. [17] studied the effect of number of passes on the various properties of micro and nano-sized B4C particles reinforced Al5083 alloy and it has been reported that a single-pass FSP leads to the formation of cluster or particle agglomeration whereas the succeeding passes completely remove the clusters and reallocate the reinforced particles in the matrix of aluminium which is attributed to enhance mechanical and tribological properties. Similar to this, Mishra et al. [2] investigated the influence of shoulder location and its traverse speed on the properties of SiC-Al5083 surface composite. It has been observed that at optimal levels of these parameters, homogeneous distribution of SiC particles was achieved which lead to a double-fold improvement in hardness of SiC reinforced Al5083 surface composite. Liu et al. [18] used a powder metallurgy technique to prepare Al-CNTs nano-composites which were further processed by FSP passes which lead to the homogenization of resulted composite and finally substantial improvement in the mechanical properties were observed.

In the present study, the surface composite of an aluminium alloy AA6061 with nano-sized SiC particles was developed using FSP technique. Further, the effect of this reinforcement on the grain size and mechanical properties has been reported.

## 2 Experimentation

### 2.1 Materials and Methods

Commercially available nano-sized SiC powder having 99.5% purity and an average particle size of 40 nm was used as reinforcement. An aluminium alloy AA6061 in the form of a plate having thickness 6 mm was used as substrate. The chemical composition of the AA6061 alloy is given in Table 1. The specimen plates were cut in the rectangular size of 100 × 60 × 6 mm as shown in Fig. 1. The two rows of blind drilled holes (each drilled hole diameter 2 mm) were prepared throughout the length of the specimen to accommodate the SiC reinforced particles for the fabrication of SiC-AA6061 surface composite using FSP.

Tool geometry is the most significant part of procedure advancement. The tool geometry assumes a scientific job in material stream and thusly administers the welding speed at which FSP can be led. A FSP tool contains a shoulder and pin. The tool has two essential restricts, (a) reasonable heating and (b) material flow. To begin with a time of tool bounce, the heating results in a general sense from the scouring among pin and workpiece. Some extra heating acknowledges deformation of the material. The tool is dove till the shoulder contacts the workpiece. The scouring between the shoulder and workpiece accomplishes the best piece of heating. From

**Table 1** Chemical composition of AA-6061 Al alloy

Elements (6061)	Mn	Fe	Mg	Si	Cu	Zn	Ti	Cr
Percentage %	0.0–0.15	0.0–0.70	0.80–1.20	0.40–0.80	0.15–0.40	0.0–0.25	0.0–0.15	0.04–0.35

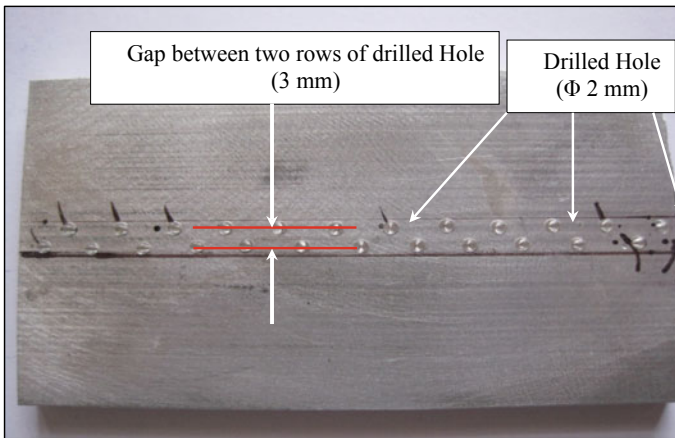


**Fig. 1** Geometry of drilled holes and specimen before FSP

**Fig. 2** FSP tool; pin diameter and pin length (5 mm)



the heating perspective, the distinctive size of pin and shoulder is gigantic, and the other game plan highlights are not major. The square pin FSP tool with shoulder estimation of 20 mm has been used in the present assessment as showed up in Fig. 2.

The SiC particles were packed in the drilled holes of the specimen as shown in Fig. 1 before performing the FSP. The surface composite (AA6061-SiC) has been formed using FSP by a single pass. After performing the experimentation through FSP, different specimens were prepared for metallurgical and mechanical testing of the developed surface composite. An ASTM E8 guideline was followed to prepare the test specimens. Tensile test has been performed on an Instron tensile testing machine. To evaluate the metallurgical properties the cross-sectional specimens were prepared and examined under a Leica optical microscope. Further, heat treatment was performed in an air furnace at 350 °C for 1 h.

Trial experimentation was done to optimize the FSP parameters in accordance with material. In present examination, trial experimentation is finished utilizing the various parameters to acquire the best effectiveness with least deformities. In present investigation, trial experimentation was led in the wake of reviewing appropriate

literature. Different processing speeds of 10–100 mm/min and rotational speeds of 500 and 2000 rpm were seen but selected 1140 rpm, and 25 mm/min was used in the trial experiment due to best suitable results near these values. From the above trial experimentation and observed processing joints at different speeds selected for trial experimentation, it was concluded that rotational speed of 1140 rpm generates best results. It was also observed that the processing speed of 25 mm/min gave best results using tool shoulder diameter of 20 mm. Friction stir processed AA-6061 reinforced with SiC at rotational speed of 1140 rpm, and 25 mm/min traverse speed by using the square tool is shown in Fig. 3.

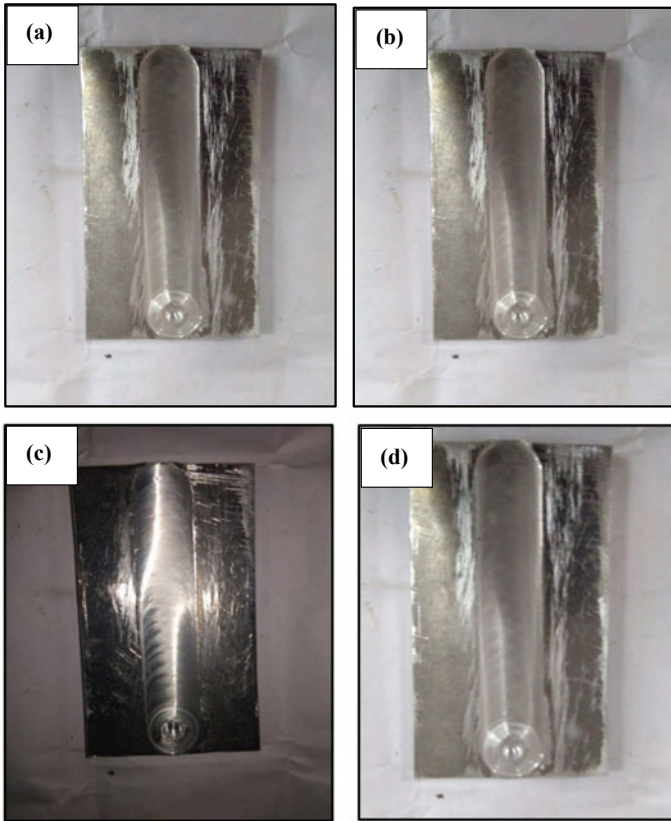


**Fig. 3** FSP specimens **a** unreinforced, **b** AA6061-SiC surface composite, **c** unreinforced heat-treated and **d** AA6061-SiC heat-treated



### 3 Result and Discussion

#### 3.1 Microstructural Analysis

The base material contains prolonged grains which comprise of a space involved by a consistent crystal lattice. The dark lines enveloping the grains are as far as possible. The ordinary size of the grain is a critical part of choosing the mechanical and metallurgical properties. A greater grain size extends creep, the never-ending winding that additions with time under a steady burden. However, at the overhauled parameters fine and equiaxed recrystallized grain structure was found in (stir zone) SZ as a result of dynamic recrystallization. Fine grains having normal grain breadth of  $8.3\ \mu\text{m}$  are seen in the present examination with a tool shoulder width of 20 mm. The significant issue during the arrangement of surface composites utilizing FSP is to incorporate an enormous volume portion of reinforcements with uniform circulation of particles at ideal degree of preparing parameters. Many researchers [24, 25] have also reported that with one pass it is very difficult to uniformly distribute the particles as the mechanism of intermixing and complex material flow restricts this phenomenon with only single pass. Therefore, some researchers suggested multiple passes for better particle distribution during FSP.

Figure 4 shows the effect of heat treatment on grain size of stir zone processed at a constant speed of 30 mm/min with tool shoulder diameter of 20 mm. The average grain size at the stir zone (SZ) increases after heat treatment. The small value of average grain size of  $8.3\ \mu\text{m}$  was achieved at tool rotational speed of 1140 rpm with 20 mm tool shoulder diameter. Low value of tool temperature generates less heat, which further provides less time for the grain growth due to fast cooling rate, as a result fine grains were observed. Table 2 represents the change in grain size after heat treatment at  $350\ ^\circ\text{C}$  in air furnace. It has been observed that the reinforcement particles (SiC) have been more uniformly dispersed after heat treatment compared to as processed AA6061-SiC surface composite as shown in Fig. 4.

#### 3.2 Microhardness

The microhardness value of the FSPed surface composite of unreinforced, AA6061-SiC and AA6061-SiC heat-treated after single pass is shown in Fig. 5. The mean hardness value of AA6061 base materials was found to be  $80 \pm 1.29\ \text{HV}$ . It is clear from Fig. 5 that the normal hardness of AA6061 FSPed was almost  $88 \pm 2.56\ \text{HV}$ , which is higher as compared to base AA6061 composite. Grain modification and re-precipitation of helper phase are the two fundamental contemplations which are liable for this expanded hardness of FSPed AA6061 compound. At first, base AA6061 compound has extended grains with an ordinary size of  $26\ \mu\text{m}$  and tremendous intricate formed discretionary phase particles which are then substituted by fine equiaxed grain structure and re-scattering of accelerates all through the mix zone by

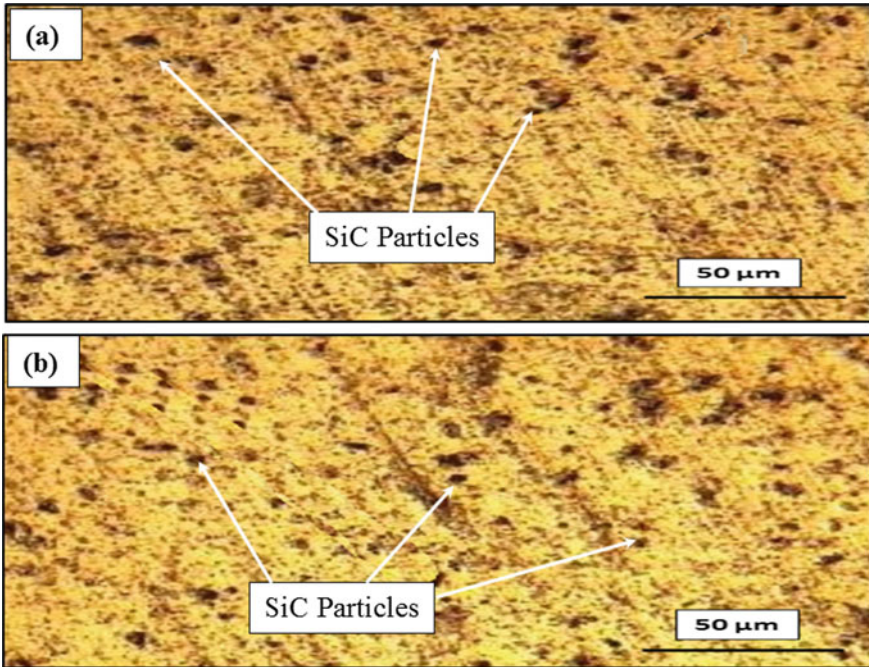


**Fig. 4** Optical micrographs of FSP **a** AA6061-SiC and **b** AA6061-SiC heat-treated at 350 °C

**Table 2** Microstructure results of stir zone

Tool type	Specimen type	FSP traverse speed (mm/min)	Tool rotational speed	Grain size (μm)
Square	Without HT	30	1140	8.3
Square	HT	30	1140	10.2

the thermo-mechanical method of FSP. Nevertheless, these secondary phase elements don't melt in the mix zone. In this way, essentially deterioration of particles happens [26, 27]. AA6061 blend strengthened with SiC either uninhibitedly or in total structure displays an enhancement in the hardness multifaceted nature to FSPed AA6061 compound and base AA6061 composite. The improved hardness is, all things considered, inferable from uniform movement of SiC atom brings about separations staying and quelling grain growth, extraordinary interfacial holding between the matrix and particles.

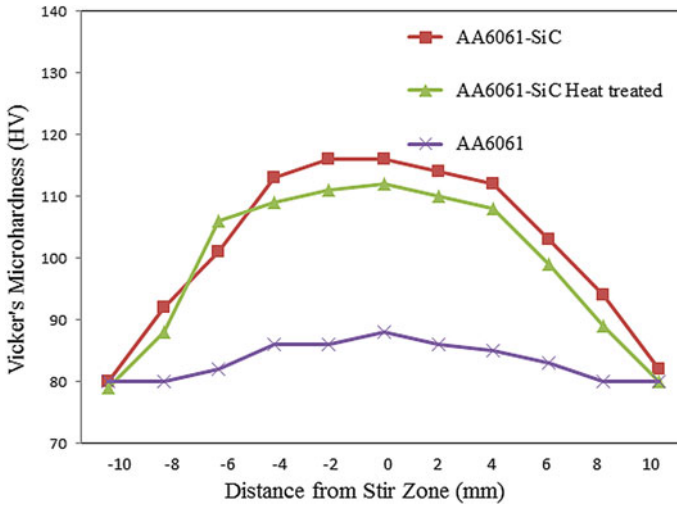


Fig. 5 Microhardness across the crosswise sector of FSP AA6061 alloy

### 3.3 Tensile Properties

Tensile tests were done to choose the tensile strength of FSPed tests and base Al6061 composite. It is shown that all the FSPed composite models demonstrated higher tensile strength with a resulting drop in the prolongation when contrasted with base Al6061 material. Among the FSPed tests, SiC reinforced AA6061 structure composites exhibited the most outrageous tensile strength of 346 MPa. While heat-treated AA6061-SiC and AA6061 composite show a definitive tensile strength of 335 MPa and 292, respectively. Then again, FSPed AA6061 compound shows higher stretching conversely with other FSPed tests and base AA6061 mix. AA6061 network reinforcement was cultivated by grain refinement, particles dissipating and re-accelerates. The tensile properties of the present work are identical with values revealed in the writing. Bauri et al. [25] have represented tensile strength of 296 and 337 MPa, and % extension of 25 and 33% for base A15083 compound and FSPed A15083 material separately. The properties fluctuation essentially be represented by the concoction synthesis, handling parameters, and morphology of reinforcement utilized.

## 4 Conclusions

In view of the investigational results, the accompanying conclusions were drawn:

1. Single-pass of FSP significantly distributes the SiC particles in AA6061 alloy and this resulted in substantial grain modification and re-precipitation of secondary phases.

2. Typical hardness of AA6061-SiC, AA6061-SiC heat-treated and base AA6061 are  $116 \pm 2.3$ ,  $112 \pm 1.88$  and  $88 \pm 1.3$ , respectively
3. The hardness of AA6061-SiC and heat-treated AA6061-SiC is nearly 1.45 and 1.4 times higher than base AA6061 alloy hardness.
4. A total of 335 MPa and 292 MPa tensile strength is exhibited by base AA6061 alloy and heat-treated AA6061-SiC composite, respectively. Whereas, without heat-treated AA6061-SiC composite hold maximum tensile strength as 346 MPa.

## References

1. Ni, D.R., Wang, J.J., Zhou, Z.N., Ma, Z.Y.: Fabrication and mechanical properties of bulk NiTi/Al composites prepared by friction stir processing. *J. Alloy. Compd.* **586**, 368–374 (2014)
2. Mishra, R.S., Mahoney, M.W., McFadden, S.X., Mara, N.A., Mukherjee, A.K.: High strain rate superplasticity in a friction stir processed 7075 Al alloy. *Scripta Mater.* **42**, 163–168 (1999)
3. Valiev, R.Z., Korznikov, A.V., Mulyukov, R.R.: Structure and properties of ultrafine-grained materials produced by severe plastic deformation. *Mater. Sci. Eng., A* **168**, 141–148 (1993)
4. Sabirov, I., Murashkin, M.Y., Valiev, R.Z.: Nanostructured aluminium alloys produced by severe plastic deformation: new horizons in development. *Mater. Sci. Eng., A* **560**, 1–24 (2013)
5. Uddin, M., Basak, A., Pramanik, A., Singh, S., Krolczyk, G.M., Prakash, C.: Evaluating hole quality in drilling of Al 6061 alloys. *Materials*, **11**(12), 2443 (2018)
6. Prakash, C., Singh, S., Singh, M., Antil, P., Aliyu, A.A.A., Abdul-Rani, A.M., Sidhu, S.S.: Multi-objective optimization of MWCNT mixed electric discharge machining of Al–30SiC p MMC using particle swarm optimization. In *Futuristic Composites*, pp. 145–164, Springer, Singapore (2018)
7. Basak, A.K., Pramanik, A., Prakash, C.: Deformation and strengthening of SiC reinforced Al-MMCs during in-situ micro-pillar compression. *Mater. Sci. Eng. A* **763**, 138141 (2019)
8. Miracle, D.B.: Science and metal matrix composites e from science to technological significance. *Compos. Sci. Technol.* **65**, 2526–2540 (2005)
9. Yadav, D., Bauri, R.: Friction stir processing of Al-TiB<sub>2</sub> in situ composite: effect on particle distribution, microstructure and properties. *J. Mater. Eng. Perform.* **24**, 1116–1124 (2015)
10. Mishra, R.S., Mahoney, M.W.: Friction stir processing: a new grain refinement technique to achieve high strain rate superplasticity in commercial alloys. *Mater. Sci. Forum* 357e359, 507–514 (2001)
11. Wang, Y., Fu, R., Jing, L., Li, Y., Sang, D.: Grain refinement and nanostructure formation in pure copper during cryogenic friction stir processing. *Mater. Sci. Eng., A* **703**, 470–476 (2017)
12. Jain, V.K.S., Muhammed, P.M., Muthukumaran, S., Babu, S.P.K.: Microstructure, mechanical and sliding wear behavior of AA5083eB4C/SiC/TiC surface composites fabricated using friction stir processing. *Trans. Indian Inst. Met.* **71**, 1519–1529 (2018)
13. Ma, Z.Y., Liu, F.C., Mishra, R.S.: Superplastic deformation mechanism of an ultrafine-grained aluminum alloy produced by friction stir processing. *Acta Mater.* **58**, 693–4704 (2010)
14. Ma, Z.Y., Sharma, S.R., Mishra, R.S.: Microstructural modification of As-cast Al-Si-Mg alloy by friction stir processing. *Metall. Mater. Trans. A* **37**, 3323–3336 (2006)
15. Prakash, C., Singh, S., Sharma, S., Garg, H., Singh, J., Kumar, H., Singh, G.: Fabrication of aluminium carbon nano tube silicon carbide particles based hybrid nano-composite by spark plasma sintering. *Mater. Today-Proc.* **21**, 1637–1642 (2020)
16. Guo, J.F., Liu, J., Sun, C.N., Maleksaeedi, S., Bi, G., Tan, M.J., Wei, J.: Effects of nano-Al<sub>2</sub>O<sub>3</sub> particle addition on grain structure evolution and mechanical behaviour of friction-stir-processed Al. *Mater. Sci. Eng., A* **602**, 143–149 (2014)

17. Yuvaraj, N., Aravindan, S., Vipin.: Fabrication of Al5083/B4C surface composite by friction stir processing and its tribological characterization. *J. Mater. Sci. Technol.* **4**, 398–410 (2015)
18. Singh, S., Prakash, C., Antil, P., Singh, R., Królczyk, G., Pruncu, C.I.: Dimensionless analysis for investigating the quality characteristics of aluminium matrix composites prepared through fused deposition modelling assisted investment casting. *Materials* **12**(12), 1907 (2019)
19. Palanivel, R., Dinaharan, I., Laubscher, R.F., Davim, J.P.: Influence of boron nitride nanoparticles on microstructure and wear behavior of AA6082/TiB<sub>2</sub> hybrid aluminum composites synthesized by friction stir processing. *Mater. Des.* **106**, 195–204 (2016)
20. Amra, M., Ranjbar, K., Dehmlaei, R.: Mechanical properties and corrosion behavior of CeO<sub>2</sub> and SiC incorporated Al5083 alloy surface composites. *J. Mater. Eng. Perform.* **24**, 3169–3179 (2015)
21. Hosseini, S.A., Ranjbar, K., Dehmlaei, R., Amirani, A.R.: Fabrication of Al5083 surface composites reinforced by CNTs and cerium oxide nano particles via friction stir processing. *J. Alloys Compd.* **622**, 725–733 (2015)
22. Du, Z., Jen, M., Feng, J., Bi, G., Wei, J.: Fabrication of a new Al-Al<sub>2</sub>O<sub>3</sub>-CNTs composite using friction stir processing (FSP). *Mater. Sci. Eng., A* **667**, 125–131 (2016)
23. Eskandari, H., Taheri, R., Khodabakhshi, F.: Friction-stir processing of an AA8026-TiB<sub>2</sub>-Al<sub>2</sub>O<sub>3</sub> hybrid nanocomposite: microstructural developments and mechanical properties. *Mater. Sci. Eng., A* **660**, 84–96 (2016)
24. Jain, V.K.S., James, V., Muthukumar, S.: Effect of first and second passes on microstructure and wear properties of titanium dioxide-reinforced aluminium surface composite via friction stir processing. *Arabian J. Sci. Eng.* **44**, 949–957 (2019)
25. Bauri, R., Yadav, D., Suhas, G.: Effect of friction stir processing (FSP) on microstructure and properties of Al-TiC in situ composite. *Mater. Sci. Eng., A* **528**, 4732–4739 (2011)
26. Sato, Y.S., Park, S.H.C., Kokawa, H.: Microstructural factors governing hardness in friction-stir welds of solid-solution-hardened Al alloys. *Metall. Mater. Trans. A* **32**, 3033–3042 (2001)
27. Khodabakhshi, F., Gerlich, A.P., Svec, P.: Reactive friction-stir processing of an Al-Mg alloy with introducing multi-walled carbon nano-tubes (MW-CNTs): microstructural characteristics and mechanical properties. *Mater. Char.* **131**, 359–373 (2017)

# Segregation and Recycling of Plastic Solid Waste: A Review



Kapil Chawla, Rupinder Singh, and Jaspreet Singh

**Abstract** In today's world, the management of plastic waste is the biggest environmental challenge. Increased production of plastic solid waste (PSW) materials like high-density polyethylene (HDPE), nylon, Acrylonitrile butadiene styrene (ABS), polycarbonate (PC), etc., are creating new challenges to researchers and also encouraging new areas of research. Landfilling of PSW is one of the ancient methods of managing the plastic waste but it produces methane gas which causes global warming. So, recycling is the only way to reduce the PSW. This paper explains various separation and recycling techniques for PSW along with different techniques of additive manufacturing (AM) that can accommodate these waste materials to some extent.

**Keywords** Plastic solid waste · High-density polyethylene · Acrylonitrile butadiene styrene (ABS) · Polycarbonate (PC) · Additive manufacturing

## 1 Introduction

In today's world, plastic becomes a critical part of human life due to its numerous applications. But the most common problem with plastic is that it cannot be easily degraded and generally takes hundreds of years to brutalize under normal conditions [1]. Plastics are widely used from household to aircraft, shopping bags, packaging firms, toys, wrapping materials, etc. Polymer waste seems to be the major factor for increase in plastic solid waste production, and from last few decades, polymer consumption has increased up to 100 million tones which directly impact on human environment [2, 3]. Plastic solid waste (PSW) contains highly toxic elements traces which are harmful to environment and from last 50 years plastic production has increased rapidly to meet daily demand [4]. One of the methods to reduce the PSW

---

K. Chawla · J. Singh (✉)  
Lovely Professional University, Jalandhar 144411, India  
e-mail: [erjassi03@yahoo.in](mailto:erjassi03@yahoo.in)

R. Singh  
NITTTR, Chandigarh, India

© Springer Nature Singapore Pte Ltd. 2020  
C. Prakash et al. (eds.), *Advances in Materials Science and Engineering*,  
Lecture Notes in Mechanical Engineering,  
[https://doi.org/10.1007/978-981-15-4059-2\\_17](https://doi.org/10.1007/978-981-15-4059-2_17)

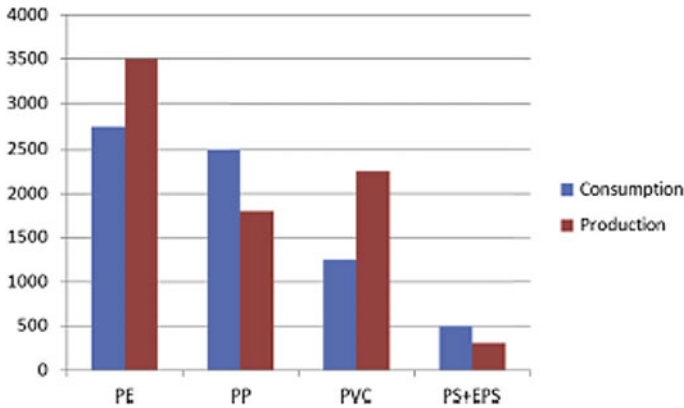


**Fig. 1** Production and consumption of plastic products in India. *Source* Govt. of India Statistics, Analysis by Tata Strategic

is to be recycled the same but the problem with the virgin material is that they cannot be recycled after four times because thermal degradation reduces the strength of the thermoplastic material [5]. High-density polyethylene (HDPE) and low density polyethylene (LDPE) are major household plastic solid wastes. Landfilling of PSW is one of the ancient methods of managing the plastic waste but it produces methane gas which causes global warming 21 times more than carbon dioxide [6]. Production and consumption of polymer directly depend upon supply and demand. But in India, demand and supply vary significantly. Figure 1 shows the production and consumption variation of plastic products in India (report generated by Tata Strategic).

Generally, plastics are categorized into two categories, i.e., thermosetting (which cannot be recycled) and thermoplastic (which can be recycled up to some certain number of cycles.) The frequently used plastic polymers, i.e., thermosetting and thermoplastics along with their applications have been shown in Table 1.

Before plastic recycling, collection and segregation need to be done for identification of different polymers.

## 2 Separation/Identification of Polymers

After collecting plastic waste, the first step is to segregate the different polymers. Manual segregation depends upon personal's experience. After segregation, recycling is to be done which requires huge investment along with machinery [8]. There are so many techniques available for the polymer identification such as differential scanning calorimeter (DSC) [9], eddy-current technique [10], near infrared (NIR) [11], gravity separation [12], electric conductivity-based separation [13], laser-induced

**Table 1** Different plastic polymers with their applications [7]

Thermosetting	Applications	Thermoplastics	Applications
Polyurethane	Coatings and adhesives, building insulation, refrigerators and freezers, furniture and bedding, footwear and automotive	Polyethylene terephthalate (PET)	PET bottles, packaging films, carpet yarn and staple fiber
Urea formaldehyde	Wrinkle-resistant fabrics, cotton blends, agriculture and wall cavity fillers	Polyamides	Rope, threads, tyres, brushes, bearing, gears and cams
Polyester	Bottles of Water, beer, juice, detergent, technical yarn and staple fiber	Polypropylene	Clear bags, carpet, rugs and mats
Melamine	Laminating flooring, dinnerware, dry and erase boards	Polycarbonate	Electrical and telecommunications and hardware
Epoxy	Adhesive and coating materials, coating	Polyvinyl chloride	Medical, electrical, construction, automobile and clothing
Silicon	Adhesive, lubricant cooking utensils, thermal and electrical insulations	Polylactic acid (PLA)	Cups, bags, disposable garments, and decomposing packaging materials
Faturan	Umbrellas and prayer beads	ABS	Drain pipes, musical instruments and automotive trim components
Bakelite	Electrical systems, insulating bases and systems	Polystyrene	CD cases, smoke detector housing and dinnerware
Phenol formaldehyde	Laboratory countertops, billiard balls, fiber glass cloths, coating and adhesives	HDPE	Toys, bottles, pipes, wires and cable insulations
Vinyl ester	Marine industry, tanks and vessels and laminating process	LDPE	Trays, screen cards, packaging of computer hardware's and optical disk drivers



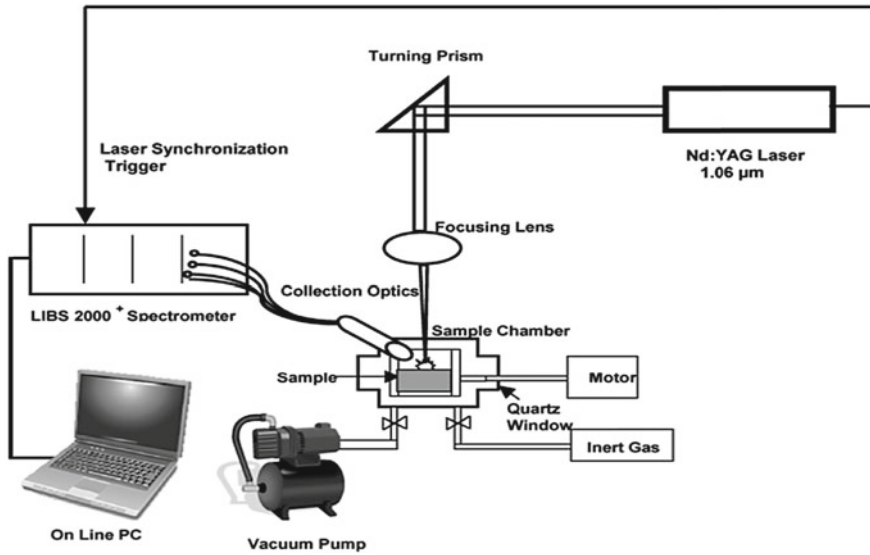


Fig. 2 Schematic of LIBS [17]

breakdown spectroscopy (LIBS) [14], X-ray fluorescence [15] and froth flotation method [16]. Only few techniques are explained below:

## 2.1 LIBS

It is a technique used to determine hydrogen and carbon constituents present in polymer with the help of spectral analysis [17]. This process is basically used for identifying LDPE, HDPE, PS and PVC by using Nd:YAG laser beam for identification of plastic material [18]. In this process, Nd:YAG laser strike on identified plastic material to determine hydrogen and carbon constituents. Basic setup representation of LIBS process is as shown in Fig. 2. One of the biggest advantages of this process is reliability and easy identification of different polymers depending upon purity level.

## 2.2 X-ray Fluorescence

This technique is also known as quantitative analysis. It is used to determine flame retardants materials present in plastic polymers and also use to determine the chemical composition of materials like cements, polymers and oils with the help of X-ray. The material to be inspected is placed in X-ray tube and will produce X-ray radiation equivalent to optical color light. Different colors show different energy levels. Time

to measure particles depends upon the number of elements to be determined and varies from few seconds to 30 min. This process is applicable to most of the polymers but size of particle should lie between 2 and 4 mm.

### 2.3 Froth Flotation Process

Froth floatation process is another separation technique of plastic polymer. Many authors recommended froth floatation as one of the cheapest methods of polymer segregation [19–23]. But few researchers found that it is not suitable for large-scale segregation and is preferred for mineral processing and for mixed plastic segregation only. Barlaz et al. have used calcium lignin sultanate as wetting agent, whereas pine oil and methyl isobutyl carbinol as frothing agent [24]. Figure 3 shows the working of froth floatation process. Material is inserted into the tank where it mixed with hot water with the help of electromagnetic feeder. After that it mixed with alkaline solution for alkaline treatment to make pulp. After pulp formation, it feeds into vibrating tank for rinsing with cold water. Wetted material rinsed with cold water fed into another tank for chemical treatment. The alkaline solution is transferred into conditioning bank where floated and non-floated parts separated. The main requirement of this setup is it requires proper heating system, huge space for installation and requires frequent cleaning [25].

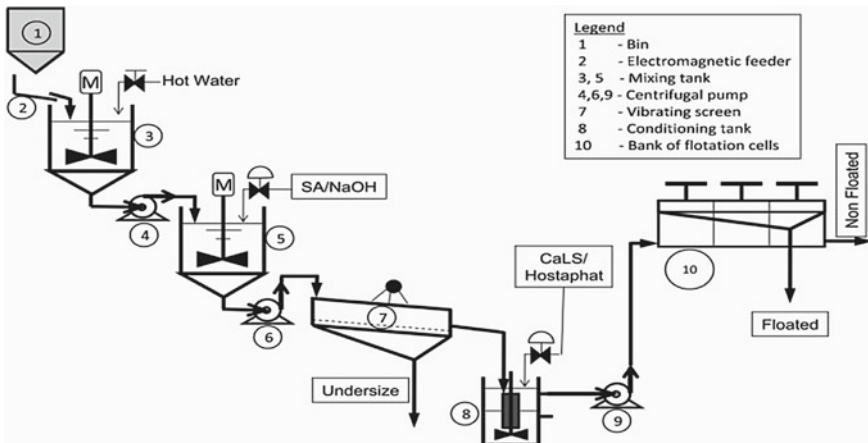


Fig. 3 Schematic of froth flotation process [26]

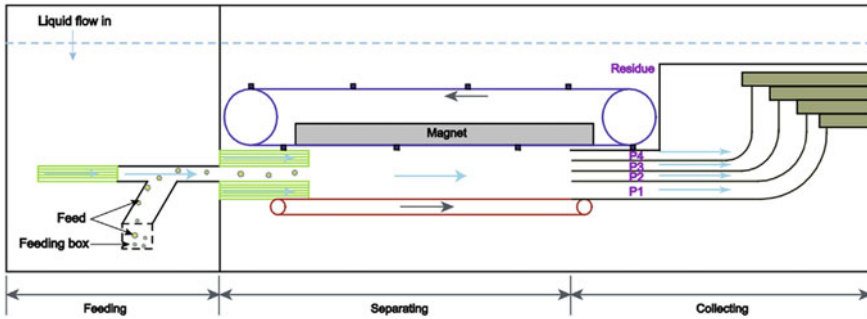


Fig. 4 Schematic of magnetic density separator [30]

## 2.4 Magnetic Density Separation

This technique is used to separate LDPE, HDPE and PP from contaminated materials like wood, rubber and from each other. The major advantage of this process is that the complex materials get separated in a single step without changing liquid (modifier in liquid magnetic in nature) [15]. In this process, material is wet with boiling water initially to remove heavy plastics known as wetting [27]. To avoid turbulence in the system, air is discharged from box before placing particles in stainless steel box. Density and flow speed play important role as plastic flakes with thickness 1 mm takes few seconds to reach equilibrium height [28, 29] (Fig. 4).

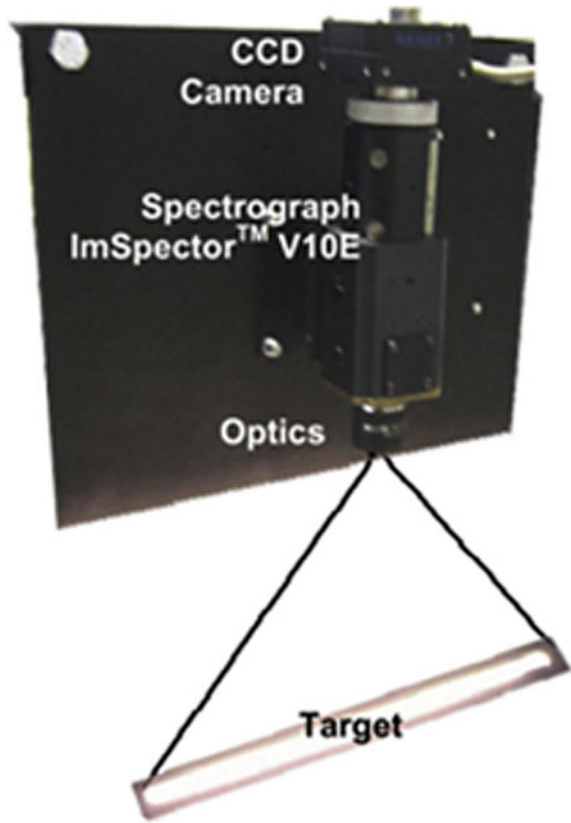
## 2.5 Hyperspectral Imaging (HSI) Technology

This technique is used to determine the composition and spatial distribution in food processing industry, pharmaceuticals, astronomy, medicine, agriculture and plastic material characterization [31–36]. It consists of hardware and software operates in spectral range. In this technique, a light beam is used to fall on a patented prism-grating-prism (PGP element) so that short and long wavelength dispersed up and down compared with respect to middle wavelength. Image spectral gives separate value with respect to sensitive laser array elements. Using detection devices, such images help in analyzing the different values [15] (Fig. 5).

## 3 Recycling Techniques

The commonly employed recycling techniques have been explained below:

**Fig. 5** Schematic of hyperspectral imaging (HSI)



### ***3.1 Primary Recycling***

This is popular method for converting plastic waste into original product. It uses semi-clean or clean scrap after sorting them from contaminated part. One of the limitations of this technique is due to excessive contamination, and it is not suitable for municipal solid waste (MSW).

### ***3.2 Secondary Recycling***

This process means recycling of PSW by mechanical means [37]. Both primary and secondary are mechanically recycling techniques of PSW. Primary technique includes different steps such as shredding, contamination and flakes separation, converted into granular forms, removing of glue by drying in oven and finally chemical washing using caustic soda. After separation of contamination from PSW, secondary recycling was executed. Secondary technique includes various methods like

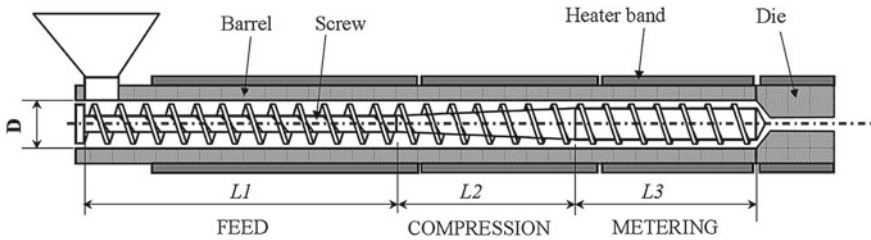


**Fig. 6** Working of single screw extruder [38]

screw extrusion, blow molding, injection molding, etc. Screw extrusion method of secondary recycling is discussed below.

Various varieties of extruders are available in market according to their operations, shapes and size. Nowadays, single and twin-screw extruder are commercially utilized and both have various operating parameters [38, 39]. In this method, material in the form of granules is put into the barrel with the help of hopper. The heater present in barrel melts the material and screw forces it in forward direction toward the die. There are some parameters affecting the wire formation. Speed is the most important parameter. Higher speed results in improper melting of plastic, whereas lower speed over melts the material which leads to the formation of multiple heating zones. Pressure is another critical parameter that helps in creating back pressure. It should be up to 500 psi required for material to come out from die and thus wire is formed. The schematic diagram of single screw extruder is shown in Fig. 6.

### 3.3 Tertiary Recycling

Sometimes, primary and secondary recycling appears difficult as MSW is a collection of heterogeneous components. Tertiary recycling is also known as energy sustainability, as primary and secondary recycling does not contribute toward energy sustainability (means origination of raw material from plastic solid waste). Tertiary recycling recovers monomers from PSW by depolymerization processes like solvolysis and thermolysis. Tertiary recycling includes various processes like cracking, pyrolysis (in absence of air), gasification (in control environment), etc. [40].

### 3.4 Quaternary Recycling

After again and again recycling, polymer starts losing its properties and finally leads to landfilling. But landfilling leads to produce more harmful gases. So, to overcome this problem, many researchers suggested that by incineration [41] energy can be recovered from waste which leads to reduction in plastic waste. Plastics are generally

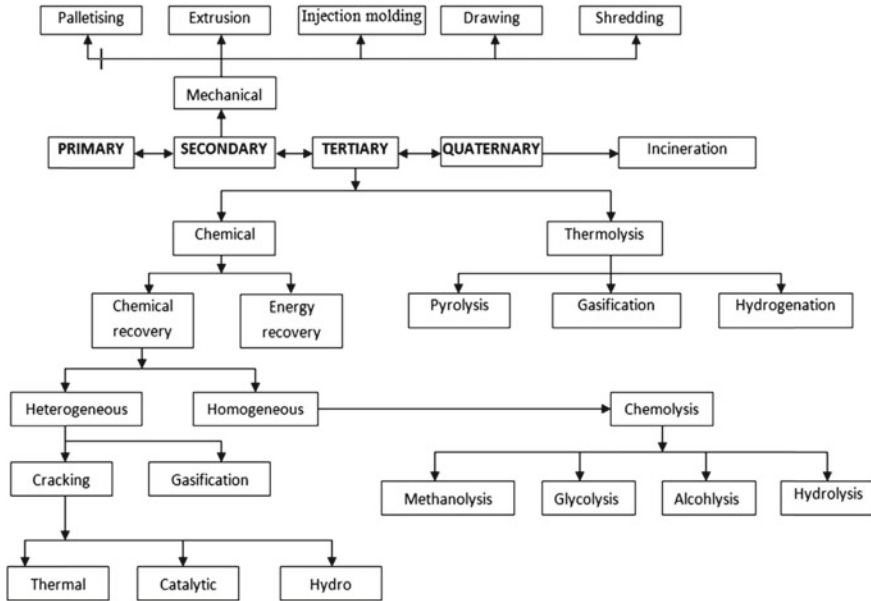


Fig. 7 Schematic of various recycling techniques of PSW

derived from crude oils and having high calorific value [42], mainly emit air pollutants like CO<sub>2</sub>, SO<sub>x</sub>, NO<sub>x</sub>, polycyclic aromatic hydrocarbons (PAHs) and polychlorinated dibenzofurans (PCDFs). There are few methods to control these harmful pollutant particles that include: (i) flue gas cooling, (ii) acid neutralization, (iii) filtration, (iv) ammonia addition to combustion chamber, etc. [43]. The schematic diagram of different recycling techniques of PSW has been shown in Fig. 7.

#### 4 Application of Recycled Plastics

Nowadays, recycled plastic/polymers are highly utilized in industries for manufacturing various products as industries are focused on cost reduction and polymers are replacing wood, ceramics, etc., because of their lightweight, hygiene and economical [44]. Polymers are not even used in manufacturing industries but also used in tissue engineering. Singh et al. prepared filament wire using polymer waste (LDPE and HDPE) with or without reinforcement of Fe (10% and 6% by weight) using single screw extruder. Different mechanical properties were measured like shore D hardness, peak strength and break strength. Singh et al. [45] utilized ABS plastic material to fabricate pen drive case with the help of FDM at different orientations (0°–90°) with part thickness of 0.254 mm and observed better morphology and surface hardness at 0° inclinations as compared to other inclinations as inclination plays

an important role. Further, biomedical implant (hip joint) has been successfully fabricated using ABS with the help of FDM and vapor smoothing process has been employed for improving the surface finish [46].

## **5 Additive Manufacturing and Its Different Techniques**

Additive manufacturing (AM) is well known for its ability to make 3D objects by depositing layer on layer [47]. Composite parts with complex geometries can be fabricated easily by AM techniques with less material waste. Also, size and geometry can be controlled with the help of CAD as compared to conventional machining process [48]. There are various techniques use to print polymer composite but they depend upon processing speed, final product performance, cost and material type. There are various rapid prototyping (RP) techniques which are briefly explained below:

### ***5.1 Fused Deposition Modeling (FDM)***

FDM commonly used thermoplastics like PC, ABS, PLA, etc., for polymer composite printing because of their low melting point. FDM works on a principle where layers are fused and solidify together into desired final part. FDM offers some advantages firstly multiple nozzles can be operated simultaneously so that printed parts can be having required composition. Second advantage is in terms of low operating cost and easy to operate. With some advantages there are few disadvantages firstly extruded material should have suitable melt viscosity. Second supports structure used during printing cannot easily detach (Fig. 8).

### ***5.2 Stereolithography (SLA)***

This technique uses photopolymer that polymerize into 2D pattern layer with the help of UV laser. It based on the principle when one layer is cured platform lowers and another layer is ready to cure. Main advantage of SLA is nozzle free clogging technique and high-resolution printed parts can be obtained. Along with advantages, there are few disadvantages first is limited to certain polymers only and second is high operating cost (Fig. 9).

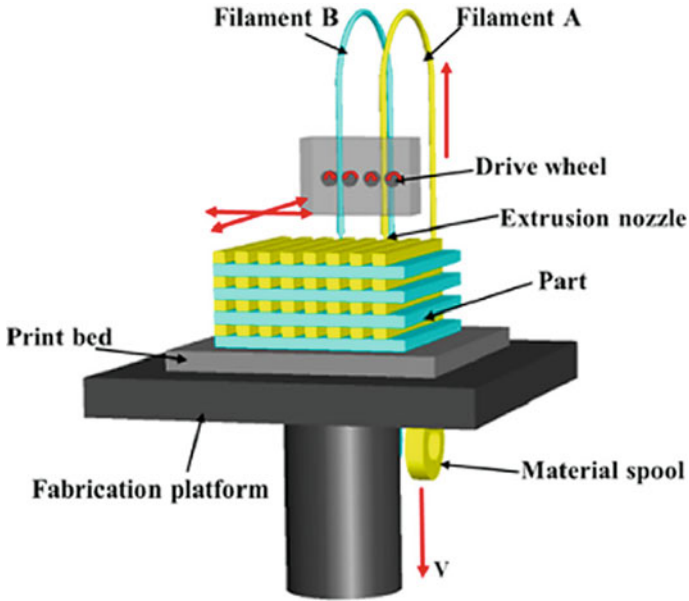


Fig. 8 FDM schematic [48]

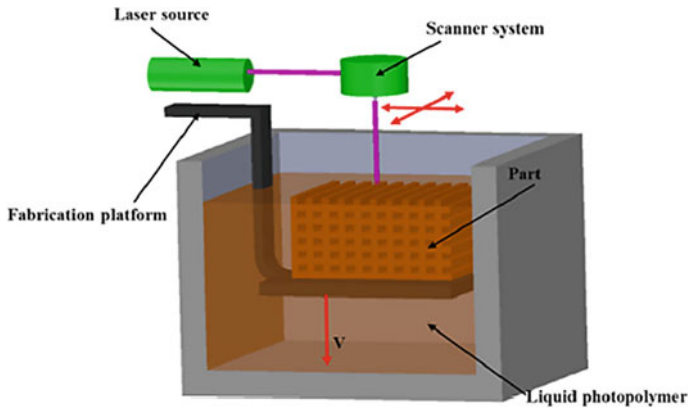
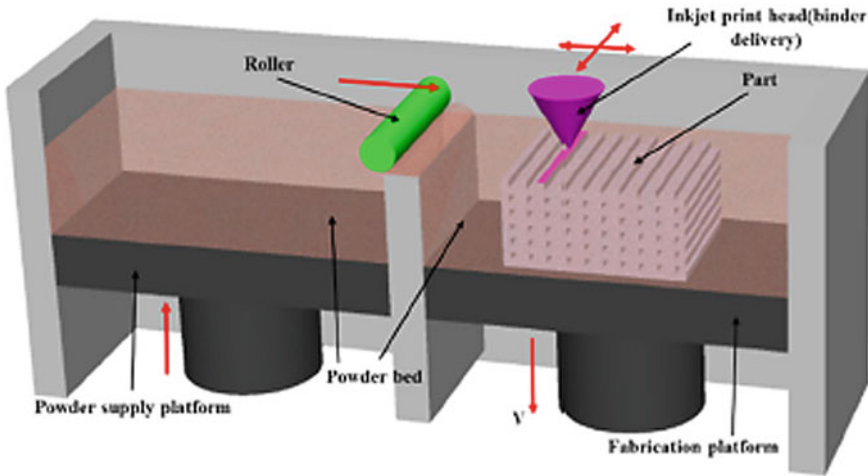


Fig. 9 Schematic of SLA [49]

### 5.3 Powder Bed and Inkjet Head Printing (3DP)

It based on powder processing technique. Firstly, powder is spread on the bed and then joined in desired layer by depositing a liquid binder with inkjet print head. As first layer cured working bed lower and next powder layer spreads this process repeats till desired pattern is formed. Key advantage of 3DP is any polymer material available





**Fig. 10** Schematic of 3DP [50]

in powder form can be printed by this technology. Generally, binder contamination may cause clogging (Fig. 10).

#### **5.4 Selective Laser Sintering (SLS)**

It is similar to 3DP except that a liquid binder is used in 3DP, whereas laser beam to sinter polymer powder in SLS. Required shape is obtained molecular diffusion of powder and shape generally formed by deposition of layer on layer by molecular interaction. Materials used in SLS are polycaprolactone (PCL) and Polyamide (PA) (Fig. 11).

#### **5.5 3D Printing**

This technique is used to create 3D shapes with the help of syringe head that can move in three dimensional but working head remains stationary. Key advantage of 3D printing includes flexibility for printing hydrogels. There are some other AM techniques also like 3D plotting, digit light processing (DLP) [53], liquid deposition modeling (LDM) [54], fiber encapsulation additive manufacturing (FEAM), etc. [55] (Fig. 12 and Table 2).

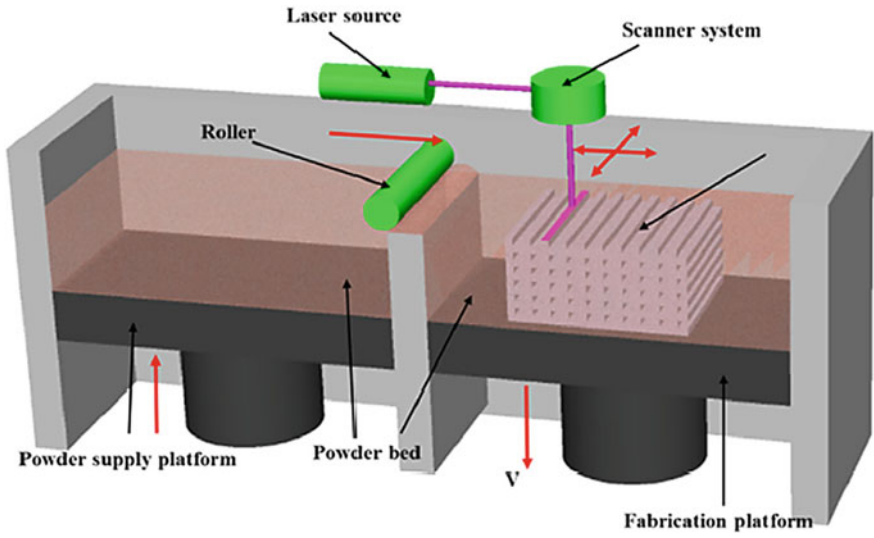


Fig. 11 Schematic of SLS [51]

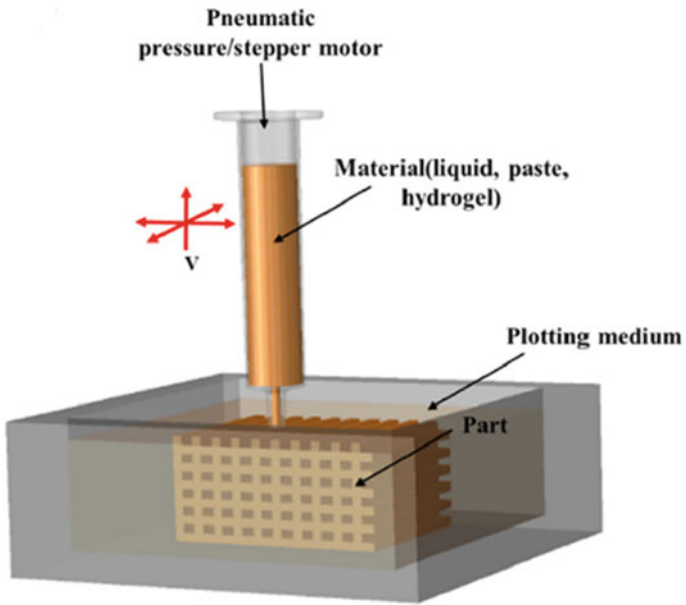


Fig. 12 Schematic of 3D printing [52]

**Table 2** Different 3D techniques with advantage and disadvantages

Technique	Polymer material	Starting material	Principle	Advantage	Dis advantage	Factors affecting printing quality
SLA	Photocurable resin (epoxy or acrylate-based resin)	Liquid photopolymer	Laser scanning and UV-induced curing	High printing resolution	Material limitation, cytotoxicity and high cost	Scan speed, laser power intensity and curing time
SLS	PCL and polyimide powder	Powder	Laser scanning and heat-induced sintering	Good strength, easy removal of support powder	High cost and powdery surface	Laser power, scan speed and power particle size
3DP	Any materials can be supplied as powder and binder needed	Powder	Drop-on-demand binder printing	Low cost, multi-material capability, easy removal of support powder	Clogging of binder jet and binder contamination	Powder size, binder viscosity and disposition speed
3D	PCL, PLA and hydrogel	Liquid or plotting paste	Pressurized syringe extrusion, and heat or UV-assisted curing	High printing resolution and soft materials capability	Low mechanical strength and slow	Material viscosity and deposition speed
FDM	Thermoplastics, such as PC, ABS, PLA and nylon	Filament	Extrusion and deposition	Low cost, good strength and multi-material capability	Anisotropy and nozzle clogging	Layer thickness, raster width, air gap, raster angle and printing orientation

## 6 Conclusion and Future Scope

In this paper, different methods of PSW management along with various recycling techniques were discussed. The literature review reveals that landfilling is not the solution to discard the PSW as it produces harmful gases (mainly methane contributes to global warming) and consume lot of space. Researchers employed various techniques to separate the ingredients of PSW, each having their own respective advantages and disadvantages. But among all techniques, froth flotation process can handle huge quantity of PSW without separating contamination. Further, polymers are petroleum bi-product, so energy recovery can be done using incineration for the sustainability of natural resources. Finally, various techniques of AM that can be helpful in managing/utilizing the PSW along with their advantages and disadvantages have been discussed.

**Acknowledgements** The authors are thankful to Manufacturing Research Laboratory (GNDEC, Ludhiana) for providing the research facilities.

## References

1. Gondal, M.A., Siddiqui, M.N.: Identification of different kinds of plastics using laser-induced breakdown spectroscopy for waste management. *J. Environ. Sci. Health Part A Toxic/Hazard Subst. Environ. Eng.* **42**, 89–97. *Earth Sci. J.* (2007)
2. Takoungsakdakun, T., Pongstabodee: Separation of mixed post-consumer PET-POM-PVC plastic waste using selective flotation. In: *Separation and Purification Technology*, vol. 54, pp. 248–252. Taylor and Francis (2007)
3. Intermediate Technology Development Group (ITDG): *Green Ending: Fine Point*, U.K., Hands On Rugby, U.K. (2004)
4. Gu, L., Ozbakkaloglu, T.: Use of recycled plastics in concrete: a critical review. In: *Waste Management*. Elsevier, Amsterdam (2016)
5. Singh, N., Hui, D., Singh, R., Ahuja, I.P.S., Feo, L.: Recycling of plastic solid waste: a state of art review and future applications. *Waste biodegradation. Compos. Part B* **115**, 409–422 (2017)
6. Ackerman, F.: Waste management and climate change. In: *Local Environment*, vol. 5, pp. 223–229. Taylor and Francis (2000)
7. Yu, J., Sun, L., Ma, C., Qiao, Y., Yao, H.: Thermal degradation of PVC: a review. In: *Waste Management*, vol. 48, pp. 300–14. Elsevier, Amsterdam (2016)
8. Kalantar, Z.N., Karim, M.R., Mahrez, A.: A review of using waste and virgin polymer in pavement. In: *Construction Build Materials*, vol. 33, pp. 55–62. Elsevier, Amsterdam (2012)
9. Frick, A., Rochman, A.: Characterization of TPU-elastomers by thermal analysis (DSC). In: *Polymer Testing*, vol. 23, pp. 413–417. Elsevier, Amsterdam (2004)
10. Cui, J., Forssberg, E.: Mechanical recycling of waste electric and electronic equipment: a review. *J. Hazard. Mater.* **99**, 243–263 (2003)
11. Rigamonti, L., Grosso, M., Møller, J., Martinez, Sanchez, V., Magnani, S., Christensen, T.H.: Environmental evaluation of plastic waste management scenarios. In: *Resource Conservation Recycle*, vol. 85, pp. 42–53. Wiley, New York (2014)
12. Shent, H., Pugh, R.J., Forssberg, E.: A review of plastics waste recycling and the flotation of plastics. In: *Resource Conservation Recycle*, vol. 25, pp. 85–109. Elsevier, Amsterdam (1999)

13. Xue, M.: Research on polymer composites of replacement prostheses. *Int. J. Biomed. Eng. Technol.* **7**, 18–27 (2011)
14. Russo, R.: In: *Laser Induced Breakdown Spectroscopy*, pp. 477–489. Cambridge University Press (2006)
15. Maio, F.D., Rem, P., Hu B., Serranti S., Bonifazi G.: The W2Plastics project: exploring the limits of polymer separation. *Open Waste Manag. J.* **3**, 90–8 (2010)
16. Alter, H.: Application of the critical surface tension concept to items in our everyday life. *J. Adhesion* **9**, 135–140 (1978)
17. Russo, R.: *Laser Induced Breakdown Spectroscopy*, pp. 477–489. Cambridge University Press (2006)
18. Gondal, M.A., Siddiqui, M.N.: Identification of different kinds of plastics using laser-induced breakdown spectroscopy for waste management. *J. Environ. Sci. Health Part A Toxic/Hazard. Substan. Environ. Eng.* **42**, 1989–1997 (2007)
19. Marques, G.A., Tenorio J.A.S.: Use of froth flotation to separate PVC/PET mixtures. *Waste Manag.* **20**, 265–269. (2000)
20. Takoungsakkadun, T., Pongstabodee, S.: Separation of mixed post-consumer PET-POM-PVC plastic waste using selective flotation. *Sep. Purif. Technol.* **54**, 248–252 (2007)
21. Fraunholz, N.: Separation of waste plastics by froth flotation—a review, Part 1. *Mineral Eng.* **17**, 261–268 (2004)
22. Fraunholz, N.: *Plastics flotation*. Ph.D. thesis. Delft University of Technology, the Netherlands (1997)
23. Shent, H., Pugh, R.J., Forssberg, E.: A review of plastics waste recycling and the flotation of plastics. *Resour. Conserv. Recycl.* **25**, 85–109 (1999)
24. Bendimerad, S., Tilmatine, A., Ziane, M., Dascalescu, L.: Plastic wastes recovery using free-fall tribo electric separator. *Int. J. Environ. Stud.* **66**, 529–538 (2009)
25. *Polymer blends handbook*, vol. 2. Springer, Berlin (2014). <http://dx.doi.org/10.1007/978-94-007-6064-6>
26. Carvalho, T., Durao, F., Ferreira, C.: Separation of packaging plastics by froth flotation in a continuous pilot plant. *Waste Manag.* **30**, 2209–2215 (2010)
27. Hu, B., Fraunholz, N., Rem, P.C.: Wetting technologies for high-accuracy sink float separations in water-based media. *Open Waste Manag. J.* **3**, 71–80 (2002)
28. Bakker, E.J., Rem, P.C., Fraunholz, N.: Upgrading mixed polyolefin waste with magnetic density separation. *Waste Manag.* **29**, 1712–1717 (2009)
29. Hu, B.: *Magnetic density separation of polyolefin waste*, vol. 41. Delft, the Netherlands: Doctoral thesis of Delft University of Technology. ISBN 978-94-6169-526-0 (2014)
30. Serranti, S., Luciani V., Bonifazi, G., Hu, B., Rem, P.C.: An innovative recycling process to obtain pure polyethylene and polypropylene from household waste. *Waste Manag.* **5**, 12–20 (2015)
31. Ferris, D., Lawhead, R., Dickman, E., Holtzapple, N., Miller, J., Grogan, S.: Multimodal hyperspectral imaging for the noninvasive diagnosis of cervical neoplasia. *J. Lower Genital Tract Disease* **5**, 65–72 (2005)
32. Serranti, S., Luciani, V., Bonifazi, G., Hu B., Rem P.C.: An innovative recycling process to obtain pure polyethylene and polypropylene from household waste. *Waste Manag.* **35**, 12–20 (2015)
33. Goetz, A.F.H., Vane, G., Solomon, T.E., Rock, B.N.: Imaging spectrometry for earth remote sensing. *Science* **228**, 1147–1153 (1985)
34. Monteiro, S., Minekawa, Y., Kosugi, Y., Akazawa, T., Oda, K.: Prediction of sweetness and amino acid content in soybean crops from hyperspectral imagery. *ISPRS J. Photogramm. Remote Sens.* **62**, 2–12 (2007)
35. Serranti, S., Gargiulo, A., Bonifazi, G.: Hyperspectral imaging for process and quality control in recycling plants of polyolefin flakes. *J. Near Infrared Spectrosc.* **20**, 573–581 (2012)
36. Bonifazi, G., Serranti, S.: Hyper spectral imaging based techniques in particles and particulate solids systems characterization. In: *The 5th international conference for conveying and handling of particulate solids: chapter-05, Sorrento, Italy* (2006)

37. Mastellone, M.L.: Thermal treatments of plastic wastes by means of fluidized bed reactors. Ph.D. thesis. Department of Chemical Engineering, Second University of Naples, Italy (1999)
38. Covas, J.A., Gaspar-Cunha, A.: A computational investigation on the effect of polymer rheology on the performance of a single screw extruder. *Erheopt* **1**, 41–62 (2001)
39. Hopewell, J., Dvorak, R., Kosior, E.: Plastics recycling: challenges and opportunities. *Philos. Trans. R. Soc. B Biol. Sci.* **364**, 2115–2126 (2009)
40. Kumar, S., Panda, A.K., Singh, R.K.: A review on tertiary recycling of high-density polyethylene to fuel. *Resour. Conserv. Recycl.* **55**, 893–910 (2011)
41. Scott, G.: Green polymers. *Polym. Degrad. Stab.* **68**(1), 1–7 (2000)
42. Dirks, E.: Energy Recovery from Plastic Waste in Waste Incineration Plants. Hanser Verlag Publish, pp. 746–769 (1996)
43. Yassin, L., Lettierim, P., Simons, S.J.R., Germana, A.: Energy recovery from thermal processing of waste: a review. In: *Energy Sustainability Development*, vol. 158, pp. 97–103. Elsevier, Amsterdam (2005)
44. Burat, F., Guney, A., Kangal, M.O.: Selective separation of virgin and postconsumer polymers (PET and PVC) by flotation method. *Waste Manag.* **29**, 1807–1813 (2009)
45. Singh, R.: Some investigations for small sized product fabrication with FDM for plastic components. *Rapid Prototyp. J.* **19** (2012)
46. Singh, J., Singh, R., Singh, H.: Dimensional accuracy and surface finish of biomedical implant fabricated as rapid investment casting for small to medium quantity production. *J. Manuf. Process.* **25**, 201–211 (2017)
47. Singh, S., Prakash, C., Ramakrishna, S.: 3D printing of polyether-ether-ketone for biomedical applications. *Eur. Polym. J.* **114**, 234–248 (2019)
48. Singh, H., Singh, S., Prakash, C.: Current trends in biomaterials and bio-manufacturing. In: *Biomanufacturing*, pp. 1–34. Springer, Cham (2019)
49. Singh, S., Singh, G., Prakash, C., Ramakrishna, S.: Current status and future directions of fused filament fabrication. *J. Manuf. Process.* **55**, 288–306 (2020)
50. Poomathi, N., Singh, S., Prakash, C., Patil, R.V., Perumal, P.T., Barathi, V.A., Balasubramanian, K.K., Ramakrishna, S., Maheshwari, N.U.: Bioprinting in ophthalmology: current advances and future pathways. *Rapid Prototyp. J.* **25**, 496–514 (2019)
51. Gibson, I., Shi, D.: Material properties and fabrication parameters in selective laser sintering process. *Rapid Prototyp. J.* **3**, 129–136 (1997)
52. Pandey, A., Singh, G., Singh, S., Jha, K., Prakash, C.: 3D printed biodegradable functional temperature-stimuli shape memory polymer for customized scaffoldings. *J. Mech. Behav. Biomed. Mat.* 103781 (2020)
53. Cooperstein, I., Layani, M., Magdassi, S.: 3D printing of porous structures by UVcurable O/W emulsion for fabrication of conductive objects. *J. Mater. Chem. C* **3**(9), 2040–2044 (2015)
54. Postiglione, G., Natale, G., Griffini, G., Levi, M. and Turri, S.: Conductive 3D microstructures by direct 3D printing of polymer/carbon nanotube nanocomposites via liquid deposition modeling. *Compos. Part A: Appl. Sci. Manuf.* **76**, 110–114 (2015)
55. Saari, M., Cox, B., Richer, E., Krueger, P.S., Cohen, A.L.: Fibre encapsulation additive manufacturing: an enabling technology for 3D printing of electromechanical devices and robotic components. In: *3D Print. Addit. Manuf.* **2**, 32–39 (2015)

# Vibration Response of Metal-Ceramic Based Functionally Graded Plate Using Navier Solution



Yogesh Kumar, Dheer Singh, and Ankit Gupta

**Abstract** In this paper, the vibrational response of the functionally graded plate has been carried out using non-polynomial based algebraic shear deformation theory. Hamilton's variational principle has been used in deriving the governing equations. The Navier solution technique has been employed to solve the governing equation in conjunction with boundary conditions which are simply supported. In addition to these, the power-law governing equations have been considered for calculating the effective material properties of FGM and its mechanical properties are considered to be changing in the direction of thickness. The non-dimensional frequency has been evaluated for several vibrating modes of functionally graded thin and thick plates. The frequency parameter has also been evaluated for different aspect ratios and thickness ratios.

**Keywords** Functionally graded material (FGM) · Plate theory · Vibration analysis · Close form solution · Hamilton's principle · Navier approach

## 1 Introduction

Functionally graded structures are the innovative composite materials where the properties of the material change continuously in the preferred direction from purely metallic to purely ceramic. Extensive literature has been published in the area of FGM structures. In this context, Zhang et al. [1] presented an extensive review based on the buckling and vibration analysis of FGM plate. Gupta et al. [2–4] investigated the vibration analysis of porous gradient structure using non-polynomial HSNDT. Kanu et al. [5] presented a review on smart FGMs and analyzed buckling and vibration analysis based on fracture problems. Kurtaran [6] studied the dynamic response of FG plates and shows the effects of plate's shape on vibration response. Thai and Kim [7] analyzed the vibration and bending analysis of FG structures using HSDT. Kumar et al. [8] proposed the research work on geometrically nonlinear analysis of

---

Y. Kumar · D. Singh · A. Gupta (✉)  
Shiv Nadar University, G.B. Nagar, Uttar Pradesh, India  
e-mail: [ankit.gupta1@snu.edu.in](mailto:ankit.gupta1@snu.edu.in)

© Springer Nature Singapore Pte Ltd. 2020  
C. Prakash et al. (eds.), *Advances in Materials Science and Engineering*,  
Lecture Notes in Mechanical Engineering,  
[https://doi.org/10.1007/978-981-15-4059-2\\_18](https://doi.org/10.1007/978-981-15-4059-2_18)

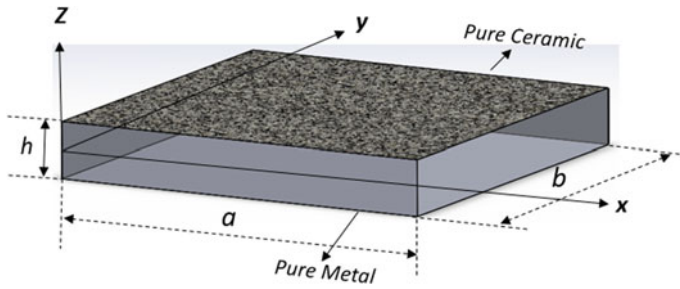


**Fig. 1** Functionally graded (FG) plates and its geometric coordinates

FGM plate using HSDT. Zenkour et al. [9] employed the 3-D elasticity solution for an exponentially graded thick structures. Birman et al. [10] proposed the research article on the modeling and study of FGM structures. Reddy et al. [11] emphasized the comprehensive analysis of functionally graded (FG) plates. Benveniste et al. [12] suggested a new methodology to study the application of Mori-Tanaka’s theory [13] in composite materials.

In the current research paper, HSDT has been considered for the vibrational analysis of a functionally graded plate. The power-law distribution and Hamilton’s principle have been used for deriving the governing equations. Navier solution method has been employed to solve the governing equations. The effects of various parameters like volume fraction index, side to thickness ratio ( $a/h$ ) on the fundamental frequency of FGM have been reported in the subsequent section.

The functional grade plate is shown in Fig. 1, where the plate thickness  $h$ , length  $a$  and width  $b$  the corresponding coordinates are  $x$ ,  $y$ , and  $z$ .

## 2 Formulation

### 2.1 Displacement Field

The displacement field used in this study work for the functional grade plate, reported by Thai [7] and expressed the following equations:

$$\begin{aligned}
 \bar{u}_1(x, y, z, t) &= \bar{u}(x, y, t) - z \frac{\partial \bar{w}_b}{\partial x} - \frac{4z^3}{3h^2} \left( \frac{\partial \bar{w}_s}{\partial x} \right) \\
 \bar{u}_2(x, y, z, t) &= \bar{v}(x, y, t) - z \frac{\partial \bar{w}_b}{\partial y} - \frac{4z^3}{3h^2} \left( \frac{\partial \bar{w}_s}{\partial y} \right) \\
 \bar{u}_3(x, y, z, t) &= \bar{w}_b(x, y, t) + \bar{w}_s(x, y, t)
 \end{aligned}
 \tag{1}$$



where  $\bar{u}$  and  $\bar{v}$  are the displacements in the  $x$  and  $y$  directions.  $\bar{w}_b$  is the bending component and  $\bar{w}_s$  is the shear component of the transverse displacement [7].

$$\begin{aligned}
 \varepsilon_{xx} &= \frac{\partial \bar{u}_1}{\partial x} = \frac{\partial \bar{u}}{\partial x} - z \frac{\partial^2 \bar{w}_b}{\partial x^2} - \frac{4z^3}{3h^2} \left( \frac{\partial^2 \bar{w}_s}{\partial x^2} \right) \\
 \varepsilon_{yy} &= \frac{\partial \bar{u}_2}{\partial y} = \frac{\partial \bar{v}}{\partial y} - z \frac{\partial^2 \bar{w}_b}{\partial y^2} - \frac{4z^3}{3h^2} \left( \frac{\partial^2 \bar{w}_s}{\partial y^2} \right) \\
 \varepsilon_{xy} &= \frac{\partial \bar{u}_1}{\partial y} + \frac{\partial \bar{u}_2}{\partial x} = \frac{\partial \bar{u}}{\partial y} + \frac{\partial \bar{v}}{\partial x} - 2z \frac{\partial^2 \bar{w}_b}{\partial x \partial y} - \frac{8z^3}{3h^2} \left( \frac{\partial^2 \bar{w}_s}{\partial x \partial y} \right) \\
 \varepsilon_{xz} &= \frac{\partial \bar{u}_1}{\partial z} + \frac{\partial \bar{u}_3}{\partial x} = \left( 1 - \frac{4z^2}{h^2} \right) \frac{\partial \bar{w}_s}{\partial x} \\
 \varepsilon_{yz} &= \frac{\partial \bar{u}_2}{\partial z} + \frac{\partial \bar{u}_3}{\partial y} = \left( 1 - \frac{4z^2}{h^2} \right) \frac{\partial \bar{w}_s}{\partial y}
 \end{aligned} \tag{2}$$

## 2.2 Energy Equations

1. **Strain Energy:** Strain energy variation in FG plate can be calculated by:

$$\delta U = \int_A \int_{-\frac{h}{2}}^{+\frac{h}{2}} (\sigma_{xx} \delta \varepsilon_{xx} + \sigma_{yy} \delta \varepsilon_{yy} + \sigma_{xy} \delta \varepsilon_{xy} + \sigma_{xz} \delta \varepsilon_{xz} + \sigma_{yz} \delta \varepsilon_{yz}) dA dz \tag{3}$$

where stress resultants are  $\mathbf{n}$ ,  $\mathbf{m}$  and  $\mathbf{q}$  define by given Eq. (4):

$$\begin{aligned}
 (n_{xx}, n_{yy}, n_{xy}) &= \int_{-\frac{h}{2}}^{+\frac{h}{2}} (\sigma_{xx}, \sigma_{yy}, \sigma_{xy}) dz \\
 (m_{xx}^b, m_{yy}^b, m_{xy}^b) &= \int_{-\frac{h}{2}}^{+\frac{h}{2}} (\sigma_{xx}, \sigma_{yy}, \sigma_{xy}) z dz \\
 (m_{xx}^s, m_{yy}^s, m_{xy}^s) &= \int_{-\frac{h}{2}}^{+\frac{h}{2}} (\sigma_{xx}, \sigma_{yy}, \sigma_{xy}) \frac{4z^3}{3h^2} dz
 \end{aligned}$$

$$\begin{aligned}
 q_{xy} &= \int_{-\frac{h}{2}}^{+\frac{h}{2}} \left(1 - \frac{4z^2}{h^2}\right) \sigma_{xy} dz \\
 q_{yz} &= \int_{-\frac{h}{2}}^{+\frac{h}{2}} \left(1 - \frac{4z^2}{h^2}\right) \sigma_{yx} dz
 \end{aligned}
 \tag{4}$$

- The Work done  $\delta V$  expressed with help of Eq. (5) Where the transverse load is  $p$

$$\delta V = - \int_A p \delta(\bar{w}_b + \bar{w}_s) dA
 \tag{5}$$

- The kinetic energy  $\delta K$  expressed with help of Eq. (6A).

$$\begin{aligned}
 \delta K &= \int_V (\dot{u}_1 \delta \dot{u}_1 + \dot{u}_2 \delta \dot{u}_2 + \dot{u}_3 \delta \dot{u}_3) \rho(z) dAdz \\
 \delta K &= \int_A \left\{ \begin{aligned}
 &I_0[\dot{u} \delta \dot{u} + \dot{v} \delta \dot{v} + (\dot{w}_b + \dot{w}_s) \delta(\dot{w}_b + \dot{w}_s)] \\
 &- I_1 \left[ \dot{u} \frac{\partial \delta \dot{w}_b}{\partial x} + \frac{\partial \dot{w}_b}{\partial x} \delta \dot{u} + \dot{v} \frac{\partial \delta \dot{w}_b}{\partial y} + \frac{\partial \dot{w}_b}{\partial y} \delta \dot{v} \right] \\
 &+ I_2 \left[ \frac{\partial \dot{w}_b}{\partial x} \times \frac{\partial \delta \dot{w}_b}{\partial x} + \frac{\partial \dot{w}_b}{\partial y} \times \frac{\partial \delta \dot{w}_b}{\partial y} \right] \\
 &+ cI_3 \left[ \dot{u} \frac{\partial \delta \dot{w}_s}{\partial x} + \frac{\partial \dot{w}_s}{\partial x} \delta \dot{u} + \dot{v} \frac{\partial \delta \dot{w}_s}{\partial y} + \frac{\partial \dot{w}_s}{\partial y} \delta \dot{v} \right] \\
 &+ cI_4 \left[ \frac{\partial \dot{w}_b}{\partial x} \times \frac{\partial \delta \dot{w}_s}{\partial x} + \frac{\partial \dot{w}_s}{\partial x} \times \frac{\partial \delta \dot{w}_b}{\partial x} + \frac{\partial \dot{w}_b}{\partial y} \times \frac{\partial \delta \dot{w}_s}{\partial y} + \frac{\partial \dot{w}_s}{\partial y} \times \frac{\partial \delta \dot{w}_b}{\partial y} \right] \\
 &+ c^2 I_6 \left[ \frac{\partial \dot{w}_s}{\partial x} \times \frac{\partial \delta \dot{w}_s}{\partial x} + \frac{\partial \dot{w}_s}{\partial y} \times \frac{\partial \delta \dot{w}_s}{\partial y} \right]
 \end{aligned} \right\} dA
 \end{aligned}
 \tag{6B}$$

In Eq. (6B), **dot** superscript represents the differentiation with respect to time (**t**). Where, Mass density is  $\rho(z)$ ,  $c = \frac{4}{3h^2}$  and  $I_i$  represents mass inertia, defined as the following:

$$(I_0, I_1, I_2, I_3, I_4, I_6) = \int_{-\frac{h}{2}}^{+\frac{h}{2}} (1, z, z^2, z^3, z^4, z^6) \rho(z) dz
 \tag{7}$$

**2. Hamilton’s Principle:** Applying Hamilton’s Principle in the FGMs plate

$$0 = \int_0^T (\delta U + \delta V - \delta K) dt \quad (8)$$

When substituting all the value of  $\delta U$ ,  $\delta V$  and  $\delta K$  in Eq. (8)

$$\int_A \left\{ \begin{aligned} & \left( n_{xx} \times \frac{\partial \delta \bar{u}}{\partial x} - m_{xx}^b \times \frac{\partial^2 \delta \bar{w}_b}{\partial x^2} - m_{xx}^s \times \frac{\partial^2 \delta \bar{w}_s}{\partial x^2} \right) \\ & + \left( n_{yy} \times \frac{\partial \delta \bar{v}}{\partial y} - m_{yy}^b \times \frac{\partial^2 \delta \bar{w}_b}{\partial y^2} - m_{yy}^s \times \frac{\partial^2 \delta \bar{w}_s}{\partial y^2} \right) \\ & + \left( n_{xy} \left( \frac{\partial \delta \bar{u}}{\partial y} + \frac{\partial \delta \bar{v}}{\partial x} \right) - 2m_{xy}^b \times \frac{\partial^2 \delta \bar{w}_b}{\partial x \partial y} - 2m_{xy}^s \times \frac{\partial^2 \delta \bar{w}_s}{\partial x \partial y} \right) \\ & + \left( q_{xz} \times \frac{\partial \delta \bar{w}_s}{\partial x} \right) + \left( q_{yz} \times \frac{\partial \delta \bar{w}_s}{\partial y} \right) \\ & - p \delta (\bar{w}_b + \bar{w}_s) \\ & - I_0 [\ddot{u} \delta \dot{u} + \dot{v} \delta \dot{v} + (\dot{w}_b + \dot{w}_s) \delta (\dot{w}_b + \dot{w}_s)] \\ & + I_1 \left[ \dot{u} \left[ \frac{\partial \delta \dot{w}_b}{\partial x} + \frac{\partial \dot{w}_b}{\partial x} \delta \dot{u} + \dot{v} \frac{\partial \delta \dot{w}_b}{\partial y} + \frac{\partial \dot{w}_b}{\partial y} \delta \dot{v} \right] \right. \\ & \left. - I_2 \left[ \frac{\partial \dot{w}_b}{\partial x} \times \frac{\partial \delta \dot{w}_b}{\partial x} + \frac{\partial \dot{w}_b}{\partial y} \times \frac{\partial \delta \dot{w}_b}{\partial y} \right] \right. \\ & + c I_3 \left[ \dot{u} \frac{\partial \delta \dot{w}_s}{\partial x} + \frac{\partial \dot{w}_s}{\partial x} \delta \dot{u} + \dot{v} \frac{\partial \delta \dot{w}_s}{\partial y} + \frac{\partial \dot{w}_s}{\partial y} \delta \dot{v} \right] \\ & \left. - c I_4 \left[ \frac{\partial \dot{w}_b}{\partial x} \times \frac{\partial \delta \dot{w}_s}{\partial x} + \frac{\partial \dot{w}_s}{\partial x} \times \frac{\partial \delta \dot{w}_b}{\partial x} + \frac{\partial \dot{w}_b}{\partial y} \times \frac{\partial \delta \dot{w}_s}{\partial y} + \frac{\partial \dot{w}_s}{\partial y} \times \frac{\partial \delta \dot{w}_b}{\partial y} \right] \right. \\ & \left. - c^2 I_6 \left[ \frac{\partial \dot{w}_s}{\partial x} \times \frac{\partial \delta \dot{w}_s}{\partial x} + \frac{\partial \dot{w}_s}{\partial y} \times \frac{\partial \delta \dot{w}_s}{\partial y} \right] \right\} dA = 0 \quad (9) \end{aligned}$$

Integrating Eq. (9) by parts, then formulate coefficients  $\delta \bar{u}$ ,  $\delta \bar{v}$ ,  $\delta \bar{w}_b$  and  $\delta \bar{w}_s$ , after that the governing equations of motion will be found.

$$\delta \bar{u} = \left( \frac{\partial n_{xx}}{\partial x} + \frac{\partial n_{xy}}{\partial y} \right) = I_0 \ddot{u} + I_1 \ddot{u} \frac{\partial \ddot{w}_b}{\partial x} - c I_3 \frac{\partial \ddot{w}_s}{\partial x} \quad (10A)$$

$$\delta \bar{v} = \left( \frac{\partial n_{xy}}{\partial x} + \frac{\partial n_y}{\partial y} \right) = I_0 \ddot{v} - I_1 \frac{\partial \ddot{w}_b}{\partial y} - c I_3 \frac{\partial \ddot{w}_s}{\partial y} \quad (10B)$$

$$\begin{aligned} \delta \bar{w}_b &= \left( \frac{\partial^2 m_{xx}^b}{\partial x^2} + \frac{\partial^2 m_{yy}^b}{\partial y^2} + 2 \frac{\partial^2 m_{xy}^b}{\partial x \partial y} + p \right) \\ &= I_0 (\ddot{w}_b + \ddot{w}_s) + I_1 \left( \frac{\partial \ddot{u}}{\partial x} + \frac{\partial \ddot{v}}{\partial y} \right) - I_2 \nabla^2 \ddot{w}_b - c I_4 \nabla^2 \ddot{w}_s \end{aligned} \quad (10C)$$

$$\delta \bar{w}_s = \left( \frac{\partial^2 m_{xx}^s}{\partial x^2} + \frac{\partial^2 m_{yy}^s}{\partial y^2} + 2 \frac{\partial^2 m_{xy}^s}{\partial x \partial y} + \frac{\partial^2 q_{xz}}{\partial x} + \frac{\partial^2 q_{yz}}{\partial y} + p \right)$$

$$= I_0(\ddot{w}_b + \ddot{w}_s) + cI_3\left(\frac{\partial \ddot{u}}{\partial x} + \frac{\partial \ddot{v}}{\partial y}\right) - cI_4\nabla^2\ddot{w}_b - c^2I_6\nabla^2\ddot{w}_s \tag{10D}$$

### 2.3 Constitutive Equations

Power-law distribution used for the calculation of Young’s modulus  $E(z)$  shown in Eq. (11) [7]

$$E(z) = E_m + (E_c - E_m)\left(0.5 + \frac{z}{h}\right)^k \tag{11}$$

$$\begin{Bmatrix} \sigma_{xx} \\ \sigma_{yy} \\ \sigma_{xy} \\ \sigma_{xz} \\ \sigma_{yz} \end{Bmatrix} = \frac{E(z)}{1-\nu} \begin{bmatrix} 1 & \nu & 0 & 0 & 0 \\ \nu & 1 & 0 & 0 & 0 \\ 0 & 0 & \frac{1-\nu}{2} & 0 & 0 \\ 0 & 0 & 0 & \frac{1-\nu}{2} & 0 \\ 0 & 0 & 0 & 0 & \frac{1-\nu}{2} \end{bmatrix} \begin{Bmatrix} \varepsilon_{xx} \\ \varepsilon_{yy} \\ \varepsilon_{xy} \\ \varepsilon_{xz} \\ \varepsilon_{yz} \end{Bmatrix} \tag{12}$$

Putting Eq. (2) into Eqs. (12) and (13–15) into Eq. (3).

$$\begin{Bmatrix} n_{xx} \\ n_{yy} \\ n_{xy} \end{Bmatrix} = C_0 \begin{bmatrix} 1 & \nu & 0 \\ \nu & 1 & 0 \\ 0 & 0 & \frac{1-\nu}{2} \end{bmatrix} \begin{Bmatrix} \frac{\partial \ddot{u}}{\partial x} \\ \frac{\partial \ddot{v}}{\partial x} \\ \frac{\partial \ddot{u}}{\partial x} + \frac{\partial \ddot{v}}{\partial x} \end{Bmatrix} + C_1 \begin{bmatrix} 1 & \nu & 0 \\ \nu & 1 & 0 \\ 0 & 0 & \frac{1-\nu}{2} \end{bmatrix} \begin{Bmatrix} -\frac{\partial^2 \ddot{w}_b}{\partial x^2} \\ -\frac{\partial^2 \ddot{w}_b}{\partial y^2} \\ -2\frac{\partial^2 \ddot{w}_b}{\partial x \partial y} \end{Bmatrix} + cC_3 \begin{bmatrix} 1 & \nu & 0 \\ \nu & 1 & 0 \\ 0 & 0 & \frac{1-\nu}{2} \end{bmatrix} \begin{Bmatrix} -\frac{\partial^2 \ddot{w}_s}{\partial x^2} \\ -\frac{\partial^2 \ddot{w}_s}{\partial y^2} \\ -2\frac{\partial^2 \ddot{w}_s}{\partial x \partial y} \end{Bmatrix} \tag{13}$$

$$\begin{Bmatrix} m_{xx}^b \\ m_{yy}^b \\ m_{xy}^b \end{Bmatrix} = C_1 \begin{bmatrix} 1 & \nu & 0 \\ \nu & 1 & 0 \\ 0 & 0 & \frac{1-\nu}{2} \end{bmatrix} \begin{Bmatrix} \frac{\partial \ddot{u}}{\partial x} \\ \frac{\partial \ddot{v}}{\partial x} \\ \frac{\partial \ddot{u}}{\partial x} + \frac{\partial \ddot{v}}{\partial x} \end{Bmatrix} + C_2 \begin{bmatrix} 1 & \nu & 0 \\ \nu & 1 & 0 \\ 0 & 0 & \frac{1-\nu}{2} \end{bmatrix} \begin{Bmatrix} -\frac{\partial^2 \ddot{w}_b}{\partial x^2} \\ -\frac{\partial^2 \ddot{w}_b}{\partial y^2} \\ -2\frac{\partial^2 \ddot{w}_b}{\partial x \partial y} \end{Bmatrix} + cC_4 \begin{bmatrix} 1 & \nu & 0 \\ \nu & 1 & 0 \\ 0 & 0 & \frac{1-\nu}{2} \end{bmatrix} \begin{Bmatrix} -\frac{\partial^2 \ddot{w}_s}{\partial x^2} \\ -\frac{\partial^2 \ddot{w}_s}{\partial y^2} \\ -2\frac{\partial^2 \ddot{w}_s}{\partial x \partial y} \end{Bmatrix} \tag{14}$$

$$\begin{Bmatrix} m_{xx}^s \\ m_{yy}^s \\ m_{xy}^s \end{Bmatrix} = cC_3 \begin{bmatrix} 1 & \nu & 0 \\ \nu & 1 & 0 \\ 0 & 0 & \frac{1-\nu}{2} \end{bmatrix} \begin{Bmatrix} \frac{\partial \ddot{u}}{\partial x} \\ \frac{\partial \ddot{v}}{\partial x} \\ \frac{\partial \ddot{u}}{\partial x} + \frac{\partial \ddot{v}}{\partial x} \end{Bmatrix} + cC_4 \begin{bmatrix} 1 & \nu & 0 \\ \nu & 1 & 0 \\ 0 & 0 & \frac{1-\nu}{2} \end{bmatrix} \begin{Bmatrix} -\frac{\partial^2 \ddot{w}_b}{\partial x^2} \\ -\frac{\partial^2 \ddot{w}_b}{\partial y^2} \\ -2\frac{\partial^2 \ddot{w}_b}{\partial x \partial y} \end{Bmatrix} + c^2C_5 \begin{bmatrix} 1 & \nu & 0 \\ \nu & 1 & 0 \\ 0 & 0 & \frac{1-\nu}{2} \end{bmatrix} \begin{Bmatrix} -\frac{\partial^2 \ddot{w}_s}{\partial x^2} \\ -\frac{\partial^2 \ddot{w}_s}{\partial y^2} \\ -2\frac{\partial^2 \ddot{w}_s}{\partial x \partial y} \end{Bmatrix} \tag{15}$$

$$\begin{Bmatrix} q_{xz} \\ q_{yz} \end{Bmatrix} = A^s \begin{bmatrix} 1 & 0 \\ 0 & 1 \end{bmatrix} \begin{Bmatrix} \frac{\partial \bar{w}_s}{\partial x} \\ \frac{\partial \bar{w}_s}{\partial y} \end{Bmatrix} \tag{16}$$

where  $C_0, C_1, C_2, C_3, C_4, C_5$  and  $A^s$  are the coefficients of stiffness defined by:

$$(C_0, C_1, C_2, C_3, C_4, C_5) = \int_{-\frac{h}{2}}^{+\frac{h}{2}} (1, z, z^2, z^3, z^4, z^6) \frac{E(z)}{1 - \nu^2} dz \tag{17A}$$

$$A^s = \int_{-\frac{h}{2}}^{+\frac{h}{2}} \left( 1 - \frac{4z^2}{h^2} \right) \frac{E(z)}{2(1 - \nu)} dz \tag{17B}$$

Equation (18A–18D) is shown the equation of motion in terms of displacements:

$$\begin{aligned} C_o \left( \frac{\partial^2 \bar{u}}{\partial x^2} + \frac{1 - \nu}{2} \frac{\partial^2 \bar{u}}{\partial y^2} + \frac{1 + \nu}{2} \frac{\partial^2 \bar{v}}{\partial x \partial y} \right) - C_1 \nabla^2 \frac{\partial \bar{w}_b}{\partial x} \\ - cC_3 \nabla^2 \frac{\partial \bar{w}_s}{\partial x} = I_0 \ddot{\bar{u}} - I_1 \left( \frac{\partial \ddot{\bar{w}}_b}{\partial x} \right) - cI_3 \left( \frac{\partial \ddot{\bar{w}}_s}{\partial x} \right) \end{aligned} \tag{18A}$$

$$\begin{aligned} C_o \left( \frac{\partial^2 \bar{v}}{\partial y^2} + \frac{1 - \nu}{2} \frac{\partial^2 \bar{v}}{\partial x^2} + \frac{1 + \nu}{2} \frac{\partial^2 \bar{u}}{\partial x \partial y} \right) - C_1 \nabla^2 \frac{\partial \bar{w}_b}{\partial y} \\ - cC_3 \nabla^2 \frac{\partial \bar{w}_s}{\partial y} = I_0 \ddot{\bar{v}} - I_1 \left( \frac{\partial \ddot{\bar{w}}_b}{\partial y} \right) - cI_3 \left( \frac{\partial \ddot{\bar{w}}_s}{\partial y} \right) \end{aligned} \tag{18B}$$

$$\begin{aligned} C_1 \nabla^2 \left( \frac{\partial \bar{u}}{\partial x} + \frac{\partial \bar{v}}{\partial y} \right) - C_2 \nabla^4 \bar{w}_b - cC_4 \nabla^4 \bar{w}_s + p = I_0 (\ddot{\bar{w}}_b + \ddot{\bar{w}}_s) \\ + I_1 \left( \frac{\partial \ddot{\bar{u}}}{\partial x} + \frac{\partial \ddot{\bar{v}}}{\partial y} \right) - I_2 \nabla^2 \ddot{\bar{w}}_b - cI_4 \nabla^2 \ddot{\bar{w}}_s \end{aligned} \tag{18C}$$

$$\begin{aligned} cC_3 \nabla^2 \left( \frac{\partial \bar{u}}{\partial x} + \frac{\partial \bar{v}}{\partial y} \right) - cC_4 \nabla^4 \bar{w}_b - c^2 C_5 \nabla^4 \bar{w}_s + A^s \nabla^2 \bar{w}_s + p = I_0 (\ddot{\bar{w}}_b + \ddot{\bar{w}}_s) \\ + cI_3 \left( \frac{\partial \ddot{\bar{u}}}{\partial x} + \frac{\partial \ddot{\bar{v}}}{\partial y} \right) - cI_4 \nabla^2 \ddot{\bar{w}}_b - c^2 I_6 \nabla^2 \ddot{\bar{w}}_s \end{aligned} \tag{18D}$$

### 2.4 Analytical Solution

Applying the Navier solution to the functional grade plate as shown below.

$$\begin{aligned}
 \bar{u}(x, y, t) &= \sum_{m=1}^{\infty} \sum_{n=1}^{\infty} \bar{U}_{mn} e^{i\omega t} \cos \alpha x \sin \beta y \\
 \bar{v}(x, y, t) &= \sum_{m=1}^{\infty} \sum_{n=1}^{\infty} \bar{V}_{mn} e^{i\omega t} \sin \alpha x \cos \beta y \\
 \bar{w}_b(x, y, t) &= \sum_{m=1}^{\infty} \sum_{n=1}^{\infty} \bar{W}_{bmn} e^{i\omega t} \sin \alpha x \sin \beta y \\
 \bar{w}_s(x, y, t) &= \sum_{m=1}^{\infty} \sum_{n=1}^{\infty} \bar{W}_{smn} e^{i\omega t} \sin \alpha x \sin \beta y
 \end{aligned} \tag{19A}$$

where  $\alpha = \frac{m\pi}{a}$ ,  $\beta = \frac{n\pi}{b}$  and  $i = \sqrt{-1}$ .

Where  $\omega$  is the angular frequency and  $p$  is the transverse load

$$p(x, y) = \sum_{m=1}^{\infty} \sum_{n=1}^{\infty} q_{mn} \sin \alpha x \sin \beta y \tag{19B}$$

The coefficient  $q_{mn}$  can be represented as:

$$q_{mn} = \frac{4}{ab} \int_0^a \int_0^b p(x, y) \sin \alpha x \sin \beta y \tag{19C}$$

Substitute Eq. (19A) and Eq. (19B) in Eq. (18), then the analytical solution has been obtained and the stiffness matrix coefficients and mass matrix coefficients are calculated from the above equations are shown in Eq. (20).

$$\left( \begin{bmatrix} K_{11} & K_{12} & K_{13} & K_{14} \\ K_{12} & K_{22} & K_{23} & K_{24} \\ K_{13} & K_{23} & K_{33} & K_{34} \\ K_{14} & K_{24} & K_{34} & K_{44} \end{bmatrix} - \omega^2 \begin{bmatrix} M_{11} & 0 & M_{13} & M_{14} \\ 0 & M_{22} & M_{23} & M_{24} \\ M_{13} & M_{23} & M_{33} & M_{34} \\ M_{14} & M_{24} & M_{34} & M_{44} \end{bmatrix} \right) \begin{Bmatrix} \bar{U}_{mn} \\ \bar{V}_{mn} \\ \bar{W}_{bmn} \\ \bar{W}_{smn} \end{Bmatrix} = \begin{Bmatrix} 0 \\ 0 \\ q_{mn} \\ q_{mn} \end{Bmatrix} \tag{20}$$

### 2.5 Results and Discussion

The fundamental frequency values are being validated in the present research work and compared with the different non-dimensional frequency (NDF) of a functionally graded plate governed by various HSDT's. The non-dimensional parameter  $\hat{\omega} = \omega h \sqrt{\rho_c / E_c}$  is used for the analysis and the different properties of materials used are shown in Table 1.

**Table 1** Material properties of functionally graded plate [7]

S. No.	Properties	Ti-6AL-4 V	Al <sub>2</sub> O <sub>3</sub>	ZrO <sub>2</sub>
1	Young's modulus	105.7	380	200
2	Density $\rho$ (kg/m <sup>3</sup> )	4429	3800	5700
3	Poisson's ratio ( $\nu$ )	0.3	0.3	0.3

Table 2 shows that the present work has been validated using non-polynomial based algebraic shear deformation theory (HSDT) given by Thai and Kim [7]. The current results reported for the non-dimensional frequency of *Al/Al<sub>2</sub>O<sub>3</sub>* of thin and thick square FGM plates are in good agreement with HT Thai's work [7]. The validation of the FG plate fabricated using *Al/Al<sub>2</sub>O<sub>3</sub>* for various side to thickness ratios (*a/h*) and power-law indexes, as well as various modes of vibration have been carried out. It has been found that most of the values of non-dimensional fundamental frequencies are absolutely validated and some show the error of approximately 1% in each mode of vibration.

The non-dimensional fundamental frequency analysis of material *Ti-6AL-4V/ZrO<sub>2</sub>* and *Ti-6AL-4V/Al<sub>2</sub>O<sub>3</sub>* for thin and thick square FG plates have been carried out for several values of side to thickness ratios and power-law indexes and the results reported in both Tables 3 and 4 shows that the NDF value is decreasing as the values of the volume fraction index increase. Further, as the thickness ratio increase, the non-dimensional frequency of the plate will decrease.

The non-dimensional frequency analysis of *Ti-6AL-4V/Al<sub>2</sub>O<sub>3</sub>* and *Ti-6AL-4V/ZrO<sub>2</sub>* for thin FGM plates has been done for several values of aspect ratios (*a/b*) using power-law indexes. The analysis has been performed at fixed side to thickness ratios (*alh = 10*). Results reported in both Tables 5 and 6. The non-dimensional frequency values are decreasing with the increasing values of volume fraction index, i.e., decreasing the ceramic content in the functionally graded plate.

### 3 Conclusions

In this study, the non-polynomial based algebraic HSDT has been considered for the vibrational behavior of the functionally graded plate using Navier solution. It has been found that the natural frequency reduces as the power-law index increases. It is also concluded that the vibration frequency will decrease with an increase in side to thickness ratio. The effect of power-law index and side to thickness ratio has also been reported for rectangular plates in addition to square plates. It is shown in the above results that as the FGM plate is changed from square to rectangular shape, the fundamental frequency of the plate increases. The vibration analysis results given in this study are useful for researchers working in this domain.

**Table 2** Result validation based on HSDT [7] and present work for  $Al/Al_2O_3$

$a/h$	Mode	$P = 0$		$P = 1$		$P = 4$		$P = 10$	
		HSDT [7]	Present	HSDT [7]	Present	HSDT [7]	Present	HSDT [7]	Present
5	1(1,1)	0.2113	0.2112	0.1631	0.1631	0.1378	0.1378	0.1301	0.1301
	2(1,2)	0.4623	0.4625	0.3607	0.3607	0.298	0.298	0.2771	0.2771
	3(2,2)	0.6688	0.6688	0.5254	0.5245	0.4284	0.4284	0.3948	0.3948
10	1(1,1)	0.0577	0.0577	0.0442	0.0442	0.0381	0.0381	0.0364	0.0364
	2(1,2)	0.1377	0.1376	0.1059	0.1053	0.0903	0.0903	0.0856	0.0866
	3(2,2)	0.2113	0.2113	0.1631	0.1631	0.1378	0.1388	0.1301	0.1304
20	1(1,1)	0.0148	0.0148	0.0113	0.0112	0.0098	0.0098	0.0094	0.0094



**Table 3** Non-dimensional frequencies ( $\omega$ ) using *Ti-6AL-4 V/Al<sub>2</sub>O<sub>3</sub>* material

<i>a/h</i>	Mode	Power-Law Index ( <i>P</i> )					
		<i>P</i> = 0	<i>P</i> = 0.5	<i>P</i> = 1	<i>P</i> = 4	<i>P</i> = 10	<i>P</i> = 50
5	1(1,1)	0.2113	0.1726	0.1543	0.1294	0.1206	0.1092
	2(1,2)	0.4623	0.3799	0.3396	0.2795	0.259	0.2375
	3(2,2)	0.6688	0.5517	0.4933	0.4015	0.3706	0.3423
10	1(1,1)	0.0577	0.0469	0.042	0.0357	0.0335	0.0300
	2(1,2)	0.1376	0.1122	0.1004	0.0847	0.0792	0.0713
	3(2,2)	0.2113	0.1726	0.1543	0.1294	0.1206	0.1092
20	1(1,1)	0.0148	0.012	0.0108	0.0092	0.0086	0.0077
	2(1,2)	0.0365	0.0297	0.0266	0.0227	0.0212	0.0190
	3(2,2)	0.0577	0.0469	0.042	0.0357	0.0335	0.0300

**Table 4** Non-dimensional frequencies ( $\omega$ ) using *Ti-6AL-4 V/ZrO<sub>2</sub>* material

<i>a/h</i>	Mode	Power-Law Index ( <i>P</i> )					
		<i>P</i> = 0	<i>P</i> = 0.5	<i>P</i> = 1	<i>P</i> = 4	<i>P</i> = 10	<i>P</i> = 50
5	1(1,1)	0.2113	0.1985	0.1933	0.1872	0.1835	0.1773
	2(1,2)	0.4623	0.4358	0.4239	0.4065	0.3893	0.387
	3(2,2)	0.6688	0.6319	0.6142	0.5854	0.5735	0.5592
10	1(1,1)	0.0577	0.0541	0.0527	0.0515	0.0505	0.0485
	2(1,2)	0.1376	0.1292	0.1258	0.1223	0.12	0.1156
	3(2,2)	0.2113	0.1985	0.1933	0.1872	0.1835	0.1773
20	1(1,1)	0.0148	0.0139	0.0135	0.0132	0.013	0.0125
	2(1,2)	0.0365	0.0342	0.0333	0.0326	0.032	0.0307
	3(2,2)	0.0577	0.0541	0.0527	0.0515	0.0505	0.0485

**Table 5** Non-dimensional frequencies ( $\omega$ ) using *Ti-6AL-4 V/Al<sub>2</sub>O<sub>3</sub>* material

<i>a/b</i>	Mode	Power-law index and <i>a/h</i> = 10					
		<i>P</i> = 0	<i>P</i> = 0.5	<i>P</i> = 1	<i>P</i> = 4	<i>P</i> = 10	<i>P</i> = 50
1	1(1,1)	0.0577	0.0469	0.042	0.0357	0.0335	0.03
	2(1,2)	0.1376	0.1122	0.1004	0.0847	0.0792	0.0713
	3(2,2)	0.2113	0.1726	0.1543	0.1294	0.1206	0.1092
1.5	1(1,1)	0.0919	0.0748	0.0669	0.0568	0.0531	0.0477
	2(1,2)	0.2574	0.2106	0.1883	0.1572	0.1464	0.1329
	3(2,2)	0.323	0.2646	0.2366	0.1965	0.1827	0.1665
2	1(1,1)	0.1376	0.1122	0.1004	0.0847	0.0792	0.0713
	2(1,2)	0.4047	0.3321	0.2969	0.2453	0.2276	0.2081
	3(2,2)	0.4623	0.3799	0.3396	0.2795	0.259	0.2375

**Table 6** Non-dimensional frequencies ( $\omega$ ) using *Ti-6AL-4 V/ZrO<sub>2</sub>* material

<i>a/b</i>	Mode	Power-law index and <i>a/h</i> = 10					
		<i>P</i> = 0	<i>P</i> = 0.5	<i>P</i> = 1	<i>P</i> = 4	<i>P</i> = 10	<i>P</i> = 50
1	1(1,1)	0.0577	0.0541	0.0527	0.0515	0.0505	0.0485
	2(1,2)	0.1376	0.1292	0.1258	0.1223	0.12	0.1156
	3(2,2)	0.2113	0.1985	0.1933	0.1872	0.1835	0.1773
1.5	1(1,1)	0.0919	0.0862	0.084	0.0818	0.0802	0.0772
	2(1,2)	0.2574	0.2421	0.2356	0.2277	0.2232	0.2159
	3(2,2)	0.323	0.304	0.2958	0.2851	0.2795	0.2708
2	1(1,1)	0.1376	0.1292	0.1258	0.1223	0.12	0.1156
	2(1,2)	0.4047	0.3813	0.3709	0.3564	0.3492	0.339
	3(2,2)	0.4623	0.4358	0.4239	0.4065	0.3893	0.387

## References

- Zhang, N., Khan, T., Guo, H.: Functionally graded materials: an overview of stability, buckling, and free vibration analysis. *Adv. Mater. Sci. Eng.* Article ID 1354150, 18 p (2019)
- Gupta, A., Talha, M.: Influence of porosity on the flexural and vibration response of gradient plate using non polynomial higher-order shear and normal deformation theory. *Int. J. Mech. Mater.* **14**, 277–296 (2018)
- Gupta, A., Talha, M.: Large amplitude free flexural vibration analysis of finite element modeled FGM plates using new hyperbolic shear and normal deformation theory. *Aerosp. Sci. Technol.* **67**, 287–308 (2017)
- Gupta, A., Talha, M.: Recent development in modeling and analysis of functionally graded materials and structures. *Prog. Aerosp. Sci.* **79**, 1–14 (2015). <https://doi.org/10.1016/j.ast.2017.04.015>
- Kanu, N.J., Vates, U.K.: Fracture problems, vibration, buckling, and bending analyses of functionally graded materials: a state-of-the-art review including smart FGMS. *Part. Sci. Tech.* (2017). ISSN: 0272-6351
- Kurtaran, H.: Shape effect on free vibration of functionally graded plates. *Int. J. Eng. Appl. Sci. (IJEAS)* **6**(4), 52–67 (2014)
- Thai, H.-T., Kim, S.-E.: A simple higher-order shear deformation theory for bending and free vibration analysis of functionally graded plates. *Compos. Struct.* **96**, 165–173 (2013)
- Suresh Kumar, J., Sidda Reddy, B.: Geometrically nonlinear analysis of functionally graded material plates using higher order theory. *Int. J. Eng. Sci. Technol.* **3**(1), 279–288 (2011)
- Zenkour, A.M.: Benchmark trigonometric and 3-D elasticity solutions for an exponentially graded thick rectangular plate. *Arch. Appl. Mech.* **77**(4), 197–214 (2007)
- Birman, V., Byrd, L.W.: Modeling and analysis of functionally graded materials and structures. *Appl. Mech. Rev.* **60**, 195 (2007)
- Reddy, J.N.: Analysis of functionally graded plates. *Int. J. Numer. Methods Eng.* **47**(1–3), 663–684 (2000)
- Benveniste, Y.: A new approach to the application of Mori–Tanaka’s theory in composite materials. *Mech. Mater.* **6**(2), 147–157 (1987)
- Mori, T., Tanaka, K.: Average stress in matrix and average elastic energy of materials with misfitting inclusions. *Acta Metall.* **21**(5), 571–574 (1973)

# Influence of the Microstructural and Mechanical Properties of Reinforced Graphene in Magnesium Matrix Fabricated by Friction Stir Processing



Nazish Alam, Md. Manzar Iqbal, Chander Prakash, Subhash Singh, and Animesh Basak

**Abstract** The aim of the present research work is to find out the influence of uniform dispersion of different volume percentages of graphene nanoparticles into magnesium matrix, fabricated by friction stir processing (FSP). These composites can be used in various applications, particularly in electrical, automobile and aerospace industries due to its lightweight and good electrical and mechanical properties. The friction processed surface of pure magnesium and composites were characterized through X-ray diffraction (XRD). Mechanical properties such as tensile test of the friction stir processed (FSPed) composites were performed in universal testing machine and the specimen was prepared according to standard dimension by wire EDM. The initial properties of the material were compared to the FSPed pure magnesium matrix composites. The role of various volume percentages of reinforcement by FSP resulted in grain refinements as well as improved the mechanical properties of the FSPed composite.

**Keywords** Friction stir processing · Metal matrix composites · Pure magnesium · Graphene · Tensile strength · X-ray diffraction (XRD)

## 1 Introduction

Researchers defined “composite” as a combination of two or more than two materials which are different from each other and produce a distinctive material which is better than the parent materials [1]. This illustration of composite is correct for any

---

N. Alam · Md. M. Iqbal · S. Singh (✉)

Department of Production and Industrial Engineering, National Institute of Technology, Jamshedpur, Jharkhand 831014, India  
e-mail: [Subh802004@gmail.com](mailto:Subh802004@gmail.com)

C. Prakash

School of Mechanical Engineering, Lovely Professional University, Phagwara, Punjab 144411, India

A. Basak

Adelaide Microscopy, The University of Adelaide, Adelaide, SA, Australia

© Springer Nature Singapore Pte Ltd. 2020

C. Prakash et al. (eds.), *Advances in Materials Science and Engineering*,

Lecture Notes in Mechanical Engineering,

[https://doi.org/10.1007/978-981-15-4059-2\\_19](https://doi.org/10.1007/978-981-15-4059-2_19)

composites; nonetheless, at a recent time “composite” represent reinforced plastics. Metal matrix composites (MMCs) are fabricated by metallic matrix which is continual along with matrix it contains one or more reinforcing part which is discontinuous. Aluminium is mostly used as metal matrix for the commercial work done on MMCs. The reason of popularity of aluminium is its resistance towards environment, light weight and effective mechanical properties; these benefits are also the reasons why aluminium is used as metal matrix. The high temperature of melting of aluminium is enough to serve numerous application needs, still sufficiently low to give composite processing judiciously convenient. Many reinforcing agents like continual boron, oxides of aluminium ( $\text{Al}_2\text{O}_3$ ), carbides of silicon ( $\text{SiC}$ ), whiskers, fibers (short) and fibers of graphite [2]. Composites of magnesium essentially utilize nearly identical properties as by composites of aluminium. In general, the selection of matrix between magnesium and aluminium is done on the footing of resistance towards corrosion against light weight. Magnesium is less dense than aluminium; however, magnesium is more active in corrosive atmosphere. The thermal conductivity of magnesium is low, which becomes a factor during its selection. MMCs incorporate the properties possessed by ceramic as well as the properties possessed by metals, leading to high shear strength as well as compressive strength and it can be utilized at high temperature. MMCs has become an area of interest for researchers in many fields such as automobile and aerospace, because of its low-cost reinforcement availability and evolution of various methods which results in replicable properties and microstructure [3]. The fascinating mechanical properties possessed by MMCs such as high strength, good thermal stability and specific modulus obtained is also high, all these properties were reported substantially [4, 5]. Besides this, the issues related to development of MMCs are, (a) fiber may get damaged, (b) the microstructure obtained is not uniform, (c) connection between the two fibers, and (d) substantial interfacial reaction could be stayed away with non-continuous reinforcement [6]. The welding Institute of UK first succeeded in developing the technique of friction stir welding (FSW) in 1991 [7]. Later on FSW after finding many applications in aerospace industries, FSW gradually modified into friction stir processing (FSP), which also enticed observations of many researchers [8, 9]. FSP is method of severe plastic deformation which helps in achieving better surface properties [10, 11]. Major benefit of FSP is that the casting defects are absent and microstructure obtained is fine [12]. Severe deformation plastically along with inflict stirring action of tool leads to many benefits of FSP [13], like microstructure becomes fine and cast alloys become homogenous and parts which is fabricated by powder metallurgy [14–20] and manufacturing of metal matrix composites and its homogenization is one of its many benefits [21–27]. In FSP, a tool pin which is rotating is feed into the part of metal surface which is to be fabricated or processed and then tool pin is traversed along a fixed path. Heat is produced because of friction between the tool pin and the metal surface. This heat is only responsible for plastic deformation which is taking place in processing area. When tool is moved then deformed metals starts recrystallizing, leads to homogenization and refinement of grain structure of stirring zone [28, 29]. FSP has proved to be potent in making fine grain size, of wrought aluminium or cast aluminium based alloys, and this is achieved through recrystallization.

Friction stir processing (FSP) process parameters and geometry of tool are important parameters that may be changed to get uniform distribution of material. This is evident that the distribution of particles is influenced by process parameters; reinforcing particles will not distribute when axial force applied is less, but when the force applied axially is high then it will compel particles to throw out particles from surface [30–35]. If travel speed is increased then heat input will be decreased and that leads to an incomplete flow of material required for distribution of particle [36], and hence number of passes of FSP is increased for enhancing the distribution of particle by instigating more stirring and mixing [37, 38]. For improvement of particle distribution, usually speed of rotation is increased and travel speed is lowered [36, 38]. Many researchers have carried out different works on metal matrix with graphene oxide or graphene as its reinforcement. Dasari et al. [39] in his work, with the help of Scanning electron microscope (SEM), showed that graphene oxide (GO) particles are distributed throughout the aluminium matrix which is necessary to enhance the mechanical properties. He showed that increasing the percentage of GO in the MMC leads to improved hardness because of development of more fine and close-packed microstructure. Indentation test showed that with increase in GO nature of failure becomes ductile to brittle.

Asgharzadeh et al. [40] had reported that the tensile properties of composite is not just affected by the amount of graphene added to composite but also the method of processing and chemical composition of matrix had also a notable effect on composite. Also, showed that few-layer graphene oxide (FLGO) reinforced composites have exhibited better mechanical properties in comparison to monolithic samples of aluminium whether it was gas atomized or mechanically milled samples. It was concluded through that, MM-FLGO attain increased hardness and compressive yield strength as compared to monolithic MM Al, he also concluded through his work that MM-FLGO composite improves hardness by 61% and compressive strength by 20% in comparison to GA-FLGO. Liu et al. [41] in his work showed that, with increase in amount of reduced GO as reinforcement also increases the Vickers's hardness of the aluminium reinforced with reduced graphene oxide (rGO). It was also noticed that the rGO is evenly spread on the surface of aluminium.

Huang et al. [42] have been fabricated bamboo fiber reinforced epoxy (BF/EF) composites through resin transfer molding process with varying percentage (about 42%) of fiber. It was found that mechanical properties such as tensile strength, Young's modulus increased by decreasing the diameter of bamboo fiber. Also, hygrothermal test exhibited that BF/EF composites were showed very sensitive to moisture absorption and lead to negative effects in the properties of composites. Mohan et al. [43] synthesized short banana fiber reinforced epoxy polymer composite cylinder through resin impregnation method. For that nano clay particles have been filled into a banana fiber. Scanning electron microscope (SEM) micrographs showed that interfacial and load transfer capacity of fiber-matrix have been improved which resulted in enhancing the mechanical properties of composites. Atul et al. [44] studied the application of carbon fiber reinforced silicon carbide (C/SiC) in aerospace industry which is fabricated by chemical vapour infiltration (CVI) and needling methods. Composites have varying properties; therefore, rotary ultrasonic milling is employed

for machining of composites. SEM micrographs showed that SiC was uniformly dispersed into the samples which resulted in improving the strength of the composites and also the space within structure was very small. From the experiment a combination of optimum machining parameters like material density =  $2.34 \text{ g/cm}^3$ , feed rate =  $150 \text{ mm/min}$  and axial depth of cut =  $0.02 \text{ mm}$  was found. It was also found that by decreasing the material density, tool wear decreased.

After going through the literature published in previous years related to fabrication of MMCs, literature gap has been found and there is very limited work that has been done on metal matrix composites using friction stir processing that concluded that uniform dispersion of reinforcement in the matrix is not achieved by other processing techniques such as casting, or powder metallurgy, etc. according to the research papers. Also, if uniform dispersion of reinforced materials was not achieved that will result in a drop in the mechanical properties of metal matrix composite. Therefore, by using friction stir processing to fabricate the MMCs can achieve the uniform dispersion of reinforcement in the matrix.

## 2 Materials and Methodology

For, the purpose of fabrication of metal matrix composite, magnesium billet is selected as matrix of the composite and graphene is selected as a reinforcement. For that different specification of raw materials listed below:

### 1. Magnesium

The magnesium billets were purchased from Parshwamani Metals, Mumbai, Maharashtra, India. The properties of the magnesium are listed in Table 1.

### 2. Graphene

The Graphene nanoparticles were purchased from Ad-Nano Technologies Private Limited, Shimoga, Karnataka, India. The properties of graphene Nanopowders are listed in Table 2.

This billet must be cut in such a way so that friction stir processing can be done over it. So, the dimension which is selected for magnesium plate is 6 mm thickness, 60 mm width, and 100 mm length as shown in Fig. 1. In order to achieve this dimension of magnesium plate, we have used power hacksaw machine so that the aforesaid dimension can be achieved from the magnesium billet. In order to perform

**Table 1** Specification of magnesium

Specification	
Colour	Grey white
Purity	>99.8%
Weight	7.5 kg

**Table 2** Specification of Graphene

Specification	
Colour	Black powder
Purity	>99%
Average thickness ( $z$ )	7.5 kg
Average lateral dimension ( $X$ & $Y$ )	1–4 nm
Numbers of layers	5 $\mu\text{m}$
Surface area	–400 $\text{m}^2/\text{g}$



**Fig. 1** Preparation of magnesium specimen from magnesium billet

the friction stir processing, we must prepare an FSP tool, for that first we have selected tool material as D-3 Tool steel whose composition has already been discussed previously. The dimension of the tool is as follows:

1. Tool pin is 5.5 mm in length, and
2. Tool pin smaller diameter is 3 mm whereas
3. Tool pin larger diameter is 4 mm,
4. Shoulder diameter of Tool is 18 mm, whereas
5. Length of the shoulder of tool is 25 mm.

Friction stir processing tool is prepared with the help of center lathe machine and the tool used is a ceramic tool for cutting the shape of FSP tool as shown in Fig. 2. A groove is made in the magnesium plate with the help of a shaper machine. This groove is generated in the magnesium plate, is used for the filling of nano-sized graphene powder. After filling of groove with graphene powder, magnesium plate is tightly fixed in the milling machine with the help of a fixture as shown in Fig. 3. Now,



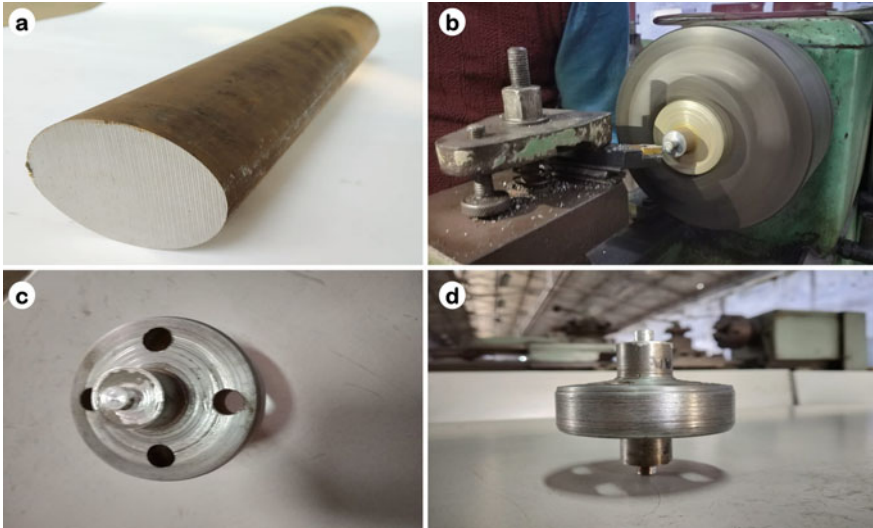


Fig. 2 Procedure for making tool of FSP

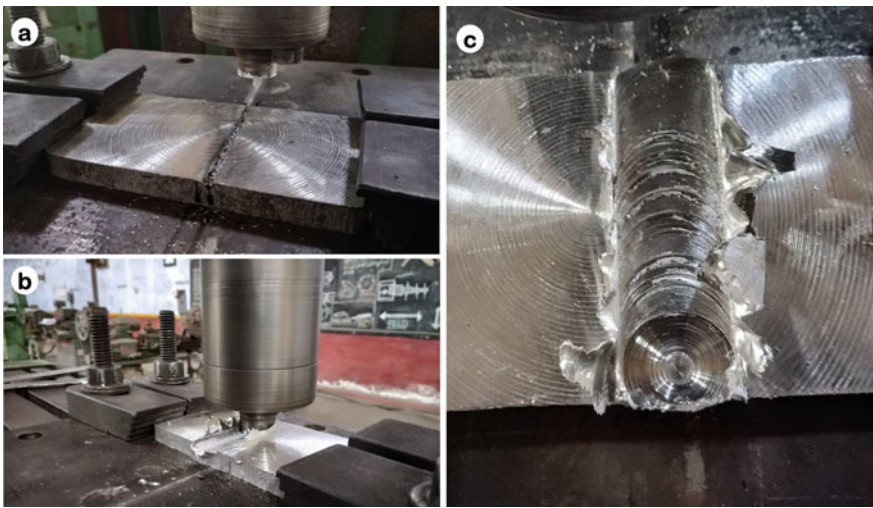


Fig. 3 Steps involved in working of FSP

tool produced for the FSP to be carried out is fixed in the tool post of the milling machine. Now, different combinations of process parameters are tried and listed in Table 3.



**Table 3** Different process parameter

Tool speed (rpm)	630	1000	1600
Feed rate of tool (mm/min)	10	16	25
Angle of tilt (degree)	0	1	1.5

But out of many combinations we tried, it was found that following process parameters stated below are well and good under our conditions:

1. Tool speed—1000 rpm
2. Feed rate of tool—10 mm/min
3. Angle of tilt—1.5°.

### 3 Results and Discussions

This section explains about the mechanical properties achieved by the composites, which is prepared by the friction stir processing.

#### 3.1 Tensile Test

For tensile testing, the FSPed samples were first milled and cut as per ASTM standard as shown in Fig. 4 into the following shape by the wire-cut EDM machine as shown in Fig. 5.

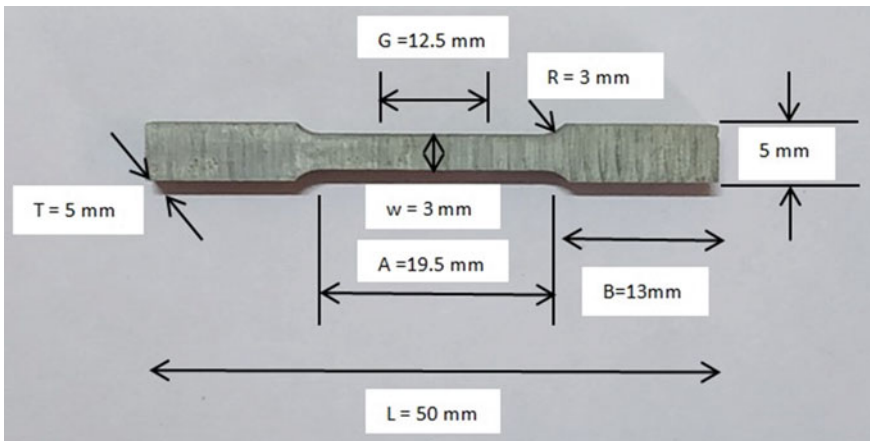


**Fig. 4** Various dimensions of tensile test specimen



**Fig. 5** Tensile sample after wire EDM process

Six test samples were prepared are as follows:

1. Pure magnesium sample (Pure Mg).
2. Friction stir processed pure magnesium sample with 0 vol. % Gr. (FSPed Mg).
3. Friction stir processed pure magnesium sample with 10 vol. % Gr. (10Gr/Mg).
4. Friction stir processed pure magnesium sample with 20 vol. % Gr. (20Gr/Mg).
5. Friction stir processed pure magnesium sample with 30 vol. % Gr. (30Gr/Mg).
6. Friction stir processed pure magnesium sample with 40 vol. % Gr. (40Gr/Mg).

The tensile samples were then tested for tensile strength in the Universal Testing Machine (20KN). The results obtained are listed in Table 4.

As it can be clearly observed from Fig. 6, with increasing graphene vol. %, the tensile strength of the composite increases, reaches maximum at 30 vol. % Graphene content and then decreases for 40 vol. % reinforcement.

Similarly, same trend is observed in Fig. 7 for the different parameters of elongation which indicates that the ductility of the composite increases with the increase in the volume percentage of graphene in the composite, but its ductility tends to decrease after certain amount of reinforcement.

**Table 4** Shows the result of tensile sample

	Pure Mg.	FSPed Mg	10Gr/Mg	20Gr/Mg	30Gr/Mg	40Gr/Mg
TS (MPa)	71.6	87.6	87.7	96.6	138.4	117.2
% ELONG.	11.2	14.6	15.5	10.2	25.0	19.9

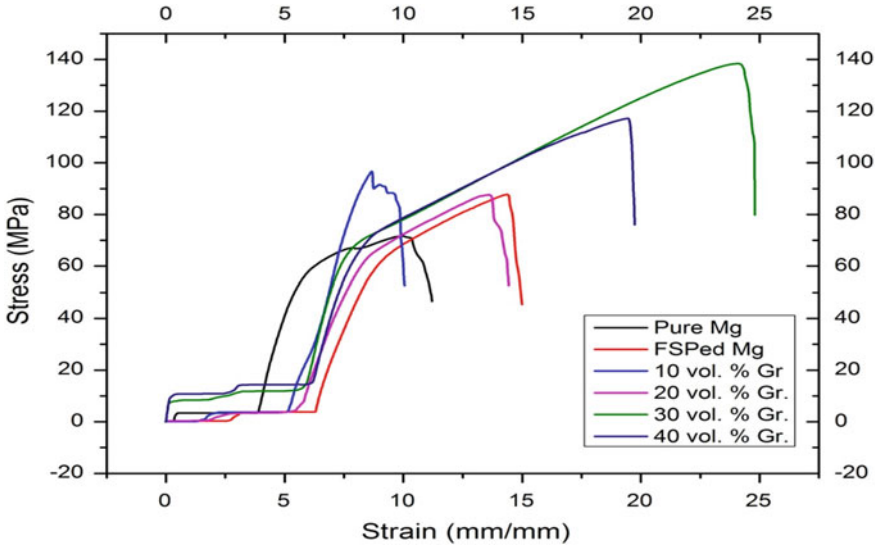


Fig. 6 Stress-strain plots for pure Mg, FSPed and with various volume percentage of graphene

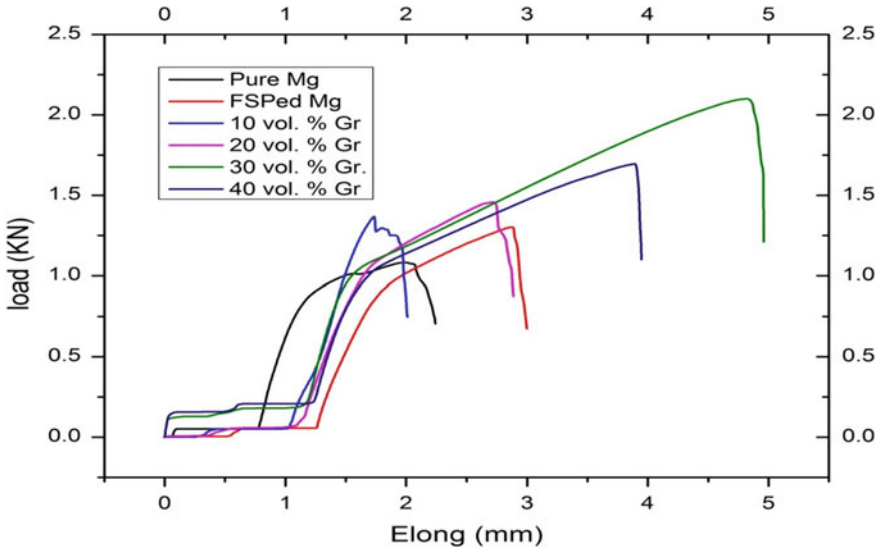


Fig. 7 Load versus Elongation curve of pure Mg, FSPed and with various volume percentage of graphene

### 3.2 X-ray Diffraction Analysis

X-ray diffraction (PANalytical Empyrean) analysis was performed using an incident Cu K $\alpha$  radiation ( $\lambda = 1.5418 \text{ \AA}$ ), at a tube voltage 30 kV with a step size of 0.013 and a counting time of 37.995 s/step with 2 theta values between 15° and 90°. In Fig. 8, we can find the diffraction pattern of pure magnesium sample, here diffraction pattern shows peaks at  $2\theta = 32.2, 34.4, 36.6, 47.8, 63.1, 68.6$  out of which the maximum intensity is found at  $2\theta = 36.6$  and corresponding interlayer spacing(d-spacing) is 2.45 Å. We can also find the diffraction pattern of magnesium and graphene composite sample, here diffraction pattern shows peaks at  $2\theta = 34.2, 34.3, 36.6, 47.7, 62.8$  out of which the maximum intensity is found at  $2\theta = 34.2$  and the corresponding interlayer spacing is 2.61 Å. The crystal structure is a hexagonal lattice structure.

The chemical found in the composite is magnesium and carbon. The XRD analysis shows that the amount of carbon present in the composite is very low as compared to the magnesium. The reason for the very low amount of presence of carbon is the low mass of graphene in the composite. In FSP, continuous rotation of the tool pin and shoulder resulted in formation of shear and compression stress. Furthermore, temperature was increased due to contact of tool and workpiece resulted in shear stress development along the pin column and generating the shear texture distribution.

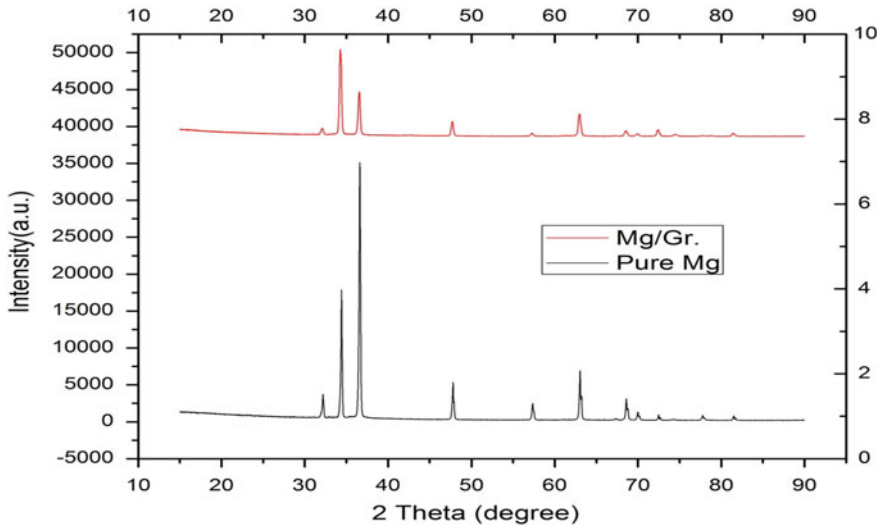


Fig. 8 XRD analysis of pure Mg and with a various composition of graphene

## 4 Conclusions

In the current work, friction stir processing set up was done on the modified milling machine. A metal matrix composite is successfully fabricated with magnesium as matrix and graphene as reinforcement and the process used for the fabrication was friction stir processing. Effects of reinforcement in magnesium were studied and obtained the optimum percentage of graphene at which the mechanical properties were improved. From result and discussions, it can be concluded that:

1. As the volume percentage of graphene increases in the composite, its strength increases then decreases after 30 vol.% of graphene.
2. Also, concluded that with the increase in volume percentage of reinforcement the ductility of the composite material increases.
3. As the rotational speed of milling machine is increased, we observed that the composite material obtained is having tunnel.
4. From XRD analysis, we can say that peaks obtained are prominent and sharp, also percentage of crystallization is more in composite when compared with the pure magnesium.

## References

1. Mazumdar, S.K.: Composites Manufacturing: Materials, Product, and Process Engineering, 1st edn. CRC Press, Boca Raton (2001)
2. Girod, F.A., Quenisset, J.M., Naslain, R.: Discontinuously-reinforced aluminum matrix composites. *Compos. Sci. Technol.* **30**(3), 155–184 (1987)
3. Chou, T.W., Kelly, A., Okura, A.: Fibre-reinforced metal-matrix composites. *CompoSites* **16**(3), 187–206 (1985)
4. Howes, M.: Ceramic-reinforced MMC fabricated by squeeze casting. *JOM* **38**(3), 28–29 (2016)
5. Nardone, V.C., Prewo, K.M.: On the strength of discontinuous silicon carbide reinforced aluminum composites. *Scr. Metall.* **20**(1), 43–48 (1986)
6. Nutt, S.R.: Defects in silicon carbide whiskers. *J. Am. Ceram. Soc.* **67**(6), 428–431 (1984)
7. Thomas, W.M.W., Nicholas E.D., Needham, J.C., Murch, M.G., Temple-Smith, P., Dawes, C.J.: Friction stir welding process developments and variant techniques. *SME Summit*. 1–21 (1991)
8. Mishra, R.S., Mahoney, M.W., McFadden, S.X., Mara, N.A., Mukherjee, A.K.: High strain rate superplasticity in a friction stir processed 7075 Al alloy. *Scr. Mater.* **42**(2), 163–168 (1999)
9. Ma, Z.Y., Mishra, R.S., Mahoney, M.W.: Superplastic deformation behavior of friction stir processed 7075 Al alloy. *Acta Mater.* **50**(17), 4419–4430 (2002)
10. Hofmann, D.C., Vecchio, K.S.: Submerged friction stir processing (SFSP): an improved method for creating ultra-fine-grained bulk materials. *Mater. Sci. Eng., A* **402**(1–2), 234–241 (2005)
11. Dolatkhan, A., Golbabaei, P., Besharati Givi, M.K., Molaiekiya, F.: Investigating effects of process parameters on microstructural and mechanical properties of Al5052/SiC metal matrix composite fabricated via friction stir processing. *Mater. Des.* **37**, 458–464 (2012)
12. Mishra, R.S., Mahoney, M.W.: Friction stir Welding and Processing. ASM International, Materials Park, Ohio (2007)
13. Mishra, R.S., Ma, R.S.: Friction stir welding and processing. *Mater. Sci. Eng. R Rep.* **50**(1–2), 1–78 (2005)

14. Prakash, C., Singh, S., Ramakrishna, S., Królczyk, G., Le, C.H.: Microwave sintering of porous Ti–Nb–HA composite with high strength and enhanced bioactivity for implant applications. *J. Alloy Comp.* **824**, 153774 (2020)
15. Prakash, C., Singh, S., Sharma, S., Garg, H., Singh, J., Kumar, H., Singh, G.: Fabrication of aluminium carbon nano tube silicon carbide particles based hybrid nano-composite by spark plasma sintering. *Mater. Today Proc.* **21**, 1637–1642 (2020)
16. Prakash, C., Singh, S., Pabla, B.S., Sidhu, S.S., Uddin, M.S.: Bio-inspired low elastic biodegradable Mg–Zn–Mn–Si–HA alloy fabricated by spark plasma sintering. *Mater. Manuf. Process.* **34**, 357–368 (2019)
17. Prakash, C., Singh, S., Gupta, M.K., Mia, M., Królczyk, G., Khanna, N.: Synthesis, characterization, corrosion resistance and in-vitro bioactivity behavior of biodegradable Mg–Zn–Mn–(Si–HA) composite for orthopaedic applications. *Mater.* **11**, 1602 (2018)
18. Prakash, C., Singh, S., Verma, K., Sidhu, S.S., Singh, S.: Synthesis and characterization of Mg–Zn–Mn–HA composite by spark plasma sintering process for orthopedic applications. *Vacuum.* **155**, 578–584 (2018)
19. Oh-Ishi, K., McNelley, T.R.: Microstructural modification of as-cast NiAl bronze by friction stir processing. *Metall. Mater. Trans. A* **35**(9), 2951–2961 (2004)
20. Tsujikawa, M., Somekawa, H., Chung, S.W., Higashi, K.: Development of constitutive equation on superplastic RS P/M Mg–Y–Zn alloy. *Mater. Trans.* **46**(10), 2287–2290 (2005)
21. Bauri, R., Yadav, D., Suhas, G.: Effect of friction stir processing (FSP) on microstructure and properties of Al–TiC in situ composite. *Mater. Sci. Eng. A* **528**(13–14), 4732–4739 (2011)
22. Berbon, P.B., Bingel, W.H., Mishra, R.S., Bampton, C.C., Mahoney, M.W.: Friction stir processing: a tool to homogenize nanocomposite aluminum alloys. *Scr. Mater.* **44**(1), 61–66 (2001)
23. Cavaliere, P.: Mechanical properties of friction stir Processed 2618/Al<sub>2</sub>O<sub>3</sub>/20p metal matrix composite. *Compos. A Appl. Sci. Manuf.* **36**(12), 1657–1665 (2005)
24. Hodder, K.J., Izadi, H., McDonald, A.G., Gerlich, A.P.: Fabrication of aluminum-alumina metal matrix composites via cold gas dynamic spraying at low pressure followed by friction stir processing. *Mater. Sci. Eng. A* **556**, 114–121 (2012)
25. Morisada, Y., Fujii, H., Mizuno, T., Abe, G., Nagaoka, T., Fukusumi, M.: Modification of thermally sprayed cemented carbide layer by friction stir processing. *Surf. Coat. Technol.* **204**(15), 2459–2464 (2010)
26. Morisada, Y., Fujii, H., Nagaoka, T., Fukusumi, M.: MWCNTs/AZ31 surface composites fabricated by friction stir processing. *Mater. Sci. Eng. A* **419**(1–2), 344–348 (2006)
27. Lee, C.J., Huang, J.C., Hsieh, P.J.: Mg based nano-composites fabricated by friction stir processing. *Scr. Mater.* **54**(7), 1415–1420 (2006)
28. Ma, Z.Y., Sharma, S.R., Mishra, R.S.: Effect of multiple-pass friction stir processing on microstructure and tensile properties of a cast aluminum-silicon alloy. *Scr. Mater.* **54**(9), 1623–1626 (2006)
29. Elangovan, K., Balasubramanian, V., Valliappan, M.: Effect of tool pin profile and tool rotational speed on mechanical properties of friction stir welded AA6061 aluminium alloy. *Mater. Manuf. Process.* **23**(3), 251–260 (2008)
30. Shafiei-Zarghani, A., Kashani-Bozorg, S.F., Zarei-Hanzaki, A.: Microstructures and mechanical properties of Al/Al<sub>2</sub>O<sub>3</sub> surface nano-composite layer produced by friction stir processing. *Mater. Sci. Eng. A* **500**(1–2), 84–91 (2009)
31. Yang, M., Xu, C., Wu, C., Lin, K.C., Chao, Y.J., An, L.: Fabrication of AA6061/Al<sub>2</sub>O<sub>3</sub> nano ceramic particle reinforced composite coating by using friction stir processing. *J. Mater. Sci.* **45**(16), 4431–4438 (2010)
32. Mishra, R.S., Ma, Z.Y., Charit, I.: Friction stir processing: a novel technique for fabrication of surface composite. *Mater. Sci. Eng., A* **341**(1–2), 307–310 (2003)
33. Mahmoud, E.R.I., Takahashi, M., Shibayanagi, T., Ikeuchi, K.: Wear characteristics of surface-hybrid-MMCs layer fabricated on aluminum plate by friction stir processing. *Wear* **268**(9–10), 111–1121 (2010)

34. Tewari, A., Spowart, J.E., Gokhale, A.M., Mishra, R.S., Miracle, D.B.: Characterization of the effects of friction stir processing on microstructural changes in DRA composites. *Mater. Sci. Eng. A* **428**(1–2), 80–90 (2006)
35. Wang, W., Shi, Q., Liu, P., Li, H. and Li, T.: A novel way to produce bulk SiCp reinforced aluminum metal matrix composites by friction stir processing. *J. Mater. Process. Technol.* **209**(4), 2099–2103 (2009)
36. Chang, C.I, Wang, Y.N, Pei, H.R., Lee, C.J, Du, X.H., Huang, J.C.: Microstructure and mechanical properties of Nano-ZrO<sub>2</sub> and Nano-SiO<sub>2</sub> particulate reinforced AZ31-Mg based composites fabricated by friction stir processing. *Key Eng. Mater.* **351**, 114–119 (2007)
37. Mahmoud, E.R.I., Takahashi, M., Shibayanagi, T., Ikeuchi, K.: Effect of friction stir processing tool probe on fabrication of SiC particle reinforced composite on aluminium surface. *Sci. Technol. Weld. Joining* **14**(5), 413–425 (2009)
38. Azizieh, M., Kokabi, A. H. and Abachi, P.: Effect of rotational speed and probe profile on microstructure and hardness of AZ31/Al<sub>2</sub>O<sub>3</sub> nanocomposites fabricated by friction stir processing. *Mater. Des.* **32**(4), 2034–2041 (2011)
39. Dasari, B.L., Morshed, M., Nouri, J.M., Brabazon, D., Naher, S.: Mechanical properties of graphene oxide reinforced aluminium matrix composites. *Compos. B Eng.* **145**, 136–144 (2018)
40. Asgharzadeh, H., Sedigh, M.: Synthesis and mechanical properties of Al matrix composites reinforced with few-layer graphene and graphene oxide. *J. Alloy. Compound.* **728**, 47–62 (2017)
41. Liu, J., Khan, U., Coleman, J., Silva, B., Rodriguez, P., Nahar, S., Brabazon, D.: Graphene oxide and graphene nanosheet reinforced aluminium matrix composites: powder synthesis and prepared composite characteristics. *Mater. Des.* **94**, 87–94 (2016)
42. Huang, J.K., Young, W.B.: The mechanical, hygral, and interfacial strength of continuous bamboo fiber reinforced epoxy composites. *Compos. B Eng.* **166**, 272–283 (2019)
43. Mohan, T.P., Kanny, K.: Compressive characteristics of unmodified and nanoclay treated banana fiber reinforced epoxy composite cylinders. *Compos. B Eng.* **169**, 118–125 (2019)
44. Babbar, A., Sharma, A., Jain, V., Jain, A.K.: Rotary ultrasonic milling of C/SiC composites fabricated using chemical vapor infiltration and needling technique. *Mater. Res. Express.* **6**(8) (2019)

# Strength Properties of M40 Concrete with Rice Husk Ash as Partial Replacement of Cement



Jaspreet Singh, Vishal kumar, Harkamal Singh, and Amar Singh

**Abstract** Strong material is key factor in measuring strength of a structure. For strong structure, strength of material used should be high enough. If the concrete is basically a condition and eco-friendly makes it more sustainable. That is the better idea to make the structure eco-friendly, and also the use of material is less. The purpose of the study is to expedite the improvement of infrastructure with help of high-strength concrete. The study has one of the major advantages that we can use the waste material produced during farming in the improvement of strength of material and in the construction part of mega structures. Research has indicated that concrete consisting rice husk ash as some percentage of cement weight has improved the performance of concrete. RHA contains 19–21% ash content with respect to weight of rice husk.

**Keywords** Pozzolanic material · Rice husk ash (RHA)

---

J. Singh (✉) · V. kumar · H. Singh · A. Singh  
Lovely Professional University, Phagwara, Punjab 144411, India  
e-mail: [jaspreet.singh025@gmail.com](mailto:jaspreet.singh025@gmail.com)

V. kumar  
e-mail: [ervishal@icloud.com](mailto:ervishal@icloud.com)

H. Singh  
e-mail: [Harkamal.18266@lpu.co.in](mailto:Harkamal.18266@lpu.co.in)

A. Singh  
e-mail: [amarsinghnagi@gmail.com](mailto:amarsinghnagi@gmail.com)

© Springer Nature Singapore Pte Ltd. 2020  
C. Prakash et al. (eds.), *Advances in Materials Science and Engineering*,  
Lecture Notes in Mechanical Engineering,  
[https://doi.org/10.1007/978-981-15-4059-2\\_20](https://doi.org/10.1007/978-981-15-4059-2_20)



# 1 Introduction

## 1.1 Preface

Rice production in world is about 58 billion t/y, which is on the rise, while the world population and rice consumption are increasing day by day.

The combustion ashes of the shells produced to an average of 19% by weight of the rice husk. Before 1970, the ORS was generally produced by the uncontrolled burning, and the crystals with poor pozzolanic properties were released.

## 2 Salient Features

- Concrete with RHA shows more resistance to extreme conditions in comparison with plain cement concrete.
- It is more economical than plain cement concrete.
- It increases the workability of concrete.
- Cohesiveness and plasticity of concrete increase with the addition of RHA.
- Unit weight of RHA concrete is inversely proportional to RHA content.
- Durability of concrete is enhanced, and reduction in corrosion is absorbed.
- RHA enhances the impermeability of concrete.
- RHA has eco-friendly properties and is responsible for capital cost reduction of a structure.
- Low-cost tiles and concrete blocks for building are made using RHA.

## 3 Physical Properties

- It feels soft when touched.
- It leaves the grey colour in hand when touched.
- The particle size is really very small with irregular shape (Table 1).

**Table 1** Physical properties of RHA

S. No.	Properties	Particulars
1	Appearance	Grey coloured
2	Shape of particle	Irregular
3	Mineralogy	Non-crystalline
4	Size of granule	<45 micron
5	Odour	No odour
6	Sp.Gr.	2.41

**Table 2** Chemical properties of RHA

S. No.	Particulars	Ratio (%)
1	SiO <sub>2</sub>	86.95
2	Al <sub>2</sub> O <sub>3</sub>	0.21
3	Fe <sub>2</sub> O <sub>3</sub>	0.11
4	CaO	0.3–2.2
5	MgO	0.2–0.6
6	Na <sub>2</sub> O	0.1–0.8
7	K <sub>2</sub> O	2.15–2.30
8	Loss on ignition	3.15–4.4

## 4 Chemical Properties

See Table 2.

## 5 Literature Review

### 5.1 Compressive Strength

#### Anil Kumar Suman [1]

In this work, the concrete strength at 7, 14 and 28 days interval is measured. Envelope used rice ash is obtained from Kamal solvent extractions pvt ltd. which is located in Rajnandgaon (Chhattisgarh). With increase in combustion temperature, the silica content in the ash increases.

RHA improves the concrete properties besides reducing environmental polluter factors. It was suggested that up to 30% of substitution of RHA is feasible without compromising the strength of concrete.

Kartini et al. [2] studied replacement of 20 and 30% ordinary Portland cement by wt. of RHA and with/without Sp, six (6) series of concrete specimens were cast, namely OPC, RHA20, RHA30, OPCSp, RHA20Sp and RHA30Sp.

#### Flexural strength

Akeke et al. [3] experimentally examined the structural concrete by using OPC with RHA. In the study which he conducted on bending properties to examine the MOR, the values obtained after 28 days were noted and the tensile strength values are 1.84, 1.57 and 0.83 N/mm<sup>2</sup> at 10, 18 and 22% substitution. This research is therefore a performance investigation percentage replacement of RHA and ordinary Portland cement in structural concrete.

Abdelalim [4] explained the performance of concrete in rigid roads with variation in percentage of rice husk ash with cement weight for concrete quality mixture M40.

In the result, he found less strength reduction in 5 and 10% of replacement. First of all, there is an increase in the flexural strength, but after 10% replacement, the value starts decreasing. Similarly, for 15, 20 and 25% replacement, the flexural strength keeps on decreasing.

**Split Tensile Strength**

Akeke et al. [3] experimentally studied the influence of the introduction of rice husk ash. He burned it for about 48 h in open air and uncontrolled combustion process. The temperature while experimenting was 400–6000 °C. The sample was collected and sieved through BS 75 um sieve size, and the colour found was grey. Assay was carried out at volume percentages of replacing 10, 20 and 25% (Table 3).

At 10% replacement, the split tensile strength was found 1.94 N/mm<sup>2</sup>, whereas at 20%, it was found 1.17. Similarly, at 30%, the value found as 0.91 only. Hence, by raising the content of RHA, split tensile strength was found decreasing.

Ramakrishnan S, Velraj Kumar G and Ranjith S (2006) explained the performance of concrete for rigid concrete surface replacing different percentages of rice ash up by weight of cement for concrete quality control mixture M40. In his research paper, he studied the influence of the rice husk ash (RHA) on the performance of various concrete parameters to produce an economic concrete for rigid pavements. Results of 28th-day split tensile strength for different percentage of RHA are as follows (Fig. 1).

The split tensile strength of the cement using rice husk ash concrete found less impact on 5 and 10% replacement. First of all, split tensile strength increases, but

**Table 3** Result of split tensile strength

S. No.	% replacement (%)	Breaking load	Split tensile strength (28 days)
1	10.00	304,738	1.94
2	20.00	91,500	1.17
3	30.00	79,500	0.91

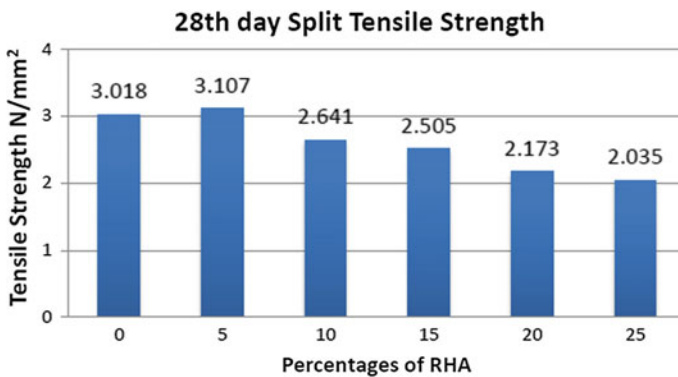


**Fig. 1** Split tensile strength test

after 10% replacement, the value starts decreasing. Similarly, for 15, 20 and 25% replacement, the split tensile strength keeps on decreasing.

## 6 Methodology Used for Mix Design

### 6.1 Concrete Mix Design

The compressive strength is said to be the important parameter of concrete. Therefore, the design mix should be prepared keeping in view the permissible limits and minimum requirements with appropriate workability. Codal provision of IS:10262-2009 was followed. Following three steps must be followed for proportioning of concrete mixes.

- (i) Selection of appropriate ingredients like fine and coarse aggregates, water and cement.
- (ii) Relative quantities of components to have economical concrete.
- (iii) Every phase of concrete making is to be carefully conducted.

### 6.2 Properties of Cement and Aggregates

See Tables 4, 5 and 6.

**Table 4** Cement properties

S. No.	Properties	Result	IS code
1	Fineness	2.125	IS code 8112-1989
2	Specific gravity	3.09	
3	Early setting time	30 min	
4	Final setting time	9.7 h	
5	Soundness	2 mm	

**Table 5** FA properties

S. No.	Properties	Outcome
1	Sp.Gr.	2.732
2	Water absorption	1%

ZONE as per IS code 383-1970 III

**Table 6** Coarse aggregate properties

S. No.	Size of coarse aggregate (mm)	Property	Result
1	20	Specific gravity	2.71
		Water absorption	0.55%
2	10	Specific gravity	2.68
		Water absorption	0.50%

## 7 Preparation of Mix Design

- In this project, we are using the M40 grade of concrete mix design for testing purpose.
- Mix design proportions are given in Table 7.

### 7.1 Testing of Specimens

Specimens, after casting were tested at 7 and 28 days interval of curing.

### 7.2 Compressive Testing Machine

The test samples were de-moulded after 24 h. Then, they were poured in water tank for the predefined time. After desired time of testing, samples were taken out of the tank and allowed for drying surface for 12–15 min; samples were tested in compressive testing machine (CTM) at the load rate of 5 KN/sec recommended as per IS code: 516-1959 (Fig. 2).

### 7.3 Result and Discussions

See Table 8 and Fig. 3.

**Table 7** Mix design of M40 grade

Mix ratio	Cement	Sand	CA	Water
Ratio	1	1.64	2.36	0.45
Quantity	442 kg/m <sup>3</sup>	734.9 kg/m <sup>3</sup>	1048.53 kg/m <sup>3</sup>	176.5 kg/m <sup>3</sup>

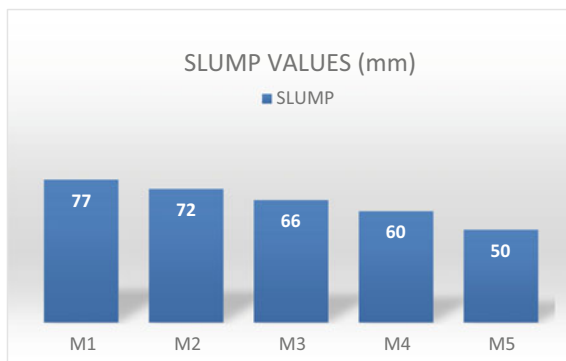
**Fig. 2** Compressive testing machine



**Table 8** Result of slumps

Mix	RHA replacement (%)	Slump value (mm)
M1	0	77
M2	5	72
M3	10	66
M4	15	60
M5	20	50

**Fig. 3** Slump value results



### 7.4 Compressive Strength

Six cubes sized 150 mm × 150 mm × 150 mm that were cast are to be tested at 7 days and 28 days of curing for each mix, except for concrete mix containing carbon nanotubes. Nine numbers of cubes of concrete were cast and tested after 28 days of curing.

### 7.5 Result of Compressive Strength Test

See Table 9 and Fig. 4.

**Table 9** Compressive strength results

Concrete MIX	RHA replacement (%)	Compressive strength (N/mm <sup>2</sup> )	
		7 days	28 days
M1	0	33.5	47.6
M2	5	36.7	49.1
M3	10	34.6	46.2
M4	15	31.9	40.1
M5	20	27.4	35.3
M6	25	21.1	27.4

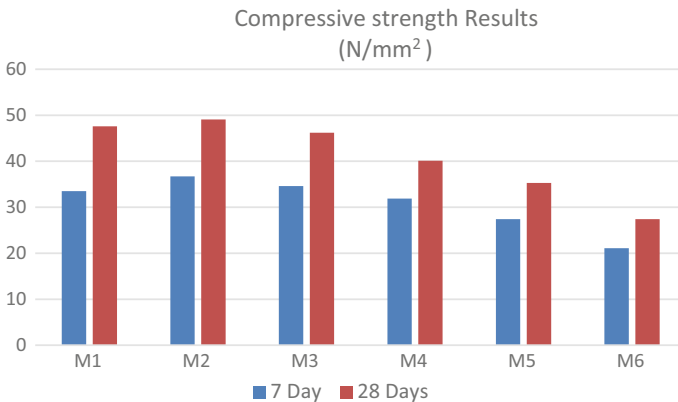


**Fig. 4** Result of compressive strength

**Table 10** Split tensile strength of concrete

Sample	ST strength (N/mm <sup>2</sup> )	
	7 days	28 days
M1	2.163	3.021
M2	2.360	3.178
M3	1.921	2.643
M4	1.814	2.517
M5	1.586	2.118
M6	1.443	2.041

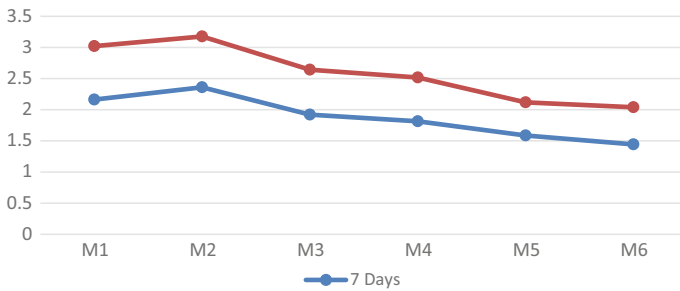


**Fig. 5** Split tensile strength

### 7.6 Splitting Tensile Strength

Six cubes sized 100 mm × 100 mm × 500 mm that were cast are to be tested at 7 days and 28 days of curing for each mix, except for concrete. Nine numbers of cubes of concrete were cast and tested after 28 days.

### 7.7 Results of Split Tensile Strength Test

See Table 10 and Fig. 5.

### 7.8 Comparing Results

- As the project done is with RHA and without RHA, we need to compare the results of the two.
- Now, below is the comparison of results of the project in the form of table and graphical representation.



### 7.9 Compressive Strength Result Comparison

See Table 11 and Figs. 6 and 7.

**Table 11** Result comparison

Mix	RHA replacement (%)	Compressive strength (N/mm <sup>2</sup> )		Flexure strength (N/mm <sup>2</sup> )
		7 days	28 days	28 days
M1	0	33.5	47.6	3.037
M2	5	36.7	49.1	3.350
M3	10	34.6	46.2	3.151
M4	15	31.9	40.1	2.516
M5	20	27.4	35.3	2.185
M6	25	21.1	27.4	1.975

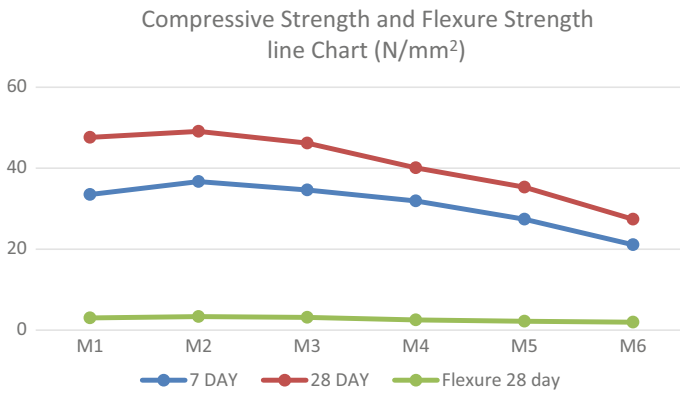


**Fig. 6** Comparison of compressive and flexure strength

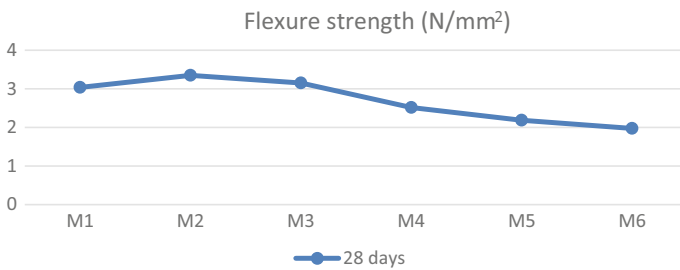


**Fig. 7** Flexure strength of concrete

- From the above outcomes, we can conclude that the strength (compressive) of concrete can be enhanced if a correct proportion of RHA is mixed properly.
- Flexure strength came out to be good at M2 grade in our testing, and after further increase in RHA, we notice a sudden decrease in flexure strength.

## References

1. Suman, A. K., Saxena, A. K., Arora T. R.: Assessment of concrete strength using partial replacement of cement for rise husk ash. *Int J Soft Comput Eng (IJSCE)*, ISSN, 2231–2307 (2015)
2. Kartini, K., Mahmud, H.B., Hamidah, M.S.: Strength properties of Grade 30 rice husk ash concrete. In: 31st Conference on Our World in Concrete & Structures (2006)
3. Akeke, G.A., et al.: Structural properties of rice husk ash concrete. *Int. J. Eng.* **3**(3), 8269 (2013)
4. Abdelalim, A.M.K., Abdelaziz, G.K., Zahran, R.: Transport and microstructure properties of rice husk ash concrete. *Sci. Bull. Fac. Eng. Ain Shams Univ.* **39**(3), 21–34 (2004)
5. Alvarez, M.: Marine durability characteristics of rice husk ash-modified reinforced concrete. In: Proceedings of the 4th LACCEI International Latin American and Caribbean Conference for Engineering and Technology (LACCET'06), Breaking Frontiers and Barriers in Engineering: Education, Research and Practice (2006)
6. Arpana: Rice husk ash-admixture to concrete. In: 2nd National conference on Advances in Concrete Technology, pp. 93–98 (2004, February 26–27)
7. Bui, D.D., Hu, J., Stroeven, P.: Particle size effect on the strength of RHA blended gap-graded Portland cement concrete. *Cem. Concr. Compos.* **27**(3), 357–366 (2005, March)
8. Pande, A. M., Makarande S. G.: Effect of rice husk ash on concrete. *Int J Eng Res Appl (IJERA)* ISSN, 2248–9622 (2013)
9. Fadzil, A.M., Azmi, M.J.M., Hisyam, A.B.B., Azizi, M.A.K.: Engineering properties of ternary blended cement containing rice husk ash and fly ash as partial cement replacement materials. *ICCBT A* **10**, 125–134 (2008)
10. Rao, G.V.R., Sheshagiri Rao, M.V.: High performance concrete with rice husk ash as mineral admixture. *ICI J.* 17–22 (2003, April–June)
11. de Sensale, G.R.: Strength development of concrete with rice-husk ash. *Cem. Concr. Compos.* **28**, 158–160 (2006)
12. Givi, A.N., et al.: Assessment of the effects of rice husk ash particle size on strength, water permeability and workability of binary blended concrete. *Constru. Build. Mater.* **24**(11), 2145–2150 (2010)
13. Givi, A.N., et al.: Contribution of rice husk ash to the properties of mortar and concrete: a review. *J. Am. Sci.* **6**(3), 157–165 (2010)
14. Mahmud, H.B., Chia, B.S., Hamid, N.B.A.A.: Rice husk ash-an alternative material in producing high strength concrete. In: International Conference on Engineering Materials, June 8–11, 1997, Ottawa, Canada, pp. 275–284
15. Hossain, K.M.A.: Properties of volcanic pumice based cement and lightweight concrete. *Cem. Concr. Res.* **34**(2), 283–291 (2004)
16. Kad, N., Vinod, M.: Review research paper on influence of rice husk ash on the properties of concrete. *Int. J. Res.* **2**(5), 631–635 (2015)
17. Kulkarni, M.S. et al.: Effect of rice husk ash on properties of concrete. *J. Civ. Eng. Environ. Technol.* (2014). ISSN 2349-8404
18. Nagrale, S.D., Hajare, H., Modak, P.R.: Utilization of rice husk ash. *Carbon* **6** (2), 42 (2012).

19. Obilade, I.O.: Use of rice husk ash as partial replacement for cement in concrete. *Int. J. Eng.* **5**(04), 8269 (2014)
20. Rajput, J., Yadav, R.K., Chandak, R.: The effect of rice husk ash used as supplementary cementing material on strength of mortar. *Int J Eng Res Appl* **3**(3), 133–136 (2013)

# Influence of Graphene on Mechanical Behavior of EVA Composite at Low Strain Rate Loading



Kanwer Ajit Singh, Dinesh Kumar , and Prashant Jindal 

**Abstract** The present study is aimed to examine the mechanical behavior of graphene reinforced EVA composites at low strain rate loading under the influence of the varying composition of graphene. Composites of EVA-based graphene have been successfully prepared by using sigma mixing approach followed by Injection molding. Uniform dispersion of graphene in the EVA matrix has been validated by using FESEM technique. Tensile results show that the strength of the EVA/Graphene composite has been increased with the increase in the composition of graphene in the EVA matrix. In comparison to pure EVA, a significant improvement of 25% has been observed in the strength of EVA/Graphene composite with a minor composition of Graphene (5wt%). Effect of varying strain rates ( $0.001\text{ s}^{-1}$ ,  $0.01\text{ s}^{-1}$ , and  $0.1\text{ s}^{-1}$ ) has also been studied and it has been noticed that the strength of EVA/Graphene composite material has been increased with the increase in strain rate. Young's modulus of EVA/Graphene composite with 7–10 wt% of graphene has been increased in the range of 21–27% in comparison to pure EVA. Uniform dispersion of Graphene and their adhesion with EVA matrix are the suggested reason for significant improvement in mechanical properties of EVA-based composite material. The present study could be beneficial for various low load-bearing applications of EVA-based composite materials.

**Keywords** EVA · Graphene · Sigma mixing · Injection molding · Young's modulus

---

K. A. Singh · D. Kumar (✉) · P. Jindal  
University Institute of Engineering & Technology, Panjab University,  
Chandigarh 160014, India  
e-mail: [dnsharma327@gmail.com](mailto:dnsharma327@gmail.com)

K. A. Singh  
e-mail: [kanwerajit2036@gmail.com](mailto:kanwerajit2036@gmail.com)

P. Jindal  
e-mail: [jindalp@pu.ac.in](mailto:jindalp@pu.ac.in)

© Springer Nature Singapore Pte Ltd. 2020  
C. Prakash et al. (eds.), *Advances in Materials Science and Engineering*,  
Lecture Notes in Mechanical Engineering,  
[https://doi.org/10.1007/978-981-15-4059-2\\_21](https://doi.org/10.1007/978-981-15-4059-2_21)

## 1 Introduction

Nowadays, polymers are in high demand because of their excellent physical properties [1]. Polymers possess high strength to weight ratio, corrosion-free characteristics, ease of fabrication, lower cost, lightweight, etc. But there are some limitations with the use of polymer such as; low strength, low melting point, fatigue, failure under periodic loading, etc. Therefore, modification of these polymers is required to sustain with fluctuating load and temperature conditions. This modification of polymers may require the addition of some foreign material into the base matrix [2, 3]. Therefore, polymer composite fabrication has been drawn great interest by scientists to achieve better properties than the polymer possesses alone. Mechanically strong material like graphene and carbon nanotubes can be used as filler material to improve the mechanical properties of pure polymer [4, 5]. The improvement in the mechanical performance of polymer-based composite material mainly depends on the extent of dispersion of filler material [6]. There are several methods that have been established in the past by various scientists to fabricate high strength polymer-based composite material by achieving uniform dispersion of filler material.

Park et al. [7] used polyethylene (PE) based graphene nanocomposites for mechanical characterization under the influence of the varying composition of Graphene. Researchers reported noticeable improvement of 12 folds and 3 folds in tensile modulus of LDPE and HDPE, respectively, with 5 wt% of graphene oxide in comparison to pure PE. Jindal et al. [8] worked on PC/MWCNTs composites for evaluating their mechanical properties at the varying composition of MWCNTs. This group observed an improvement of 95% in elastic modulus and 150% in hardness of composites with 2 wt% composition of MWCNTs. Stark et al. [9] worked on Dynamic Mechanical Analysis EVA polymer. They reported that the glass transition temperature of EVA at the frequency level lies between  $-40$  and  $-20$  °C. Tapas Kulia et al. [10] performed Dynamic Mechanical Testing on Dodecyl amine-modified graphene/linear low-density polyethylene nanocomposites and observed that the neat linear low-density polyethylene has low storage modulus as compared to amine-modified graphene/linear low-density polyethylene. The same group of researchers [11] studied the mechanical behavior of functionalized graphene (ODA-G)/EVA composites and reported that tensile strength of the composites with 1 wt% of ODA-G has been improved by 74% in comparison to pure EVA. Composites of graphene possess better mechanical, thermal and electrical properties [1, 12]. Jindal et al. [13] prepared Poly (methyl acrylate) (PMMA)/Multi-Walled Carbon Nanotubes (MWCNTs) and observed that hardness and modulus for composites with 5wt% composition of MWCNTs have been enhanced by 44% and 27%, respectively, in comparison to pure PMMA. Bing Na et al. [14] reported that the impact strength of HDPE/EVA composites has been increased by 6 times in comparison to pure HDPE.

Tayebi et al. [15] worked on Graphene oxide (GO) and reduced graphene oxide (RGO) reinforced low-density polyethylene (LDPE)/EVA composites. They reported that Young's modulus of 7 wt% (both RGO and GO) composites has been improved by 92% and 65%, respectively, in comparison to pure LDPE. Guo et al. [16] worked

on EVA/Ethylene-1-butene copolymer(EtBC) composite to evaluate their mechanical properties under compressive and tensile loading. Scientists reported improved tensile and compressive strength of composite material in comparison to pure EVA.

Serban et al. [17] used polyamide 12-based polymer to observe the effect of strain rate and temperature variation on its mechanical properties. A noticeable improvement of 410 and 185% was observed in Young's modulus and tensile strength, respectively, in equivalence to pure polymer. Jindal et al. [18] used polycarbonate (PC) and Multi-walled carbon nanotube composite(MWCNT-PC) to evaluate the mechanical properties at different strain rates. Researchers observed that at 2wt% concentration of MWCNTs, the impact strength is increased in the range of 10–20% in comparison to pure PC. George and Bhowmick [19] reported improved electrical, mechanical, and thermal properties carbon nanofiber reinforced EVA composites in comparison to pure EVA. A low wt% (1wt%) of carbon fiber was found sufficient to improve, tensile strength by 61% in comparison to pure EVA. Yuan et al. [20] prepared graphene reinforced EVA composites by using in situ polymerization to evaluate their electrical conductivity by varying the composition of Graphene. With a low concentration of RGO and PANI (4.0wt% and 8.0wt%, respectively) the conductivity of EVA is enhanced up to  $1.07 \times 10^{-1} \text{ S cm}^{-1}$ . Cheng et al. [21] reported improved mechanical properties of poly (methyl methacrylate) PMMA by reinforcing it with EVA. Zhang et al. [22] prepare EVA and organ clay composite by melt intercalation with twin-extruder mixing. They concluded that Intercalate ability of EVA has been increased as VA content is increased from 6 to 12 wt%. Zhang et al. [23] choose a range of strain rate and temperature for basalt fiber reinforced polymer composites (BFRP) to evaluate their tensile strength. With the variation of strain rate from  $19 \text{ s}^{-1}$  to  $133 \text{ s}^{-1}$ , tensile strength and toughness increased by 45.5% and 17.3%, respectively, in comparison to pure polymer. Kim et al. [24] reported that EVA/NR foam with 90% of EVA and 10% of NR formed at  $165 \text{ }^\circ\text{C}$  has high tear strength and rebound resilience in comparison to pure EVA foam.

After the comprehensive study of previous work, it has been observed that limited work has been done on the static mechanical characterization of EVA-based composite. Few reports are available on the tensile characterization of EVA-based composite material at varying composition of filler material. No work to best of our knowledge has been reported on the influence of varying strain rate on graphene reinforced EVA-based composite material. As EVA is used in various low load-bearing applications, therefore, the influence of varying strain rates becomes important to analyze their effect on the mechanical performance of the composite material. Therefore, the present study has been undertaken to evaluate the mechanical performance of EVA/Graphene composite under the influence of varying strain rates and composition of graphene.

## 2 Experimental Section

### 2.1 Materials and Methods

Pure PU beads of EVA have been used as base material and Graphene has been used as filler material. Twin-screw extrusion [25] followed by Injection molding [21–24] have been used for the fabrication EVA-based Graphene composites. Beads of pure EVA (10 gm) have been poured in the hopper of sigma mixture and temperature and RPM of the equipment have been set at 225 °C and 25 rpm, respectively. After melting of EVA, Graphene has been poured to the hopper of sigma mixture and material in the form of lumps has been obtained by varying the composition of Graphene (1, 3, 5, 7, and 10wt%). These lumps are further used for the fabrication of dog-boned specimen (ASTM d638 type V). Specimens of pure EVA have also been fabricated by the same techniques for evaluating the influence of Graphene on the mechanical behavior of EVA. Before using for Injection molding, lumps have been used for FESEM to assure the distribution of Graphene into EVA matrix. Representation of different compositions of EVA/Graphene composite based on the percentage of graphene in the composite is given in Table 1.

Figure 1 shows the FESEM image of the EVA/Graphene composite. Dark portion shows the EVA and the highlighted portion is graphene because EVA has high electron density than graphene. Wrinkles prove the presence of graphene in the EVA/Graphene matrix [25, 26].

Fourier Transform-Infrared Spectroscopy (FTIR) of graphene is shown in Fig. 2. In this Fig, the carbon–carbon bond [C=C] is represented by the peak at  $1626\text{ cm}^{-1}$  (wave number) [27, 28].

### 2.2 Mechanical Characterization

Tensile tests have been performed on micro Universal Testing Machine (UTM) having an axial load capacity of 1KN, and a stroke length of 50 mm. A small pre-load has been applied to the specimen to ensure the grip of the specimen into the fixture. These tests have been performed at room temperature and humidity of 55%.

**Table 1** Nomenclature of EVA-based Graphene composite material

NAME	Composition of Graphene in EVA (wt%)
EVA1	1
EVA3	3
EVA5	5
1EVA7	7
EVA10	10

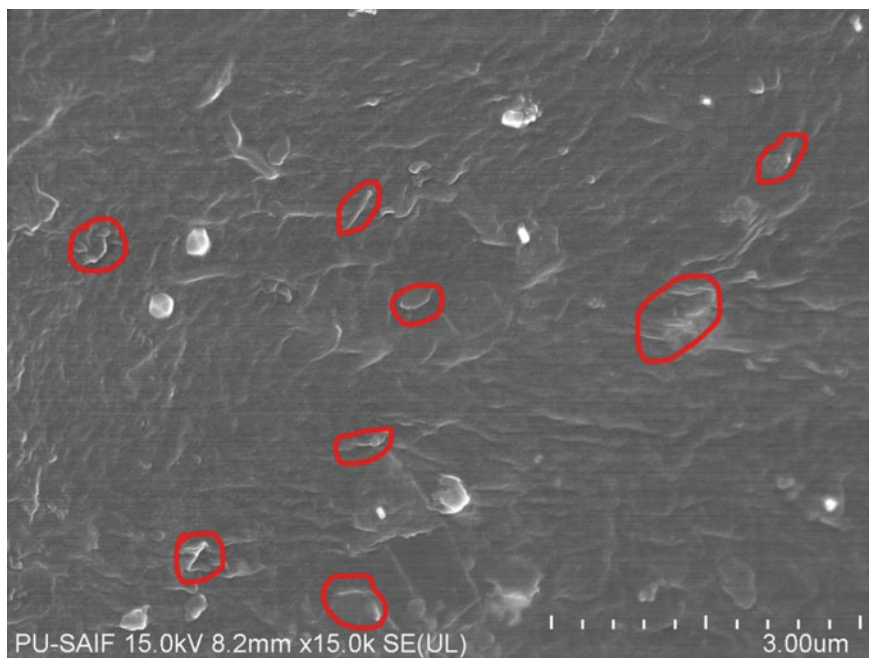


**Fig. 1** FESEM images of 10wt% EVA/Graphene composite

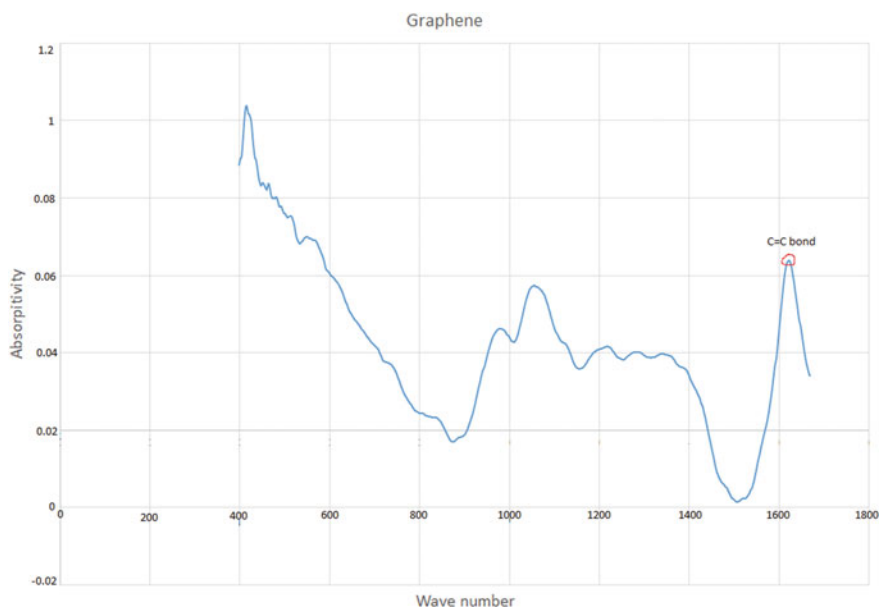


**Fig. 2** FTIR spectra of pure Graphene



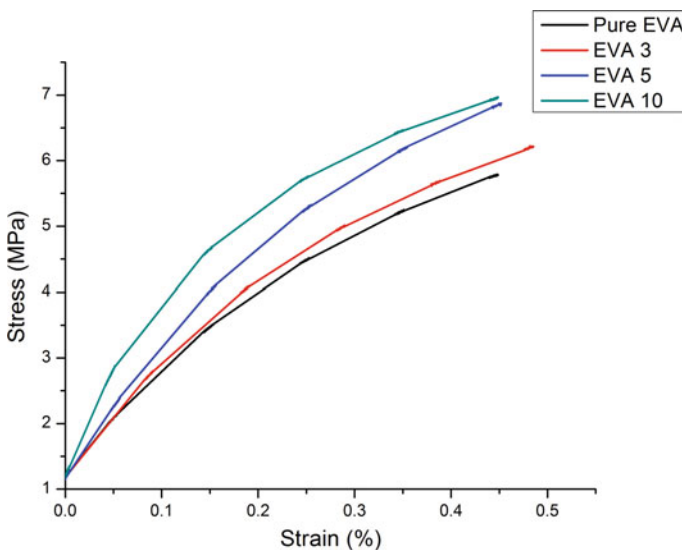
### 3 Results and Discussion

Figure 3 shows stress–strain plots of pure EVA and its composites with 3, 5 and 10wt% of Graphene. As Figure indicates, with the increase in the composition of Graphene, the tensile strength of EVA/Graphene composite has been increased in comparison to pure EVA.

Three strain rates ( $0.1 \text{ s}^{-1}$ ,  $0.01 \text{ s}^{-1}$ , and  $0.001 \text{ s}^{-1}$ ) have been taken into consideration to analyze their individual effect and it has been observed that tensile strength of EVA/Graphene composite has been increased with the increase in strain rate. The value of tensile strength for pure EVA has been observed as 5.09 MPa, 5.34 MPa and 5.78 MPa for  $0.001 \text{ s}^{-1}$ ,  $0.01 \text{ s}^{-1}$ , and  $0.1 \text{ s}^{-1}$ , respectively. A significant increase in 13.55% of tensile strength of pure EVA has been observed when the strain rate increases from  $0.001 \text{ s}^{-1}$  to  $0.1 \text{ s}^{-1}$ . The value of tensile strength of EVA has been increased for all the composition of Graphene under the influence of increasing strain rate.

Tensile strength of EVA/Graphene composite with 5wt% concentration of graphene has been observed as 5.39 MPa, 5.87 MPa and 6.79 MPa at  $0.001 \text{ s}^{-1}$ ,  $0.01 \text{ s}^{-1}$ , and  $0.1 \text{ s}^{-1}$ , respectively. Improvement of 25% in tensile strength of 5wt% composite has been observed as the strain rate increases from  $0.001 \text{ s}^{-1}$  to  $0.1 \text{ s}^{-1}$ . Similarly, an improvement of 26% has been observed in the tensile strength of 10wt% EVA/Graphene composite when the strain rate increases from  $0.001 \text{ s}^{-1}$  to  $0.1 \text{ s}^{-1}$ .

Figure 4 shows the stress–strain plot for 10wt% EVA/Graphene composite at different strain rates. Figure 4 clearly depicts the tensile strength of composite increases



**Fig. 3** Stress–strain plots for EVA/Graphene composites with varying composition of Graphene at a strain rate of  $0.1 \text{ s}^{-1}$

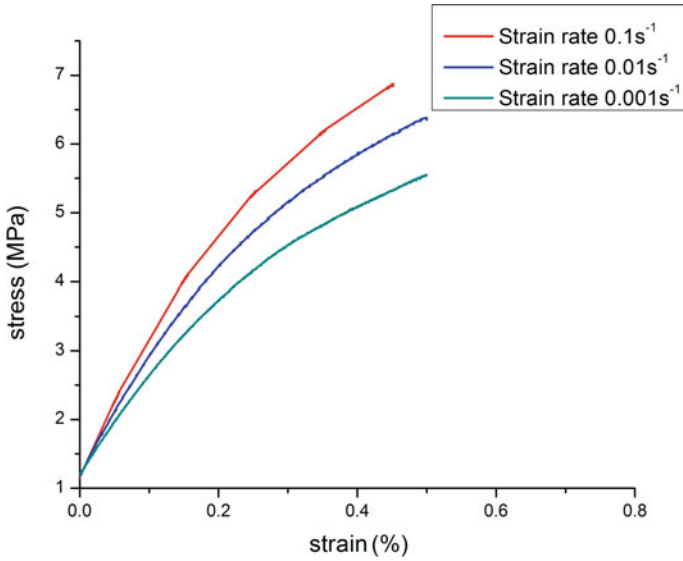
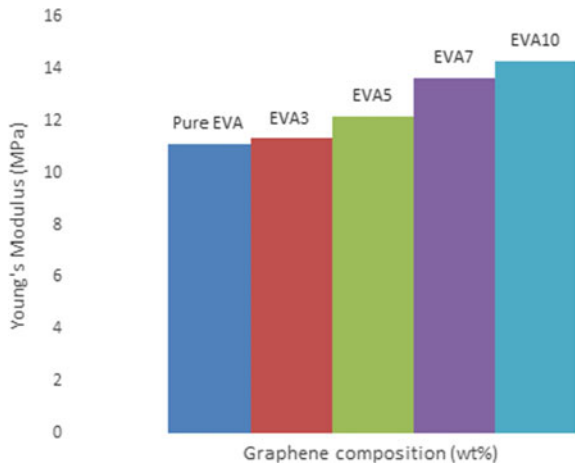


**Fig. 4** Stress–strain plots for 10wt% EVA/Graphene composite at a varying strain rate

with the increase in strain rate. Tensile strength of 5.5 MPa has been observed at a strain rate of 0.001 s<sup>-1</sup> which increases to 6.4 MPa and 6.8 MPa for strain rate of 0.01 s<sup>-1</sup> and 0.1 s<sup>-1</sup>, respectively.

Figure 5 shows the variation in Young’s modulus of EVA/Graphene composite under the influence of varying composition of Graphene. It has been observed that the modulus of composite material increases with the increase in Graphene composition. The value of Young’s modulus for pure EVA has been observed as 11.1 MPa which peaks to 11.4 MPa, 12 MPa, 13.5 MPa, and 14.2 MPa, respectively for 3, 5, 7,

**Fig. 5** Variation in Young’s modulus of EVA/Graphene composite at the varying composition of Graphene



and 10wt% of Graphene into EVA matrix. A significant improvement in the range of 21–27% has been observed for 7–10wt% composition of Graphene in comparison to pure EVA. Reinforcement with mechanically strong material like Graphene has a significant effect on the static mechanical performance of EVA-based composite material. Their uniform dispersion and adhesion with EVA matrix are the suggested reasons for significant enhancement in the mechanical properties of composite material. As Graphene sheet has a large surface area therefore the linkage between EVA and Graphene will be more which increases the strength of composite material. This implies that composite material has gained in mechanical performance and can be used for low load-bearing applications instead of pristine polymer.

## 4 Conclusions

From the present work, the following conclusions can be drawn:

1. Composites of EVA with uniformly dispersed Graphene have been successfully prepared by using Sigma mixing followed by Injection molding.
2. As EVA gets melted twice, therefore, there is no probability of the moisture content in the composite material therefore, properties obtained are the actual properties of the material.
3. Tensile strength of the EVA-based Graphene composite material has been increased under the influence of the increasing composition of Graphene and increasing strain rate.
4. Young's modulus of EVA-based Graphene composite material also increases with the increase in strain rate. A significant increase of 21–27% has been observed for 7–10wt% composition of Graphene into EVA matrix.
5. After evaluating the present research work, it is safe to conclude that the composition of Graphene around 7–10wt% is sufficient to improve the mechanical behavior of EVA-based composite material under low strain rate loading.
6. Uniform dispersion Graphene and their better adhesion and with EVA molecules are the suggested reasons for significant improvement in mechanical properties.
7. Further work can be done on the evaluation of the mechanical behavior of EVA/Graphene composite material under dynamic loading conditions.

**Acknowledgements** This research work is financially supported by the Ministry of Human Resource Development (MHRD) under the project (17-11/2015-PN-1).

**Conflict of Interest** Authors declare no conflict of interest during present research work.

## References

1. Mittal, G., Dhand, V., Rhee, K.Y., Park, S.-J., Lee, W.R.: *J. Ind. Eng. Chem.* **21**, 11–25 (2015)
2. Bansal, S.A., Singh, A.P., Kumar, S.: *Int. J. Appl. Mech.* **10**(07), 1850072 (2018). <https://doi.org/10.1142/S1758825118500722>
3. Bansal, S.A., Singh, A.P., Kumar, A., Kumar, S., Kumar, N., Goswamy, J.K.: *J. Compos. Mater.* **52**(16), 2179–2188 (2018). <https://doi.org/10.1177/0021998317741952>
4. Moghadam, A.D., Omrani, E., Menezes, P.L., Rohatgi, P.K.: *Compos. Part B Eng.* **77**, 402–420 (2015)
5. Bansal, S.A., Singh, A.P., Kumar, S.: *AIP Conference Proceedings* (2016). 1728, 020459 (2016). <https://doi.org/10.1063/1.4946510>
6. Noh, Y.J., Joh, H.-I., Yu, J., Hwang, S.H., Lee, S., Lee, C.H., Kim, S.Y., Youn, J.R.: *Sci. Rep.* **5**, 9141 (2015)
7. Park, S., He, S., Wang, J., Stein, A., Macosko, C.W.: *Polym. Test.* **104**, 1–9 (2016). <https://doi.org/10.1016/j.polymer.2016.09.058>
8. Jindal, P., Goyal, M., Kumar, N.: *Mater. Des.* **54**, 864–868 (2014, January). <https://doi.org/10.1016/j.matdes.2013.08.100>
9. Stark, W., Jaunich, M.: *Polym. Test.* **30**(2), 236–242 (2011). <https://doi.org/10.1016/j.polymertesting.2010.12.003>
10. Kuila, T., Bose, S., Mishra, A.K., Khanra, P., Kim, N.H., Lee, J.H.: *Polym. Test.* **31**(1), 31–38 (2012). <https://doi.org/10.1016/j.polymertesting.2011.09.007>
11. Kuila, T., Khanra, P., Mishra, A.K., Kim, N.H., Lee, J.H.: *Polym. Test.* **31**(2), 282–289 (2012). <https://doi.org/10.1016/j.polymertesting.2011.12.003>
12. Kim, H., Abdala, A.A., Macosko, C.W.: *Macromolecules.* **43**(16), 6515–6530 (2010). <https://doi.org/10.1021/ma100572e>
13. Jindal, P., Sain, M., Kumar, N.: *Mater. Today Proc.* **2**(4–5), 1364–1372 (2015). <https://doi.org/10.1016/j.matpr.2015.07.055>
14. Na, B., Zhang, Q., Fu, Q., Zhang, G.: *K. Shen. Polymer.* **43**, 7367–7376 (2002)
15. Tayeibi, M., Ahmad Ramazani S.A., Hamed Mosavian, M.T., Tayeibi, A.: *Polym. Adv. Technol.* **26**(9), 1083–1090 (2015). <https://doi.org/10.1002/pat.3537>
16. Guo, C., Zhou, L., Lv, J.: *Polym. Polym. Compos.* **21**(7), 449–456 (2013). <https://doi.org/10.1002/app>
17. Serban, D.A., Weber, G., Marsavina, L., Silberschmidt, V.V., Hufenbach, W.: *Polym. Test.* **32**, 413–425 (2013). <https://doi.org/10.1016/j.polymertesting.2012.12.002>
18. Jindal, P., Pande, S., Sharma, P., Mangla, V., Chaudhury, A., Patel, D., Singh, B.P., Mathur, R.B., Goyal, M.: *Compos. Part B Eng.* **45**(1), 417–422 (2013). <https://doi.org/10.1016/j.compositesb.2012.06.018>
19. George, J. J., Bhowmick, A. K.: *Nanoscale Res. Lett.* 508–515 (2008). <https://doi.org/10.1007/s11671-008-9188-3>
20. Yuan, N.Y., Ma, F.F., Fan, Y., Liu, Y.B., Ding, J.N.: *Compos. Part A.* **43**(12), 2183–2188 (2012). <https://doi.org/10.1016/j.compositesa.2012.06.003>
21. Cheng, S., Chen, C.: *Eur. Polymer J.* **40**, 1239–1248 (2004). <https://doi.org/10.1016/j.eurpolymj.2003.11.022>
22. Zhang, F., Sundararaj, U.: *Polym. Compos.* **25**(5), 535–542 (2004). <https://doi.org/10.1002/pc.20047>
23. Zhang, H., Yao, Y., Zhu, D., Mobasher, B., Huang, L.: *Polym. Test.* **51**, 29–39 (2016). <https://doi.org/10.1016/j.polymertesting.2016.02.006>
24. Kim, M.S., Park, C.C., Chowdhury, S.R., Kim, G.H.: *J. Appl. Polym. Sci.* **94**(5), 2212–2216 (2004). <https://doi.org/10.1002/app.21174>
25. Kumar, D., Kaur, A., Aggarwal, Y.K., Uniyal, P., Kumar, N., Jindal, P.: *I Manager: J. Mat. Sci.* **5**(3), 8–14 (2017)
26. Kumar, D., Jindal, P.: *Mater. Res. Express.* **6**, 1–10 (2019). <https://doi.org/10.1088/2053-1591/ab3ad7>

27. Kumar, D., Kumar, N., Jindal, P.: *Mater. Today Proc.* **5**(2), 5636–5640 (2018). <https://doi.org/10.1016/j.matpr.2017.12.156>
28. Bansal, S.A., Singh, A.P., Kumar, S.: *J. Nanosci. Nanotechnol.* **18**, 1–7 (2018). <https://doi.org/10.1166/jnn.2018.16336>
29. Kumar, S., Singh, A.P., Bansal, S.A.: *Mater. Res. Express* (2018). <https://doi.org/10.1088/2053-1591/AACFC0>

# Development and Electrical Properties of Titanium Dioxide-Based Polymer Nanocomposite Structures



Sudhanshu Singh , Nitesh Singh Rajput, Deepshikha Rathore, and Umesh Kumar Dwivedi

**Abstract** In the present work, we have prepared polymeric nanocomposites of various weight levels of polymer along with metal oxide. Further, the crystallographic and basic examinations were finished. In continuation, after the anode development of the readied tests, the electrical measurement were performed. This test work has demonstrated the better outcomes in all space, viz. structural and electrical properties, which will make it appropriate for different electrical and mechanical applications. The best instances of such arranged structures are supercapacitor, high energy storing devices, and multi-layered capacitors etc.

**Keywords** Nanocomposites · PVDF and TiO<sub>2</sub>

## 1 Introduction

Titanium dioxide (TiO<sub>2</sub>) is a semiconductor material with a wide assortment of utilization [1]. Titanium dioxide has been utilized for a long time (approx 90 years) in a tremendous scope of mechanical and buyer merchandise including color sharpened sunlight-based cells, paints, coatings, cements, paper and paperboard, plastics and elastic, printing inks, covered textures and materials, impetus frameworks, pottery, floor covers, roofing materials, beautifiers and pharmaceuticals, water treatment specialists, sustenance colorants and in car items, and so on [2–5]. TiO<sub>2</sub>, the oxide of the metal titanium, happens normally in a few sorts of shake and mineral sands. Titanium is the ninth most basic component in the worlds outside layer [6, 7]. TiO<sub>2</sub> is regularly thought of as being artificially dormant. Titanium dioxide (TiO<sub>2</sub>) is a white strong inorganic substance that is thermally steady, non-combustible, ineffectively solvent,

---

S. Singh · N. S. Rajput (✉) · D. Rathore · U. K. Dwivedi  
Amity University Rajasthan, SP-1, Kant Kalwar, NH-11C, RIICO Industrial Area, Jaipur,  
Rajasthan 303002, India  
e-mail: [niteshthakur72@yahoo.com](mailto:niteshthakur72@yahoo.com)

S. Singh  
e-mail: [singhs1183@yahoo.com](mailto:singhs1183@yahoo.com)

© Springer Nature Singapore Pte Ltd. 2020  
C. Prakash et al. (eds.), *Advances in Materials Science and Engineering*,  
Lecture Notes in Mechanical Engineering,  
[https://doi.org/10.1007/978-981-15-4059-2\\_22](https://doi.org/10.1007/978-981-15-4059-2_22)

and not named risky as indicated by the United Nations' (UN) Globally Harmonized System of Classification and Labeling of Chemicals (GHS) [8–10].

PVDF is a claim to fame plastic material in the fluoropolymer family. PVDF is a polar polymer with amazing compound, mechanical, and electrical properties. PVDF has been generally utilized in numerous fields, for example, ultra filtration and micro-filtration layers, terminal cover in lithium-particle batteries, microwave transducers, and its interesting applications such as piezoelectric and pyroelectric materials. Contrasted with other fluoropolymer, it has a simpler liquefy process in view of its moderately low softening purpose of around 177 °C [11, 12]. It has a low density (1.78 g/cm<sup>3</sup>). It is notable that nanoparticles are typically used to improve the properties of polymer by straightforward mixing and the interfacial communication among polymer and nanoparticles is urgent to the upgrade [13, 14].

The most generally utilized oxide for photograph reactant applications attributable to its ease and high action is TiO<sub>2</sub> [15–17]. The revelation of the photolysis of water on the outside of TiO<sub>2</sub> in 1972 propelled for many years of serious examination into the hidden synthetic and physical procedures included [18, 19]. Regardless of much gathered proof, an altogether persuading clarification regarding why blended stage tests of anatase and rutile outflank the individual polymorphs has stayed tricky [20, 21]. One long-standing contention is the vigorous arrangement of the band edges of the rutile and anatase polymorphs of TiO<sub>2</sub> [22].

In this work, we study that the composite films of TiO<sub>2</sub> and PVDF were made by softening press process and structural, thermal, and dielectric properties of these structures have been considered.

## 2 Materials and Methods

### 2.1 Nanopolymeric Composite Films Preparation

Cleaned TiO<sub>2</sub> powder from Thermo Fisher Scientific, India, and PVDF powder from Aldrich, USA, was utilized in the readiness of the composite structures. The sanitized powder of TiO<sub>2</sub> (50 wt% proportion) was blended in the PVDF control in pastel and mortar till 30 min. The powder blend was kept in a hardened bucket in the hot press machine. The blend was warmed up to a temperature of 200 °C, and afterward, a weight of 200 kg/cm<sup>2</sup> was connected for 10 min. The temperature of the bite, the dust was brought down to room temperature (30 °C) and afterward the weight was discharged. A similar technique for planning was embraced for other synthesis of the composite structures. The deliberate thickness of the composite film was about 0.5 mm. The roundabout indium terminals having a zone of  $2.0 \times 10^{-3}$  cm<sup>2</sup> were vacuum stored on one surface of the film, and on the other surface, indium is vacuum kept on a bigger area.

The morphology of the readied dainty films was analyzed utilizing a Zeiss EVO 18 special edition scanning electron microscope. The prepared samples were covered

with gold in programmed sputter coater (Quorum-Q150RS), and after that moved to the electron magnifying instrument to be analyzed under connected voltage 20 kV. The X-Ray diffraction estimation was performed to acquire the auxiliary data in different sorts of unadulterated and composite structures utilizing diffractometer. The X-Ray diffraction sweeps of different examples, for example, unadulterated PVDF, 40 wt% TiO<sub>2</sub> + PVDF composite film, 50 wt% TiO<sub>2</sub> + PVDF composite film, 60 wt% TiO<sub>2</sub> + PVDF composite film and unadulterated TiO<sub>2</sub> were taken. The XRD sweeps were recorded utilizing Anchor Scan Xpert-Pro.

Magneto-dielectric setup—The example is set at the focal point of the electromagnet, and a LCR meter ascertains the dielectric/capacitance/electrical property of the example. The current of the electromagnet is fluctuated which changes the attractive field connected to the example. The LCR meter estimates the electrical properties at various estimations of attractive field. Recurrence subordinate estimation (20–120 MHz) can likewise be completed.

### 3 Results and Discussion

#### 3.1 Scanning Electron Microscopy [Structural Properties]

Figure 1 underneath demonstrates the normal SEM pictures of 50 wt% of TiO<sub>2</sub> and PVDF composite structures. In the SEM results, it was done at the zoom level of 120,000 $\times$  and high control up to 20 kV (Zeiss Instrument, USA), of the readied tests and the outcomes demonstrate the correct installing of the polymer (PVDF) and metal oxide (TiO<sub>2</sub>). These additionally demonstrate that the uniform structure of TiO<sub>2</sub> with PVDF, which makes it reasonable for appropriate and uniform electrical gadget [23–26], where there is an exceptionally less deviation in the electrical properties, or possibly noise, will be there in it.

#### 3.2 Dielectric Measurement (Dielectric Constant)

The dielectric estimation was finished with the assistance of impedance analyzer (MEIA instruments, Switzerland). In the device, the dielectric consistent ( $k$ -values) has been determined at different temperature run. In the outcomes, at the lower temperature, TiO<sub>2</sub>:PVDF indicates less  $k$ -value, which shows its uses at low-temperature applications. As the temperature has been expanded, the  $k$ -values arrived at its most extreme qualities. It portrays the center-level temperature range that will be the ideal arrangement of the vast majority of the high energy storing devices [27–29], multi-layered capacitors [27, 30, 31], supercapacitors [32–34], and so on. All these data were taken at high recurrence of 1 kHz. While at higher temperature, the  $k$ -values got stringent behaviour because of the entry of the glass transient temperature



for the PVDF. The  $k$ -values ranges from 50 to 60, while the temperature changed from room temperature, i.e., 25 °C to around 180 °C (Fig. 2).

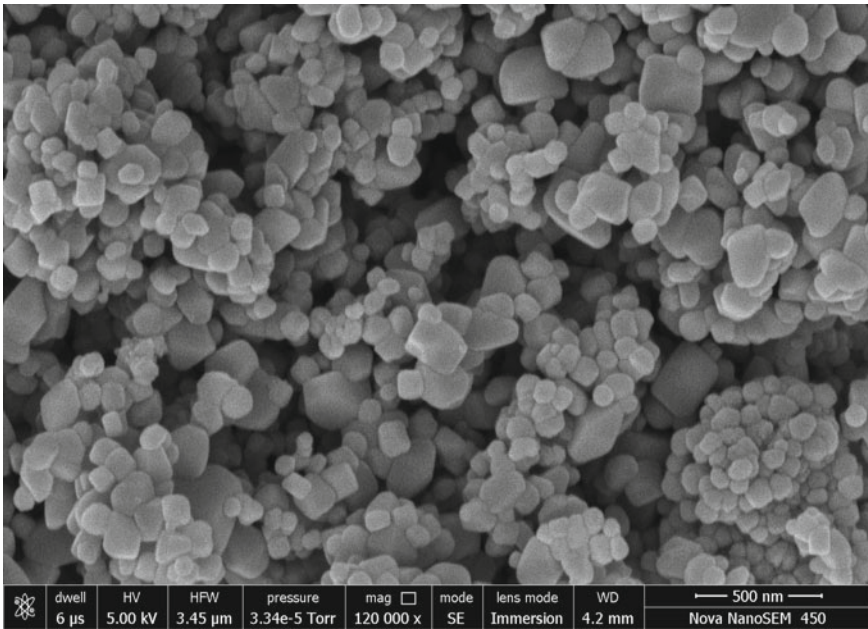
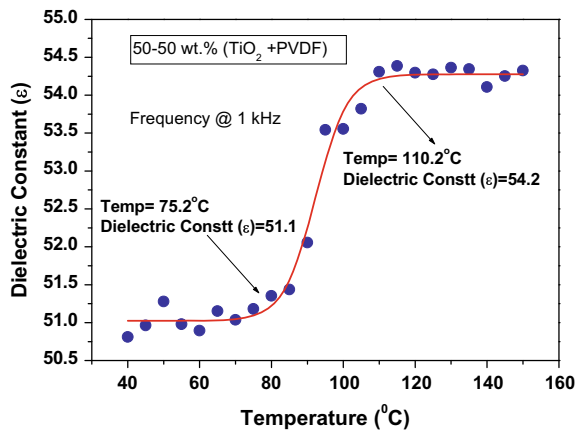


Fig. 1 SEM of the sample

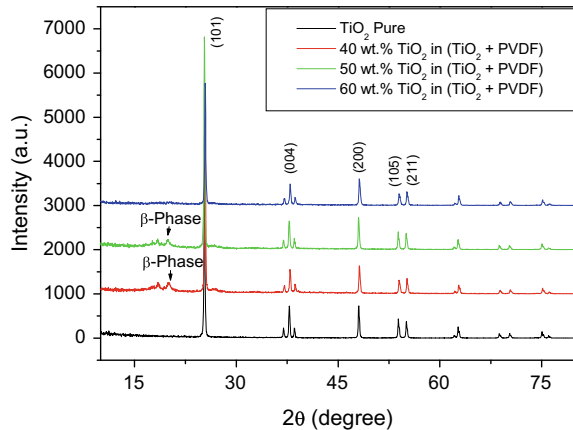
Fig. 2 50 wt% (TiO<sub>2</sub> + PVDF) temperature versus dielectric constant @ 1 KHz



### 3.3 X-Ray Diffraction (XRD) (Crystallographic Properties)

The XRD example of the of unadulterated PVDF, Pure  $\text{TiO}_2$  and diverse filler centralization of  $\text{TiO}_2$ : PVDF composite structures at room temperature are appeared in Fig. 3. The graph shows the ( $\beta$ -stage) rutile stage development of  $\text{TiO}_2$  in all the synthesis of various filler convergence of  $\text{TiO}_2$ : PVDF composite with no extra stage at room temperature. X-beam diffraction crests for planes (101), (004), (200), (105), and (211) at relating Bragg Angles  $2\theta = 25.24^\circ$ ,  $37.81^\circ$ ,  $48.05^\circ$ ,  $53.99^\circ$ , and  $55.07^\circ$  authenticate the development of rutile structure of  $\text{TiO}_2$  in the composite structures at room temperature. From Fig. 4, it has been seen that the pinnacle positions are indistinguishable for all the distinctive filler focus composite tests at room temperature, which shows that there is no critical change in the grid parameters as likewise exhibited in the work done by different scientists [1–6, 11–18, 24–28, 34, 35]. The majority of the diffraction tops on comparing the Bragg edges ( $2\theta$ ) coordinate with the standard information for a rutile—structure (JPCDS 36-1451) of  $\text{TiO}_2$ —which shows that the nearness of PVDF does not influence in the advancement of new precious stone directions or change in special directions of  $\text{TiO}_2$ . No diffraction pinnacle has been seen at  $2\theta = 13^\circ$  in the unadulterated  $\text{TiO}_2$  and diverse filler convergence of  $\text{TiO}_2$  in PVDF composite structures as appeared in Fig. 3 The power of the pinnacles increases with the expansion in the filler centralization of  $\text{TiO}_2$  in the composite structures. This demonstrates expanded crystallinity (Table 1).

**Fig. 3** XRD pattern of different filler concentration of  $\text{TiO}_2$



### 3.4 Electrical Characterizations (Capacitance, Conductance, Resistance, D Factor, Phase Angle, and Inductance Measurement)

The electrical investigations have been finished with the assistance of impedance analyzer instrument (USA Inc). In this instrument, the temperature fluctuations have been gotten for estimating capacitance, conductance, and impedance estimations of

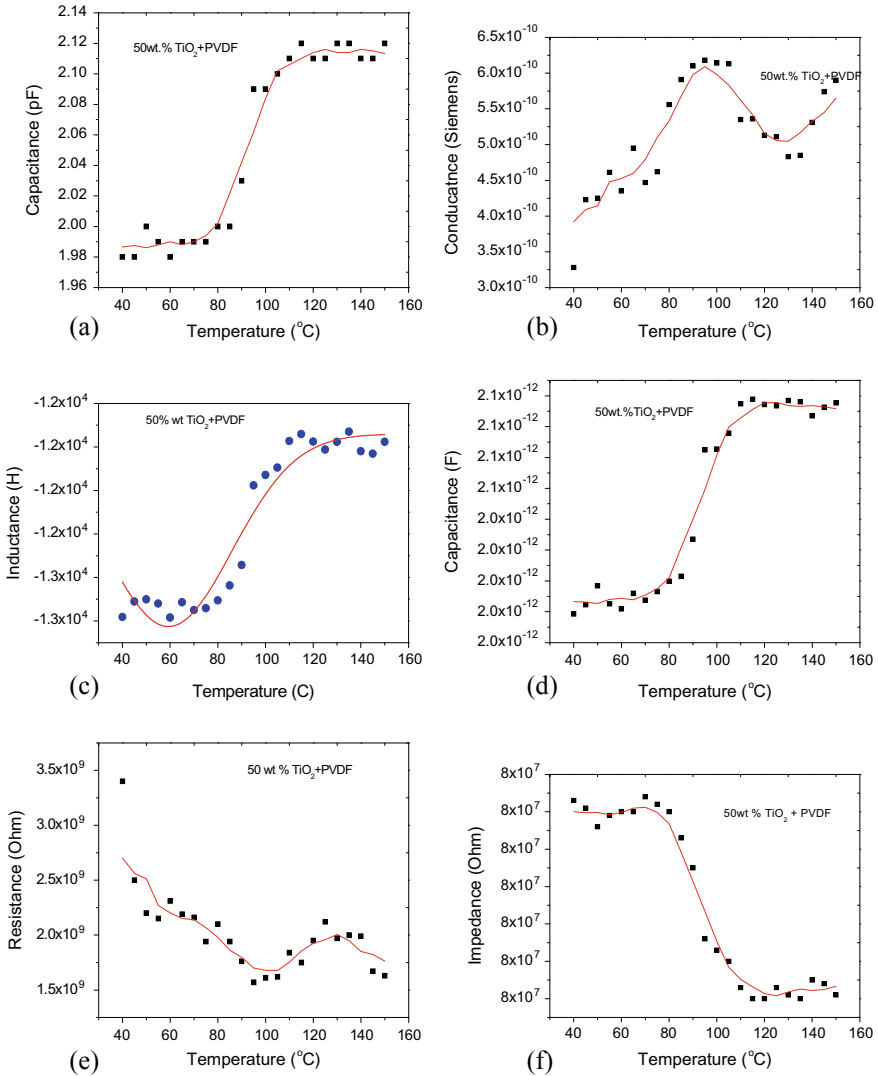


Fig. 4 a–h Various electrical parameter values

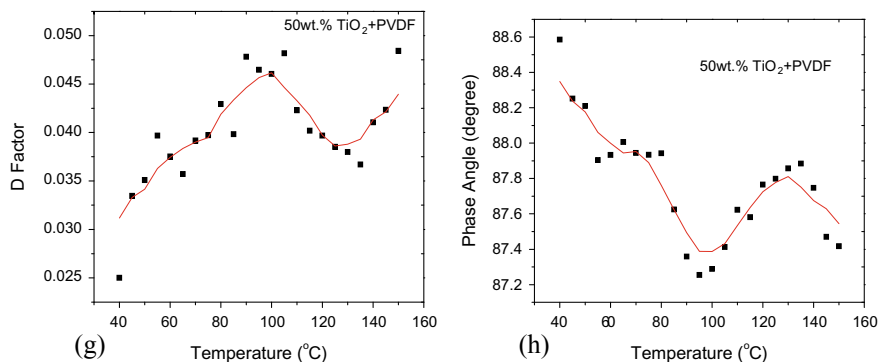


Fig. 4 (continued)

Table 1 Peaks in XRD

TiO <sub>2</sub> wt% in (TiO <sub>2</sub> + PVDF) composite films	2 $\theta$	Peak value	Average peak value	<i>D</i> factor	Crystallite size (nm)	Average crystallite size (nm)	Lattice strain
100% TiO <sub>2</sub>	25.3223	4804.45	2081.031	0.1584180	50.80657544	44.53798503	0.0031
100% TiO <sub>2</sub>	37.805	725.3921		0.1851363	44.83507976		0.0024
100% TiO <sub>2</sub>	48.0381	713.25		0.2264126	37.97229988		0.0022
20% TiO <sub>2</sub>	25.295	3609	2435.5	0.4975836	16.17466001	15.74418418	0.0097
20% TiO <sub>2</sub>	–	–		–	–		–
20% TiO <sub>2</sub>	48.065	1262		0.5614778	15.31370835		0.0055
40% TiO <sub>2</sub>	25.4350	3836.46	1672.891	0.1800645	44.70874921	39.5240995	0.0035
40% TiO <sub>2</sub>	37.895	558.6027		0.2184097	38.01496135		0.0028
40% TiO <sub>2</sub>	48.125	623.6092		0.2399067	35.84858794		0.0023
50% TiO <sub>2</sub>	25.295	4819.239	2068.498	0.1536664	52.37479084	44.34772421	0.0030
50% TiO <sub>2</sub>	37.805	650.3962		0.1982548	41.86834708		0.0025
50% TiO <sub>2</sub>	48.035	735.8589		0.2215798	38.80003472		0.0022
60% TiO <sub>2</sub>	25.415	2765	1285.798	0.1814200	44.3729559	39.90915498	0.0035
60% TiO <sub>2</sub>	37.925	487.277		0.2106552	39.41788707		0.0027
60% TiO <sub>2</sub>	48.125	605.1167		0.2393190	35.93662196		0.0023
80% TiO <sub>2</sub>	25.325	4407	2302.667	0.4398365	18.29934231	17.22565625	0.0085
80% TiO <sub>2</sub>	37.865	1060		0.5449553	15.23444295		0.0069
80% TiO <sub>2</sub>	48.155	1441		0.4740801	18.14318349		0.0046

the readied tests of different weight rates of the examples. As the temperature was expanded, the capacitance expanded in the diagrams, which showed that the TiO<sub>2</sub> assumed an indispensable job for electrical applications for models, supercapacitor, multi-layered capacitors, and so on. Same sort of wonders and examination had been appeared for the conductance and impedance investigation moreover. Regardless of this one of a kind marvels, sooner or later the every single electrical parameter were get strayed results, which were occurred because of some clamor at the structural condition like some other natural reasons [36]. The capacitance worth changed from 1.98 to 2.12 pF during the temperature differences of 25–160 °C. This will be the most ideal condition for these polymer composite structure as in super capacitors applications.

In a similar way, the conductance esteems are likewise moving toward its most elevated worth. In continuation, the obstruction estimations were taken for the 50 wt% of the PVDF: TiO<sub>2</sub> tests for the temperature scope of 250–1600 °C. The impedance esteems came in the negative reason (approx –100 mH), due to the properties of displaying vitality. Obstruction esteems were likewise differed inside 200 MΩ territory, which shows the profoundly resistive conduct of PVDF. The dielectric loss property of PVDF: TiO<sub>2</sub> and stage point of the examples, show its counter inverse properties for a similar temperature extend. So, overall at the given and consistent recurrence, as the temperature get changed, the conduct of the examples was turned out to be one of a kind, which will demonstrate it as superior electrical applications [37].

So, from the basic, morphological, crystallographic, and electrical outcomes, it is seen that after the different emphases of fluctuating level of PVDF: TiO<sub>2</sub>, 50 wt% is the best ideal incentive for making tests. The best solvents are acetone and chloroform for this sort of work having PVDF: TiO<sub>2</sub> blends. Mixture strategies, sol–gel process, finger cathodes are the best method for making tests for this work. The best electrical outcomes were acquired in the scope of close to room temperature 25 °C, that makes it exceptionally extraordinary to work with in anyplace, without the intrusion of need of profoundly, exorbitant, and modern labs [35–38].

The resistance, inductance, capacitance, conductance, *D* factor, and stage point esteems exhibited different working zones for different applications in the field of science, technology, engineering, and mathematics (STEM) space. The less qualities zone are best appropriate for low-temperature applications, while the center temperature reason is best for the majority of the everyday schedule machines, while to wrap things up, the higher temperature reason zone is best appropriate for high temperature zone, for example, in aviation, atomic, warm enterprises, etc.

## 4 Conclusion

From the all electrical and morphological investigations, we might be in a situation to express that the PVDF-based polymer nanocomposites are showing great conduct with the adjustments in temperature. This sort of properties is best appropriate for detecting applications just as better directing applications in the zone of electrical

and hardware. Additionally, stage edge plot versus temperature is portraying its reasonableness for the exchanging conduct applications.

**Acknowledgements** I might want to recognize the asset people at MRC, MNIT Jaipur, just as my associates at Amity University Rajasthan Jaipur for all portrayals and aiding me.

**Area of conflict and funding** The authors have no region of contention in this exploratory work. Likewise there is no financing decided on this work.

## References

1. Diebold, U.: Structure and properties of TiO<sub>2</sub> surfaces: a brief review. *Appl. Phys. A* **76**(5), 681–687 (2003)
2. Gan, W.C., Majid, W.A.: Effect of TiO<sub>2</sub> on enhanced pyroelectric activity of PVDF composite. *Smart Mater. Struct.* **23**(4), 045026 (2014)
3. Lee, J.G., Kim, S.H., Kang, H.C., Park, S.H.: Effect of TiO<sub>2</sub> on PVDF/PMMA composite films prepared by thermal casting. *Macromol. Res.* **21**(4), 349–355 (2013)
4. Charlot, B., Gauthier, S., Garraud, A., Combette, P., Giani, A.: Polymer pyroelectric sensors: PVDF/PMMA blend thin film. Last accessed 25 Aug 2019
5. Berger, C.M., Tokariev, O., Orzessek, P., Hospach, A., Fang, Q., Bram, M., Buchkremer, H.P.: Development of storage materials for high-temperature rechargeable oxide batteries. *J. Energy Storage* **1**, 54–64 (2015)
6. Alami, A.H.: Experimental assessment of compressed air energy storage (CAES) system and buoyancy work energy storage (BWES) as cellular wind energy storage options. *J. Energy Storage* **1**, 38–43 (2015)
7. Jaiswal, A., Chalasani, S.C.: The role of carbon in the negative plate of the lead–acid battery. *J. Energy Storage* **1**, 15–21 (2015)
8. Schneider, L., Kötter, E.: The geographic potential of power-to-gas in a German model region-trier-amprion 5. *J. Energy Storage* **1**, 1–6 (2015)
9. Thomas, P., Satapathy, S., Dwarakanath, K., Varma, K.B.R.: Dielectric properties of poly (vinylidene fluoride)/CaCu<sub>3</sub>Ti<sub>4</sub>O<sub>12</sub> nanocrystal composite thick films. Preprint at [arXiv:1301.4056](https://arxiv.org/abs/1301.4056) (2013)
10. Kumar, N., Nath, R.: Ferroelectric polarization switching in KNO<sub>3</sub>: PVDF films. *J. Phys. D Appl. Phys.* **36**(11), 1308 (2003)
11. Kumar, N., Nath, R.: Ferroelectric phase stability studies in potassium nitrate: polyvinylidene fluoride composite films. *J. Appl. Phys.* **97**(2), 024105 (2005)
12. Shi, H., Magaye, R., Castranova, V., Zhao, J.: Titanium dioxide nanoparticles: a review of current toxicological data. *Part. Fibre Toxicol.* **10**(1), 15 (2013)
13. Jian, L., Chilan, C.: The preparation and tribological properties of PVDF/TiO<sub>2</sub> nanocomposites. *Polym. Plast. Technol. Eng.* **49**(7), 643–647 (2010)
14. Simões, A.Z., Aguiar, E.C., Riccardi, C.S., Moura, F., Longo, E., Varela, J.A.: Structure and ferro/piezoelectric properties of SrBi<sub>4</sub>Ti<sub>4</sub>O<sub>15</sub> films deposited on TiO<sub>2</sub> buffer layer. *J. Alloy. Compd.* **477**(1–2), 85–89 (2009)
15. Kumar, S., Verma, N.K., Singla, M.L.: Size dependent reflective properties of TiO<sub>2</sub> nanoparticles and reflectors made thereof. *Dig. J. Nanomater. Biostructures* **7**(2), 607–619 (2012)
16. Santana-Aranda, M.A., Morán-Pineda, M., Hernández, J., Castillo, S., Gomez, R.: Physical properties of TiO<sub>2</sub> prepared by sol-gel under different pH conditions for photocatalysis. *Superf. Y Vacío* **18**(1), 46–49 (2005)
17. Wang, J.C., Chen, P., Chen, L., Wang, K., Deng, H., Chen, F., Fu, Q.: Preparation and properties of poly (vinylidene fluoride) nanocomposites blended with graphene oxide coated silica hybrids. *Express Polym. Lett.* **6**(4) (2012)

18. Prasad, K., Prasad, A., Chandra, K.P., Kulkarni, A.R.: Electrical conduction in 0–3 BaTiO<sub>3</sub>/PVDF composites. *Integr. Ferroelectr.* **117**(1), 55–67 (2010)
19. Li, Y.C., Tjong, S.C., Li, R.K.Y.: Dielectric properties of binary polyvinylidene fluoride/barium titanate nanocomposites and their nanographite doped hybrids. *EXPRESS Polym. Lett.* **5**(6) (2011)
20. Senić, Ž., Bauk, S., Vitorović-Todorović, M., Pajić, N., Samolov, A., Rajić, D.: Application of TiO<sub>2</sub> nanoparticles for obtaining self-decontaminating smart textiles. *Sci. Tech. Rev.* **61**(3–4), 63–72 (2011)
21. Iwagoshi, J., Dillingham, T.R., Stufflebeam, T., Ewen, C.: A study of vapor deposited PVDF/TiO<sub>2</sub> nanoparticle films by XPS. *Surf. Sci. Spectra* **21**(1), 10–18 (2014)
22. Scanlon, D.O., Dunnill, C.W., Buckeridge, J., Shevlin, S.A., Logsdail, A.J., Woodley, S.M., Watson, G.W.: Band alignment of rutile and anatase TiO<sub>2</sub>. *Nat. Mater.* **12**(9), 798 (2013)
23. Aliyu, A.A.A., Abdul-Rani, A.M., Ginta, T.L., Prakash, C., Axinte, E., Fua-Nizan, R.: Investigation of nanoporositities fabricated on metallic glass surface by hydroxyapatite mixed EDM for orthopedic application. *Malays. J. Fundam. Appl. Sci.* **13**(4–2), 523–528 (2017)
24. Singh, S., Dwivedi, U.K.: Fabrication and morphological characterization of barium titanate-based polymeric nanocomposite thin films. In: *Multifunctional Nanocarriers for Contemporary Healthcare Applications*, pp. 50–59. IGI Global, Pennsylvania (2018)
25. Khan, M., Pawar, H., Kumari, M., Rathore, D., Dwivedi, U.K.: Comparative study of physicochemical properties of CoFe<sub>2</sub>O<sub>4</sub>/MWCNT nanocomposites (2019)
26. Mishra, N., Nishad, K.K., Mehto, V.R., Rathore, D., Pandey, R.K.: Unstrained PbSe/CdSe core shell nanostructures for broad band absorber and narrow band IR emitters. *J. Mater. Sci.: Mater. Electron.* **29**(12), 10214–10221 (2018)
27. Kumar, S., Hong, H., Choi, W., Akhtar, I., Rehman, M.A., Seo, Y.: Acrylate-assisted fractal nanostructured polymer dispersed liquid crystal droplet based vibrant colored smart-windows. *RSC Adv.* **9**(22), 12645–12655 (2019)
28. Choudhary, M., Singh, T., Dwivedi, M., Patnaik, A.: Waste marble dust-filled glass fiber-reinforced polymer composite Part I: Physical, thermomechanical, and erosive wear properties. *Polym. Compos.* (2019)
29. Singh, S., Dey, S.S., Singh, S., Kumar, N.: Preparation and characterization of barium titanate composite film. *Mater. Today: Proc.* **4**(2), 3300–3307 (2017)
30. Mitra, S., Gupta, S., Joseph, A. M., Dwivedi, U.K.: Study of domain switching using piezoresponse force microscopy in Ca<sub>0.4</sub> Sr<sub>0.6</sub> Bi<sub>4</sub> Ti<sub>4</sub>O<sub>15</sub> Thin Film for Electromechanical Applications. *Electron. Mater. Lett.* **15**(2), 159–165 (2019)
31. Mishra, N., Rathore, D., Pandey, R.K.: A comparative study of conventional type II and inverted core–shell nanostructures based on CdSe and ZnS. *Opt. Quant. Electron.* **50**(2), 107 (2018)
32. Pawar, H., Kumar, D., Rathore, D., Dwivedi, U.K.: Synthesis and characterization of MnFe<sub>2</sub>O<sub>4</sub>/graphene/epoxy nanocomposites. *Appl. Innov. Res. (AIR)* **1**(1), 75–77 (2019)
33. Rathore, D., Mitra, S., Kurchania, R., Pandey, R.K.: Physicochemical properties of CuFe<sub>2</sub>O<sub>4</sub> nanoparticles as a gas sensor. *J. Mater. Sci.: Mater. Electron.* **29**(3), 1925–1932 (2018)
34. Singh, P., Rathore, D.: A biosensor system using nickel ferrite nanoparticles. In: *AIP Conference Proceedings*, vol. 1728, no. 1, p. 020259. AIP Publishing (2016)
35. Vishnoi, R., Gupta, S., Dwivedi, U.K., Singhal, R.: Optical and structural modifications of copper-fullerene nanocomposite thin films by 120 MeV Au ion irradiation. *Radiat. Phys. Chem.* **108**442 (2015)
36. Kurchania, R., Rathore, D., Pandey, R.K.: Size dependent strain and nanomagnetism in CoFe<sub>2</sub>O<sub>4</sub> nanoparticles. *J. Mater. Sci.: Mater. Electron.* **26**(12), 9355–9365 (2015)
37. Kanchan, S., Singh, M., Singh, M.: Performance enhancement of three-way catalytic converter using external heating source: an experimental approach. *Int. J. Veh. Struct. Syst. (IJVSS)*, **8**(3) (2016)
38. Singh, V.K., Sadhukhan, P., Barman, S.R.: Quasiperiodic Sn monolayer on 10-fold Al-Ni-Co quasicrystal surface at room temperature. In: *AIP Conference Proceedings*, vol. 2115, No. 1, p. 030275. AIP Publishing (2019)

# Investigation of Structural and Electronic Properties of BaX (X = S, Se, and Te): A DFT Study



Agnibha Das Majumdar, Neha Munjal, Uma Kamboj, and Karan Dogra

**Abstract** The current paper is about the properties of barium chalcogenides compounds, using the first-principle total energy calculations within linear combination of atomic orbital method. The work is basically built up using density functional theory with the coordination of CRYSTAL coding. Becke and PBE scheme was used as the exchange-correlation potential for constructing Kohn–Sham Hamiltonian. Several structural and electronic properties, such as lattice constant ( $a$ ), bulk modulus ( $B_0$ ) and bandgap ( $E_g$ ), have been studied. All the results obtained were found to be in good agreement with the earlier works.

**Keywords** DFT · Barium chalcogenides · LCAO · Structural properties · Electronic properties

## 1 Introduction

A compound semiconductor is made up of two different materials from two dissimilar groups of the periodic table. The BaX compounds belong to II-VI group. Barium chalcogenides are inorganic crystalline solid and are colourless. The present bandgap for BaS is 3.88 eV, for BaSe is 3.58 eV, and for BaTe is 3.08 eV. At ideal temperature and pressure, these compounds exhibit closed-shell ionic structural system. Also, they have shown their stability in rock salt (B1) structure.

In the past, as there was only the high production of silicon as a semiconductor material, (Earlier, silicon was largely produced as a semiconductor material while) compound semiconductors were not commercialized in a wider way. However, in recent years, semiconductor prices are reduced. Presently semiconductor compounds are commercialized in a wide manner.

---

A. Das Majumdar · N. Munjal (✉) · U. Kamboj  
Department of Physics, Lovely Professional University, Phagwara, Punjab, India  
e-mail: [nehamunjal28@gmail.com](mailto:nehamunjal28@gmail.com)

K. Dogra  
Department of Physics, Punjab University, Chandigarh, Punjab, India

© Springer Nature Singapore Pte Ltd. 2020  
C. Prakash et al. (eds.), *Advances in Materials Science and Engineering*,  
Lecture Notes in Mechanical Engineering,  
[https://doi.org/10.1007/978-981-15-4059-2\\_23](https://doi.org/10.1007/978-981-15-4059-2_23)



Also, those compounds are having great importance through their fundamental properties, and overcome the gap between silicon and recent days' semiconductor compounds.

As barium chalcogenides compounds like BaS, BaSe, BaTe and their various alloys, are having a short wavelength, those are used optoelectronic applications. Now it is important to understand their structural and electronic properties for their usage in all types of electronic displays.

The article is organized as various sections: In Sect. 2, literature have been explored. In Sect. 3, computational methods and in Further in segment 4, results and discussions for structural properties are presented. Finally, the conclusion has been presented in Sect. 5.

## 2 Literature Review

The electronic and structural properties of barium chalcogenides compounds have been calculated by Bouhemadou et al. [1]. In this work, they have two approximations i.e. Local Density Approximation (LDA) and Generalised Gradient approximation (GGA). The calculated bulk modulus and lattice constant at a stable state agree with the previous computational and experimental data. They concluded that their calculated band gaps are in the best approximation with other computational values but slightly differ with experimental ones. The electronic properties of barium chalcogenides were systematically observed by Lin et al. [2] using the correlation with density functional theory. In this paper, Cambridge serial total energy package (CASTEP) has been used for stimulation. The properties of an electronic system of the semiconductor compounds having oxygen atoms within it always differ from the compounds having no oxygen atoms within it. Their results predict that energy bandgap can be adjustable by emerging the oxygen atom into the lattice system. Tuncel et al. [3] used DFT as inbuilt in SIESTA code to determine the elastic, structural, lattice dynamical and thermodynamic properties of barium chalcogenides in rock salt and CsCl structure. In this work, the bulk modulus, the pressure derivative of bulk moduli, lattice constants, transition pressures, elastic constants, etc. have been determined and the outcoming values are, usually, closely in tune with existing experimental values and some computational data. The elastic as well as structural properties of barium chalcogenides under a high-pressure condition have been calculated by Arya et al. [4] using interionic potential of two-body problem approaches with a modified charge of ion. In B1 structural phase to B2 structural phase for the barium chalcogenides compounds, the equation of states has been predicted and observed that at a particular pressure phase transition occurs. They concluded that the determined values of transitional pressure from one phase to another phase, the percentage of volume collapsed, cohesive energies and lattice constant of the BaX compounds are in excellent agreement. It has also been shown that the cohesive energy decreases as X changes from S to Te. It suggests that BaTe is more compressible than BaS. Bhardwaj et al. [5] have calculated structural phase transition

under high pressure for the BaO, BaSe, and BaTe compounds with a help of ionic interaction potential approach of a three-body system, which is a MTBIP approach and also it has been revised by integrating the covalency effects. They have assumed a zero-point energy effect. This zero-point energy can be defined by the ground state energy in which the compounds can make some band. Using some parameters from the standard model, they have obtained that the values for the phase transition pressures obtained from the TBIP approach show an excellent contract with experimental values. Also, with the variation of cation–anion radii ratio, the pressure for the phase transition from NaCl to CsCl structure varies inversely. Drablia et al. [6] have used FP-LAPW method. In this work, they have used both LDA and GGA. They have determined the various properties of barium chalcogenides compounds and in chalcogenides compound series they have used O, S, Se, Te and Po elements in the stable phase. The electronic band structure calculations predict that except BaO compound among the above compounds all are having the bandgap of indirect type, whereas the bandgap of BaO is direct. The dielectric function is having an imaginary part. That part has shown various certain interband transitions. The reflectivity has been also calculated. And the obtained values are in good contract with other previously done computational data. First-principles calculations have been used by Haj Hassan and Akbarzadeh [7] to determine the bond structures and properties related to elastic constants of the BaX compounds. This study has been done for those compounds at stable phase as well as at the phase where high pressure applied Full potential-linearized augmented plane wave (FP-LAPW) method has been performed, which is a density functional study with WEIN2K code. They have used LDA first with the combination of GGA and then again without the combination of GGA for total energy optimization with exchange-correlation functions.

BaX compounds have shown a transition from B1 phase to B2 phase under some standard condition. For investigating the properties they have utilized LDA in and without a combination of GGA. At certain different values of unit cell's volumes, the total energy calculations have been done at the stable phase and the results were fitted with the Brich–Murnaghan's equation of state. For the BaX compounds, the optical and electronic properties have been calculated with the DFT by Pourghazi and Dadsetani [8]. They have studied mainly NaCl (B1) crystal structure. FP-LAPW method has been used to obtain the electronic band structures of the barium chalcogenides compounds. For constructing the Hamiltonian equation, the WIEN2K code has been used. GGA scheme is used for the exchange-correlation potential treatment. The spin–orbit coupling was taking place to calculate the optical and electronic properties and then the same process had been followed without the spin–orbit coupling also to find the same properties. Also, some important parameter like dielectric function, the reflectivity, the optical absorption coefficient, and the energy loss function has been calculated. Their calculations revealed that the inclusion of the spin–orbit coupling decreases the energy band gap by about 0.27 eV, 0.24 eV and 0.16 eV for BaTe, BaSe and BaS, respectively. Benamrani et al. [9] have performed energy optimization with first-principle study within the pseudo-potential plane wave method as inbuilt in ABINIT to investigate the properties of BaX in B1 as well as B2 structures. The vibrational, elastic and dynamical properties have been determined within the

LDA. By changing the volume of unit cells the dependence of the pressure with the structural, vibrational and lattice dynamical parameters have been calculated simultaneously. It was concluded in this work that the vibrational and elastic properties and also the lattice dynamics are determined with the help of DFT approach and the results for elastic constant values are in an excellent agreement with another observed data using LDA-FP-LAPW method.

### 3 Computational Method

Linear combination of atomic orbital, a first-principle approach has been done to determine the structural and electronic properties of barium chalcogenides compounds in this paper. For the calculations, the Kohn–Sham Hamiltonian is solved in the DFT as present in the CRYSTAL06 code. The Kohn–Sham Hamiltonian built taking into an account the Becke exchange program and PBE correlation scheme. To calculate the structural properties of barium chalcogenides the energy optimization was done by minimizing the total energy with respect to the unit cell volume for each crystal structure. The calculated results are verified with the existing results. The self-consistent calculations are used taking into account 84 k points of the Brillion zone irreducible with sufficient tolerance level. The self-consistency has been achieved by 55% mixing within nine cycles.

#### 3.1 Result and Discussion

In the structural properties lattice constant and bulk modulus of BaX compounds in B1 structure as well as in B2 structure have been computed by the total energy optimization with the variation of volume of primitive cell of the crystal by LCAO method. Figures 1, 2, 3, 4, 5 and 6 represent the energy versus volume curve for the XH. In these figures, the dots represent the calculated energies through DFT and the curves represent the fitted energies to the Birch–Murnaghan equation of state, which is represent mathematically by

$$E(V) = E_0 + \frac{9V_0B_0}{16} \left\{ \left[ \left( \frac{V_0}{V} \right)^{\frac{2}{3}} - 1 \right]^3 B'_0 + \left[ \left( \frac{V_0}{V} \right)^{\frac{2}{3}} - 1 \right]^2 \left[ 6 - 4 \left( \frac{V_0}{V} \right)^{\frac{2}{3}} \right] \right\}.$$

Here,  $E(V)$  is energy corresponds to a particular volume,  $E_0$  is equilibrium energy,  $V_0$  is the corresponding volume and  $B_0$  is bulk modulus and  $B'_0$  is the pressure derivative of bulk modulus.

In Table 1 structural parameters are shown.

The electronic band structures of barium chalcogenides compounds have been examined in the stable state of lattice constant and are shown in Figs. 7, 8 and 9. In

**Fig. 1** Energy versus volume plot (B1)

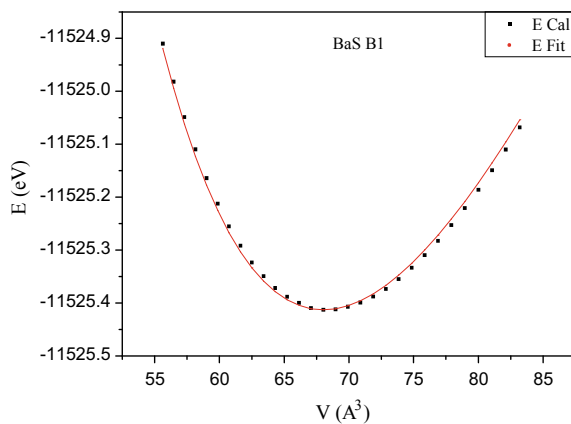


**Fig. 2** Energy versus volume plot for BaS (B2)

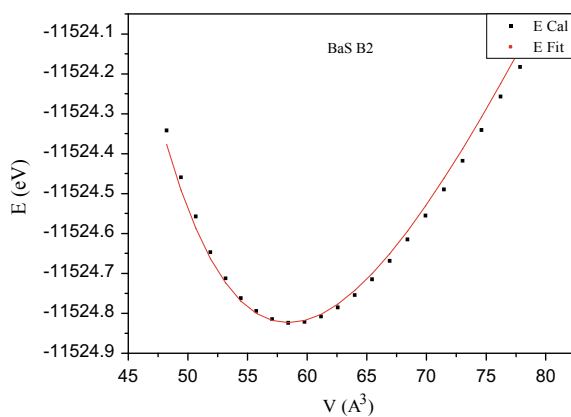


**Fig. 3** Energy versus volume plot for BaSe (B1)

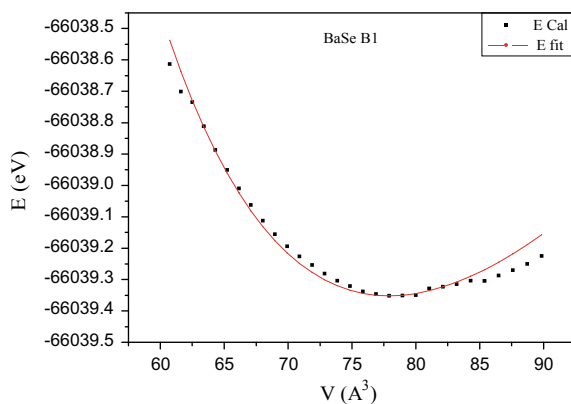


**Fig. 4** Energy versus volume plot for BaSe (B2)

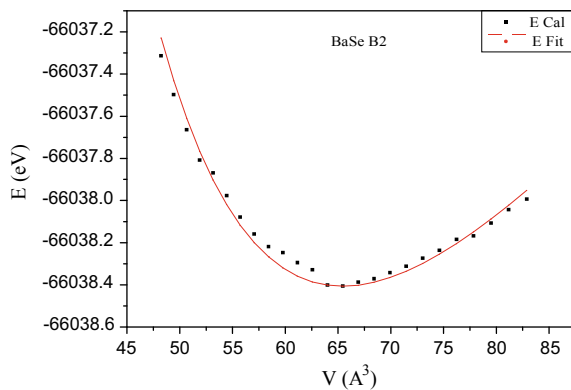


**Fig. 5** Energy versus volume plot for BaTe (B1)

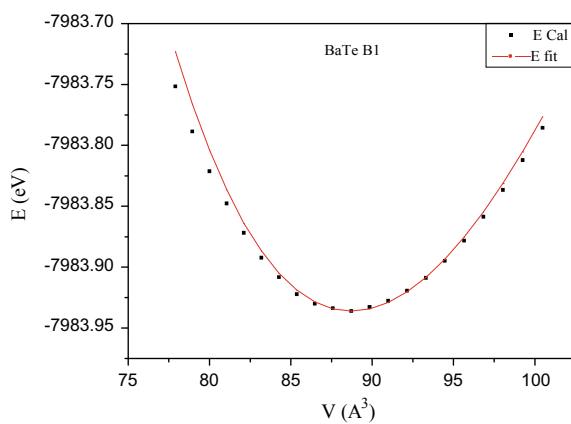


**Fig. 6** Energy versus volume plot for BaTe (B2)

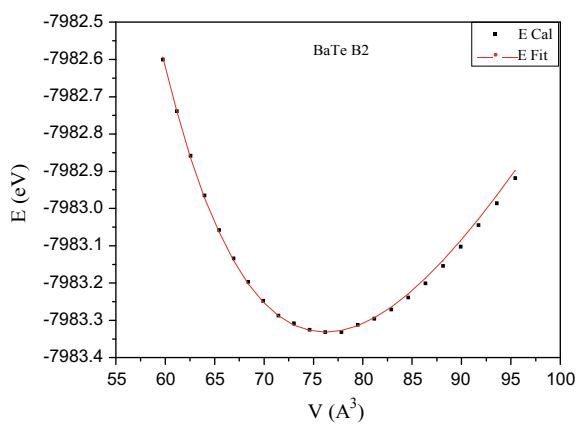
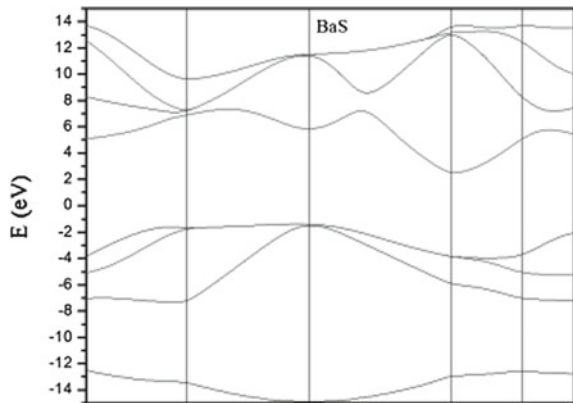


**Table 1** Present and previously calculated lattice parameter (a), bulk modulus ( $B_0$ ) for the barium chalcogenides compounds

Compound	BaS (B1)	BaS (B2)	BaSe (B1)	BaSe (B2)	BaTe (B1)	BaTe (B2)
<i>Lattice constant</i>						
Present work	6.48	3.88	6.78	4.03	7.08	4.24
Others calculations	6.27 [4], 6.4 46 [7], 6.27 2 [9]	3.73 [9], 3.76 [3]	6.668 [7], 6.48 [9], 6.45 [3]	3.87 [9], 3.84 [3]	7.079 [7], 6.8 68 [9], 6.87 [3]	4.117 [9], 4.08 [3]
<i>Bulk modulus</i>						
Present work	48.8	57	44	48	41	43
Others calculations	43.43 [4], 4 8.45 [7], 50 86 [9]	52.62 [7], 56 74 [9], 57.23 [3]	41.29 [7], 46.25 [9]	46.28 [7], 48 62 [9]	33.02 [7], 35 41 [9]	39.81 [7], 39 51 [9]

**Fig. 7** Plot for energy band gap of BaS



the Brillouin zone, W(0.5, 0.25, 0.75), L(0.5, 0.5, 0.5),  $\Gamma$ (0.0, 0.0, 0.0), X(0.5, 0.0, 0.0), W(0.5, 0.25, 0.75) and K(0.375, 0.375, 0.75) are the various symmetry points considered.

It has been observed from the figures that BaS, BaSe and BaTe have indirect ( $\Gamma$ -X) bandgap.

These values are consistent with the previous calculations. The calculated results of band gaps for barium chalcogenides are given in Table 2.

**Fig. 8** Plot for energy band gap of BaSe

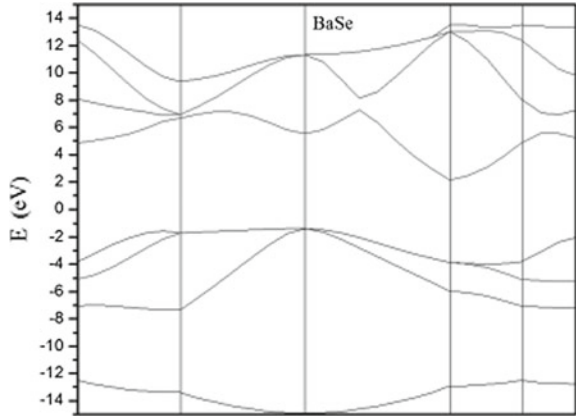


**Fig. 9** Plot for energy band gap of BaTe

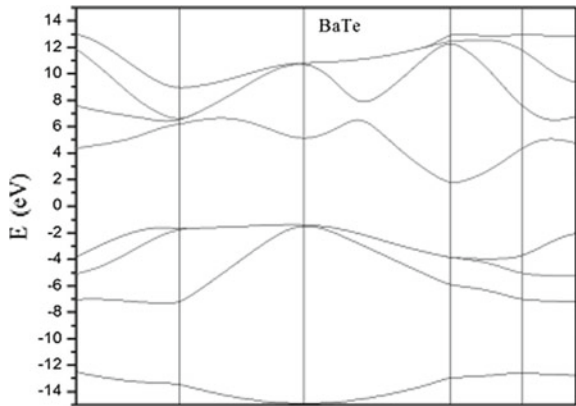


**Table 2** Experimental energy gap value for barium chalcogenides

Compounds	Present work	Others calculations
BaS	3.72	2.330 [8], 3.07 [1]
BaSe	3.52	2.081 [8], 2.77 [1]
BaTe	3.02	1.607 [8], 2.36 [1]

## 4 Conclusion

In summary, LCAO method has been used to perform first-principle calculations to investigate the structural and electronic properties of the BaX compounds. It has been observed that according to total calculated energy the B1 phase for barium chalcogenides is more stable as compare to B2 phase. The calculated energy band gap for BaX are 3.72, 3.52 and 3.02 eV. The calculated structural and electronic properties for barium chalcogenides are in excellent contract with previous studies.

## References

1. Bouhemadu, A., Khenata, R., Zegrar, F., Sahnoun, M., Baltache, H., Reshak, A.H.: Ab initio study of structural, electronic, elastic and high pressure properties of barium chalcogenides. *Comput. Mater. Sci.* **38**, 263–270 (2006)
2. Lin, G.Q., Gong, Hao, Ping, Wu: Electronic properties of barium chalcogenides from first-principles calculations: tailoring wide-band-gap II-VI semiconductor. *Phys. Rev. B* **71**, 085203 (2005)
3. Tuncel, E., Colakoglu, K., Deligoz, E., Ciftci, Y.O.: A first-principles study on the structural, elastic, vibrational, and thermo dynamical properties of BaX (X = S, Se, and Te). *J. Phys. Chem. Solids* **70**, 371–378 (2009)
4. Arya, Balwant S., Aynyas, Mahendra, Sanyal, Sankar P.: High pressure study of structural and elastic properties of barium chalcogenides. *Indian J. Pure Appl. Phys.* **46**, 722–726 (2008)
5. Bhardwaj, P., Singh, S., Gaur, N.K.: Structural and elastic properties of barium chalcogenides (BaX, X = O, Se, Te) under high pressure. *Cent. Eur. J. Phys.* **6**(2), 223–229 (2008)
6. Drablia, S., Meradji, H., Ghemid, S., Boukhris, N., Bouhafsand, B., Nouet, G.: Electronic and optical properties BaO, BaS, BaSe, BaTe and BaPo compounds under hydrostatic pressure. *Mod. Phys. Lett. B* **23**, 065–3079 (2009)
7. El Haj Hassan, F., Akbarzadeh, H.: First-principles elastic and bonding properties of barium chalcogenides. *Comput. Mater. Sci.* **38**, 362–368 (2006)
8. Pourghazi, A., Dadsetani, M.: Electronic and optical properties of BaTe, BaSe and BaS from first principles. *Phys. B* **370**, 35–45 (2005)
9. Benamrani, A., Kassali, K., Bouamama, Kh: Pseudopotential study of barium chalcogenides under hydrostatic pressure. *High Press. Res.* **30**, 207–218 (2010)